Aerodynamic Mechanisms of Flapping Flight

Mustafa Perçin

Aerodynamic Mechanisms of Flapping Flight

Proefschrift

ter verkrijging van de graad van doctor
aan de Technische Universiteit Delft,
op gezag van de Rector Magnificus prof. ir. K. C. A. M. Luyben,
voorzitter van het College voor Promoties,
in het openbaar te verdedigen op
woensdag 23 september 2015 om 10:00 uur

door

Mustafa PERÇİN

ingenieur luchtvaart- en ruimtevaart
geboren te İzmir, Turkije.

Dit proefschrift is goedgekeurd door:

Promotor	Prof. dr. F. Scarano
Copromotor	Dr. ir. B. W. van Oudheusden
Copromotor	Dr. G. C. H. E. de Croon

Samenstelling promotiecommissie:

Rector Magnificus,	voorzitter
Prof. dr. F. Scarano,	Technische Universiteit Delft, promotor
Dr. ir. B. W. van Oudheusden,	Technische Universiteit Delft, copromotor
Dr. G. C. H. E. de Croon,	Technische Universiteit Delft, copromotor

Onafhankelijke leden:

Prof. dr. ir. F. van Keulen,	Technische Universiteit Delft
Prof. dr. N. L. O. Çetiner-Yıldırım,	İstanbul Technical University
Prof. dr. L. David,	Université de Poitiers
Dr. F. T. Muijres,	Wageningen University
Prof. dr. ir. L. L. M. Veldhuis,	Technische Universiteit Delft, reservelid

This research is supported by the Dutch Technology Foundation STW, which is part of the Netherlands Organisation for Scientific Research (NWO) and partly funded by the Ministry of Economic Affairs (project number 11023).

Cover photo by:	Mustafa Perçin
Cover design by:	Özge Başkan & Mustafa Perçin
Printed by:	Ipskamp Drukkers BV

ISBN 978-94-6259-843-0

An electronic version of this dissertation is available at
http://repository.tudelft.nl/.

İstikbal göklerdedir.

M. Kemal Atatürk

Contents

1

Introduction

For once you have tested flight you will walk the earth with your eyes turned skywards, for there you have been and there you will long to return.

Leonardo da Vinci

1

Nature has always been a great source of inspiration for human beings for ages. Mankind has curiously examined and tried to understand the various mechanisms used by the other life forms. Beyond doubt, flight has been one of the most intriguing topics to humans after watching birds and insects with wonder and envy for centuries. The desire of flying like natural fliers by flapping wings emerges in different spots of the history of humanity: from the legendary flight of Icarus to the sun by using wings made of feathers and wax in Greek mythology to the human-powered ornithopter designs of Leonardo da Vinci and the legendary flight of Hezarfen Ahmet Celebi jumping from the Galata tower in Istanbul with bird-inspired wings in the 16th century (Fig. 1.1). Despite this long-lasting admiration, the first flight of humans happened in a balloon rather than on wings in the late 18th century. It took more than another century until the first powered airplane flight with fixed wings was performed thanks to the diligent efforts of the Wright brothers particularly between 1899 and 1905 (Grant, 2007). Since then, our knowledge about fixed-wing aerodynamics has increased substantially, whereas the mysteries of flapping-wing aerodynamics remained mostly unresolved. However, the recent increase of interest in the field of micro aerial vehicles (MAVs) has again stimulated attention to flapping-wing aerodynamics particularly in the last two decades, as conventional modes of flight (i.e., fixed and rotary wing) were discovered to be relatively insufficient in terms of efficiency and maneuverability at the intended flight regimes, which are characterized by low Reynolds number.

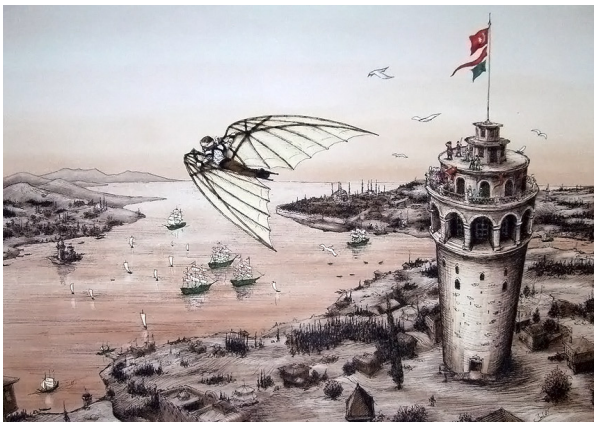

Figure 1.1: An illustration of the legendary flight of Hezarfen Ahmet Celebi (adapted from BilimDurağı, 2015)

In his survey, Carmichael (1981) defined the Reynolds number realm related to flight to cover 10 orders of magnitude from 1 to 10^9. He investigated this spectrum in 12 segments indicating that in the regime up to 10^6, man and nature are present together in flight. As shown in the flight Reynolds number spectrum in (Fig. 1.2), insect flight takes place in the range from 10^2 to 10^4, while birds fly in the Reynolds number range of 10^4 to 10^6 (Lissaman, 1983). Most of the MAVs, due to their small size and low flight speed, operate at Reynolds numbers 10^4 to 10^5 (Shyy et al, 1999).

Comparison of different modes of flight from an aerodynamics point of view in the intended flight regimes reveals prominent differences. Figure 1.3 presents an overview

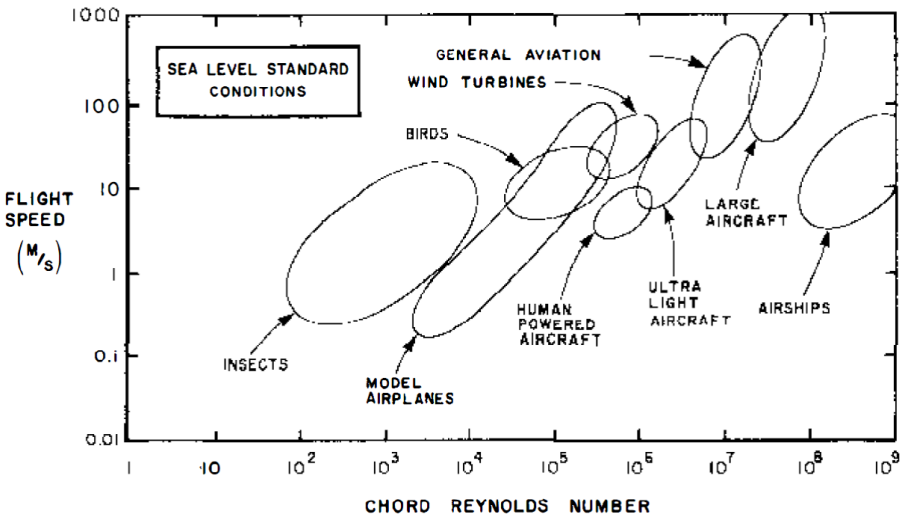

Figure 1.2: Flight Reynolds number spectrum (adapted from Lissaman, 1983)

of maximum lift coefficients reported in the literature for a range of Reynolds numbers including a variety of different cases from experiments on hovering insects to measurements on smooth airfoils in a steady free-stream flow (Jones and Babinsky, 2010). The shaded area represents experiments in steady flow, whereas the remaining part refers to unsteady or three-dimensional experiments. It is clear that in general the steady flow case of airfoils performs reasonably well at high Reynolds numbers yet the performance deteriorates at low Reynolds numbers even when insect wing geometries are used. However, switching to the unsteady regime by means of flapping-wing motion evidently increases the aerodynamic performance at these scales. Strikingly, the overall maximum lift coefficient is achieved at a very low Reynolds number ($Re \approx 10^2$), which can be explained from the occurrence of the dynamic stall and the formation of the leading edge vortex (LEV, see Section 2.2.1).

It is clear that flapping-wing aerodynamics is more productive than the conventional means of force generation in the low Reynolds number flight regimes. This is discussed and exemplified also in the context of different MAV designs in the following sections of this chapter. On the other hand, flapping-wing flight is a considerably complicated unsteady and three-dimensional phenomenon, which requires an elaborate investigation by means of advanced experimental or numerical techniques. In this respect, the present thesis pursues an experimental exploration of the aerodynamic mechanisms of flapping-wing phenomena by use of state-of-the-art flow measurement techniques, which are capable of providing time-resolved three-dimensional information. The study is divided into two parts, in which flapping-wing aerodynamics is investigated in the context of a flapping-wing MAV and in a generic experimental setup to gain more fundamental understanding, respectively.

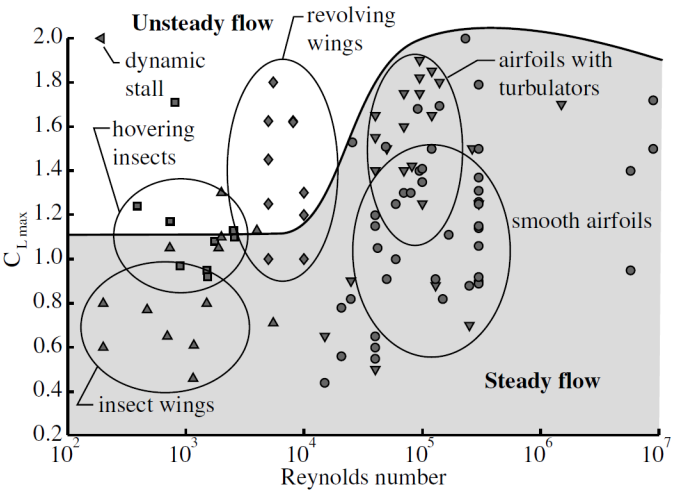

Figure 1.3: Maximum lift coefficient vs. Reynolds number (adapted from Jones and Babinsky, 2010)

1.1. Micro aerial vehicles

Micro aerial vehicles (MAVs) are generally defined as the class of unmanned aerial vehicles (UAVs) that have overall dimensions not larger than 15 cm according to the definition by the Defense Advanced Research Agency (DARPA) (Li, 2008). The stringent MAV definition by DARPA also includes other key design requirements in addition to the maximum dimension: a maximum weight of 100 grams with a payload of 20 grams; endurance of 60 minutes; maximum flight speed of 15 m/s (Sirohi, 2013). Alternatively, in a broader sense, MAVs can be regarded as flying air vehicles with length scales similar to small birds and insects.

The low-speed flight regime and unmanned flight capability of MAVs make them suitable for several military and commercial missions such as surveillance, reconnaissance and gathering intelligence in environments that are hazardous or physically inaccessible for humans. The envisaged features of performing slow or hovering flight and maneuvering with ease allow MAV operations in building interiors and complex environments but also necessitate aerodynamically efficient designs in low Reynolds number flight regimes. In general, three different approaches can be distinguished in the design of MAVs: firstly, fixed-wing designs that are primarily based on conventional force generation mechanisms of attached flow over the wings similar to large scale aircraft; secondly, rotary-wing designs in which forces are generated by the rotating blades; and thirdly, flapping-wing designs which are inspired from biological flyers and make use of various unconventional force generation mechanisms.

1.1.1. Fixed-wing MAVs

Fixed-wing configurations are undoubtedly the most straightforward approach both in terms of manufacturing and aerodynamic design. The aerodynamics of fixed-wing flight

has been investigated thoroughly over the last century and is mostly well-understood from low-speed incompressible flow regimes to high-speed compressible flow regimes. However, fixed-wing MAVs lack hovering capability (unless a hybrid fixed-rotary wing design approach is taken) as it is always necessary for the wing to experience a forward flight speed in order to generate lift, which makes fixed-wing MAVs unsuitable for operations indoors or in confined spaces. Even during slow forward flight, fixed-wing designs are not aerodynamically efficient due to the increased thickness of the boundary layer at relatively low Reynolds numbers and in turn increased viscous drag. Moreover, in the Reynolds number range of MAVs, the laminar boundary layer is prone to separate under an adverse pressure gradient. At moderate values of the Reynolds number the separation is usually followed by a transition to turbulence enabling the flow to reattach on the wing further downstream. This phenomenon is known as laminar separation bubble and it limits the lift coefficient while increasing the drag (Lissaman, 1983). It was also shown that for Reynolds numbers smaller than 50,000, the separated laminar boundary layer may not transition to turbulent regime in time to attach to the airfoil surface again (Carmichael, 1981), leading to stall with an associated loss of lift and a dramatic increase in the pressure drag.

One of the most famous examples of the fixed-wing MAVs is the Black Widow MAV (Fig. 1.4a) from the technology company AeroVironment (Grasmeyer and Keennon, 2001). In order to fit in the official MAV definition while maximizing the wing area, it is designed as a flying wing and the early prototype had a disc planform which was shown to have some potential to increase the lift to drag ratio. The first prototype was able to perform a 9 second flight in 1996. In 1997, the endurance had been increased to 16 minutes by use of lithium batteries. Further improvements of the design led to the final configuration which has a wing span of 15.24 cm and a mass less than 100 grams. It is able to reach an endurance of 30 minutes and a maximum configuration range of 2 km. The flight speed of approximately 13.4 m/s makes it a suitable platform only for outdoor missions. It is also equipped with a colour video camera that downlinks the video to the pilot.

Clearly, the span length of fixed-wing MAVs is constrained by the maximum dimension definition, whereas the wing area is increased to maximize lift generation. These two aspects lead to low aspect ratio wing designs, for which two coherent counter-rotating vortices are present near the wing tips (i.e. tip vortices). The vortices strengthen with increasing angle of attack and may even cover the complete wing surface. The presence of these vortical structures have twofold effect on the aerodynamic performance. First, low aspect ratio wings generate enhanced lift at high angles of attacks due to low pressure region of these vortices on the suction side of the wing (Mueller and DeLaurier, 2003). Second, due to strong downwash created by these vortices and thus decrease of the effective angle of attack, the wing experiences relatively high induced drag (Anderson, 2001). To minimize this effect, the Naval Research Laboratory came up with a concept that also has a low aspect ratio wing and is equipped with two propellers mounted at the leading edge wing tips (Kellogg et al, 2001). The propellers rotate in the opposite direction of the tip vortices in order to decrease the induced drag. Their Micro Tactical Expendable (MITE) air vehicle family consists of a number of different configurations with a chord length of approximately 23 cm and a span length ranging from 20 cm to 46 cm depending on the payload weight. The MITE 2 (Fig. 1.4b), which has a span length of 35.5 cm, can carry an

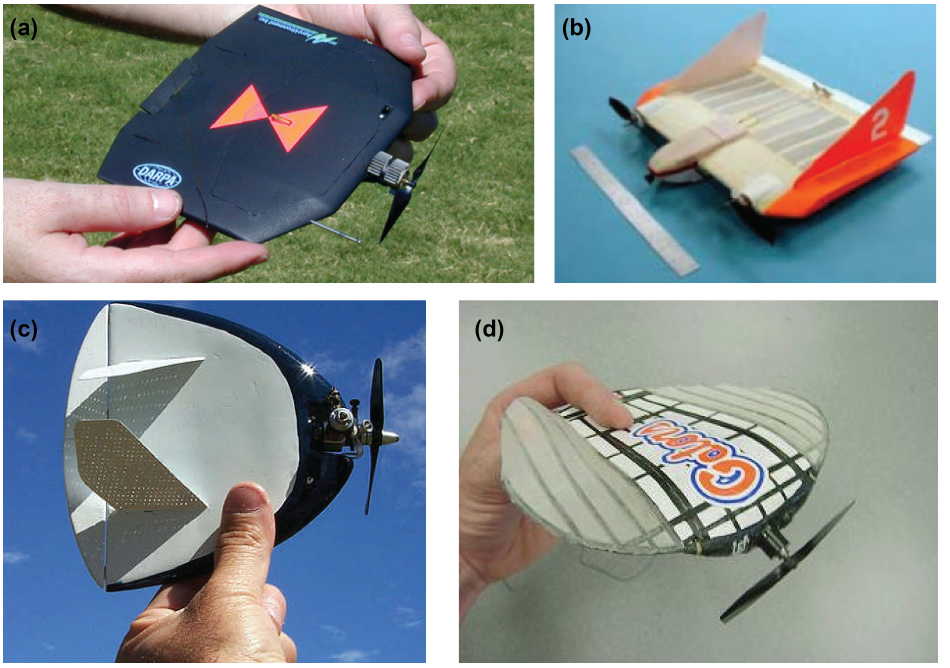

Figure 1.4: **a** Black Widow MAV from AeroVironment (adapted from Li, 2008), **b** the Mite 2 air vehicle (adapted from Kellogg et al, 2001), **c** Trochoid aircraft (adapted from Morris and Holden, 2000), **d** flexible wing MAV of University of Florida (adapted from Ifju et al, 2002)

analog camera with a mass of 28 grams and can achieve a flight duration of 20 minutes in an airspeed range of 4.5 to 9 m/s. Despite their relatively small forward flight speeds, the MITE air vehicles do not satisfy the MAV size definition.

Another aspect of relevance to these kind of fixed-wing MAV configurations is that low aspect ratio wings are susceptible to rolling instabilities, which is even enhanced by the presence of the tip vortices (Lian et al, 2003). On the other hand, it was shown for particularly circular wing planforms that control surfaces are not really effective due to occurrence of a strong vortical flow. Morris and Holden (2000) from the MLB company modified their initial circular wing planform into a trochoidal shape (Fig. 1.4c) which has 11 % less surface area than a circular wing for the same aspect ratio. However, with the wing dimensions increasing with longitudinal location, this brings in desirable aerodynamic properties similar as for a delta wing planform while also increasing the effectiveness of the control surfaces. Their 20 cm Trochoid MAV with a video transmission and stability augmentation system is capable of performing a 20 minute flight at flight speeds ranging from 4.5 to 27 m/s.

Moreover, in the operation regime of MAVs, velocity fluctuations in the free stream due to gusts or turbulence can have a strong impact on the flight behaviour because the magnitude of these disturbances can easily reach the same order of magnitude as the MAV's flight speed (Shyy et al, 1999). In order to get a favourable aerodynamic performance in a fluctuating low Reynolds number regime, the use of flexible wings was considered and

investigated (Ifju et al, 2002; Lian et al, 2003; Smith and Shyy, 1995; Waszak et al, 2001), which can move and deform with the unsteady disturbances and lead to a smoother flight platform. Furthermore, it was shown that flexible membrane wings show more favourable stall characteristics because of their higher stall angles when compared to those of rigid wings (Waszak et al, 2001). In this context, Ifju et al (2002) designed an MAV with a span length of 15 cm at the University of Florida (Fig. 1.4d). The MAV features an electric motor with a single nose-mounted propeller and weighs approximately 40 grams. The flight speed is in the range of 5-10 m/s and the MAV has a maximum endurance of 15 minutes while carrying an on-board camera and a transmitter. The MAV itself is essentially a flying flexible membrane wing that is comprised of unidirectional carbon fiber prepreg laminate forming a leading edge spar and chordwise battens (Lian et al, 2003). The use of a flexible wing was found to result in an easier-to-control aircraft when compared to the similar vehicle with a rigid wing (Ifju et al, 2002).

In order to provide fixed-wing MAVs the ability to hover, some vehicles have been designed such that they can hover and transition to fast forward flight. The Hoverfly from Aerovironment can be given as an example for this category, which has a mass of 180 grams, can hover for 7 minutes and perform forward flight for 13 minutes at a cruise speed range of 15-20 m/s (Pines and Bohorquez, 2006). Obviously, such a design approach results in a heavier vehicle while not improving the endurance. This principally stems from the different power requirements that apply for the forward flight and hovering flight regimes. In the case of the former, the propulsion system has to deliver enough thrust to overcome drag and reach a forward flight speed that is sufficient to generate lift equal to weight of the vehicle in order to maintain level flight. Therefore, the required thrust is essentially equal to the vehicle weight (W) divided by the wing's lift-to-drag ratio (L/D). On the other hand, in the hover configuration the propulsion system needs to generate a thrust equal to the weight of the vehicle. At conventional scales, typical aircraft can achieve L/D values from 20 to 100 so that they need considerably less thrust and power to stay aloft during forward flight (Schaefer, 2008). However, it should be noted that this distinctive superiority of forward flight of fixed-wing MAVs deteriorates due to aforementioned low Reynolds number effects on the aerodynamic efficiency and low-aspect-ratio effects common to MAV designs. It is theorized that the endurance characteristics of hovering rotorcrafts may become competitive with fixed-wing MAVs at some scales (Kroo and Kunz, 2001).

1.1.2. Rotary-wing MAVs

In terms of MAVs with hover capability, rotary-wing designs are arguably the most frequently encountered configurations. This category of MAVs can be classified in groups based on the number of rotors and their orientation. Single rotor applications can be considered as scaled down versions of full size helicopters, which feature a main rotor and a smaller rear rotor to create an anti-torque. Radio-controlled (RC) models of small helicopters are commercially available (Picoo Z and Nano Falcon from Silverlit toys). Although single rotor systems are good in terms of controllability and maneuverability, they are not very favourable in terms of the complex mechanical construction, relatively large rotor and long tail boom (Bouabdallah and Siegwart, 2007). Another design approach is to make use of two counter-rotating rotors mounted in a coaxial configuration. The coaxial

rotary-wing designs are convenient in terms of their inherent compact size, however they suffer from a degraded aerodynamic efficiency due to adverse wake interference between the rotors (Bohorquez et al, 2003). Tandem or side-by-side rotor configurations eliminate this undesired effect at an expense of increasing size. The MICOR from Maryland (Fig. 1.5a) is an example of an MAV with coaxial rotors that is approximately 100 grams (Pines and Bohorquez, 2006). It has a rotor diameter of 15.24 cm and can hover for only 3 minutes, which they attributed to the poor aerodynamic performance of the coaxial rotors (Bohorquez et al, 2003). Members of the Proxflyer family developed by Proxflyer AS are other examples of coaxial rotor MAVs. The smallest member, the Picoflyer, has a rotor diameter of 60 mm and a mass of 3.3 grams including battery and control but the flight time is limited to a minute. However, the Microflyer with 128 mm rotor diameter and 7.8 grams of mass can reach 10 minutes of flight duration (Muren, 2005).

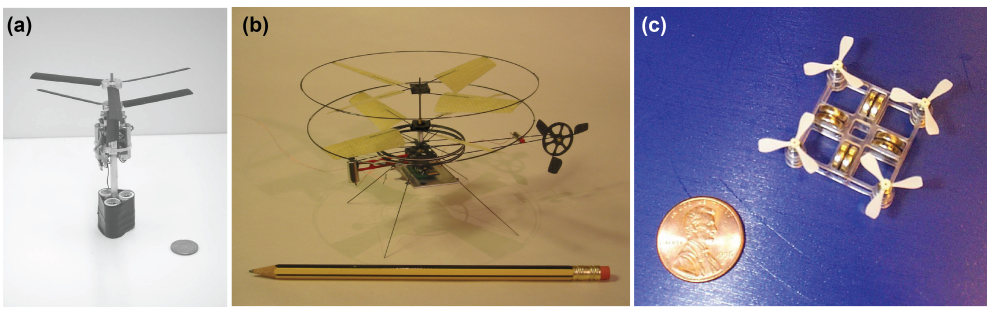

Figure 1.5: **a** MICOR from University of Maryland (adapted from Bohorquez et al, 2003), **b** Microflyer from Proxflyer AS (adapted from Muren, 2005), **c** Mesicopter from Stanford University (adapted from Kroo and Kunz, 2001)

Recently, there has been an increasing interest in the use of three or more rotors in designing UAVs. Such configurations, particularly quadrotors, are very popular mostly due to their ease of control which is accomplished by simply varying the rotational speed of the different rotors and consequently generating a moment about the center of mass. In addition to the good controllability, quadrotors have the advantages of simple construction and increased capacity of payload. On the other hand, their relatively large size and increased weight due to the number of rotors and motors, and high power consumption emerge as their weak points in terms of satisfying MAV requirements. However, recent developments in microelectronics have made it possible to build micro-size quadrotors despite having shorter endurance and no room for extra payload. For instance, the commercially available QR-1 from Traxxas has a blade circle diameter of approximately 15 cm, a mass of 33 grams featuring a six-axis stabilization system. Yet, the flight time is limited to 6-8 minutes with a fully charged battery. Another small scale example is the Mesicopter (Kroo and Kunz, 2001) from Stanford University. It is a centimeter scale quadrotor, with rotors that are even smaller than a penny (Fig. 1.5c), and it is still in the development stage.

Regardless of the different number and configuration of rotors used in the design of the MAV, the aerodynamic efficiency is influenced by the detrimental effects of the low Reynolds number operating regime similar to fixed-wing MAVs. For a hovering MAV, the figure of merit (FM) is defined as the ratio of the ideal power required to hover and the

actual power. A larger value of FM means that less power is required to generate a given thrust and for an ideal rotor FM is unity. In reality, most full-scale modern helicopter rotors operate within a figure of merit range from 0.65 to 0.85 (Pines and Bohorquez, 2006). However, the Reynolds number range at which the outer section of MAV rotors operate lies several order of magnitudes lower than for full scale rotors (i.e. in the Reynolds number range between 30,000 and 70,000) (Bohorquez et al, 2010). Thus, rotor blades experience much higher viscous drag with a consequent decrease of FM. For a rotor diameter of 15.24 cm operating at a tip Reynolds number of 40,000, the maximum achievable FM values are about 0.55 after a careful design of airfoil shape as well as spanwise distribution of airfoil type and twist (Hein and Chopra, 2007).

1.1.3. Flapping-wing MAVs

Deficiencies of conventional fixed-wing or rotary-wing approaches in terms of aerodynamic performance and thus achieving the necessary specifications for small-scale MAV designs have directed attention to the biologically inspired flapping-wing approach. It is judicious to mimic biological flyers, particularly insects and small birds, in view of their exceptional performance in the low Reynolds number flight regimes and capabilities of hovering, maneuvering with ease and performing extraordinary flight patterns such as flying backwards or sideways and landing up-side down. At this point, it is important to mention that the first appearance of winged insects dates back to the Namurian division of the Upper Carboniferous approximately 325 million years before the present (Wootton, 1981). Examination of early fossils showed that the wingspan ranged from 10 to 710 mm suggesting various adaptations in flight style. The ancestors of dragonflies, the *Protodonata*, were among the first flyers and their fossils showed similarities with the modern forms in terms of wing geometries albeit probably with less refinements. The insects have evolved successfully in terms of wings, kinematics, aerodynamics, control and sensory systems through natural selection for hundreds of millions of years (Ellington, 1999) which has led to their superior performance today. Contrary to the other two flight mechanisms referred to previously (fixed and rotary wing), the generation of forces in the flapping-wing flight of biological flyers incorporates several unconventional and complex unsteady mechanisms, which are discussed in Chapter 2.

In this section, the flapping-wing airframes are classified and explained in terms of flapping-wing configurations: (1) MAVs that use two flapping wings similar to birds, bats and a variety of insects; (2) MAVs that employ four wings such that there exists a wing pair on each side of the fuselage flapping in an opposite phase. For a more detailed and extensive classification of flapping-wing MAVs, the reader is referred to Gerdes et al (2012). The first category can be considered as the traditional method of flapping flight and most of the MAVs which use this configuration are able to perform a fast forward flight. Because of the unbalanced wing motion, these flapping-wing platforms experience significant vertical inertial oscillations. The rocking motion of the body is not favourable for camera vision and stable sensory measurements.

The MicroBat is a member of this category and was developed in California Institute of Technology (Pornsin-sirirak et al, 2000). The project was initiated in 1998 with an objective of developing a wireless radio-controlled, battery-powered flapping-wing MAV, that is the size of a small bird and weighs less than 12 grams. Another design goal of the project was to

create wings using Micro-Electro-Mechanical Systems (MEMS) technology. Accordingly, they built wings using titanium alloy metal as the wing frame and poly-monochloro-para-xylelene (parylene C) as the membrane. They performed the first successful forward flight with a prototype that has a maximum size of 15.24 cm and a mass of 11.5 grams with a Ni-Cd battery in 1999 and it lasted for only 18 seconds. Use of a Polymer Lithium Ion battery with a radio transreceiver allowed them to perform a radio-controlled flight with a duration of about 6 minutes.

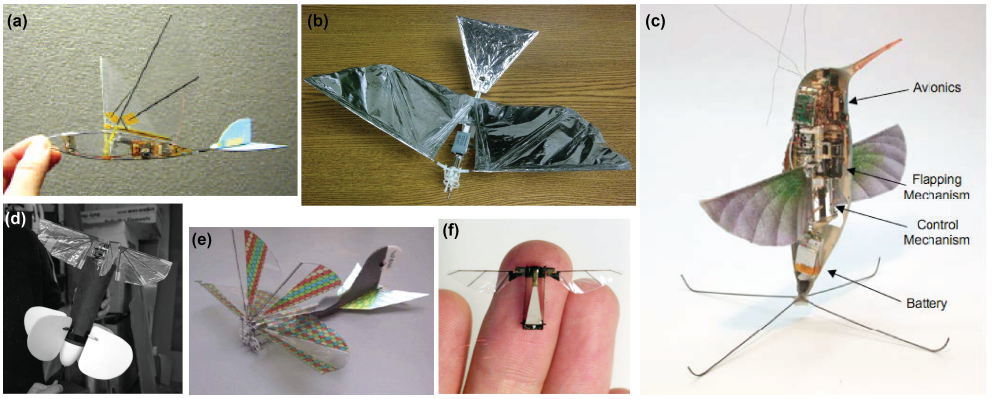

Figure 1.6: **a** Microbat from CalTech (adapted from Pornsin-sirirak et al, 2001), **b** Small bird from University of Maryland (adapted from Mueller et al, 2009), **c** Nano Hummingbird from Aerovironment (adapted from Keennon et al, 2012), **d** Mentor from SRI and University of Toronto (adapted from Zdunich et al, 2007), **e** flapping-wing MAV from Wright State University (adapted from Hsu et al, 2010), **f** Microrobotic Fly from Harward University (adapted from Wood, 2008)

University of Maryland's small and big birds also use a single pair of flapping wings to achieve sustained flight (Gerdes et al, 2012). The small bird has a wing span of 34.3 cm and it weighs approximately 13 grams including a battery and with a payload capacity of 2.5 grams. It can reach a maximum flight velocity of 4.4 m/s while flapping its wings at 7.2 Hz and stay airborne for a duration of 5 minutes (Mueller et al, 2010). On the other hand, the big bird has a wing span of 57.2 cm and a mass of 35 grams with a payload capacity of 12 grams. It has a flight duration of 8 minutes with a flapping frequency of 5 Hz and a flight velocity of 3.75 m/s. They used a 7.2 gram camera and transmitter setup on this platform to send live images to the ground station during flight (Mueller et al, 2009). Both versions are equipped with hand-made wings, built by use of thin mylar foil stretched over carbon fiber stiffeners, while control is achieved by actuating the tail in a rudder-like motion.

Arguably the most impressive member of the monoplane flapping-wing MAV category is the Nano Hummingbird developed by the AeroVironment company (Keennon et al, 2012). It was born as a part of the Nano Air Vehicle (NAV) program which was started in 2005 by DARPA with the goal of developing a new class of UAVs that employ biological mimicry with a maximum dimension of 7.5 cm, a maximum total mass of 10 grams including 2 grams of payload and a flight regime ranging from sustained hovering flight to forward flight at a speed of 10 m/s. To reach this goal, several prototypes were built

starting from a bi-plane flapping-wing model with a span length of 22.5 cm, which uses simple tail controls. It was able to perform forward flight at low speeds but was not easy to control in stationary hover condition. Decreasing the wing span brought in more difficulties in controlling the vehicle even in forward flight due to ineffectiveness of the control surfaces as a result of the low induced velocities for this reason they abandoned the use of large tail surfaces for control matters. In the latest stages, the control is achieved by means of modulating the wing twist and wing rotation for both wings independently so that the force production of both wings can be changed independently to perform the intended maneuver. The final Nano Hummingbird prototype weighs 19 grams and has a wing span of 16.5 cm. It flaps its wings at a frequency of 30 Hz and can transition between hovering flight and forward flight with a maximum flight speed of 6.7 m/s. The final version which carries also an on-board camera has a flight endurance of 4 minutes. However, the long endurance version (Saturn) without a camera system can hover for 11 minutes.

Use of two pair of wings in flapping locomotion eliminates the vertical inertial oscillations and results in a more stable platform. Furthermore, depending on the design of the flapping system, biplane MAVs could benefit from the force enhancement caused by the wing-wing interaction effect that is referred to as the clap-and-fling mechanism (see Section 2.2.3), albeit at the expense of higher power consumption. Thanks to the increased force generation, MAVs of this second class generally have the capability to hover in addition to fast forward flight.

An example of this category is the Mentor developed by SRI and University of Toronto (Zdunich et al, 2007). They built two different prototypes: one with an internal combustion engine with a total mass of 580 grams (namely SF-2.5); and another one with an electric motor weighing 440 grams (namely SF-3). Both configurations feature four wings with a maximum span of 36 cm which are driven in flapping motion only in horizontal axis and performing- clap-and-fling motion to enhance the force generation. The rotational motion of both engines is converted into oscillatory motion with a nominal frequency of 30 Hz by use of a gearbox and a rotary-to-oscillatory transmission. The control of the MAV was achieved by means of four independently actuated fins of approximately the same size with the flapping wings. They performed sustained, stable and controlled hovering flight with SF-2.5 in 2002, which lasted about a minute. Their test flight with the SF-3 model revealed that in addition to being more quiet due to the use of an electrical engine, the vehicle is very well stabilized in attitude and throttle control is easier due to reduced lag in motor control. However, the flight times were restricted due to limitation of the batteries and they recorded 20 seconds of continuous hovering flight.

The MAV from Wright State University also utilizes four-wing flapping motion as a mean of force generation (Hsu et al, 2010). The vehicle exploits clap-and-fling motion three times within a flap cycle: two times at the sides of the fuselage and once at the top. It has a wing span of 20 cm and a mass of 12.56 grams with a camera. The MAV is capable of performing difficult maneuvers such as looping, rapid turning, dashing as well as taking off, landing and hovering. They performed both indoor and outdoor flight tests and recorded a maximum flight time of 18 minutes with a 90mAh poly-lithium battery with a maximum speed of 6.7 m/s.

Beyond doubt, the most well-known member of this category is the DelFly family, which comprises variants such as the DelFly I, DelFly II, DelFly Explorer and DelFly Micro.

The DelFly family, particularly the DelFly II, and the associated flapping-wing aerodynamics underlie the scope of the current research and dissertation so that the development of the DelFly MAV family is discussed in more detail in the next section. Detailed technical explanations regarding the DelFly II are made in the relevant chapters throughout the thesis while a general overview of the design, aerodynamics and autonomy of the DelFly is given in de Croon et al (2009, 2012).

Before further explanation of the DelFly family, it is worthwhile to mention another class of flapping-wing mechanisms which are actuated by piezoelectric materials. Due to their significantly high power density (around 400 W/kg) when compared to that of insect muscle (ranging between 29 to 83 W/kg) (Wood, 2008), they offer a high potential for efficient future MAV and NAV applications. The Harvard Microrobotic Fly is an example of this category that has flapping wings powered by piezoceramic bimorph actuators. It has a wingspan of 3 cm and a mass of 60 mg. The wings are driven at the resonance frequency, i.e. 110 Hz, in order to maximize the stroke amplitude. Polyester membrane wings of 1.5 μm thickness can generate sufficient thrust to accelerate vertically (Wood, 2008). An 80 mg version of the flapping-wing robot was able to performed unconstrained stable hovering and basic controlled flight maneuvers (Ma et al, 2013). Although the prototype is still externally powered, it represents considerable evolution toward the creation of autonomous insect-sized MAVs.

The DelFly

The DelFly was born as a result of a student project in Delft University of Technology (TUDelft). This project, the design synthesis exercise (DSE), is the final project of the bachelor program in the Aerospace Engineering Faculty of TUDelft, in which a group of students are given a design mission that they have to accomplish in ten weeks. In April 2005, one of the assignments was: "To impress the jury of the first US-European Micro UAV Competition by designing a flapping wing, vision based MAV, using commercially off the shelf products, within a budget of €5000, with eleven students in ten weeks time" (Jongerius et al, 2005).

During the design process, three different ornithopter designs were tested: (1) a simple monoplane with one set of wings; (2) a biplane concept where two sets of wings were placed above each other and flapping in counter-phase; (3) a tandem wing configuration where two sets of wings were placed one behind the other which were also flapping in counter-phase. In order to assess the performance of these concepts, models were built by use of balsa wood and commonly available tissue. All three designs had the same span length (45 cm), aspect ratio (9) and nearly equivalent mass (about 17 grams) which led to two times higher wing loading for the monoplane configuration. They were all powered by a rubber band, windings of which before and after the flight together with the flight time was used to calculate the energy consumption and the flapping frequency. The results of the flight tests are shown in Table 1.1.

The capability of performing low speed flight with decent power consumption is definitely an advantage in the MAV design. Obviously, the biplane design stands out with these features as well as being a stable platform for camera-vision whereas the monoplane concept featured a rocking amplitude of 80 mm. Based on the outcome of these test configurations, the DelFly I was then designed to have a biplane flapping-wing configuration

	Monoplane	Biplane	Tandem
Average flight speed	2.35 m/s	1.40 m/s	1.36 m/s
Flapping frequency	3.69 Hz	6.17 Hz	7.90 Hz
Power consumption	1.55 W	1.44 W	2.15 W
Rocking amplitude	80 mm	0 mm	0 mm

Table 1.1: Comparison of different configurations in terms of test flight performance considered during the design of the DelFly (reproduced from Jongerius et al, 2005)

with a span length of 33 cm and a body length of 41 cm (Fig. 1.7a). The nominal flapping frequency is about 6 Hz and the MAV weighs 21 grams. A vertical V-tail with ruddervators are used for control and stability of the MAV. A crank-rod mechanism was used in order to convert rotational motion of the brushed engine to the reciprocating motion of the flapping wings. Balsa wood and carbon were used in the manufacture of the MAV frame. The wings were made of mylar foil that was strengthened by carbon rod stiffeners and leading edges of carbon-balsa-carbon construction. The students won the 'Best Exotic Design' award with the RC design in the International Micro Aerial Vehicle (IMAV) conference in Germany in 2005 although they couldn't accomplish all of the missions in the competition.

The success of the DelFly I motivated the researchers at TUDelft to further improve the initial design. In 2006, an evolved version of the DelFly, the DelFly II, was born with significant improvements (Fig. 1.7b). First, it is lighter than DelFly I with a mass of only 16 grams including an onboard camera, which is employed for observation and vision based control purposes, a transmitter for downlinking the video and a receiver for the radio control. Second, it is smaller with a wing span of 28 cm and a body length of 24 cm. Instead of a brushed engine, a brushless motor is used in the DelFly II. In the structure of body and wing frames, mainly carbon is used as the construction material. A conventional tail with a rudder and an elevator is mounted closer to the flapping wings increasing the effectiveness of the control surfaces and leading to a more efficient flight. All these improvements also resulted in a broader flight envelope. The DelFly II can perform forward flight at a maximum speed of 7 m/s, backward flight at a maximum speed of 1 m/s as well as hovering flight. The endurance is about 15 minutes with a single full battery.

In 2007, the Micro Air Vehicle Laboratory (MAVLab) group of TUDelft defined a new project goal which is to realize the DelFly Nano with a wing span of 5 cm and with similar capabilities of its older brothers. To reach this goal, an initial, intermediate prototype was built in 2008, the DelFly Micro, that has a wing span of 10 cm and a mass of 3 grams still including an on-board camera (Fig. 1.7c). In the flight tests, it was able to perform a fast forward flight up to 3 minutes.

Since then, the DelFly has been subject to many experimental (Bruggeman, 2010; de Clercq et al, 2009; Deng et al, 2014; Eisma, 2012; Groen, 2010; Percin et al, 2014a) and computational (Gillebaart, 2011; Tay et al, 2014) studies to understand the underlying aerodynamic mechanisms with the objective to improve the current design, as well as to develop autonomous flight systems (Koopmans, 2012; Tijmons, 2012). As a result, the DelFly Explorer has been released (Fig. 1.7d). It is a modified version of the DelFly II featuring a stereo vision system with on-board processing that enables the DelFly to avoid obstacles. The tail design has been changed and an aileron is adopted instead of a rudder

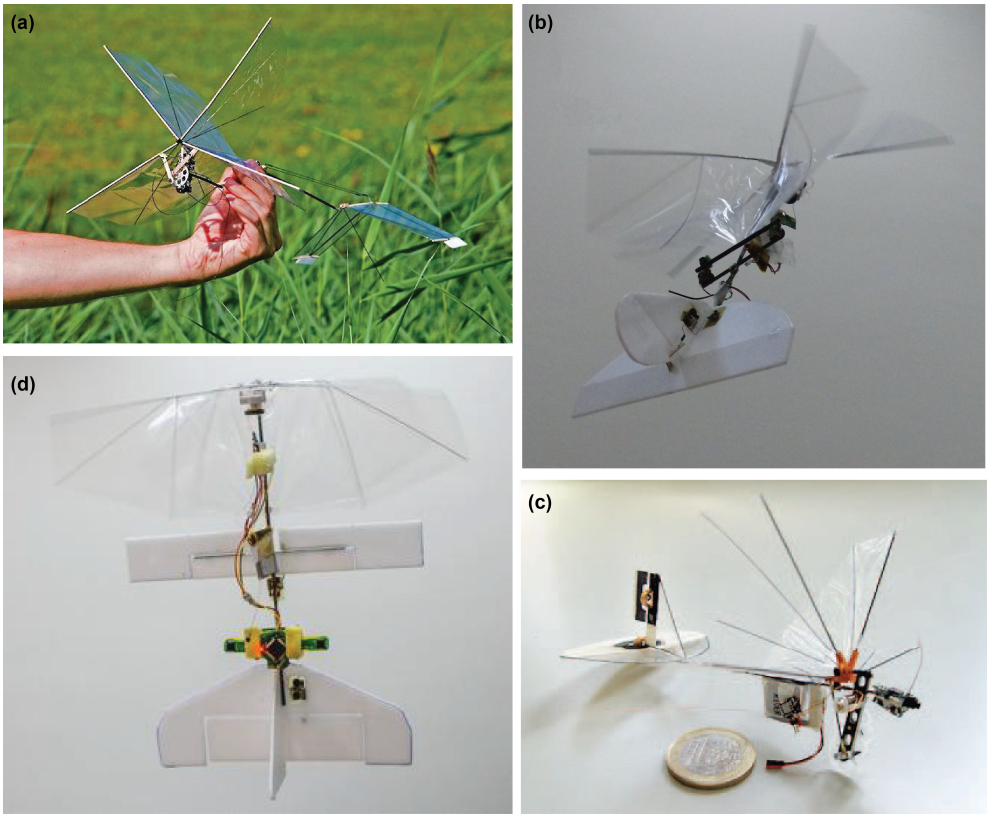

Figure 1.7: **a** DelFly I, **b** DelFly II, **c** DelFly Micro, **d** DelFly Explorer

in order to have more independent control authority on the rolling motion. The MAV is also equipped with a barometer to maintain its height. The DelFly Explorer is able to perform a fully autonomous flight in indoor spaces such that it can take off, ascend to a given altitude, and fly around for 9 minutes without the need of external control (de Wagter et al, 2014).

General overview of MAVs

MAVs of different design configurations are represented in Fig. 1.8 in terms of total mass and flight endurance with capabilities of some of them indicated below their names by letter coding. The gray-shaded region represents the DARPA MAV definition requirements of mass and endurance while the letter codes (C, L, A, V, H) correspond to the different performance capabilities, as explained in the figure caption.

Clearly, there is no MAV reported in the literature to satisfy the all these DARPA requirements. Most of the MAVs are eligible to meet the mass and maximum velocity criteria, whereas intended flight endurance and length scale levels are not reached mostly. As a matter of fact these parameters are strongly interrelated and there are trade-offs between all of them. For instance, increasing battery capacity so as to have a longer flight duration

will result in a larger total mass (which in turn might lead to a shorter endurance) or decrease of payload mass for the same total mass. Obviously, fixed-wing MAVs outperform other classes in terms of flight duration. It can be attributed to the fact that mainly forward motion of the wing is responsible for the generation of lift and power consumption of the propulsion system, that is in charge of overcoming drag, is relatively lower. However, as mentioned earlier, these designs are not suitable for indoor applications due to the requirement of fast forward motion and therefore they are not capable of performing hovering flight. On the other hand, while having a hovering capability, rotary-wing designs have clearly insufficient flight endurance: the longest endurance is about ten minutes for a configuration already without vision avionics. In that sense, flapping-wing MAVs appear to be more successful as it is possible to achieve flight durations of more than 10 minutes even with a camera and transmitting electronics.

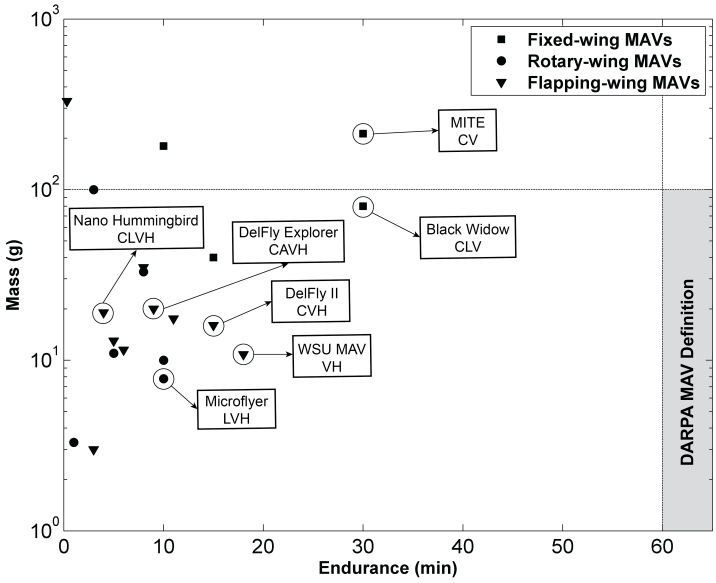

Figure 1.8: Flight endurance vs. mass of the MAVs reported in the literature with their capabilities indicated below some of their name - C: Features a camera and transmitting avionics; L: Maximum dimension smaller than 15.24 cm as required to satisfy DARPA definition; A: Capable of performing fully autonomous flight; V: Maximum flight speed smaller than 15 m/s as required to satisfy DARPA definition; H: Capable of performing hovering flight

Although different design approaches are analyzed in terms of aerodynamic efficiencies of their force generation mechanisms, it should be noted that the flight performance of an MAV system is also affected by the efficiencies of many other components such as motor, driving system and battery. For instance, as all of these MAVs rely on stored electrical energy, the energy storage capacity of batteries is often the major bottleneck in the determination of flight endurance (Sirohi, 2013). In addition to the capacity, the maximum current draw of batteries is another influential parameter on the overall performance. The introduction of lithium polymer and lithium ion batteries has brought in a

significant breakthrough in the field of MAVs and model aircrafts as they have about 600 to 700 kJ/kg energy density when compared to nickel based batteries with a maximum energy density of about 300 kJ/kg. It is obvious that further advances in the battery technology can improve the capabilities of the MAVs yet different designs are compared on the basis of current state-of-art, which proves that flapping-wing mechanisms offer great potential to be used as an efficient mean of force generation in the MAVs as widely used in nature. In this sense, the present work focuses on flapping-wing aerodynamics in order to assess its underlying mechanisms particularly those associated to the flapping-wing MAV, the DelFly II.

1.2. Aim and structure of the thesis

The aim of this thesis is twofold:

1. To investigate aerodynamic force generation mechanisms of the flapping-wing MAV, with the DelFly II as particular testbed, in order to reveal the connection between wing motion and aerodynamic behaviour, which may assist in optimizing the MAV design;

2. To gain fundamental understanding of different aerodynamic mechanisms of the flapping-wing phenomenon.

In the context of the first goal, a dedicated experimental investigation has been performed on a full scale MAV DelFly II model including flow field measurements around the flapping flexible wings and force measurements at different flight regimes for various flapping parameters of the vehicle. In the scope of the second research goal in which a more fundamental approach was taken, a generic experimental setup was realized in a water tank that is capable of modeling flapping motion with two degrees-of-freedom while acquiring unsteady forces and moments simultaneously. In this part, extensive state-of-art flow field and force measurements on flapping wings performing various different kinematics while taking wing flexibility also into account.

In chapter 2, flapping-wing motion is described with the associated terminology and the aerodynamic force generation mechanisms of flapping-wing flight are discussed in conjunction with studies in the literature. Following this introductory chapter, the thesis is divided into two parts in line with the two main objectives: (Part I) Experimental investigation of the DelFly flapping-wing aerodynamics; (Part II) fundamental research in flapping-wing aerodynamics. In the first part, force and wing deformation measurements on a hovering DelFly II are presented in chapter 3 with a special focus on the characterization of the aerodynamic and inertial components, the influence of fixing the vehicle on a balance system on the force measurements, and the effects of wing geometry and wing flexibility on the force generation. Chapter 4 presents the flow field measurements obtained by a stereoscopic particle image velocimetry (stereo-PIV) technique around the flapping wings of the DelFly II in hover condition. Temporal evolution of the three-dimensional flow structures in the wake of the flapping DelFly II wings in forward and hover condition is discussed in chapter 5. A Kriging regression technique to reconstruct three-dimensional flow fields from Stereo-PIV measurements at different planes is also introduced in this chapter. In the second part of the thesis, wing flexibility effects on the clap-and-fling type flapping motion

are discussed based on the results of flapping wing experiments in a water tank in chapter 6 with an analysis of scaling between flapping motions in air and in water. In Chapter 7 and 8 flow fields and unsteady forces on revolving-surging and revolving-pitching wings are analyzed for a wide range of motion parameters with a particular focus on the build-up of the force generation mechanisms. Finally, chapter 9 presents the major conclusions of the present study, with an outlook toward future works.

2

Flapping Wing Aerodynamics

In this chapter, flapping wing motion, as observed in natural fliers, is first discussed by describing different motion kinematics and associated terms. Subsequently, force generation mechanisms of flapping wing flight are addressed.

2.1. Kinematics of flapping flight

The natural flapping flight of birds and insects is a complicated three-dimensional phenomenon which arises from combined motions of the flapping wings and the flyer's body. In order to stay aloft or maneuver, natural flyers drive their wings in three main motions which are sweeping, pitching and plunging (heaving).

In general, the wing motion during the flapping strokes can be considered to be confined in a plane, which is referred to as the stroke plane. For simplicity in the current description of flapping wing kinematics, the stroke plane is considered to be horizontal, but it might also be inclined with respect to the horizontal axis with an angle of β. It was shown that biological flyers adjust the orientation of the stroke plane actively in an effort to maneuver as it affects the force generation and direction of the resultant force vector (David, 1978; Wang, 2005). The fore and aft motion of the wing in the stroke plane is the sweeping motion. The part of the motion in which the ventral side of the wing leads is the downstroke and that with the dorsal side leading is the upstroke. The stroke angle (ϕ) is defined as the instantaneous angle between the leading edge of the wing and the y axis in the body coordinate system (y_b), whereas the stroke amplitude (Φ) is the total angular displacement of the wing in the stroke plane (see Fig. 2.1).

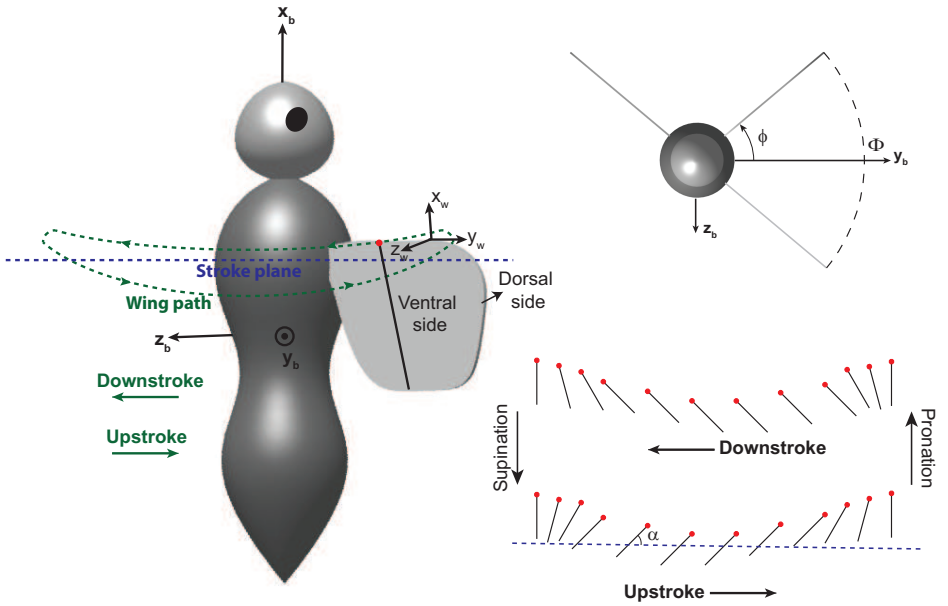

Figure 2.1: Schematic diagrams of body and wing coordinate systems and kinematics of flapping wing motion depicted on a generic insect

The pitching motion is the rotational motion of the wing about an axis parallel to the (spanwise) y axis in the wing coordinate system (y_w). It is generally performed most prominently during the stroke reversals in order to have a positive angle of attack (α) in the subsequent stroke. The wing pitch reversal at the transition from an upstroke to a downstroke is called pronation, and at the transition from a downstroke to a upstroke, it

is called supination. The pitching motion can contribute to the force production significantly during the flapping flight depending on a number of parameters such as its timing with respect to the sweeping motion of the wing and the pitch rate. These aspects of the motion are discussed in detail in 2.2.2.

The up and down motion of the wing with respect to the mean stroke plane is the heaving (or plunging) motion. The plunging motion plays an important role in determining wing tip trajectory pattern, which has a major influence on the production of aerodynamic forces (Sane and Dickinson, 2001). Many studies investigating the flapping-wing motion in insects and hummingbirds revealed two main patterns: (1) a figure-of-eight pattern, in which the downstroke and upstroke trajectories cross each other in between the stroke reversals; (2) an oval trajectory in which no crossing occurs between the stroke reversals (Ellington, 1984b). Obviously, these patterns, mostly due to the heaving motion component, determine the angle of attack experienced by the wing during the stroke and in turn affects the force and moment generation. For this reason, variations of the flapping patterns have been subject to a number of studies aiming to assess an optimal pattern with an efficient force generation (Baskan, 2009; Bos et al, 2008; Lehmann and Pick, 2007; Sane and Dickinson, 2001).

2.1.1. Non-dimensional analysis of flapping flight

Non-dimensional analysis is an appropriate tool for the characterization of the system under consideration and to find out which combination of parameters are important under given conditions. In this context, three main non-dimensional parameters related to the fluid dynamics in flapping flight are addressed in this section for different flight regimes (Shyy et al, 2010).

The Reynolds number (Re) is the ratio of inertial forces to viscous forces and therefore quantifies the relative importance of these forces for given flow conditions. In general terms, it is defined as:

$$\mathrm{Re} = \frac{\rho L_{ref} U_{ref}}{\mu} \tag{2.1}$$

where ρ is the fluid density, L_{ref} is the characteristic length, U_{ref} is the reference velocity and μ is the dynamic viscosity of the fluid. Similar to fixed-wing aerodynamics, the mean chord length ($\overline{c}$) is utilized as the reference length. However, in the case of flapping flight, the selection of the reference velocity is not as straightforward and requires careful consideration of the given flight conditions. In forward flight, common practice is to use the forward flight velocity (U_∞). It is also plausible to use the mean wing tip velocity ($U_{m,tip} = 2\Phi f R$, where f is the flapping frequency and R is the span of a single wing), especially in the situation of slow forward flight and high flapping frequency. In particular, the mean wing tip velocity is commonly used as the reference velocity in hovering flight. The corresponding definition of the Reynolds number can then be rewritten as:

$$\mathrm{Re} = \frac{\rho_f f \Phi b \overline{c}}{\mu} = \frac{\rho_f f \Phi A R \overline{c}^2}{\mu} \tag{2.2}$$

where $b = 2R$ is the wing span and AR is the aspect ratio ($AR = b^2/S$ with $S = b\overline{c}$ being the wing planform area). Alternatively, for hovering flight the Reynolds number may be de-

fined in relation to the velocity induced by the flapping wings (V_{ind}). The induced velocity can be approximated by use of the actuator disc theory, which reads for hovering flight:

$$V_{ind} = \sqrt{\frac{T}{2\rho S_d}} \tag{2.3}$$

where T is the produced thrust (equal to the vehicle weight in equilibrium hovering flight) and S_d is the disc area.

The Strouhal number (St) is a non-dimensional parameter that is relevant for the vortex dynamics and shedding behaviour of vortices in flapping wing aerodynamics. In the case of forward flight, with the full stroke amplitude of the flapping motion (ΦR, i.e., wake width) as the characteristic length and the forward flight velocity as the reference velocity, it reads:

$$\mathrm{St} = \frac{f\Phi R}{U_\infty} \tag{2.4}$$

In this form, the Strouhal number compares the flapping velocity of the wing with the forward flight velocity, which can be considered as a measure of propulsive efficiency for a flapping-wing flyer in forward flight (Shyy et al, 2007).

The reduced frequency (k) is a related similarity parameter that reflects the measure of unsteadiness in flapping wing flight. In forward flight, based on the mean chord length, the free-stream velocity and the angular frequency of the flapping motion ($2\pi f$) it is defined as:

$$k = \frac{\pi f \bar{c}}{U_\infty} \tag{2.5}$$

The reduced frequency is essentially the ratio of mean chord length to the wavelength of shed vortices in the forward flight. In hovering flight, where the forward flight velocity is zero, the mean wing tip velocity is used as the reference velocity resulting in:

$$k = \frac{\pi \bar{c}}{\Phi b} = \frac{\pi}{\Phi AR} \tag{2.6}$$

It is clear that the reduced frequency definition based on the mean wing tip velocity in hovering flight is not a function of flapping frequency but inversely proportional to the stroke amplitude and the aspect ratio, which is counter-intuitive with respect to the physical interpretation of this parameter. Therefore, it is more plausible to use the induced velocity (Eq. 2.3) as the reference velocity because it can be considered as the advection velocity of the vortical structures and therefore plays a similar role as the free-stream velocity in forward flight.

2.2. Force generation mechanisms

Natural fliers exploit numerous different unsteady aerodynamic mechanisms for the generation of forces during the flapping flight. The extent to which these mechanisms are used varies between different species based on the length scales, wing kinematics and the flight regime. Moreover, these mechanisms might be used in the case of necessity during a

particular phase of the flight. For instance, to perform a sharp maneuver or to carry an extra weight, the flying animal can enable the use of an aerodynamic mechanism simply by modifying its wing kinematics. These unsteady mechanisms are discussed in the review papers provided by Lehmann (2004); Sane (2003); Shyy et al (2010) and explained in Shyy et al (2007); Taylor et al (2010) to a great extent. In this section, the most prominent and relevant mechanisms are addressed as listed below:

1. Leading edge vortex (delayed stall)
2. Rotational forces
3. Clap-and-fling motion
4. Wake capture
5. Added mass

2.2.1. Leading edge vortex (delayed stall)

Contrary to fixed wing flight, flapping wing flight strongly relies on the occurrence of flow separation and the associated pressure fields for the generation of forces. In this respect, the phenomenon of the leading edge vortex (LEV) emerges as one of the most dominant mechanisms in flapping wing aerodynamics particularly in insect flight.

Formation of the LEV stems from the delayed (dynamic) stall of the wing during the flapping motion. In case of an airfoil with a sharp leading edge that is set in motion at an angle of attack above its stalling angle, the flow separates at the leading edge but may reattach before it reaches to the trailing edge such that the Kutta condition is maintained. In such a case, an LEV forms in the separation zone The presence of the LEV creates a low pressure region on the top surface of the wing which enhances the lift. Equivalently, the extra lift can be explained as an increase of the circulation around the wing including the contribution of the LEV so that the airfoil imparts a greater momentum to the fluid (Ellington et al, 1996). The term 'delayed stall' is used to indicate the period of time when the airfoil generates relatively high lift with the presence of an attached LEV prior to stall.

Although the discovery of the LEV in insect flight is a relatively recent, lift enhancement effects of vortices have been studied for a long time (Campbell, 1976; Hurley, 1959; Polhamus, 1971; Wu et al, 1991). Polhamus (1971) described an analytical model to predict the force generated by the presence of a vortex, namely the *leading edge suction analogy*. Although this analogy was originally developed to assess the lift characteristics of sharp-edge delta wing at low speeds, it was also used in order to explain the LEV phenomenon in flapping wing flight (Lehmann, 2004). In the case of a thin airfoil placed in a free-stream with a low angle of attack, the flow is completely attached on the upper surface and Kutta condition is established at the trailing edge. According to the thin airfoil theory, it is known that lift is generated as a result of the bound circulation of the wing. When this force is decomposed into components in the chord-normal and tangential directions, a positive upward normal force and a tangential force parallel to the chord line in the upstream direction are attained. The latter component is actually associated with the acceleration of the flow around the leading edge and thus the formation of a low pressure region. The two-dimensional aerodynamic drag becomes zero due to this leading edge

suction phenomenon under inviscid and incompressible flow conditions, which is known as d'Alembert's paradox (Katz and Plotkin, 1991). However, as the angle of attack increases and the flow separates at the leading edge, the leading edge suction force vanishes due to the formation of the LEV. Polhamus' analogy states that the increase in the normal force component due to the LEV related pressure distribution is equal to the suction force that is necessary to accelerate the flow around the leading edge (Gülçat, 2010). In other words, with the increase of the angle of attack beyond the stall limits and the formation of the LEV, the leading edge suction force rotates 90° and increases the force component normal to the airfoil surface (thus increasing lift and drag).

This force generation mechanism, however, works efficiently as long as there is a stable attached LEV. For a two-dimensional translational motion of a wing, the size of the LEV increases continuously until the flow reattachment is no longer possible. The LEV then sheds into the wake and new trailing edge vorticity forms at the trailing edge breaking the Kutta condition. Stalling of the wing causes a significant decrease in the force generation (Sane, 2003). Dickinson and Götz (1993) performed force measurements and flow visualizations on translating two-dimensional flat plate wings undergoing an impulsive start at different angles of attack. Their results showed that at angles of attack above 13.5°, a LEV is formed, which is accompanied by the development of a counter-rotating trailing edge vortex (TEV), as a result of the impulsive start and increases lift dramatically for the first two chord lengths of travel after which the LEV sheds. They observed that this alternating pattern of vortices leads to a von Karman vortex street (see Fig. 2.2).

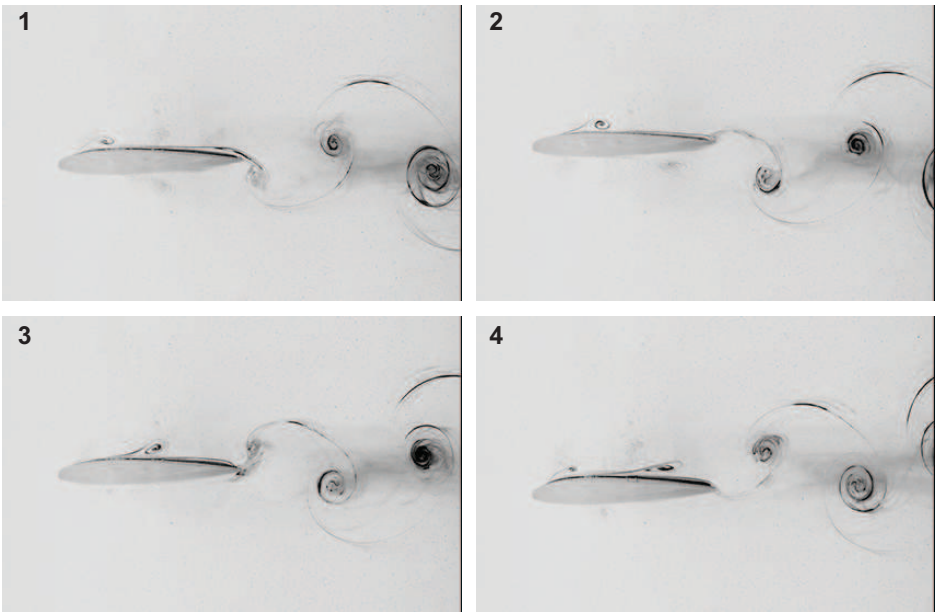

Figure 2.2: Flow around a plunging NACA 0012 airfoil placed in a free-stream flow visualized via a tin precepitation method (1. Half-way upstroke, 2. The end of upstroke, 3. Half-way downstroke, 4. The end of downstroke): The shedding of the LEV and TEV from the two-dimensional airfoil gives way to the formation of a reverse von Karman vortex street (adapted from Percin (2009))

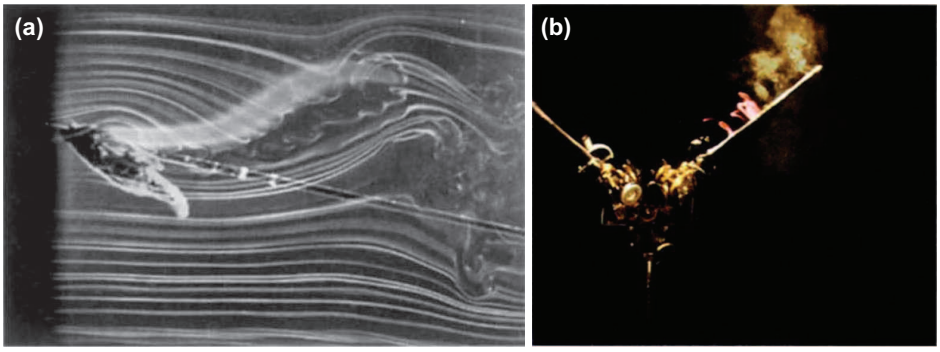

Figure 2.3: **a** Smoke flow visualization around a female hawkmoth and **b** flow visualization with smoke released from the leading edge over the inner half of one wing of the robotic flapping device; both showing the formation of an LEV during the downstroke phase of the flapping motion (adapted from Ellington et al (1996))

The first direct evidence of the LEV mechanism in insect flight was provided by Ellington et al (1996). They visualized the flow around the flapping wings of the hawkmoth *Manduca sexta* and observed an intense LEV that is created by the dynamic stall mechanism during the downstroke (Fig. 2.3a). Then in order to investigate the phenomenon, they built a three-dimensional robotic flapping device that mimics the wing kinematics of a hovering hawkmoth and carried out a flow visualization study around the flapping wings (Fig. 2.3b). Contrary to the shedding of the LEV in the two-dimensional motion of an airfoil, the LEV stays rather attached to the wing during the complete downstroke, which they explained with the presence of a spanwise flow under three-dimensional conditions. Their measurements indeed revealed that the LEV has a spiral conical shape enlarging towards the wing tip and feeding into the tip vortex after 70 % of the span. There is also a strong spanwise flow in the core of the LEV with the maximum values comparable to the wing tip velocity. Based on these observations, they hypothesized that the spanwise flow convects some of the leading edge vorticity towards the wing tip which inhibits excessive growth of the LEV analogous to the mechanism of vortex stabilization that occurs on delta wings.

However, flow field measurements on a dynamically scaled robotic model of a fruit fly (*Drosophila*) wing operating in hover condition at a Reynolds number of 160 revealed that in contrast to what was observed in the case of the flapping hawkmoth wings, the axial velocity in the vortex core is marginal, at around 2-5 % of the average wing tip velocity as reported by Birch and Dickinson (2001). Instead, it was found that a relatively strong base-to-tip flow pattern is present in the rear two-thirds of the wing reaching 40 % of the tip velocity. They used teardrop fences at two different chordwise positions in order to block the spanwise flow patterns in the core of the LEV and in the rearward region of the wing in two separate experiments to test the influence of base-to-tip flow on the attachment of the LEV. The forward blockage case, rather than increasing the LEV strength and leading to possible separation, resulted in a decrease in the vortex strength and thus in the net force. Although this finding rebuts the spanwise flow hypothesis for the vortex stability, it should still be noted that the relatively low Reynolds number of the fruit fly operation might lead to significant differences in the flow structures. Their alternative hypothesis to explain the prolonged attachment of the LEV was based on the downwash generated

by the tip vortex and wake vorticity and associated decrease of angle of attack. The lower effective angle of attack in turn limits the growth of the LEV during the flapping motion. More recently, Lentink and Dickinson (Lentink and Dickinson, 2009) claimed that the rotational accelerations (i.e. centripetal and Coriolis accelerations), which are effective at low Rossby numbers (note that the Rossby number measures Coriolis acceleration and is defined as Ro = $R_g/\overline{c}$ for a revolving wing, where R_g is the radius of gyration), are stabilizing the LEV. The correlation between the Coriolis accelerations and the attachment of the LEV (thus associated high sustained lift) was also reported by Jardin and David (2015). Clearly, although there is a consensus about the attachment of the LEV in three-dimensional flapping wing motion but the underlying stabilization mechanism still remains mainly unresolved.

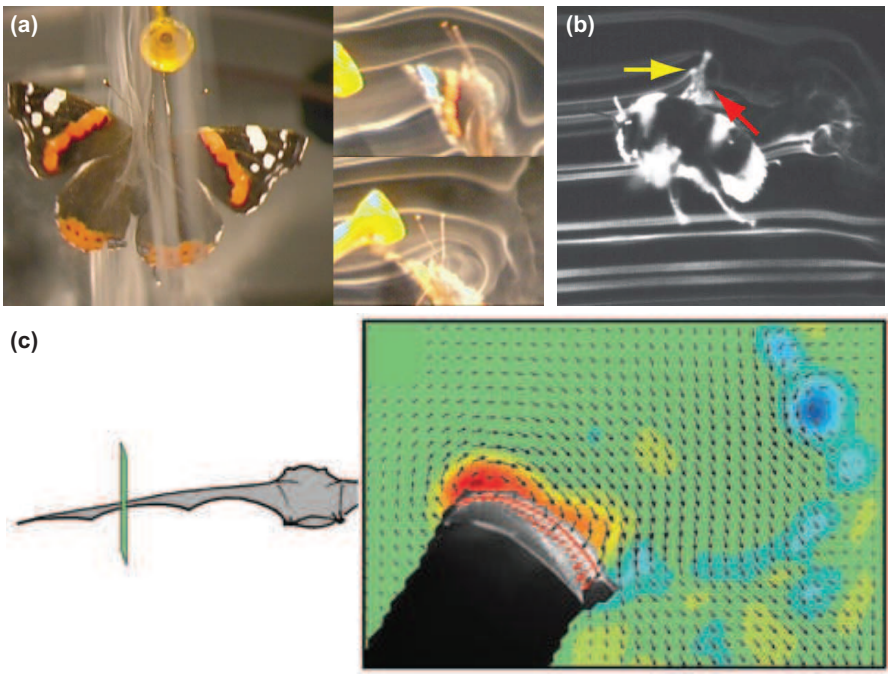

Figure 2.4: **a** Butterfly LEV structure visualized by means of smoke flow (adapted from Srygley and Thomas (2002)), **b** smoke flow visualization around a bumblebee reveals formation of an LEV with the reattaching smoke-line (indicated with red arrow) depicts the extent of the LEV (adapted from Bomphrey et al (2009)), **c** velocity field complemented with the contours of out-of-plane vorticity in a plane positioned at the 65 % semi-span position of a bat wing in slow forward flight (adapted from Muijres et al (2008))

The presence and benefit of the LEV phenomenon were also addressed in the three-dimensional flapping wing model of the fruit fly (*Drosophila melanogaster*) (Dickinson et al, 1999). In this study, the elevated force coefficients during the reciprocating motion of the wing are attributed to three main mechanisms: delayed stall, wing rotation and wake capture. The LEV mechanism works during the sweeping part of the motion, whereas the latter two are effective during the stroke reversals. Free-flying butterflies (*Vanessa atalanta*) (Fig. 2.4a) (Srygley and Thomas, 2002) and bumblebees (Fig. 2.4b) (Bomphrey et al,

2009) also exploit a LEV to generate forces and stay aloft. The use of LEV mechanism is encountered even at larger scales, i.e. in small bats when flying slowly (*Glossophaga soricina* as shown in Fig. 2.4c and *Leptonycteris yerbabuenae*) (Muijres et al, 2008, 2014). It was shown that these bats are able increase lift up to 40 % by exploiting the LEV and reaching a maximum lift coefficient of 4.8 (Muijres et al, 2008). The LEV mechanism is even utilized by small birds during slow forward flight (Muijres et al, 2012b).

2.2.2. Rotational forces

As mentioned previously, a reciprocating flapping wing motion consists of two translational phases in which the wing sweeps at high angles of attack and during which delayed stall and LEV phenomena emerge as dominant force production mechanisms. In order to preserve a positive angle of attack during these translational phases, the wing performs pronation and supination as described in 2.1. Although the LEV mechanism accounts for the force that keeps an insect aloft, it cannot provide sufficiently high forces that an insect needs during steering maneuvers (Dickinson et al, 1999) or while carrying loads at the order of its body weight (Marden, 1987). In this regard, instantaneous force measurements on the dynamically scaled fruit fly wings revealed considerable additional force generation during stroke reversals indicating the potential of wing rotation as an important unsteady mechanism (Dickinson et al, 1999). Although the significance of pitching motion in flapping flight has been realized in the last decades, it has been already considered extensively, particularly in the context of wing flutter in the theoretical works of Fung (1993); Glauert (1929); Munk (1925); Theodorsen (1935) which were supported by experimental studies of Farren (1935); Garrick (1937); Halfman (1951); Kramer (1932); Reid (1927); Silverstein and Joyner (1939) (as cited in Sane, 2003).

In the context of the unsteady thin airfoil theory, force production as a result of pitching motion is a circulatory phenomenon. When a wing starts rotating about a spanwise axis (viz. pitching) during its revolution or translation, the Kutta condition breaks down and the stagnation point departs from the trailing edge which leads to formation of shear and vorticity. To re-establish the Kutta condition, additional circulation is generated around the wing that either adds to or subtract from the available circulation depending on the relative direction of the pitching motion. This additional circulation due to rotation of the wing is estimated by Fung (1993) using a quasi-steady equivalent-downwash model for a thin airfoil performing a rotational motion around a spanwise axis as follows (Ellington, 1984c):

$$\Gamma_{rot} = \pi(0.75 - \hat{x}_0)\omega c^2 \tag{2.7}$$

where ω is the rotational velocity and $\hat{x}_0$ is the non-dimensional distance of the rotation axis from the leading edge ($\hat{x}_0 = x_0/c$). It is clear that the circulation associated with the rotational motion is a function of rotational velocity and the position of the rotation axis. According to the theoretical estimate, the critical axis, at which the circulation changes sign, is at the three-quarter chord position, which is also verified experimentally by Granlund et al (2013); Sane and Dickinson (2002) for relatively high rotational velocities.

In addition to the position of the rotation axis, the timing of the rotation plays an important role on the force generation. Force measurements on the robotic flapping fruit fly wings revealed different force histories for advanced, symmetrical and delayed rotations

during stroke reversals (Dickinson et al, 1999; Sane and Dickinson, 2002). In the case of the advanced rotation, in which the wing rotation precedes the stroke reversal, rotational circulation has a constructive effect on the lift generated. This can be interpreted as an increase of angle of attack while the wing approaches to the end of the stroke. When the rotation is delayed with respect to the stroke reversal (viz. delayed rotation), the leading edge rotates forward relative to the translating motion resulting in a negative lift during the stroke reversal. If the wing rotation is symmetrical about the stroke reversal, the wing generates first upward and then downward force. Clearly, timing of the wing rotation can be so influential that a phase advance of 8 % from the delayed to the symmetrical case results in a 67 % of increase in the mean lift coefficient (Dickinson et al, 1999).

In summary, the rotational circulation has a remarkable lift enhancing effect in the flapping wing motion such that its contribution can reach 50 % of the total lift generation averaged throughout the stroke cycle despite its short application time (Dickinson et al, 1999). Furthermore, by changing the timing of the rotation, the force direction can be adjusted for instance to perform an intended maneuver. Studies on fruit flies showed that they change the wing rotation timing and stroke amplitude during their flapping flight (Dickinson et al, 1993; Muijres et al, 2015).

2.2.3. Clap-and-fling motion

Clap-and-fling is a lift enhancement mechanism which was first described by Weis-Fogh (1973). This relates to the wing-wing interaction phenomenon, which takes place at dorsal stroke reversal (Fig. 2.5). During the clap phase, the leading edges of the wings approach each other (Fig. 2.5-A) and pronation about the leading edges occurs until the v-shaped gap between the wings is closed (B and C). In the fling phase, the wings rotate about their trailing edges forming a gap in between (D). Subsequently, the wings start to translate apart from each other (E and F). Investigations on birds and insects showed that as well as being used continuously during the flight, some species utilize this mechanism for a limited time in order to generate extra lift, especially while carrying loads or during the take-off phase (Lehmann, 2004). Experiments on insects (Marden, 1987) showed that use of the clap-and-fling mechanism results in generation of 25 % more aerodynamic lift per unit flight muscle than conventional flapping wing motions.

Several studies have attempted to provide an explanation of the increase in the force generation due to clap-and-fling. The underlying unsteady aerodynamic mechanisms for this increase have been proposed as: 1) the attenuation of starting vortex formation at the onset of the fling (thus diminishing the Wagner effect) due to the interaction of the opposing circulation of each wing (Sane, 2003) (see Fig. 2.5-D and E); 2) the downward momentum jet formed at the end of clap, when the air trapped between the wings is forced downwards (C); 3) generation of a massive leading edge vortex (LEV) at the onset of fling (D), which was verified experimentally by Lehmann et al (2005). They performed simultaneous PIV and force measurements on dynamically scaled rigid fruit fly wings in order to investigate the effects of the clap-and-fling motion on the force production. They pointed out that clap-and-fling, depending on the stroke kinematics, may enhance the force production by up to 17 %. Detailed PIV analysis revealed that the existence of an image wing increases the circulation induced by the leading edge vortex during the early fling phase, obviously correlated with a prominent peak in both lift and drag. Furthermore, it was

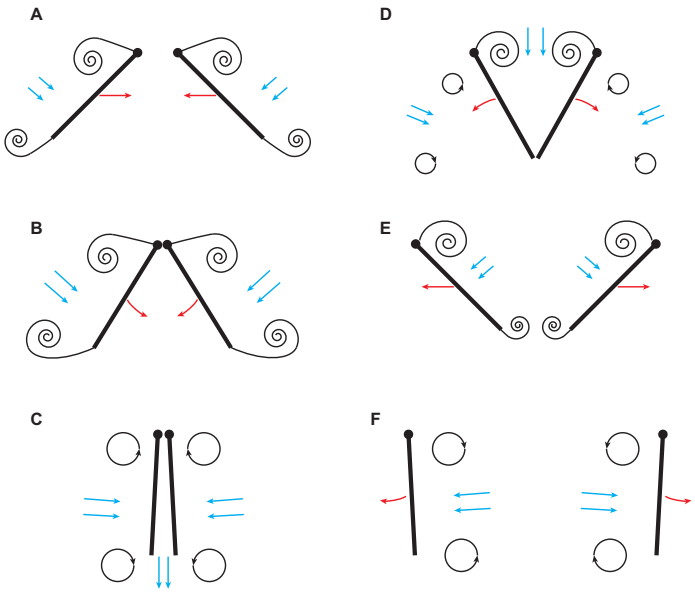

Figure 2.5: Schematic representation of clap-and-peel motion by use of two rigid wing sections with the red arrows indicating the direction of the wing motion and the blue arrows indicating the direction of the induced flow

shown that trailing edge vorticity shed during the fling phase of the motion is considerably reduced with respect to that in the single flapping wing case.

The flexibility of the wings plays an important role in the wing kinematics and force generation mechanism of the clap-and-fling motion. As a result of the wing flexibility, the fling phase occurs more like a peel, while the clap phase can be considered as reverse-peel (Ellington, 1984b). That is the reason why clap-and-fling is called clap-and-peel motion in the case of flexible wings. It was speculated that flexible wings increase lift by enhancing the circulation in the fling phase and boosting the strength of downward momentum jet in the clap phase (Ellington, 1984c). Moreover, it was indicated that flexibility reduces drag by allowing the wing to bend or reconfigure under the aerodynamic loading. Miller and Peskin (2009) investigated this phenomenon computationally by use of an immersed boundary method for a Reynolds number of 10. They found that clap-and-fling with flexible wings produces lower drag and higher lift with respect to clap-and-fling with rigid wings.

2.2.4. Wake capture

At the end of each stroke in flapping motion, the wing sheds counter-rotating leading and trailing edge vortices into the wake. Subsequently as the new stroke starts after the stroke reversal, the wing encounters its own wake which contains high energy regions (see Fig. 2.5-C and D). These regions are formed by the induced velocities of the wake vortices shed in the previous stroke. Transfer of the energetic fluid's momentum to the wing by increasing effective fluid velocity can enhance the force generation significantly at the onset of

the stroke. However, the effectiveness of the wing-wake interaction mechanism strongly depends on the magnitude and the orientation of the wake vorticity during the stroke reversal (Birch and Dickinson, 2003), which are in turn obviously affected by the wing kinematics. It is clear that the contribution of wing-wake interaction will be diminished or completely absent in the forward flight due to advection of the wake structures with respect to the wings; however, it offers a great potential for lift generation during hovering flight.

The experimental study performed by Dickinson et al (1999) verified the significance of wake capture in three-dimensional flapping wing aerodynamics. They observed two force peaks during the stroke reversal, one of which was attributed to rotational circulation. Nonetheless, their tests revealed that the other peak appears just after the wing changes direction regardless of the phase of the wing rotation. In order to investigate the source of this force contribution, they halted the flapping motion at the end of the stroke arguing that if the source is the wake capture mechanism, the wing should still continue to generate force although it is at rest. As a result, they observed that the wing continues to generate forces and the force peak appears at the same position with the peak in the continuous flapping motion in the time line. They supported force measurements with the flow visualizations via particle image velocimetry (PIV) at the instant of stroke reversal showing that the peak-induced velocities in the vicinity of the wing are sufficiently high to generate measured forces. They also mentioned the influence of wing kinematics by showing that the advanced rotation in the stroke reversal phase generates higher force due to the wake capture effect that stems from a more energetic wake.

Birch and Dickinson (2003) followed a different approach to investigate the wake capture mechanism. They performed simultaneous force and flow field measurements on the flapping wing of a dynamically scaled robot for a number of reciprocating cycles starting from rest. In order to isolate the aerodynamic influence of the wake capture mechanism, they subtracted forces and flow fields in the first stroke, from those of the fourth stroke. They argued that as the wake is just developing in the first stroke, it does not have a considerable effect on the generated forces so by using this methodology, the wake effects can be identified. Their approach revealed two major effects of the wake on the force generation: an initial augmentation that is associated with the wake capture mechanism; a following attenuation that is well correlated with the decreased effective angle of attack caused by downwash in the wake and well predicted by a quasi-steady model. However, the model was not successful in calculating the wake capture related increase in the forces, although they took into account the instantaneous velocity field, due to the unsteady nature of the wake capture phenomenon which depends on temporal changes in distribution and magnitude of vorticity.

2.2.5. Added mass

In the discussion of the LEV, rotational forces and clap-and-fling motion, it was shown that these mechanisms affect the circulation around the wing and in turn enhances force generation, therefore they are called circulatory forces. Different from these mechanisms, the wake capture mechanism is primarily based on the transfer of the fluid's momentum to the wing. The added mass effect also originates from a non-circulatory phenomenon and is also known as an acceleration reaction (Denny, 1993). When a wing accelerates, it

has to also accelerate the surrounding fluid. As a result, the wing experiences an inertial reaction force by the fluid that is accelerated. It can be considered as an increase in the inertia of the flapping wing due to the mass of the accelerated fluid, i.e. added mass or virtual mass.

Acceleration effects can be very significant in flapping flight. In his early study, Osborne (1951) attributed the large force coefficients in flapping insect flight to such acceleration forces. It was also claimed that (Lehmann, 2004) the passive rotation, bending and twisting of the wing during the stroke reversals are mainly due to inertial reaction forces (Daniel and Combes, 2002; Ennos, 1988). Despite the importance of the acceleration reaction forces, it is not straightforward to estimate their relative contribution as in most cases local accelerations of the fluid are not necessarily caused by the wing's acceleration. For instance time-dependent downwash induced by the wake structures or fluid acceleration due to flow separation will cause the exertion of acceleration reaction forces on the wing.

The added mass of an accelerating thin wing is calculated as equal to the mass of fluid in an imaginary circular cylinder that is encompassing the wing with the chord length as its diameter (Ellington, 1984a).Thus per unit span, the added mass is:

$$m' = \frac{1}{4}\rho\pi c^2 \tag{2.8}$$

The added mass force acts normal to the wing and is proportional to acceleration in the direction of the wing normal (Pitt Ford and Babinsky, 2013). The sectional lift contribution of the added mass term (Sedov, 1965) for a specific case of an airfoil accelerating in plunging and pitching motions normal to the free stream reads (Ellington, 1984a):

$$L' = \frac{1}{4}\rho\pi c^2\left[-\frac{d^2y}{dt^2} - \frac{d^2\alpha}{dt^2}c\left(\hat{x}_0 - \frac{1}{2}\right) + \frac{d\alpha}{dt}U_\infty\right] \tag{2.9}$$

where d^2y/dt^2 is the plunging acceleration (negative downwards), $d^2\alpha/dt^2$ is the pitching acceleration and $d\alpha/dt$ is the pitching velocity. The first two terms on the right hand side of the equation stand for the added mass forces due to accelerations of the plunging and pitching motions, respectively. Note that the center of added mass is located at the mid-chord position which is reasonable as a pitching acceleration around the mid-chord axis will be zero as opposite contributions from the upper and lower half will cancel each other out. The last term is a quasi-circulatory lift which is a result of the virtual or apparent circulation generated as the added mass rotates with the wing section (Ellington, 1984a). This approach has been utilized in a number of studies in combination with the blade-element theory in order to estimate the added mass contribution from wing kinematics in three-dimensional flapping motions (Jardin et al, 2012; Percin and van Oudheusden, 2015b; Sane and Dickinson, 2002; Truong et al, 2011).

I

Experimental Investigation of the DelFly Flapping-Wing Aerodynamics

3

Aerodynamic Performance of the DelFly II

In this chapter, the aerodynamic performance of the DelFly II is assessed by means of force and power consumption measurements. First, the aerodynamic and inertial components of the DelFly flapping-wing forces are identified by comparing force measurements performed in air and vacuum conditions. Then, the influence of fixing the DelFly model on a balance system on the measurement of aerodynamic forces is discussed by means of comparison to free-flight force estimations. Subsequently, effects of wing properties, such as geometry and flexibility, on the force generation and power consumption are reported. Finally, the effects of structural wing deformations on the force generation and power consumption characteristics are explored by means of dedicated wing deformation measurements.

3.1. In-air and in-vacuum measurements - identification of the aerodynamic force components

3.1.1. Introduction

The aerodynamic performance of the DelFly flapping-wing motion in terms of force generation has been carried out by means of mounting a DelFly model on a force sensor and measuring temporal variation of the forces at several selected flight operating conditions. This way of measuring forces has two major implications: (1) tethering the DelFly to a balance system limits the body motions which are present in real flight and introduces additional vibrations due to structural resonance of the body, which is discussed in detail in section 3.2; (2) the force sensor responds to aerodynamic forces and moments as well as to inertial effects and mechanical vibrations of the DelFly components. The latter makes it difficult to isolate the aerodynamic force components in the force spectrum and assess the real impact of the flapping-wing motion. In the sense of analysis of the mean forces, it is plausible to assume that the inertial force generated by the wing during upstroke is mostly canceled out by that during downstroke for a symmetrical wing motion kinematics, which results in a time-averaged value of zero. Nevertheless, proper analysis of the time-history of the aerodynamic forces requires more elaborate investigation to distinguish between the aerodynamic and inertial contributions to the resultant forces and moments. For this reason, in-vacuum force measurements were performed and the results are compared to those of the measurements in air in this section. In addition to the force measurements, also the flapping motion of the DelFly wings was captured by means of a high speed camera in both conditions in order to visualize the effect of the medium on the flapping motion kinematics and wing deformation.

3.1.2. Experimental setup

The experiments were performed in the test section of the hypersonic wind tunnel at the Aerodynamics Laboratory of Delft University of Technology. The vacuum vessel of the facility was employed to provide vacuum conditions in the test section at a pressure level of 1 mbar. For in-air measurements, the test section was filled with air at an atmospheric pressure and force measurements were repeated in the same experimental configuration to allow for a proper comparison of the two cases.

A full-scale DelFly II without a tail and on-board electronics was used as the experimental model in the measurements. The DelFly model and the force sensor were connected to a steel rod support that was mounted on the upper wall of the test section. An external laboratory DC power supply was used to power the motor controller and the brushless motor of the DelFly at a voltage difference of 4.0 V.

Six components of forces and moments were measured by use of an ATI Nano17 Titanium force sensor. The sensor is calibrated to have a maximum sensing value of 32 N in x,y and 56.4 N in z direction with a measurement uncertainty of 1% of the full-scale load with 95% confidence level. The data acquisition and synchronization system consists of two main subsystems: (1) an in-house developed microcontroller system that is mainly responsible for the regulation of the flapping frequency and the synchronization of the force measurements and high-speed imaging with the flapping motion; (2) an in-house programmed Field-Programmable Gate Array (FPGA) system of National Instruments (NI)

that is responsible for the data acquisition. The microcontroller system counts the electrical commutations of the brushless DelFly motor for high-resolution rotational information and reads a Hall sensor with its magnet placed on the wing driving gear of the model for zero-referencing. Based on this information, the system then regulates the power supplied to the DelFly motor with a very slow integrator-only controller to keep the average flapping frequency constant on the long run. The FPGA system, on the other hand, features analog input modules (NI 9239) to acquire motor commutation information, the Hall sensor signal, voltage and current fed to the brushless motor as measured in the microcontroller system in addition to two bridge analog input modules (NI 9237) to acquire the six components of forces and moments at a given data acquisition frequency. In the present experiments, the data were captured at a recording rate of 10 kHz. The test were performed for flapping frequencies in the range of 8-12 Hz.

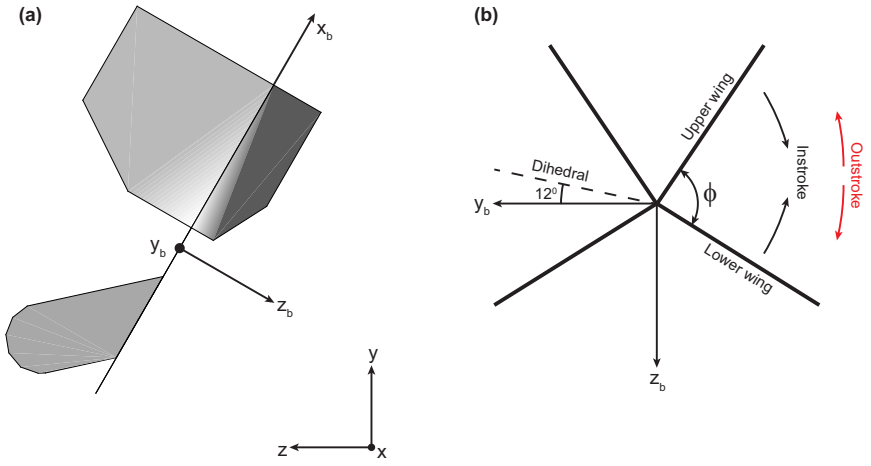

Figure 3.1: **a** Inertial (x, y, z) and body (x_b, y_b, z_b) coordinate systems, **b** front view of the wing leading edges

For a hovering flight configuration, the force in the x_b direction of the body coordinate system (which will be referred to as the X-force and which corresponds to the lift for the hover configuration, see Fig. 3.1a) is the focus of interest because it is the force component that balances the weight of the DelFly. In the absence of a forward flight velocity, the flapping-wing motion of the DelFly generates very small Z-force. As a matter of fact, the flapping-motion should theoretically produce zero net Z-force due to two main reasons: (1) the wing-normal forces generated by a single wing during the instroke and outstroke cancel each other out for a perfectly symmetrical flapping motion kinematics and thus identical wing deformation during both strokes, which results in no net flap-averaged Z-force; (2) the wing-normal forces of the upper and lower wings cancel each other out for a symmetrical orientation of the wings, which should produce net instantaneous Z-force of zero. On the other hand, in the case of the DelFly, as will be presented subsequently, the wing motion kinematics are not identical during the instroke and the outstroke. Moreover, the wings have a dihedral angle (3.1b), which brings about unequal Z-force components of upper and lower wings during the flapping motion. In consequence, the flapping-wing

motion in the hovering DelFly case generates not zero but small instantaneous and flap-averaged Z-forces.

In order to obtain the motion kinematics and wing deformation characteristics, a Photron Fastcam SA 1.1 camera was placed to observe the wings of the DelFly model in front view (Fig. 3.2). The flapping motion of the wings was recorded at an image recording rate of 1 kHz for a duration of 15 seconds to ensure that at least 10 flapping cycles were captured even at the maximum flapping frequency. In the tests, the background of the flapping wings was illuminated by a spotlight (FSP-575) to achieve a better contrast of the wing leading edges. Then, a dedicated MATLAB script was used to detect the leading edges and to calculate the stroke angle (ϕ), which is defined as the angle between the upper and the lower wings (Fig. 3.1b).

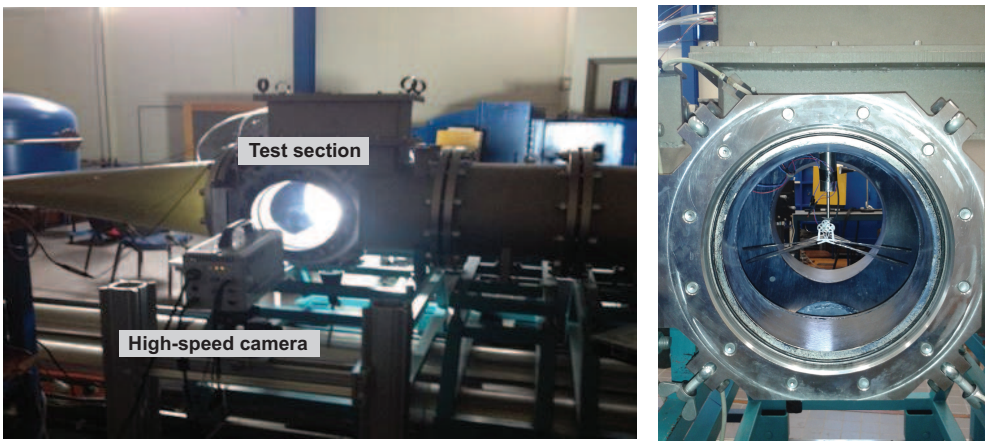

Figure 3.2: Experimental setup for the in-air and in-vacuum measurements (*left*) and a close-up view of the test section with the DelFLy II model mounted (*right*)

3.1.3. Results and discussion

In this section, the motion kinematics and force analysis results for the experiments in air and vacuum conditions are presented for the flapping frequencies of 8 and 12 Hz. In all comparison plots, in-air data are represented in blue, while in-vacuum data are in red. Note that the start of the instroke (maximum stroke angle) was selected to define the start of the flapping period.

Flapping-wing kinematics and visualization of the wing deformations

Figure 3.3a shows the temporal variation of the stroke angle plotted with respect to non-dimensional time ($t^* = t/T$, where t is time in seconds and T is the period of a flapping cycle) for two periods of the flapping motion at 8 Hz flapping frequency in air and in vacuum conditions. Moreover, the variation of the stroke angle is calculated based on the mechanical model of the driving system, assuming a constant rotation speed of the driving axis and no deformations of the system (plotted in black). The comparison of these three different cases reveals prominent differences in the kinematics. First, the maximum

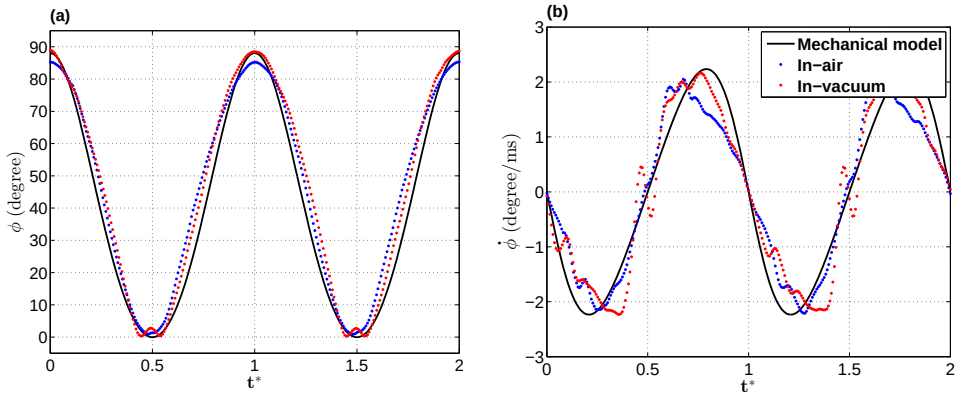

Figure 3.3: Temporal variation of **a** the stroke angle (ϕ) and **b** angular velocity ($\dot{\phi}$) vs. non-dimensional time (t^*) plotted for two periods of the flapping motion at 8 Hz wing-beat frequency in air (*blue*) and in vacuum (*red*), complemented with the prescribed motion kinematics calculated based on the mechanical model of the driving system

phase angle reaches approximately 85° in the case of in-air measurements, while it peaks at 88° in-vacuum measurements, which agrees well with the design full stroke amplitude of the DelFly flapping system. This suggests that due to the fluid forces exerted on the flexible wings, not only the mylar wing planform deforms but also the leading edges bend and the driving hinge mechanism is constrained, which results in a decrease of the maximum stroke amplitude of the flapping motion. Second, it is clear that the motion profiles in air and vacuum conditions do not overlap with that of the mechanical design with a larger deviation in the case of flapping in air. The difference is also evident in the angular velocity profiles of the three cases (Fig. 3.3b), which is calculated by differentiating the phase angle with respect to time. This can be attributed to the fact that the flapping frequency varies at the sub-period level particularly during the in-air flapping motion due to the varying loads on the motor, although the microcontroller system attempts to keep it constant at the period level. Based on the motor commutation information, the standard deviation of these sub-period fluctuations was calculated as 13 % and 5 % of the nominal flapping frequency for the in-air and in-vacuum measurements, respectively. Third, the instroke phase lasts shorter than the outstroke ($t^*_{in} = 0.47T$) in the case of flapping in air, which is also evident in the angular velocity profile (Fig. 3.3b) with a slightly higher instroke peak velocity (relative difference of 5 %). The absence of such a difference in the in-vacuum measurements suggests that it is most probably because of different flow field characteristics caused by the wing-wing interaction occurring at the start of the outstroke (i.e. clap-and-peel). On the other hand, at the end of the instroke in vacuum conditions, there appears a small hump. A close inspection of the high-speed imaging reveals that the upper and lower wings hit each other and bounce back for a stroke angle of approximately 2.5°. As the motion progresses, they approach until they touch each other gently this time and subsequently start moving apart with the start of the outstroke. Apparently, in the presence of air, the aerodynamic force exerted on each wing counteracts the inertia of the wings such that the leading edges never get in full contact.

Besides the leading edge motion kinematics, the deformation visualizations of the flapping wings reveal prominent differences between the two considered conditions (see Fig. 3.4). The wing inertia manifests its effect especially during the stroke reversal from the outstroke to the instroke ($t^* = 0$): the wing body continues moving and changes direction in motion later than the leading edge spars in the case of flapping in vacuum conditions. Such a considerable effect of the wing-inertia term on the resultant wing deformation particularly at the stroke reversals in the DelFly flapping flight was also reported by Percin et al (2011) based on the analysis of the structural dynamics of equivalent-DelFly-wings by use of a simplified analytical model. Due to this excessive movement, the wings deform and store elastic energy, analogous to a mass-spring system. This energy is then released again with the start of the instroke causing the wing surfaces to accelerate in the stroke direction at a higher rate than the leading edges, which are directly driven by the gear and hinge mechanism. As a result, the trailing edges of the wings surpass the leading edges as evident at $t^* = 0.25$. Contrary to the vacuum case, the presence of air alters the chordwise deformation behaviour substantially. Close to the end of the outstroke, the contribution of the aerodynamic effects to the wing deformation is at its minimum level due to very small wing velocities. The wing surfaces, however, move outwards due to their inertia and discharge of the elastic energy stored in the wing structure during the previous outstroke, yet this motion is dampened by the fluid force (viz. drag) resulting in more-or-less flat wing surfaces at the end of the outstroke. At the middle of the instroke ($t^* = 0.25$), the wings experience significantly higher deformation as a result of the enhanced aerodynamic contribution as the maximum stroke velocity is reached at this stage of the motion ($|\dot{\phi}| = 2.15$ degree/ms). At the end of the instroke ($t^* = 0.5$), the upper and lower wings are in full contact in vacuum, whilst the wing surfaces are still flexed outwards in air. The effect of the aerodynamic forces on the wing deformation is probably best visualized at the middle of the outstroke ($t^* = 0.75$) in view of the similar initial wing deformations at the beginning of the outstroke ($t^* = 0.5$). The overshoot of the wing surfaces is limited at the stroke reversal due to the presence of the counter-wing. Obviously, at $t^* = 0.75$ the wings are deformed more in air such that the trailing edges of the upper and lower wings are still in contact partially. This configuration constitutes the basis for the force enhancement mechanism of the DelFly, i.e., the clap-and-peel motion, due to its influence on the LEV formation as discussed in the previous chapter.

In the context of the previous discussion, it is plausible to assume that the aerodynamic and inertial contributions to the resultant wing deformation grow with increasing flapping frequency. The increase in the magnitude of the inertial component even affects the flapping kinematics as evident in the temporal variation of the stroke angle for the flapping frequency of 12 Hz (Fig. 3.5). In vacuum conditions, the outwards movement of the wing body during the stroke reversal from outstroke to instroke pulls also the leading edge spars further outwards resulting in a relatively higher total stroke amplitude of the flapping motion (approximately 3° more according to the mechanical model). Such a difference can be explained by the bending of the leading edge spars in addition to the mechanical play in the driving system. Despite the increasing influence of the inertia term, the leading edge motion kinematics remains relatively unaffected in air due to also increasing effect of aerodynamic damping for higher flapping frequencies.

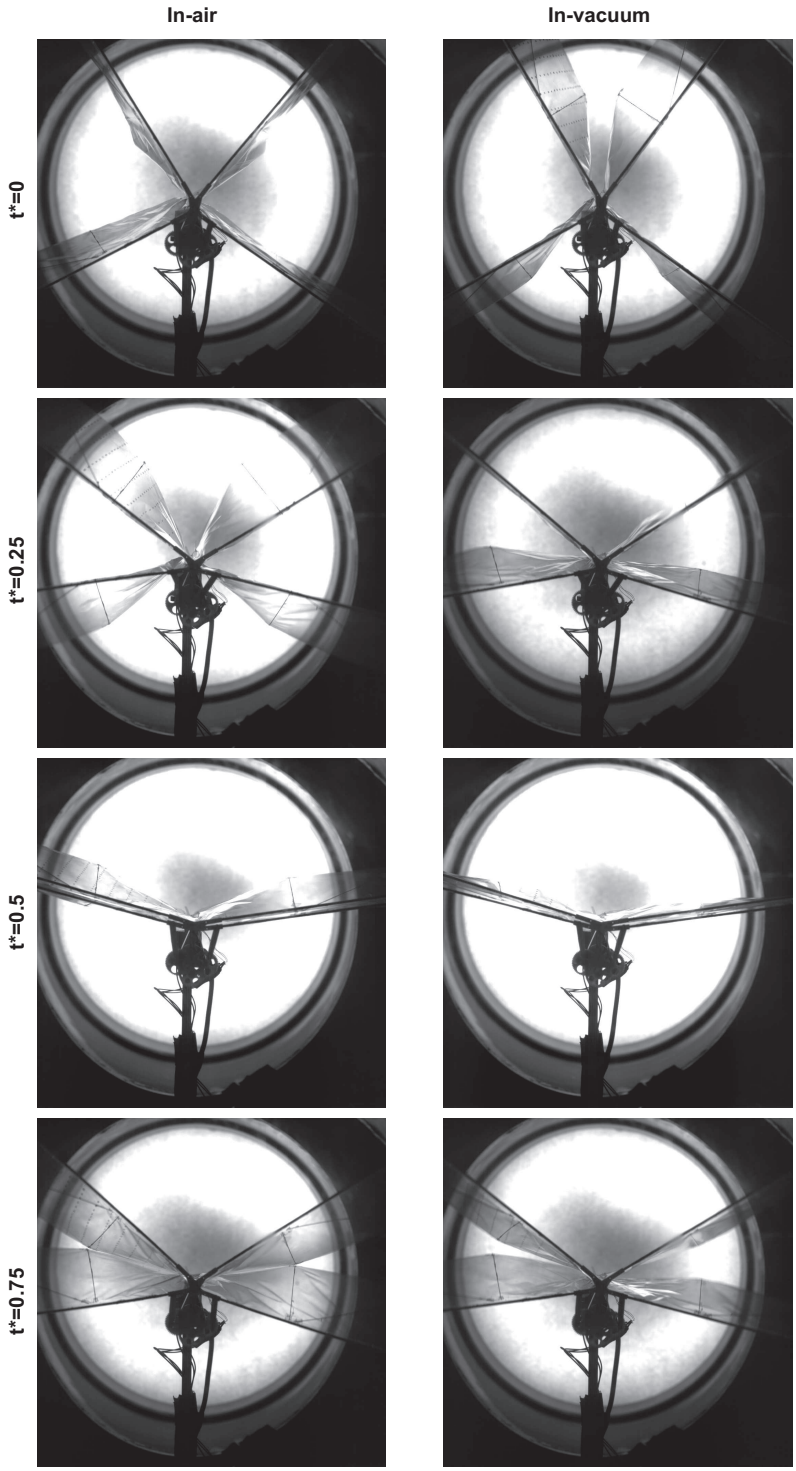

Figure 3.4: Images of the DelFly wings flapping at a frequency of 8 Hz in air (*left*) and in vacuum (*right*) at different instants of the flapping motion: end of the outstroke/start of the instroke ($t^* = 0$); middle of the instroke ($t^* = 0.25$); end of the instroke/start of the outstroke ($t^* = 0.5$); middle of the outstroke ($t^* = 0.75$)

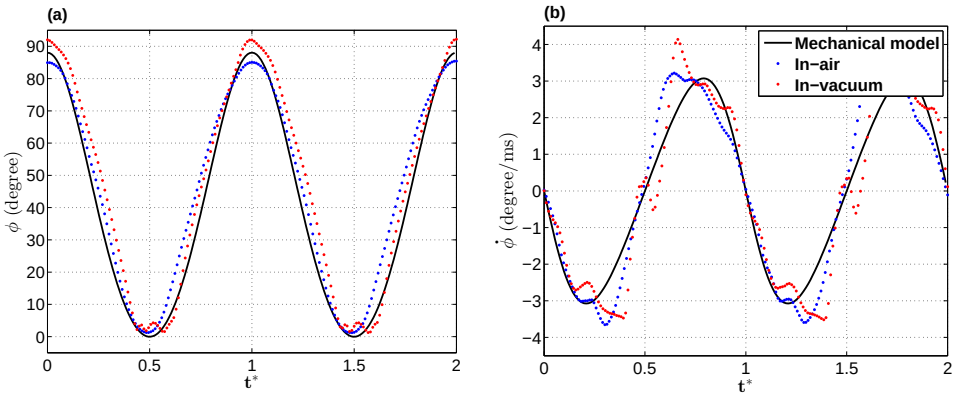

Figure 3.5: Temporal variation of the **a** stroke angle (ϕ) and **b** angular velocity ($\dot{\phi}$) vs. non-dimensional time (t^*) plotted for two periods of the flapping motion at 12 Hz flapping frequency in air (*blue*) and in vacuum (*red*), complemented with the prescribed motion kinematics calculated based on the mechanical model of the driving system

Power consumption

The power consumption that is required to sustain the flapping-wing motion of the DelFly II is calculated by multiplying the time-resolved measured values of voltage and current fed to the brushless motor. The time-varying values are then averaged over a number of flapping cycles for the in-vacuum and in-air cases for the range of test flapping frequencies considered (Fig. 3.6). In addition to these, the aerodynamic power consumption is computed as the total power consumption in air minus the power consumption in vacuum.

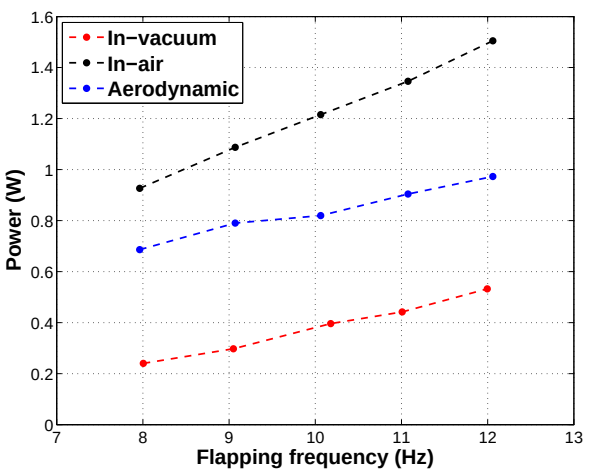

Figure 3.6: Power consumption vs. flapping frequency for the in-vacuum and in-air measurements complemented with the aerodynamic power computed as the total power consumption in air minus that in vacuum

This reveals that the greater portion of the total power consumption in air (64-74 %) is due to aerodynamic effects. Overall power consumption in air follows a linearly increasing trend with respect to the flapping frequency. Considering that the power required to drive the motor, gears and hinges is varying in the range between 0.18 to 0.2 W for the range of flapping frequencies, the power required to overcome the elastic-inertial forces reaches approximately 20 % of the total power consumption in air for the highest flapping frequency case.

Unsteady forces

As mentioned previously, the main objective of the force measurements in air and vacuum conditions is to identify the force components that are associated to the aerodynamics of the flapping-wing motion, while isolating the components that are originating from structural vibrations or wing inertia as they are also sensed by the force sensor. Under this condition can the influence of the flapping-wing aerodynamics on the force generation can be assessed and further optimization studies can be performed. For this purpose, power spectral densities of the X and Z force components in air and vacuum conditions are compared in Fig. 3.7 for the flapping frequency of 8 Hz. Note that the power spectral densities for in-air and in-vacuum measurements were calculated for the same number of flapping cycles at the given flapping frequency so that they are comparable in terms of amplitudes (energy per frequency) between the two cases. The spectrum of the X-force component in air contains two major peaks with frequencies corresponding to the first (fundamental) and second harmonics of the flapping motion in addition to a relatively less powerful third harmonic. None of these frequency components appear in the vacuum case which suggests that they can be attributed to the aerodynamic forces. For higher frequencies, the spectrum is relatively clean with very low-amplitude higher harmonics of the flapping frequency. On the other hand, the spectrum of the Z-force component is populated with high-harmonic peaks which have a higher amplitude in vacuum and are significantly damped in air. Only the first harmonic, which is essentially the flapping frequency, emerges with a higher amplitude in air than that in vacuum conditions.

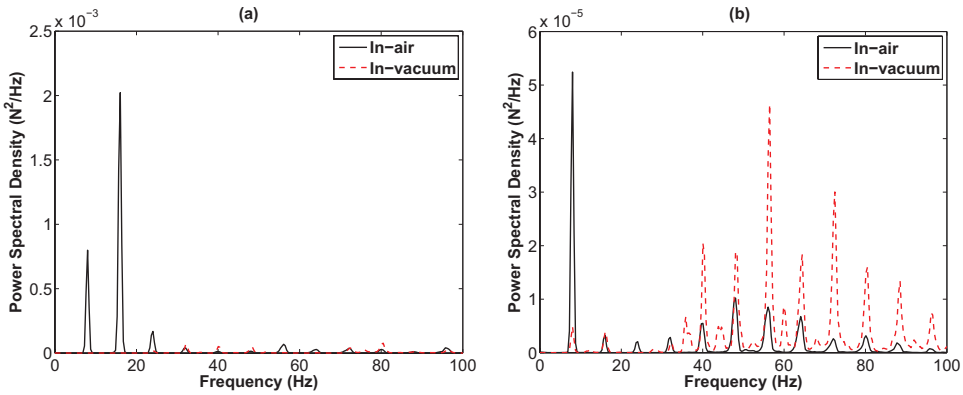

Figure 3.7: Comparison of power spectral densities of **a** X and **b** Z forces in air and vacuum conditions for a flapping frequency of 8 Hz

Flapping at a higher frequency (i.e. 12 Hz) results in slightly different power spectra (Fig. 3.8). In the spectrum of the X-force, it is clear that the first and the second harmonics of the flapping motion only appear for the case of in-air measurements, in accordance with the lower flapping frequency case. However, the third harmonic has the same amplitude both in air and vacuum conditions. This can be explained by the fact that for the flapping frequency case of 12 Hz, the frequency of the third harmonic probably corresponds a frequency of a structural mode of the DelFly body or one of the components. On the other hand, the forth and the sixth harmonics have higher amplitude in vacuum but are significantly damped in air. This suggests that these peaks likely correspond to wing structural mode excitations. In the spectrum of the Z force component, the first harmonic stands out with its amplitude higher in air than in vacuum conditions similar to lower flapping frequency case. On the other hand, the forth, fifth and seventh harmonics present opposite characteristics with higher magnitudes in vacuum conditions. This can be associated to the different structural and interaction characteristics of the wings driven by the flapping-wing inertia during the flapping motion. Accordingly, the first two harmonics are considered to be purely aerodynamic, while higher harmonics are either associated to or contaminated with structural modes of the model.

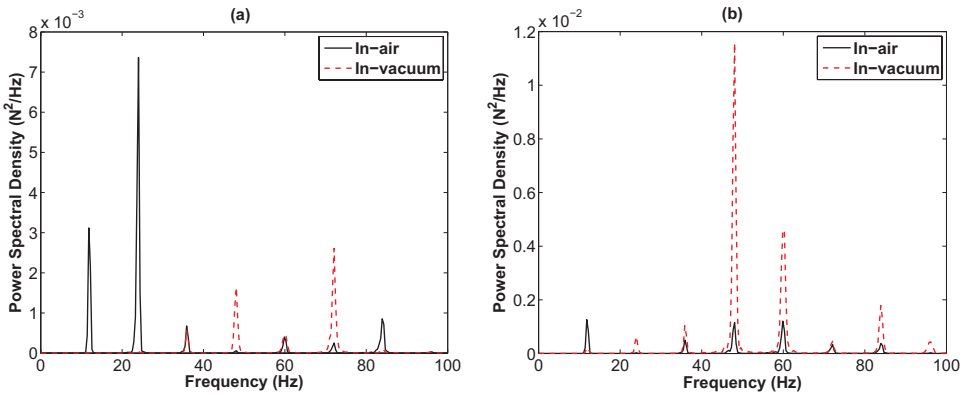

Figure 3.8: Comparison of power spectral densities of **a** X and **b** Z forces in air and vacuum conditions for a flapping frequency of 12 Hz

In order to better relate the aerodynamic force peaks in the power spectrum to the force generation mechanisms of the flapping-wing aerodynamics, further force measurements were used that were obtained with the balance system located outside of the vacuum test setup (see section 3.3.1 for the details the experimental setup). The reason for using this alternative data is twofold: first, to provide a higher quality high-speed imaging of the flapping motion; second, to minimize delays in the synchronization between the data acquisition, the flapping motion and the high-speed imaging, which occurred in the vacuum test setup due to use of additional cabling and electronics to facilitate the mounting of the experimental model inside the sealed test section. The analysis is performed for the 12 Hz flapping frequency case in hovering flight condition as it is a more realistic representation of the DelFly's hovering flight envelope.

In order to isolate the force variation occurring at the flapping frequency, the raw X-

force data were filtered by a Chebyshev II low-pass filter with -80 dB attenuation of the stop-band in MATLAB. The cut-off frequency was selected to keep only the fundamental frequency component and a forward-backward filtering technique was applied in order to prevent the time-shift of the data. The temporal variation of the X-force is then plotted for two periods of the flapping motion, in association with the stroke angle kinematics (Fig. 3.9).

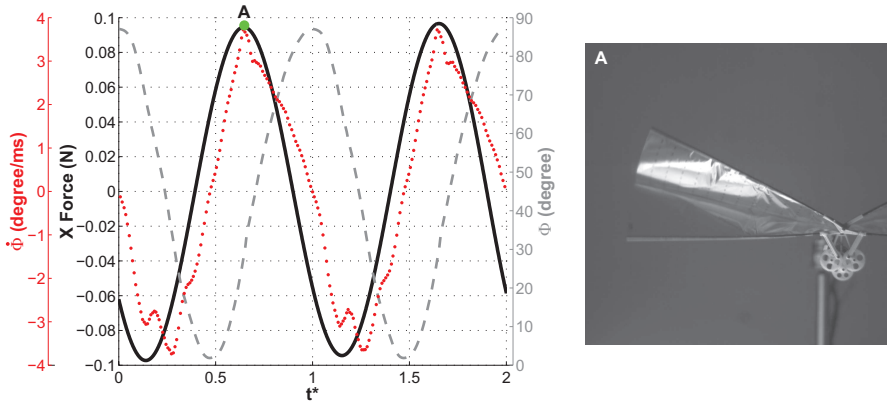

Figure 3.9: Temporal variation of the X-force component at the fundamental frequency (black) complemented with the stroke angle (ϕ, *dashed gray*) and angular velocity ($\dot{\phi}$, *red dots*)(*left*), the instant of the flapping motion that corresponds to the maximum of the X-force (*right*)

The aerodynamic force component at the flapping frequency displays a single peak during each flapping cycle. The image that corresponds to this maximum shows that it occurs when the wings peel apart at the beginning of the outstroke. This force component is clearly related to the clap-and-peel motion, which can be regarded as a force enhancement mechanism occurring only once in a flapping cycle during the stroke reversal from instroke to outstroke.

The X-force component at the second harmonic frequency obtained with a similar filtering procedure (Fig. 3.10), on the other hand, displays an in-phase variation with the stroke angular velocity. In this respect, the two peaks in the spectrum of the X-force can be understood as the force generated by the translating motion of both wings that happens twice in one complete flapping cycle (during the instroke and outstroke phases) and associated delayed stall (leading edge vortex) mechanism.

Analysis of the Z force in hover condition is more difficult because as previously mentioned, the forces generated by the wings moving in opposite phase mostly (not completely due to dihedral angle of the wings) cancel each other out which results in relatively small net Z-force production. Comparison of the Z-force in-air and in-vacuum conditions by means of power spectral densities (Fig. 3.8b) reveals that the first harmonic is the only component that has a higher amplitude in air conditions pointing to an aerodynamics related contribution for the specific case of hovering flight. This component of the Z-force varies in counter-phase to the stroke velocity (Fig. 3.11), which suggests a dominance of the lower wing in the generation of the force component. The instants where the maximum and the minimum of the Z-force variation occur confirm that the resultant force is

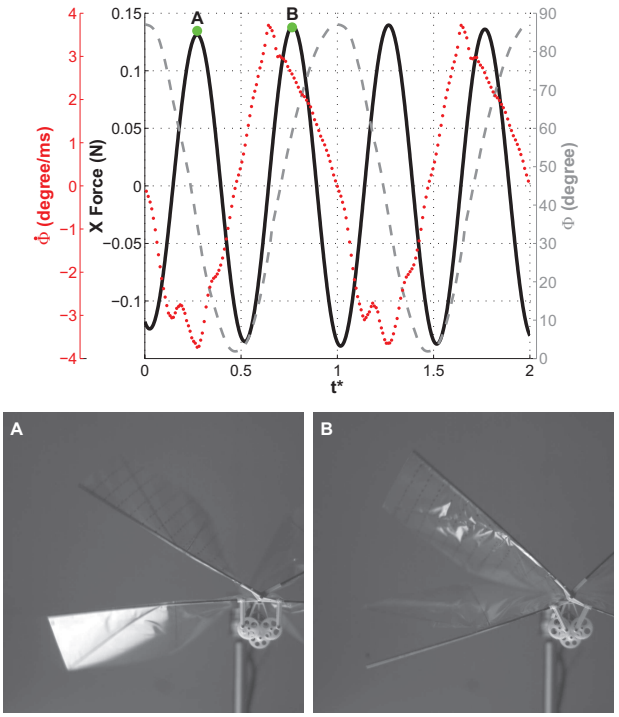

Figure 3.10: Temporal variation of the X-force component at the second harmonic frequency (black) complemented with the stroke angle (ϕ, gray) and angular velocity ($\dot{\phi}$, *red dots*)(*top*); the instants of the flapping motion that corresponds to the maximums of the X-force (*bottom*)

a consequence of the dihedral angle and the stroke velocity (see Fig. 3.1b). At the point of the maximum, which occurs during the instroke, the stroke velocity is close to the maximum value and lower wing-normal force is oriented toward the positive Z-force direction (z_b) more than that of the upper wing in the negative Z-force direction. It works in the other way for the minimum of the Z-force such that the lower wing's normal force has a relatively large component in the $-z_b$ direction. In consequence, very small positive flap-averaged Z-force (0.01 N) is produced in the hovering configuration.

Comparison of the force spectra in air and vacuum conditions have allowed to distinguish the aerodynamic and inertial components in the measured forces to some extent, as well as giving clues about the contributions of aerodynamic force generation mechanisms. It is clear that in the hovering flight configuration, the first two frequency components (the fundamental frequency and the second harmonic) of the X-force variation are associated to the aerodynamic forces so that in the following parts of the thesis, higher harmonic components are filtered out. Although the Z-force is not of primary interest in the hover configuration, it was shown that only the first harmonic in the power spectrum can be attributed to the aerodynamic forces. Moreover, due to the wing dihedral angle and the asymmetric stroke kinematics of the instroke and outstroke, the DelFly experiences a very small flap-averaged Z-force.

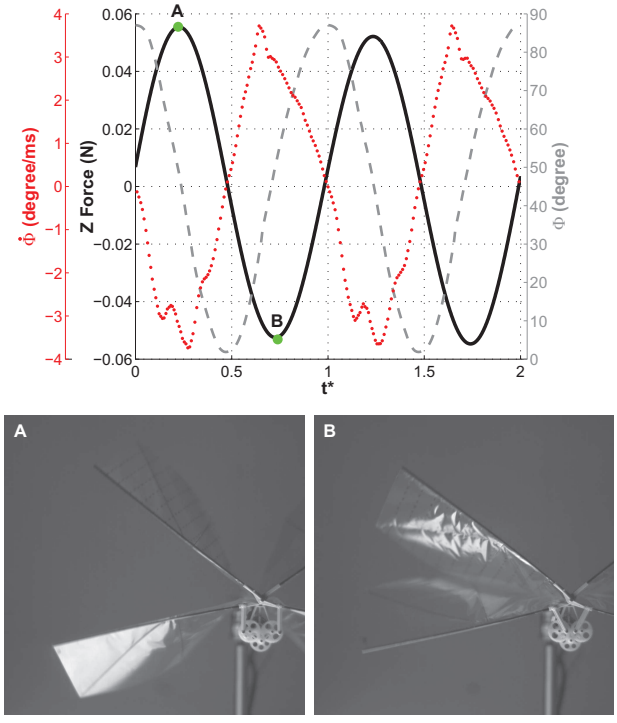

Figure 3.11: Temporal variation of the Z-force component at the fundamental frequency (*black*) complemented with the stroke angle (ϕ, *dashed gray*) and angular velocity ($\dot{\phi}$, *red dots*)(*top*); the instants of the flapping motion that corresponds to the maximum and the minimum of the Z-force (*bottom*)

Finally, to provide a complete image of the temporal variation of the filtered X-force and its relation with the power consumption, they are plotted for two periods of the flapping motion for the case of flapping at 12 Hz in hover configuration in air (Fig. 3.12-top). Additionally, the images of the flapping wing-pair at six selected phases of the flapping cycle that correspond to local extremes of the X-force and power consumption are provided in Fig. 3.12 (bottom).

For this particular case, the flapping wings produce a flap-averaged X-force of 0.177 N, which is sufficient to support the weight of a DelFly with a typical mass of 17 grams in hover configuration. At the beginning of the instroke, the X-force is at the minimum of the complete flapping cycle. At the instant A, corresponding to the stroke reversal, the upper and lower wing leading edges are more or less stationary and the wing surfaces have a small amount of deformation. As the upper and lower wings start moving inwards, the force increases gradually with increasing wing speed and deformation. The maximum force during the instroke is reached approximately at $t^* = 0.3$, when the wing is moving with nearly the maximum stroke velocity. Furthermore, the surfaces of the wings are deflected significantly resulting in an increased frontal projected wing area with its normal in the x_b direction. Obviously, in terms of X-force production, such an area is essential for the pressure fields to act on. For instance, the low pressure region formed by the LEV

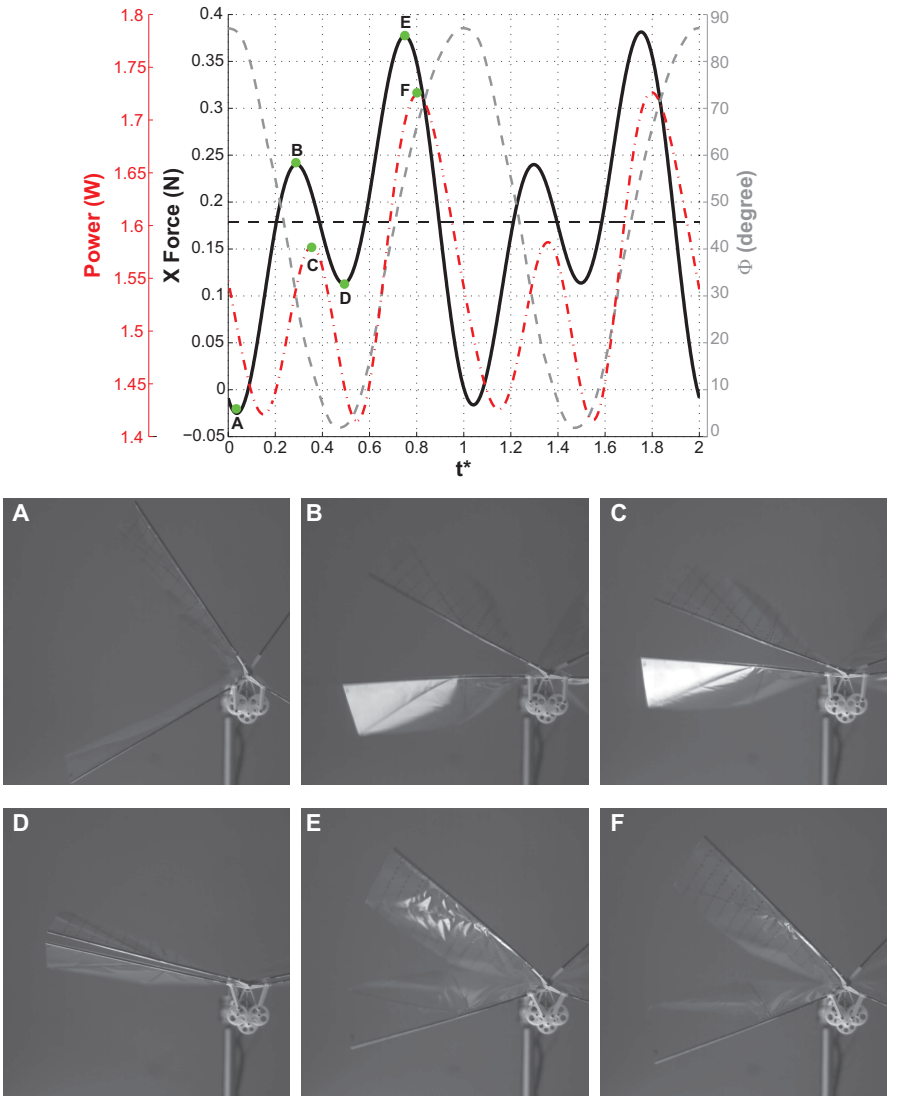

Figure 3.12: Temporal variation of the X-force (*black line*) and power consumption (*dash-dot red*) plotted for two periods of the flapping motion for the flapping frequency of 12 Hz in hover configuration of the DelFly in air conditions complemented with the variation of the stroke angle (Φ, *dashed gray*) and the flap-averaged X-force value (*dashed black*) (*top*); six instants of the flapping cycle (*bottom*) that correspond to local maximums and minimums of the X-force and power consumption variations as indicated by letters A-F in the plot above

requires a vertical wing surface area to exert on in order to generate a suction force. The power consumption during the instroke peaks slightly after the maximum of the X-force (at $t^* = 0.35$, instant C). In this period of the instroke, the stroke velocity is decreasing, which causes also a decline in the magnitude of the resultant forces. In correlation with this, the power consumption also decreases. Closer visual inspection of the high-speed photography of the flapping motion reveals that the wing surfaces deform until this stage of the motion (instant C), after which the stored elastic energy is released as the wing surfaces start moving inwards and deflect toward its neutral condition. Subsequently, the second minimum of the X-force is reached (at $t^* = 0.49$, instant D) at the end of the instroke. However, the force value is significantly higher at this stage than at the end of the outstroke. In this case, the wings clap and presumably the momentum jet generated by this wing-wing interaction contributes to the X-force production. Also note that the total frontal projected area of the wings is larger at this time than at the end of the instroke, which provides relatively larger area for the suction forces. As the peeling occurs with the start of the outstroke, the X-force starts increasing again reaching finally the maximum of the complete flapping cycle at $t^* = 0.75$ (instant E). Note that at this very stage, the maximum stroke velocity has already been passed and it is in the decreasing phase (see Fig. 3.5b). High speed image of this instant shows that although the wing leading edges are apart at a stroke angle of approximately 56°, the trailing edges are still in contact until almost the taper point of the wings. As discussed previously, this configuration promotes the growth of the LEV due to the formation of a low pressure region between the wings and the inrush of the fluid to this gap. This has twofold consequences: first, increase of the X-force due to presence of a massive LEV; second, increase of the power consumption because the low pressure region between the wings increases power requirement to peel the wings apart. The maximum of the power consumption is also off-phase with respect to the maximum of the X-force during the outstroke ($t^* = 0.8$, instant F). The lags between the maximums of the force generation and power consumption during the flapping motion are likely to stem from the structural deformation characteristics of the wings, which will be discussed in Section 3.4.

3.2. Balance-mounted and free-flight force determination of the DelFly II

3.2.1. Introduction

The increasing interest in the field of flapping-wing MAVs brings about numerous challenges in the design process due to the unsteady and three-dimensional nature of the flapping-wing aerodynamics. Particularly, determination of the performance measures with the purpose of development and optimization of a certain design by means of aerodynamic and dynamic models requires accurate experimental testing and comprehensive analysis of the data. Generally, these tests are force and flow field measurements carried out in a wind or water tunnel by satisfying geometric, kinematic and dynamic similarities or, alternatively, with measurements in free-flight conditions by use of a proper model of the flapping-wing MAV. As well as complementing each other, the results of the two different approaches may lead to incongruity in the conclusions. For instance, force and moment measurements by use of a force balance system in a wind tunnel can be conducive to describe the unsteady forces experienced by the MAV at a given flight condition both in flap-averaged and time-resolved manner (with the latter necessitating proper identification of the aerodynamic and inertial components as discussed in the previous section). Nevertheless, these are intrinsically static measurements which do not capture the flapping-wing MAV's dynamical response or stability characteristics.

In general, many researches relied on the wind tunnel measurements by use of a balance system featuring a sensitive force sensor in order to identify the lift and thrust generation mechanisms of tailless and tailed flapping-wing MAVs (Lin et al, 2006; Mazaheri and Ebrahimi, 2011; Muniappan et al, 2005; Nakata et al, 2011). However, these studies did not take the possible impact of structural vibrations into consideration as well as not comparing the balance force data with the forces estimated based on the free-flight dynamics of the MAV. Other studies, which focused on the estimation of forces experienced by free flying flapping-wing MAVs (Grauer et al, 2011; Lim et al, 2012), did not include comparison of the results with wind tunnel measurements or numerical simulations. More recently, Caetano et al (2013c) performed several flight tests in a flight arena with three-dimensional motion tracking capabilities, which cover the full flight envelope of the DelFly II. They used these data to reconstruct the time-varying forces and moments that act on the MAV during different trim conditions and maneuvers. However, their study also lacked comparison with high-precision force balance tests, which would allow to assess the fidelity of their results.

Lee and Han (2012) combined the two approaches for the determination of forces by performing tethered force measurements in a wind tunnel with a movable balance system that allowed some degree of freedom in the motion of the ornithopter with the flapping motion and free-flight tests by use of a three-dimensional visual tracking system. Nonetheless, they compared the flap-averaged forces rather than flap-cycle variations, which permits for only a crude comparison of the two methods.

In this context, the specific aim of this section is to assess the fidelity of the tethered wind tunnel and free-flight force determination techniques via the comparison of

Parts of this section have been published in the proceedings of 2014 International Conference on Unmanned Aircraft Systems (ICUAS) (Caetano et al, 2014) and in Bioinspiration and Biomimetics **10(5)** (Caetano et al, 2015)

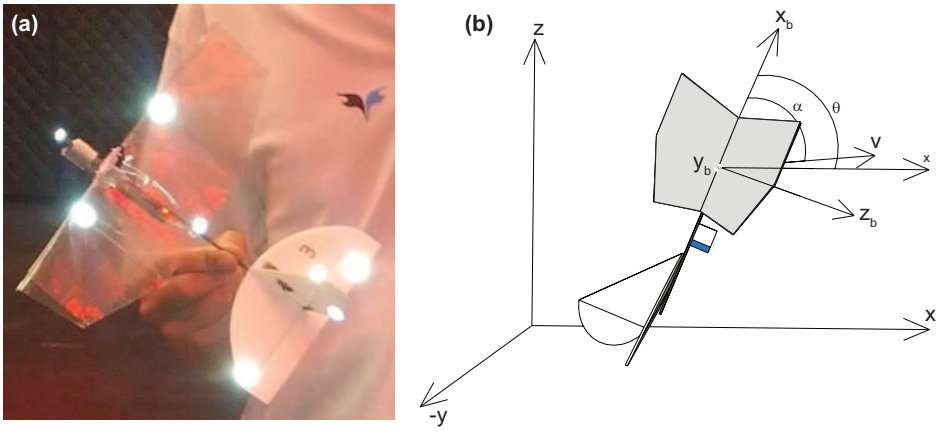

Figure 3.13: (a) Position of the markers on the DelFly for the motion tracking in the VICON system, respectively placed at the nose, the intersection point of the stiffeners and wing leading edge, the fusalage aligned with the trailing edges of the wings, fixed on the horizontal and vertical stabilizers, the elevator and the rudder; (b) inertial reference frame (x, y, z) and the body reference frame (x_b, y_b, z_b) of the DelFly with the indications of the pitch angle (θ) and the angle of attack (α) as calculated based on the relative wind angle in the $x_b z_b$ plane

the time-resolved oscillations of the forces acquired by use of the two methods. For this purpose, force measurements were performed on a DelFly II model mounted on a balance system in a wind tunnel at the trim conditions, which correspond to a number of different flight regimes covered in the free-flight tests performed by Caetano et al (2013a). Furthermore, the sources of errors in the measurement of the forces specific to the two methods are explored.

3.2.2. Experimental setup and processing methods

Free-flight experiments

The free-flight experiments were performed in the test chamber of the MAV Indoor Flight Test Laboratory of Micro Air Vehicle Integration & Application Research Institute at the United States Air Force Research Laboratory. The chamber consist of a VICON motion capture system that features 65 cameras distributed over two rows at heights of 4.6 and 7.6 meters in a total flyable volume of $21 \times 17 \times 7.6$ m^3 (Caetano et al, 2013a).

The Vicon system was used to track 8 markers placed on the fixed structure and control surfaces of a fully-equipped DelFly II model (see 3.13) at a recording rate of 200 Hz. The DelFly model has a mass (m) of 17.4 grams with its center of gravity (CG) initially located at 72 mm from the hinge point of the flapping mechanism in the $-x_b$ direction and 2 mm below the fuselage in the z_b direction. In this configuration, the MAV is capable of slow-forward flight and hovering flight. Subsequently, in order to perform the free-flight position measurements in the fast forward flight regime of the DelFly, the CG was moved forward (41.1 mm from the hinge point of the flapping mechanism in the $-x_b$ direction). A total number of 220 flight tests were conducted for different velocities and trim conditions. The three-dimensional coordinates of the 6 mm diameter markers are estimated with a positional accuracy of ±0.2 mm.

Flight path reconstruction techniques were then utilized to estimate the DelFly's states during the flight tests. First, the recorded coordinates of the 8 markers were transformed from the global (inertial) reference frame (x, y, z) to the body reference frame (x_b, y_b, z_b with its origin located at the CG). The unit vectors of the body reference frame were used to build the direct cosine matrix, from which the Euler angles were computed (Caetano et al, 2013c). Euler angles were then used to calculate the angular velocities. The linear velocities and accelerations were estimated by differentiating the position of the CG in time by use of finite differences. The results presented in this section were obtained by use of a 2-point central differencing scheme. In total, 17 states were reconstructed: Euler angles (ϕ, θ, ψ); velocity of the CG, $\vec{V} = (\vec{u}, \vec{v}, \vec{w})$; acceleration of the CG, $\vec{V} = (\vec{u}, \vec{v}, \vec{w})$; angular velocities, $\vec{\omega} = (\vec{p}, \vec{q}, \vec{r})$; angular accelerations, $\vec{\omega} = (\vec{p}, \vec{q}, \vec{r})$; aerodynamic angle of attack (α) and the side-slip angle (β).

The reconstructed states were used in order to compute the forces and moments acting on the DelFly in free-flight under a number of assumptions: non-flapping/rigid body kinematics; constant mass and inertia properties; non-moving atmosphere; non-rotating flat earth; constant air density and gravity; symmetric platform. The first two assumptions enable the development of a simple, flap-averaged model that could be used as a baseline for basic on-board controllers. Moreover, the characteristic of being a stable platform that does not require sub-flap commands for attitude and maneuver control promotes the application of these assumptions.

The general aircraft equations of motion were devised to compute the longitudinal forces acting on the MAV from the measured state variables in its plane of symmetry as shown in Eq. 3.1 (Caetano et al, 2013b), with X and Z being the X-force and Z-force, respectively.

$$\begin{aligned} X &= m(g\sin\theta + qw - rv + \dot{u}) \\ Z &= m(-g\cos\phi\cos\theta - qu + pv + \dot{w}) \end{aligned} \tag{3.1}$$

Wind tunnel experiments

The force measurements were performed in a low-speed wind tunnel (W tunnel) at the Aerodynamics Laboratory of Delft University of Technology. The wind tunnel has a contraction particularly designed and built for the DelFly experiments that ends in an open test section with cross-section dimensions of 0.6 × 0.6 m. A hot-wire anemometry system was used in order to measure the free-stream velocity in the test section so that it could be set to match the free-flight velocity values measured during the trimmed flight of the ornithopter.

The DelFly II model was mounted on a balance system that consists of the ATI Nano-17 Titanium force sensor and variable pitch and yaw mechanisms (Fig. 3.14). The mechanism allows adjustment of the pitch angle from −15° to 95°. The angle was set to predefined values based on the free-flight measurements of the DelFly. The microcontroller and FPGA systems were used for the regulation of the flapping frequency and data acquisition (note that these systems and properties of the force sensor are explained in detail in Sec. 3.1.2). Forces, moments, rotational information of the DelFly brushless motor, Hall sensor output, voltage and current were acquired at a data acquisition frequency of 12.5 kHz. A complementary high-speed imaging of the flapping wings was also conducted at a record-

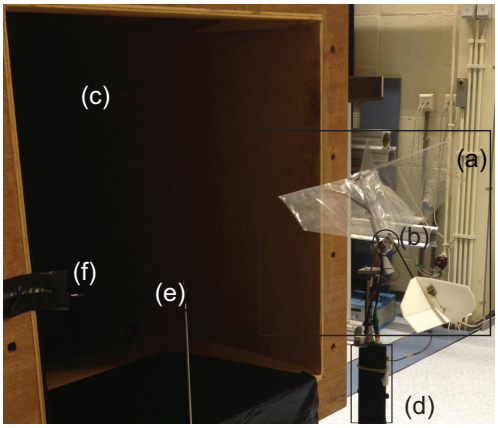

Figure 3.14: Wind tunnel experimental setup: (a) The DelFly II model; (b) ATI Nano-17 Titanium force sensor; (c) wind tunnel contraction; (d) the strut mechanism that allows attitude changes in pitch and yaw; (e) the hot-wire probe; (f) thermocouple for temperature corrections in the hot-wire measurements

ing rate of 1200 Hz in order to obtain the relationship between the rotational information of the motor and the phase angle of the flapping wings.

Similar to the previous force measurements, the raw force data were filtered by use of a Chebyshev II low-pass filter in MATLAB. However, the determination of the cut-off frequency based on the comparative analysis of the results of in-air and in-vacuum measurements may not be directly justified in this case especially for the Z-force component due to presence of the forward flight velocity. It should be noted that most of the flight conditions considered in this section are the cases of slow forward flight of the DelFly at high angles of attack, hence the free-stream flow is more influential on the Z-force component by creating significant difference between the flow conditions experienced by the lower and upper wings. Therefore, assuming that only the first harmonic of the measured Z-force is associated to the aerodynamic forces as in the case of the hovering flight will be erroneous. On the other hand, it remains plausible to assume that the first two harmonics of the X-force are associated to the aerodynamics because still the same force generation mechanisms are dominant in the production of the X-force although the magnitudes can be different. Therefore, the selected cut-off frequency should preserve at least the first two harmonics in the X-force. Different aspects in the selection of the cut-off frequency are addressed and discussed in the following section.

3.2.3. Results and discussion

Before proceeding with the comparative analysis of the results, it is of vital importance to identify the limitation of both methods in the determination of the aerodynamic forces. In the case of free-flight force analysis, an important aspect is the use of the numerical differentiation scheme as derivation of the position data in time (once for velocities and twice for accelerations) is necessary to calculate the forces. Therefore, the effects of numerical differentiation (i.c., the two-point central difference algorithm) are addressed in this section. Also an estimation of the tracking error in the free-flight measurements is

given. Regarding the balance-mounted force measurements structural vibrations of the DelFly body have a significant influence on the measured forces with their magnitudes being comparable to the aerodynamic forces particularly in the z_b direction. In this respect, the effect of the clamping position has been investigated since it can alter the structural dynamics of the body in terms of resonance frequencies.

Effects of numerical differentiation

It is evident in Eq. 3.1 that the determination of free-flight forces requires derivation of several quantities, which are rotational or translational velocities and accelerations from the acquired discrete position data. For this purpose, the common practice is to use finite difference algorithms, that can approximate the derivative values with a limited accuracy. In the present study, a second-order accurate two-point central difference algorithm is utilized for the calculation of time-derivative of the discrete time-series position and angle data, which reads:

$$\dot{x}(i\Delta t) = \frac{x((i+1)\Delta t) - x((i-1)\Delta t)}{2\Delta t} \tag{3.2}$$

where $\dot{x}$ is the time-derivative of the data (x), i is the index for discretized time and Δt is the time between two data points. Main reasons behind the selection of this scheme can be counted as: (1) its higher order of accuracy (smaller truncation error) compared to forward and backward differencing schemes; (2) to prevent the time-shift of the resultant force data; (3) relatively favourable measurement noise propagation characteristics compared to first-order accurate schemes. Regarding the last reason, it can be shown that the first-order accurate schemes (forward and backward difference algorithms) amplifies the measurement noise twice that of the central difference algorithm. When forward or backward difference algorithms are used, the standard deviation of a derived quantity ($\sigma_{\dot{x}}$) equals $\sqrt{2} \times \sigma_x \times f_{daq}$ with σ_x being the standard deviation of the measured quantity (i.e., position) and f_{daq} being the data acquisition frequency. In the case of two-point central difference scheme, it reads $\sigma_x \times f_{daq}/\sqrt{2}$.

It could also be considered to use more points for the calculation of the derivatives, however the relatively low sampling frequency of the measurements (i.e., 200 Hz) compared to the nominal flapping frequencies during the flight (9-13 Hz) will result in excessive smoothing of the data (modulation of the time signal) and thus loss of information in the resultant force oscillations. Nevertheless, the two-point central difference algorithm also acts as a low-pass filter, the influence of which should be identified for the proper analysis of the data. For this purpose, a generic sinusoidal analog signal ($x(t) = \sin(\omega t)$, where ω is the angular frequency) is considered (Bahill et al, 1982). Its time derivative is $\dot{x} = \omega \cos(\omega t)$, the Fourier transform of which is given below:

$$\dot{X}(\omega) = j\omega X(\omega) \tag{3.3}$$

For the digitized version of the signal $x_d(i\Delta t)$ at a frequency of $f_{daq} = 1/\Delta t$, Eq. 3.2 is used for the calculation time derivatives at discrete time steps. In order to transform from time domain to frequency domain, first the Z-transform is applied to Eq. 3.2 (Bahill et al, 1982):

$$\dot{X}_{d,c}(z) = \frac{X_d(z)\left(z - z^{-1}\right)}{2\Delta t} \tag{3.4}$$

Then substituting $z = e^{j\omega\Delta t} = \cos(\omega\Delta t) + j\sin(\omega\Delta t)$ gives:

$$\dot{X}_{d,c}(\omega\Delta t) = \frac{X_d(\omega\Delta t)\, j\sin(\omega\Delta t)}{\Delta t} \tag{3.5}$$

Equations 3.3 and 3.5 can now be used to assess the ratio of the magnitudes of the calculated and the true derivative. Taking into account that for a properly sampled analog signal (without aliasing), the Fourier transform of the analog signal $X(\omega)$ is equal to that of the discrete data $X_{d,c}(\omega\Delta t)$ at the sampling points. Then, the ratio is (Bahill et al, 1982):

$$\left|\frac{\dot{X}_{d,c}(\omega\Delta t)}{\dot{X}(\omega)}\right| = \frac{\sin(\omega\Delta t)}{\omega\Delta t} \tag{3.6}$$

A similar analysis was performed for the forward difference algorithm (Eq. 3.7) to investigate the frequency limitation effects of the first-order accurate schemes.

$$\dot{x}(i\Delta t) = \frac{x((i+1)\Delta t) - x((i)\Delta t)}{\Delta t} \tag{3.7}$$

Initially, application of z-transform yields:

$$\dot{X}_{d,f}(z) = \frac{X_d(z)\left(z - 1\right)}{\Delta t} \tag{3.8}$$

Then substituting $z = e^{j\omega\Delta t} = \cos(\omega\Delta t) + j\sin(\omega\Delta t)$ gives:

$$\dot{X}_{d,f}(\omega\Delta t) = \frac{X_d(\omega\Delta t)\left(\cos(\omega\Delta t) - 1 + j\sin(\omega\Delta t)\right)}{\Delta t} \tag{3.9}$$

By comparing Eqs. 3.3, 3.5 and 3.9, it is clear that forward difference algorithm introduces also a phase difference, whereas central difference algorithm does not have such an effect on the calculated derivative. For the forward difference algorithm, the ratio of amplitudes of the calculated and the true derivative is calculated as follows:

$$\left|\frac{\dot{X}_{d,f}(\omega\Delta t)}{\dot{X}(\omega)}\right| = \frac{\sqrt{2}\sqrt{1-\cos(\omega\Delta t)}}{\omega\Delta t} \tag{3.10}$$

By use of Eq. 3.6 and 3.10, the frequency characteristics of the central and forward difference algorithms can be calculated. In the free-flight measurements, the sampling frequency was 200 Hz ($\Delta t = 0.005$ s) so that the maximum frequency component that can be captured without aliasing is 100 Hz according to the Nyquist theorem. The effect of numerical differentiation on the frequency components is simulated in Fig. 3.15.

In the calculation of velocities from the measured marker positions, it is evident that the central difference algorithm attenuates the signal by 3 dB at 44 Hz, whereas it occurs at 88 Hz for the case of the forward-difference algorithm. For the accelerations, it is at the frequency of 32 Hz and 64 Hz for the central and forward difference algorithms, respectively. It is clear that first-order accurate algorithms have more favourable frequency

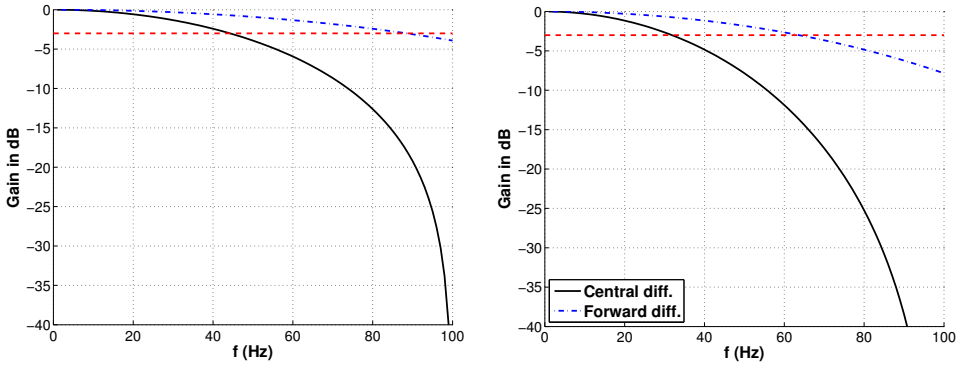

Figure 3.15: Attenuation of the magnitudes of the frequency contents **a** in the calculation of velocities and **b** accelerations by use of central difference algorithm and forward difference algorithm (dotted red line indicates an attenuation of 3 dB)

response characteristics, as they are based on a smaller time separation. However, use of these algorithms introduces a phase lag to the data and result in a time-shift in the calculated forces. Moreover, as shown above, the first-order schemes have less favourable noise propagation characteristics. These are the main reasons not to utilize first-order forward or backward difference schemes at the first place. Therefore, it is plausible to conclude that using the central difference algorithm, the frequency components of the derived velocities and accelerations, and in turn forces, until the third harmonic of the flapping frequency, which are least affected by the numerical differentiation, can be used for further analysis.

Estimation of the position measurement error

The estimation of measurement error level of the Vicon visual tracking system is a challenging procedure as it is severely affected by the DelFly's position in the flight chamber, its velocity and attitude as well as the retro-reflector size. To assess the uncertainty in the raw position data and calculated states, two different methods were utilized. First, the measurement error is assumed to be zero-mean, independent, identically distributed random variable (IID) (Mettler, 2010). Then, the data were low-pass filtered for various cut-off frequencies and the filtered data were subtracted from the measurement data to calculate the measurement residual. For the residual to meet the IID criteria, the autocorrelation should satisfy a 95 % confidence interval of $\pm 1.96/\sqrt{N}$ with N being the number of samples. Through application of this criteria, the critical cut-off frequency was obtained, which is defined as the smallest cut-off frequency for which the residual satisfies the IID criteria. The variance of the residual calculated for the critical cut-off frequency gives an estimate of the variance of the random error present in the data. Analysis of the residuals for the measured states for different flight conditions paved way to the assessment of the critical cut-off frequency, which was found to lie around the third harmonic of the flapping frequency.

The aforementioned analysis provides an estimate of the random error affecting the position and attitude data as well as facilitates the selection of the cut-off frequency. However, any systematic errors originating from the visual tracking system and algorithm are

	Velocity (m/s)			Acc. (m/s^2)			Ang. velocity (rad/s)			Force (N)	
#	u	v	w	$\dot{u}$	$\dot{v}$	$\dot{w}$	p	q	r	X	Z
1	0.013	0.017	0.017	1.79	2.40	2.40	0.26	0.25	0.05	0.031	0.041
2	0.013	0.013	0.013	1.80	1.78	1.77	0.26	0.25	0.19	0.032	0.031

Table 3.1: Uncertainties in the reconstructed states and forces for two different trimmed flight conditions: **1** $U_\infty = 0.55$ m/s, $\theta = 70^\circ$ and $f = 12.5Hz$; **2** $U_\infty = 1$ m/s, $\theta = 45^\circ$ and $f = 11.7Hz$

not taken into account. For an estimation of the total measurement error, the relative distances between the markers were used. Particularly, the distance between the markers positioned at the non-flapping and non-deflecting parts of the DelFly can provide a good reference for the estimation of the measurement uncertainty. The effects of DelFly's position in the flight chamber and its velocity on the measurement errors are also considered in this way as these reference distances and their variations from the true values are calculated for each different flight test individually. Subsequently, the uncertainties in the measured marker positions were propagated to the calculated states and resultant forces, which are shown in Table 3.1. It is clear that the resultant uncertainties in the calculated states are consistent between the two flight tests. Accordingly, the X and Z forces are determined with a similar uncertainty of about 0.03 N for the two cases.

Effects of the model clamping position

In addition to limiting the free body motions, fixing the DelFly on the balance system as is done in the wind tunnel measurements has another important consequence associated to the dynamics of the structure. The DelFly fuselage on both sides of the force sensor clamp can be viewed as two relatively flexible cantilevered beams of square section (2 × 2 mm) hollow carbon rod with non-uniform mass distributions. Due to the oscillatory nature of the flapping motion, the structural modes of these beams can be excited and in turn the resonance of the structures can interfere with the aerodynamic and inertial forces generated by the flapping wings.

In the wind tunnel experimental model, the nose-side accommodates the brushless motor, the driving system and the flapping wings, which are all mounted to the main frame. These components have a total mass of 6.4 g and connected to the fuselage at the nose. On the other hand, the tail side carries only the 4.3 g tail structure. Obviously, the lengths of these so called cantilever beams are of importance in terms of structural dynamics and depends on the clamping position of the fuselage. The nose-side of the fuselage is the critical part as the unsteady forces generated by the flapping wings and high frequency vibrations originating from the driving system and the brushless motor exert primarily on this side. On the other side of the clamp, the tail is the only source of force production, which also displays vibratory behaviour because of its interaction with the unsteady wake of the flapping wings and transmission of upstream vibrations, which is assumed to be dampened significantly.

In order to identify the effects of structural resonance on the wind tunnel force measurements, experiments were conducted by clamping the model at three different locations along the fuselage: at 35 mm distance from the nose underneath the wings (which will be called nose-clamp); at 96 mm distance from the nose behind the trailing edge of the

wings (middle-clamp); at 142 mm distance from the nose underneath the tail (tail-clamp). The variations of the X-force and Z-force components for the case of the MAV placed in a free-stream flow of 0.3 m/s velocity at 83° pitch angle while flapping at 13.3 Hz are shown in Fig. 3.16.

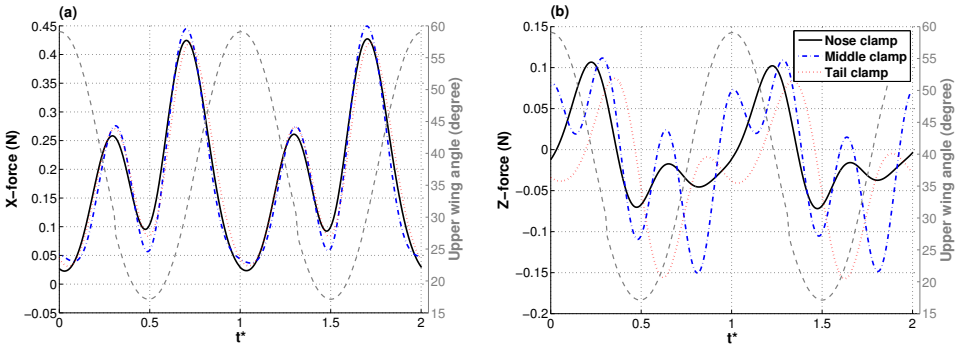

Figure 3.16: Temporal variations **a** X-force and **b** Z-force components for different clamping positions on the fuselage plotted for two periods of the flapping motion and complemented with the variations of the upper wing angle (*dashed gray*) for the case of $U_\infty = 0.3$ m/s, $\theta = 83°$ and $f = 13.3$ Hz

It should be noted that the force signals have been filtered such that the first three harmonics of the X and Z force oscillations are preserved for the investigation of clamping position effects, although they are not necessarily associated to aerodynamic forces. In the previous sections, it was shown that the free-flight estimated forces with frequency contents until the third harmonic of the flapping frequency can reliably be used for further analysis. Therefore, the similar frequency content is also preserved in the force data of the balance-mounted wind tunnel measurements.

From Fig. 3.16 it is evident that for different clamping positions, the force sensor measures very similar X-force variations. They are reasonably identical in terms of phase of the oscillations although there emerge small differences in the magnitude of peak forces particularly for that of the outstroke (maximum relative difference of 7 % between the outstroke maximums of the middle clamp and tail clamp). On the other hand, the results for the Z-force component differs substantially between different clamping positions both in terms of phase, magnitudes and even total number of local maximums in a period of flapping motion (increased importance of higher harmonics). Given the complex flow conditions (i.e., the DelFly flapping at an angle to the free-stream flow), it is not straightforward to interpret the results and decide on the correct measurement but it is clear that Z-force measurements in the wind tunnel should be scrutinized before further comparison with the force data of free-flight measurements.

Figure 3.17 display X and Z force variations for a slightly faster forward flight condition ($U_\infty = 1$ m/s, $\theta = 45°$ and $f = 11.7$ Hz). Similar to the previous case, X-force oscillations have a good agreement for different clamping positions with a maximum relative difference of 16 % between the instroke peak forces of middle clamp and tail clamp positions. The Z-force component, however, does not follow a common trend for the different clamping locations.

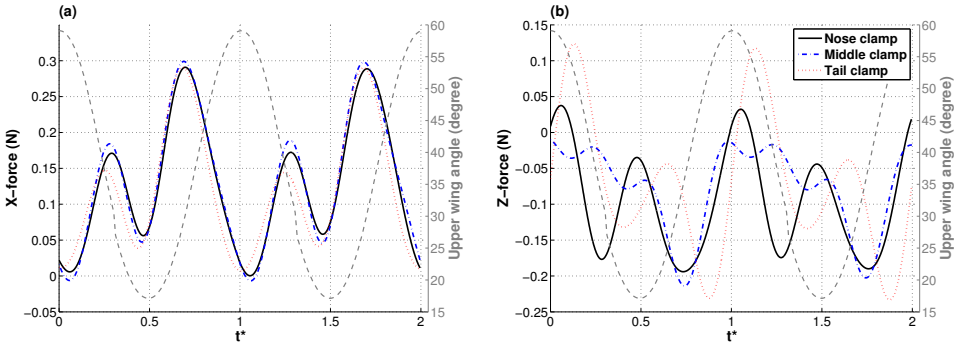

Figure 3.17: Temporal variations **a** X-force and **b** Z-force components for different clamping positions on the fuselage plotted for two periods of the flapping motion and complemented with the variations of the upper wing angle (*dashed gray*) for the case of $U_\infty = 1$ m/s, $\theta = 45°$ and $f = 11.7$ Hz

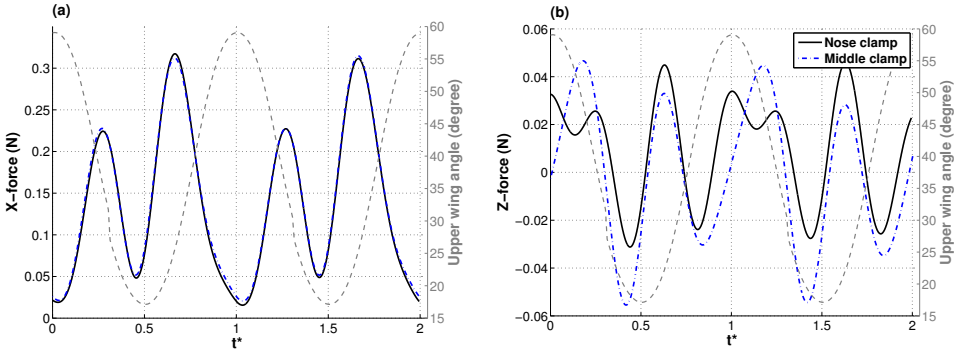

Figure 3.18: Temporal variations **a** X-force and **b** Z-force components for different clamping positions on the fuselage plotted for two periods of the flapping motion and complemented with the variations of the upper wing angle (*dashed gray*) for the case of $U_\infty = 0$ m/s, $\theta = 31.3°$ and $f = 10.3$ Hz

In case of the DelFly in hovering flight configuration flapping at 10.3 Hz (Fig. 3.18), the X-force component displays perfect agreement between the two available experimental cases, i.e., nose and middle clamp. The Z-force variations of the two cases become aligned in phase albeit having different amplitude.

Apparently, The X-force component remains mostly insensitive to the position on the fuselage where the model is fixed to the force sensor. The small differences observed in the variations of the X-force are attributed to the slightly different experimental conditions for tested clamping positions: changing interference characteristics between the DelFly model and the balance strut for different clamping positions and possible imperfections in the arrangement of the same experimental condition for all tested positions. The former assumption is supported by the observation of the better agreement between X-force variations of the nose-clamp and middle-clamp configurations in the case that there is no free-stream flow (see Fig. 3.18a). On the other hand, such small effects are not sufficient to explain the significant disparities observed for the Z-force component. These

measurements are very likely affected by the aforementioned structural dynamics of the fixed DelFly body. In order to verify the effect of structural resonance, two methods were used to assess the eigenfrequencies of the DelFly model fixed at different positions: a static impulse test which involves measurement of force vibrations after a Dirac-like impulsive force is applied on the DelFly structure; a finite elements method based analysis of the DelFly structure in CATIA, particularly modeling only the nose-side of the clamped fuselage, by use of proper material properties and similar mass distribution. The eigenfrequencies acquired by the two methods are tabulated in Table 3.2.

	Nose clamp	Middle clamp	Tail clamp
Impulse test	270	47	26.7
FEM analysis	271	42	24

Table 3.2: Eigenfrequencies of the DelFly structure acquired by static impulse test and FEM analysis in CATIA

First, it should be remarked that the first two structural modes observed in the FEM analysis are essentially pitchwise and lateral bending deformations of the DelFly fuselage with equal eigenfrequencies, which explains why the X-force component remains invariant with respect to the clamping position. It is clear that in the case of the tail clamp, the frequency of the first structural eigenmode is so low that it is very close to the second harmonic of the flapping frequency. During the flapping motion, this mode is definitely excited which results in structural vibrations that interfere with the forces associated with the flapping-wing motion. Likewise, for the middle-clamp case, the eigenfrequency lies in the range close to the third harmonic of the flapping frequency especially for high flapping frequency cases so that clamping at this position also potentially compromises Z-force measurements. Relatively better correspondence of Z-force oscillations for a lower flapping frequency for the nose-clamp and middle-clamp cases (see Fig. 3.18b) confirms this argument as in this case the third harmonic does not overlap with the eigenfrequency of the first structural mode. The difference in terms of magnitude for this case is most probably due to resonance of the tail-side of the clamped DelFly, which has a rather long length for the nose-clamp (although it is assumed that the driving excitation mostly applies on the nose-side and is dampened when transmitted toward the tail-side). The nose clamp case has a considerably higher eigenfrequency than the frequency range of considered force components. This can be attributed to relatively short beam length and in turn relatively short distance between the clamping point and application point of force oscillations and the distributed mass of DelFly driving system. Therefore, it is decided to consider wind tunnel force measurements with nose-clamp configuration for further discussion.

Comparison of the unsteady forces

In the previous sections, several factors affecting the reliability of the free-flight force estimation and wind tunnel balance-mounted measurement procedures have been discussed to achieve a suitable set of conditions for the accurate determination of unsteady aerodynamic forces of the flapping-wing MAV. Moreover, the uncertainties, particularly relevant for the case of free-flight estimation, have been assessed for a proper comparison of the two methods. Figure 3.19 displays the forces determined by the two methods for two dif-

ferent flight conditions. The first one (Fig. 3.19a) can be considered as slow forward flight of the DelFly at a high angle of attack and flapping frequency ($U_\infty = 0.3$ m/s, $\theta = 83°$ and $f = 13.3$ Hz), whereas the second case represents a relatively fast forward flight condition ($U_\infty = 1$ m/s, $\theta = 45°$ and $f = 11.7$).

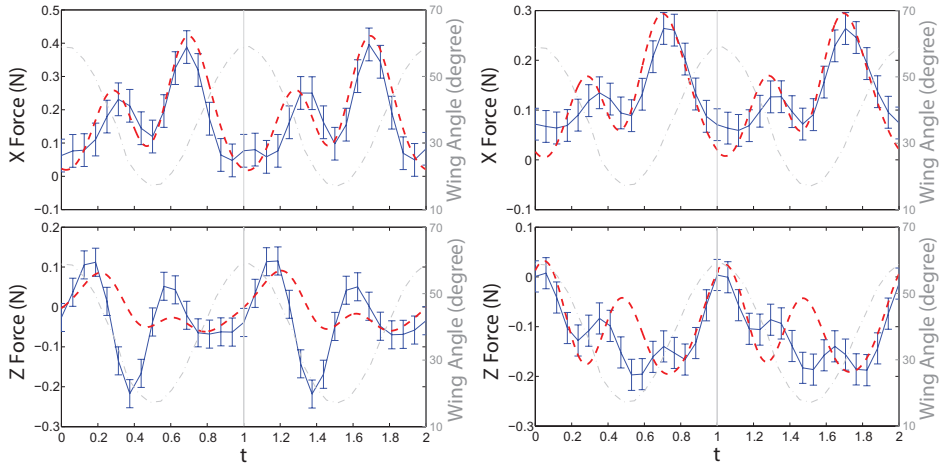

Figure 3.19: Comparison of variation of X and Z forces measured in the wing tunnel measurements by mounting the ornithopter to the balance mechanism (*dashed red*) and calculated from free-flight position data (*blue*) plotted for two periods of the flapping motion for similar flight/experimental conditions: **a** $U_\infty = 0.3$ m/s, $\theta = 83°$ and $f = 13.3$ Hz; **b** $U_\infty = 1$ m/s, $\theta = 45°$ and $f = 11.7$ Hz [note that variation of the upper wing angle is also plotted (*dashed-dot gray*) to indicate the phase of the flapping motion]

There is a good agreement between the X forces of both experimental methods for the two considered flight conditions. The forces measured via the force sensor in the wind tunnel experiments display very similar temporal variation with those calculated from the free-flight position measurements in terms of both phase and amplitude. Evidently, the deviations in the amplitudes of X-force component between the two methods are in the uncertainty range of the free-flight estimation method.

On the other hand, Z-force components of the two methods display considerably different evolutions during the time coarse of the flapping motion. Despite having slightly different evolution characteristics, there is a better correspondence for the Z-force component of the two methods in the case of fast forward flight, which is most probably due to relatively low flapping frequency, as discussed subsequently.

The difference in the determination of the Z-force component has already been attributed to the clamping position in the wind tunnel experiments, and this effect is presumably diminished by attaching the ornithopter close to the exertion point of the unsteady forces on the fuselage. Nevertheless, there are other factors that may also affect the determination of the Z-forces. The first one is the structural resonance of the aft-part of the DelFly (tail-side) when clamped under the wings (nose clamp). The natural frequency of the tail side in this case is comparable to the lowest natural frequency found in the tail clamp case (27 Hz) due to similar structure and mass distributions of both sides. There-

fore, flapping at 13.3 Hz may cause structural oscillations of the tail side, which can result in the contamination of the Z-force measurements. The second factor is associated to the fact that balance-mounted measurements limit the dynamic body motions of the ornithopter, which are present in the free-flight condition. These oscillatory body dynamics also induce varying flow conditions on the tail and the wings and result in the generation of a motion-induced force component. Obviously, this force component of dynamic origin is not produced and thus detected in the static balance-mounted configuration and it can be a further source for the discrepancies in the Z-force measurements.

Clearly, the X-force component can be successfully determined by use of both wind tunnel measurements and free-flight estimations and displays rather insensitive characteristics to the major error sources for the two methods. This justifies the validity of the balance-mounted measurements in hovering flight configuration for further investigation of flapping-wing aerodynamics of the DelFly. On the other hand, measurement of the Z-force component is challenging due to the aforementioned factors and requires special attention for a proper determination and interpretation.

3.3. Effects of flapping frequency, wing geometry and flexibility

The flapping motion of the DelFly wings consists of three main motion kinematics: first, the sweeping motion of the wings that is driven by the gear and hinge mechanism actively and can be varied in frequency but constrained in amplitude; second, the small-amplitude heaving motion that occurs due to the bending of the leading edge; third, the pitching motion of the wings that occurs passively mostly during the stroke reversals as a result of interaction between the aerodynamic, inertial and elastic forces acting on the wings. These motion and deformation characteristics play an important role determining the effective angle of attack during the instroke and outstroke phases of the flapping motion. Obviously, the fluid-structure interaction is an important aspect of the flapping flight of the DelFly in terms of both force generation and power consumption. One way to modify this interaction in order to increase the efficiency of the flapping motion is to change the wing geometry and/or stiffness of the wings, which have either direct or indirect influence on the aerodynamic, inertial and elastic force components.

The first attempt to optimize the flapping-wing performance of the DelFly by configuring the wing properties was made by Bruggeman (2010). He started with the original DelFly wings (Fig. 3.20a), which were adapted from the DelFly I, and varied three main features, i.e., the stiffener orientation, the area distribution and the aspect ratio, to investigate their impact on the force generation and power consumption. As a result of the stiffener orientation study, he built the improved wing (Fig. 3.20b) with 5 % improvement in X-force to power ratio (X/P). Although the new design generates the same amount of force for a given flapping frequency, its power consumption is 5 % lower than the original design. During this investigation, he showed that the wings with stiffeners converging toward the leading edge performs better than the wings with diverging stiffeners. Regarding the area distribution study, he built two other wings in addition to the improved wing, namely the bat-like wing and the reversed wing. The wing area and span length were kept fixed while the area distribution in the spanwise direction was varied. The bat-like wing

has an increasing chord length until 46 % half-span position (c_{max} = 93 mm) after which it decreases to the tip chord length of 63 mm. The reversed wing, on the other hand, was produced by simply mirroring the improved wing thus having a decreased chord in the inboard wing section. Force and power consumption measurements revealed that although the bat-like wing outperforms the others in terms of X/P, it does not generate enough force to support the DelFly weight in hover configuration, which was also the case for the reversed wing. The aspect ratio study was rather limited such that only the chord length was varied for a fixed span length to change the aspect ratio. The results revealed that the high-AR wing generates more force yet the improved wing still has the best performance in terms of X/P.

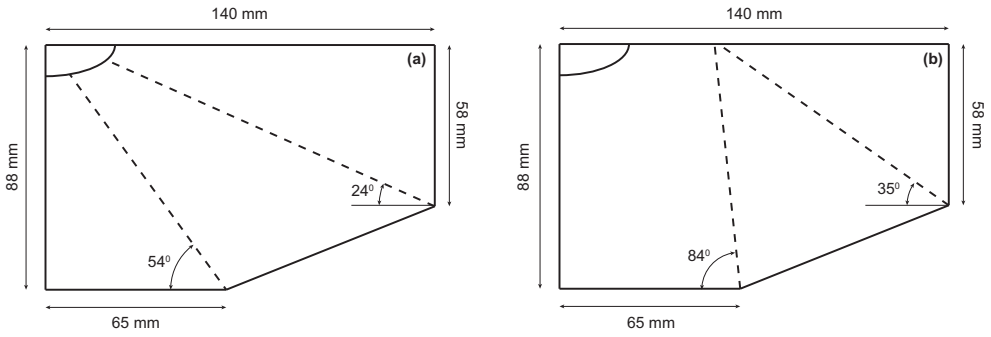

Figure 3.20: Wing layout with stiffener orientation and location of **a** the original and **b** the improved DelFly II wings

There are also a number of other investigations reported in the literature that focus on characterizing or optimizing the aerodynamic performance of flapping wings in the specific context of flapping-wing MAVs. Aditya and Malolan (2007) performed an experimental study in a wind tunnel to investigate the Strouhal number (St) effects on the propulsive characteristics of a mono-plane flapping-wing MAV in the forward flight configuration. They varied the St by varying the flapping frequency and the stroke amplitude. Their results revealed a nominal dependence of the propulsive force on the St. They also reported that high propulsive forces are generated for a limited range of St. A similar experimental study was conducted by Muniappan et al (2004), in which they investigated the effect of the stroke angle and flapping frequency on the lift characteristics of a mono-plane flapping-wing MAV. Their results showed that the lift increases with the increasing flapping frequency and stroke amplitude and decreases with the free-stream velocity. In their following study (Muniappan et al, 2005), they explored the wing aspect ratio, wing planform and torsional flexibility effects on lift and thrust production for various flapping frequencies and free-stream velocities. They tested four wings with different planform inspired from dragonfly, butterfly, hummingbird and pigeon wings. They reported that the butterfly wing planform shows better performance in terms of lift and thrust generation. Their results showed that thrust increases with increasing torsional flexibility of the wings, whereas it is not influenced by the wing aspect ratio (for the same wing area and wing shape). Lin et al (2006) examined the force generation characteristics of a conceptual flapping-wing mechanism, which mimics the flapping motion of a bird, featuring flexible

membrane wings. They carried out wind tunnel tests for different angle of attack, free-stream speed and flapping frequency settings. They concluded that the structural characteristics of the wings play an important role in the generation of forces due to changing wing deformations with increasing flapping frequency. Hu et al (2010) conducted an experimental study to assess the aerodynamic performance of a rigid and two flexible wings in both flapping and soaring (non-flapping) flight conditions. They reported that flapping flight is significantly more favourable in terms of force generation, especially in the unsteady regime with an advance ratio (i.e., the ratio of forward flight speed to wingtip velocity) being smaller than unity. They found that the less flexible nylon wing has the best overall aerodynamic performance for soaring flight, yet it performs the worst for flapping flight conditions. The rigid wing outperforms the flexible wings in terms of lift generation for flapping flight, whereas the most flexible latex wing generates the highest thrust among the three tested wing in flapping configuration. Nakata et al (2011) studied the flexible flapping-wing aerodynamics on a flapping-X-wing MAV by combining wind tunnel measurements and numerical flow simulations. Wind tunnel measurements were performed to capture the wing deformations and forces generated during the flapping flight. The numerical flow simulations, using the experimentally determined wing deformation characteristics, provided detailed and quantitative analysis of the unsteady force generation mechanisms. They mentioned the effectiveness of the clap-and-fling mechanism in addition to the importance of the wing flexibility.

In the context of previous explanations, the study presented in this section explores the influence of flapping frequency, wing flexibility and wing geometry on the force generation and power consumption of the DelFly II in hover configuration. The improved DelFly wing (Fig. 3.20b) was used as the benchmark configuration and its flexibility was varied by changing the Mylar foil thickness. In terms of wing geometry, the study mainly focuses on the effect of aspect ratio for varying span lengths, which has not been considered in the previous studies and remains relatively unexplored.

3.3.1. Experimental setup and flapping-wing parameters

The experiments were performed in a quiescent environment by use of the balance mechanism with the ATI Nano-17 Titanium force sensor described previously (see sections 3.1.2 and 3.2.2 for detailed information). A full-scale DelFly model without a tail was used as the experimental model. The FPGA and the microcontroller systems were used in combination in order to acquire voltage and current fed to the motor, the Hall sensor output and the motor phase information, six components of forces and moments at a recording rate of 12.5 kHz. The microcontroller system was used also to regulate and control the flapping motion to assure constant flapping frequency during the measurements. The flapping frequency of the wings was varied in the range from 7 to 13 Hz in the experiments to study its effects on the production of forces and power consumption. As the experiments were performed for the hovering flight condition, the X-force is the relevant force component and analyzed in this section. A Chebyshev II low-pass filter with -80 dB attenuation of the stop-band was used to filter the raw force data in MATLAB (note that the forward-backward filtering technique was used to prevent time shift of data). The cut-off frequency was selected based on the flapping frequency to keep only the first two harmonics of the X-force.

Name	Membrane thickness (μm)	b (mm)	$\overline{c}$ (mm)	S (mm^2)	AR
Ref5	5	280	80	22390	3.5
Ref10	10	280	80	22390	3.5
Ref15	15	280	80	22390	3.5
Orig10	10	280	80	22390	3.5
HAR10	10	320	80	25589	4
LAR10	10	240	80	19191	3

Table 3.3: Properties of the tested wing configurations

Several wings were built and tested in this experimental campaign. The improved wing layout (Fig. 3.20b) is used as the reference wing design. First, it is compared to the original wing design (Fig. 3.20a) to quantify the enhancement of the aerodynamic performance and justify the use of the improved wing design. Although the 5 μm thick mylar foil is the typical membrane used in the construction of the DelFly wings, these measurements were performed by using mylar foil with a thickness of 10 μm due to its higher durability such that the same wing pair can be tested for a longer time without a significant deterioration of the material characteristics, which would affect the aerodynamic performance. Subsequently, in order to study the effect of flexibility, the reference wing was built from mylar foils of different thickness, namely 5, 10 and 15 μm. Then, the reference wing was scaled up and down only in the spanwise direction to produce high aspect ratio (AR = 4) and low aspect ratio (AR = 3) wings, respectively (Fig. 3.21). These wings were also built from 10 μm mylar foil and compared with the reference wing design (AR = 3.5) of the same mylar foil thickness.

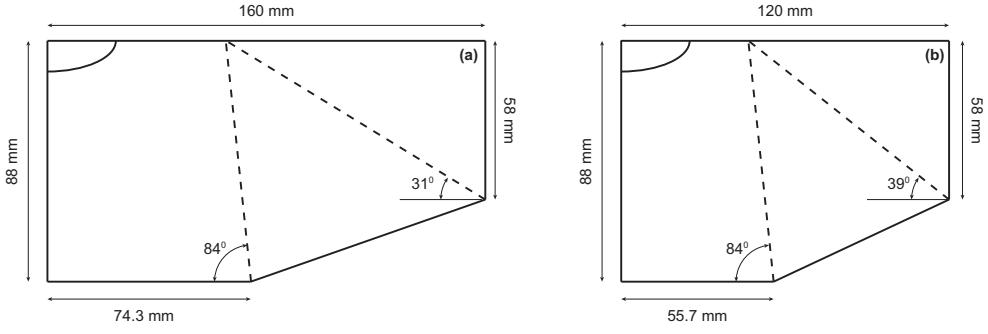

Figure 3.21: Wing layout with stiffener orientation and location of **a** the high aspect ratio (HAR10) and **b** low aspect ratio (LAR10) wings

An overview of the properties of the tested wing configurations are given in Table 3.3. A wing nomenclature was adopted in which the number in the name of the wing represents the mylar foil thickness in μm. 'Ref' is the improved wing layout, 'Orig' is the previous DelFly II wing that was downscaled from the DelFly I, 'HAR' is the high aspect ratio wing and 'LAR' stands for the low aspect ratio wing.

3.3.2. Results

Force measurement and power consumption results are presented in this section. Temporal variations of these quantities are displayed for two periods of the flapping motion, complemented with the stroke angle kinematics, whereas time-averaged values are calculated for a number of flapping cycles, considering only cycles for which the frequency of the motion lies within ±5 % of the prescribed value.

Effects of the flapping frequency

The flapping frequency effects on the force generation and power consumption are discussed via the measurements on the Ref10 wings in a frequency range from 7 to 13 Hz. In Fig. 3.22a, the temporal variation of the X-force for different flapping frequencies is depicted. The most prominent effect of the increasing flapping frequency is obviously the amplification of the X-force generation during both instroke and outstroke. The clap-and-peel mechanism is apparently active for all test frequencies resulting in higher force production during the outstroke. There is also a phase lag in the force generation becoming apparent with increasing frequency, which is presumably due to growing inertial effects on the wing deformation behaviour such that particularly during stroke reversals, the wing surface changes direction later than the wing leading edges. It is also interesting to note that the X-force does not increase quadratically with the flapping-wing velocity in the range of flapping frequencies inherent to the DelFly flight envelope. This is evident in Fig. 3.22b), in which forces are non-dimensionalized by the use of mean wingtip velocity ($U_{m,tip}$) and total planform area of the two wing pairs ($2S$) to calculate the X-force coefficient ($c_{X,tip}$). The force coefficients follow a slightly decreasing trend with increasing flapping frequency revealing that the X-force evolution displays a less-than-quadratic increase with the flapping frequency. On the other hand, it is not surprising that the aerodynamic mechanisms of the unsteady flapping-wing flight do not strictly comply with the laws of conventional fixed-wing aerodynamics. In this case, the X-force generation occurs as a results of the complicated fluid-structure interaction such that the fluid forces shape the flexible wings together with the inertial effects, which in turn influences the force generation mechanisms. Although increasing sweeping velocity increases the dynamic pressure and in turn should result in a proportional growth in the forces, it probably also promotes the chordwise wing deformation such that the effective angle of attack of the wings in the sweeping direction diminishes, resulting in a relatively weak LEV formation. In this respect, the maximum force coefficient values are attained for the lowest flapping frequency.

In accordance with the previous discussion, the flap-averaged X-force shows a quasi-linear variation with the flapping frequency (Fig. 3.23). Note that for all of the test cases, at least 45 periods were included in the calculation of the mean force and the uncertainty in the flap-averaged X-force measurements always remains lower than 0.3 % of the mean value. Based on this quasi-linear dependence, the necessary flapping frequency to keep a 17-gram DelFly aloft in the hovering configuration was calculated as 11.8 Hz for the case of Ref10 wings. The power consumption also increases with the flapping frequency linearly. Obviously, the force component that plays the major role in the determination of the power consumption is the one in the direction opposite to the sweeping motion (viz. resisting force exerted on a sweeping wing during instroke and outstroke). Apparently, the aforementioned fluid-structure interaction phenomenon has a significant influence on

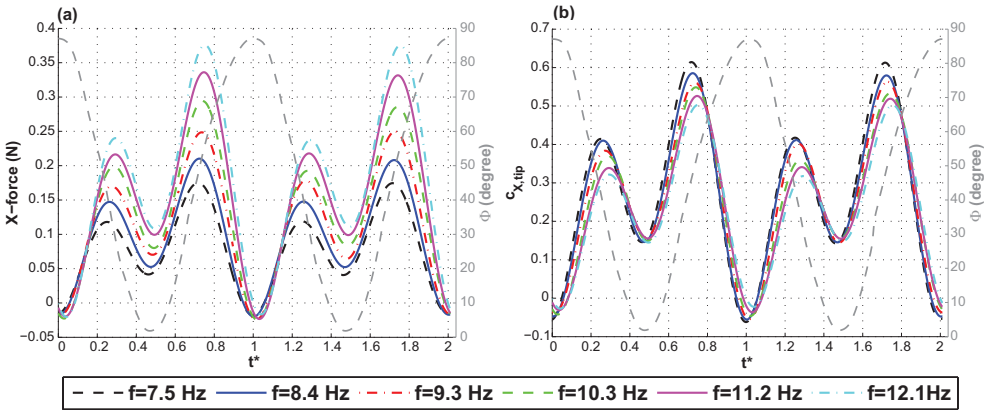

Figure 3.22: Temporal variations of the **a** X-force and **b** X-force coefficients calculated based on the mean wingtip velocity ($U_{m,tip}$) for the Ref10 wing flapping at various frequencies complemented with the stroke angle (ϕ) kinematics for two periods of the flapping motion

the resistance force exerted on each wing, which results in this less-than-quadratic trend of the power consumption with respect to flapping frequency.

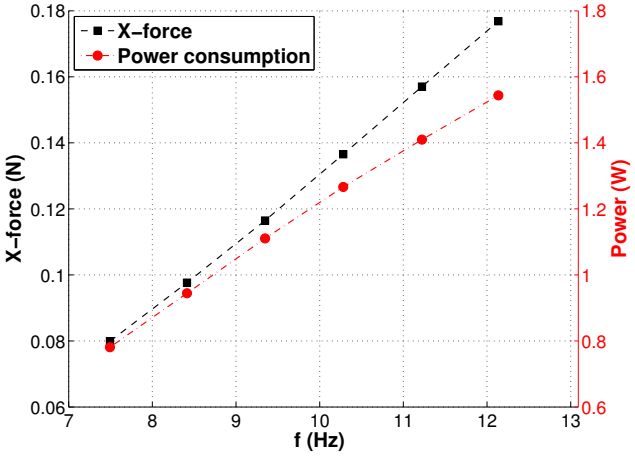

Figure 3.23: Flap-averaged X-force and power consumption for various flapping frequencies of the Ref10 wing

Comparison of the original and the improved wing performance

As an outcome of the optimization study performed by Bruggeman (2010), the stiffener orientation of the original DelFly II wings was modified to give the improved wing configuration (the reference wing), which had better overall aerodynamic efficiency. For the confirmation of this selection, the two wings (Fig. 3.20) are compared in terms of their force generation and power consumption.

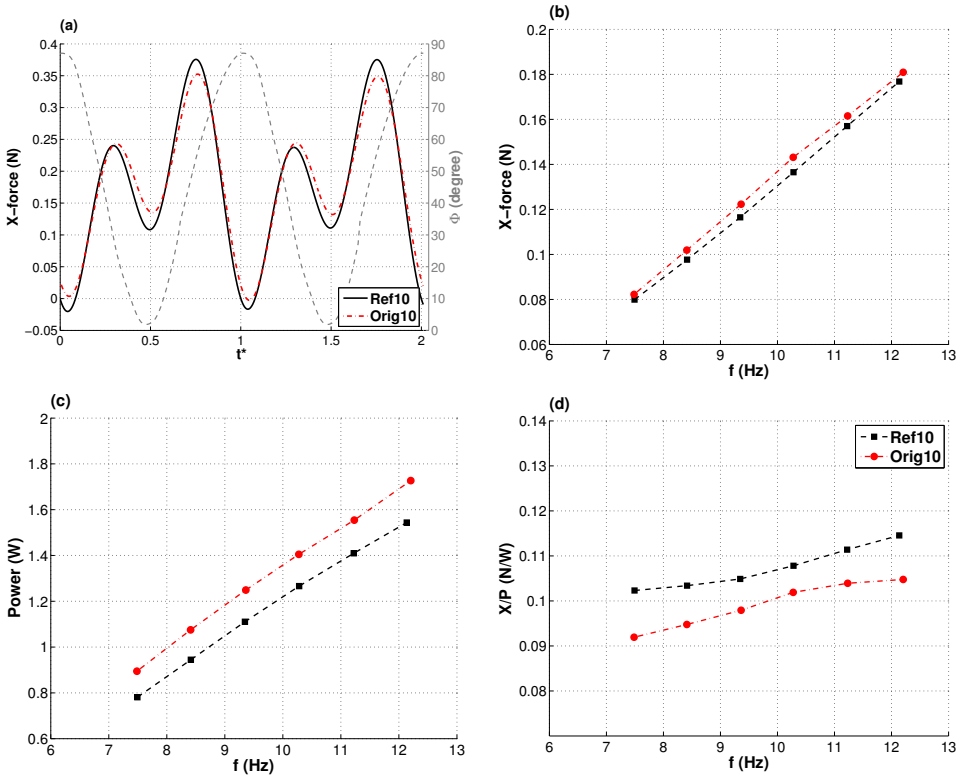

Figure 3.24: Comparison of the Ref10 and Orig10 wings in terms of aerodynamic performance: **a** Temporal evolution of the X-force for the flapping frequency of 12 Hz complemented with the stroke angle (ϕ) variation (*dashed gray*); **b** flap-averaged X-force; **c** flap-averaged power consumption; **d** X-force to power ratio (X/P)

In general, the Orig10 generates somewhat higher flap-averaged force at a given flapping frequency. For the specific case of 12 Hz flapping frequency, the time-series force data (Fig. 3.24a) reveals that the Orig10 wing outperforms the Ref10 wing only during the instroke (10 % relative difference between the mean force values of the instroke phases, note that the average of the instroke mean forces was used as the scaling factor in the calculation of the relative difference), whereas the latter generates slightly higher force during the outstroke (relative difference of 2 %). Apparently, the increased chordwise rigidity of the Ref10 wing is favourable for the clap-and-peel mechanism, presumably due to formation and positioning of the LEV, which is enhanced by promoting the between-wing suction region as shown by Groen (2010). The flap-averaged forces and power consumption values display similar characteristics for the two wings with the original wing producing more X-force at the expense of higher power consumption. Consequently, as evidenced in Fig. 3.20, the Ref10 wing performs better in terms of X/P in the complete flapping frequency range, which indicates that the necessary force to keep the DelFly airborne can be generated at a lower power consumption, that will in turn result in a longer flight endurance.

Effects of mylar foil thickness

The wing flexibility can be tuned by means of changing the thickness of the membrane which is used to form the surface of the wing. Contrary to the stiffeners providing directional support, the use of a thicker membrane material (with isotropic in-plane structural properties) essentially provides rigidity in all in-plane directions. In this regard, the aerodynamic performance of three wings built from 5, 10 and 15 μm thick Mylar foil are compared in this section.

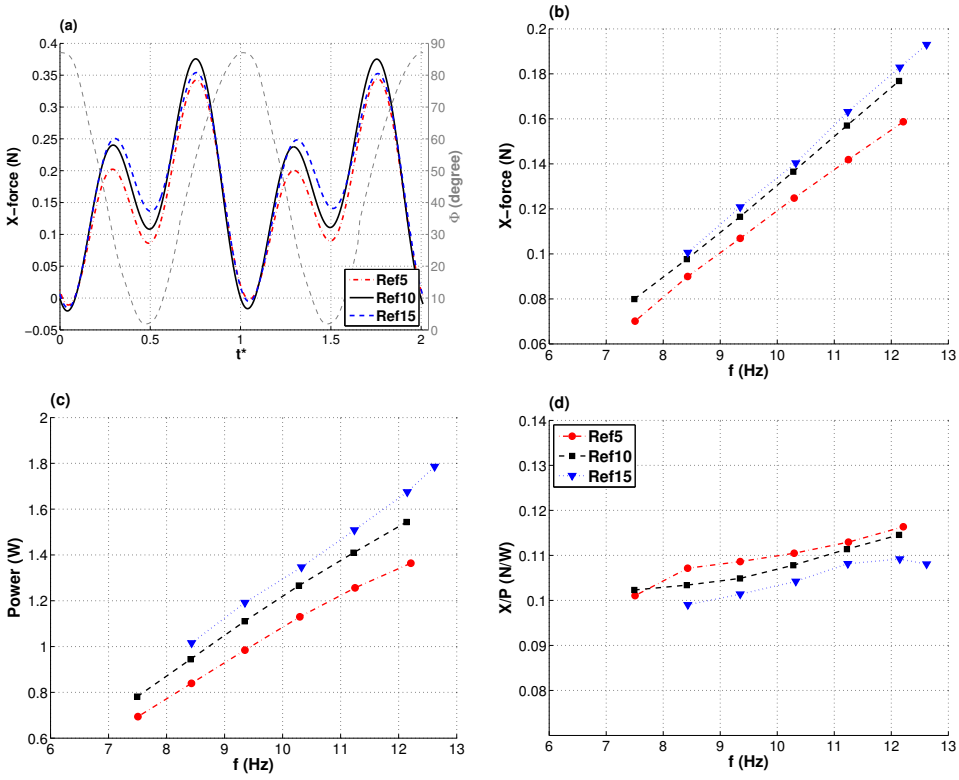

Figure 3.25: Comparison of the Ref5, Ref10 and Ref15 wings in terms of aerodynamic performance: **a** Temporal evolution of the X-force for the flapping frequency of 12 Hz complemented with the stroke angle (ϕ) variation (*dashed gray*); **b** flap-averaged X-force; **c** flap-averaged power consumption; **d** X-force to power ratio (X/P)

As shown in Fig. 3.25a, the Ref10 wing produces the highest peak force of the outstroke among the three wings, whereas the more rigid wing (Ref15) achieves the highest peak force of the instroke. The superior performance of the Ref10 wing with respect to the Ref15 wing during the outstroke (relative difference of 1.7 % between the outstroke average forces) despite having smaller flap-averaged X-force for a given flapping frequency (see Fig. 3.25b) can be attributed to the attainment of an optimum wing deformation characteristics for the clap-and-peel motion that achieves a compromise between the wing area oriented in the x_b direction, angle of attack and wing camber. This can be read such that the increased stiffness of the wings results in a smaller wing deformation that diminishes

the effective wing surface area for the pressure forces to act on, while promoting the low-pressure region between the wings and LEV circulation. Likewise, the more flexible wing can provide a larger surface area for a relatively ineffectual low-pressure region. It should be noted that the optimum wing configuration for the force generation mechanism of the outstroke, which is primarily based on the wing-wing interaction, does not necessarily produce the maximum force during the instroke, in which force generation relies on the delayed stall and associated LEV mechanism.

The Ref15 wing, as expected, consumes more power compared to the other wings due to an increased wing surface area aligned vertical to the stroke direction. Such an orientation has a twofold effect: (1) the promotion of flow separation which together with the increased area brings about a larger drag; (2) an increased added mass effect due to a larger volume of fluid around the wing to be accelerated or decelerated during the flapping motion, which also increases the resisting force to the motion. In this respect, the power consumption decreases with decreasing Mylar foil thickness.

As a result, the Ref5 wing has the best performance in terms of X/P with slightly higher values than those of the Ref10 wing for the given range of flapping frequencies. However, the difference is marginal (maximum 3.6 % relative difference) that the degradation of the aerodynamic efficiency can be afforded for the sake of the favourable characteristics of the Ref10 wing. The flapping frequency required to generate enough force for supporting the DelFly in hover with the Ref5 wings is approximately 12.6 Hz, whereas it is around 11.7 Hz with the Ref10 wings. This is beneficial as flapping at a lower frequency reduces the wearing of the DelFly driving system and wing structure. Moreover, the thicker membrane is more durable in the case of crashes and in terms of possible tearing during the flapping motion.

Effects of wing aspect ratio

The aspect ratio is an effectual parameter on the aerodynamic efficiency of wings both in steady and unsteady flow conditions and it can be modified either by changing the chord or the span length of the wing. In the design of MAVs, as it is aimed to fulfill the dimension criteria defined by authorities, the span length is either kept fixed or selected to be as small as possible. On the other hand, for a revolving wing, the tangential wing velocity increases with the distance from the rotation axis. In this context, the present study focuses on effect of varying span length while keeping the mean chord-length constant.

In terms of X-force generation, the HAR10 wing has the best performance by generating higher force throughout the complete cycle (see Fig. 3.26a), which results in a remarkable difference in the flap-averaged force values (Fig. 3.26b), while emerging as the most power-consuming configuration among the test wings (Fig. 3.26c). The LAR10 wing produces the lowest force for a given flapping frequency although it is the least power consuming wing. The HAR10 wing generates highest force for a given power consumption and outperforms the other configurations in this aspect as well (Fig. 3.26d). It is clear that the HAR10 wing configuration is more advantageous based on these aerodynamic indicators despite the fact that it extends the largest dimension of the ornithopter (i.e., the span length) by 4 cm. It is possible to generate enough force to hover by flapping HAR10 wings at a frequency of 10 Hz, which consumes 4 % less power with respect to a hovering DelFly with the Ref10 wings at a flapping frequency of 11.7 Hz. The LAR10 wings never reaches

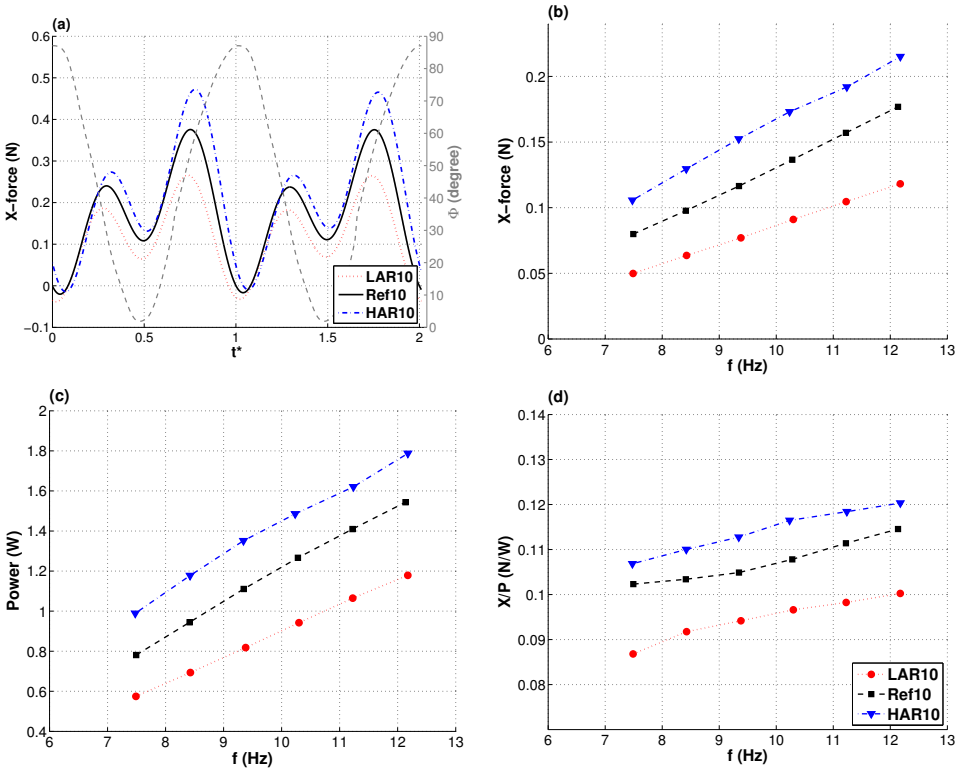

Figure 3.26: Comparison of the Ref10, LAR10 and HAR10 wings in terms of aerodynamic performance: **a** Temporal evolution of the X-force for the flapping frequency of 12 Hz complemented with the stroke angle (ϕ) variation (*dashed gray*); **b** flap-averaged X-force; **c** flap-averaged power consumption; **d** X-force to power ratio (X/P)

hovering force level for a 17 gram DelFly II model in the investigated flapping frequency range.

It is important to note that scaling the Ref10 wings only in the spanwise direction to build the high and low aspect ratio wings also changes the wing planform area so that the increase in the forces is not solely the result of changing the span length but also partially originates from the associated change in wing surface area. In order to assess this, a blade-element approach was used to calculate the integral quantity of the area and square of the tangential velocity for a half-wing as follows:

$$SU^2 = \int_0^R c(r)(\omega r)^2 dr \tag{3.11}$$

where r is the distance from the rotation axis (i.e., wing root) and ω is the angular velocity of the sweeping wing motion. In addition to this, tip velocities of the wings for a given flapping frequency were calculated and all acquired quantities of the HAR10 and LAR10 wings were normalized with those of the Ref10 wing. The results are tabulated below:

In Table 3.4, the X-force ratios were calculated as a mean value over the tested flap-

	X-force	SU^2	$U^2_{m,tip}$
HAR10/Ref10	1.28 ± 0.05	1.5	1.3
LAR10/Ref10	0.66 ± 0.02	0.63	0.73

Table 3.4: Comparison of mean X-force generation and dynamic properties of the LAR10, Ref10 and HAR10 wings

ping frequencies. It is obvious that the HAR10 wing has an additional area moving with a relatively high velocity compared to the Ref10 wing, which results in a greater SU^2 value. Nevertheless, the increase of the X-force does not scale with the SU^2 ratio. Instead, there is good correlation between the ratio of the square of the mean tip velocities and the mean X-forces of the two cases. On the other hand, the X-force ratio of the LAR10 and Ref10 wings is better correlated with the SU^2 ratio. Although it is rather difficult to comment on this comparative analysis, it is clear that increasing the span length while keeping the mean chord length fixed (i.e. increasing the wing surface area) does not necessarily result in an increase in accordance with the increase of dynamic pressure and the wing area. Apparently, the aeroelastic nature of the phenomenon causes significant variations between the profile geometries of the tested wings, that results in the observed appreciable deviations in the force generation characteristics.

It is evident that the comparative discussion covered in this section will not be complete without considering the structural deformations of the wings and their variations for different test cases, which is explored in the following section.

3.4. Flapping-wing structural deformation

3.4.1. Introduction

It has been mentioned and discussed several times in the previous sections that structural deformation of the flapping wings has an important effect on the aerodynamic performance of the DelFly flapping flight. The wings deform under the effects of aerodynamic, inertial and elastic forces during the course of a flapping cycle. The complex fluid-structure interaction determines the shape of the flapping wings, which in turn affects the force production. This interrelation is sensitive to the structural properties of the wings as well as the flapping motion kinematics and wing geometry. As shown in the previous section, changing stiffener orientation results in a better X/P for an equivalent amount of X-force production or using a thicker Mylar foil as the wing surface membrane increases the X-force at the expense of a higher power consumption. In this respect, it is of importance to assess the deformation characteristics of the flapping wings and relate them to the observed differences in the force production and power consumption of the wings with different structural properties.

Literature reports a number of studies aiming to acquire wing deformations in flapping-wing flight of insects. The deformation characteristics of the DelFly wings bear resemblance to that of insect wings in view of their light construction [0.5 – 5 % of the total body mass for insects (Ellington, 1984a) and 7 % of the total mass for the DelFly II]. Moreover, the wing deformations are predominantly passive in both cases as there is no muscular control of the wing flexure in insect flight (Combes and Daniel, 2003b) in contrast to bats and birds. Early studies provided essentially qualitative observations and re-

ported the occurrence of considerable camber and spanwise twist in several insects, e.g., locusts (Baker and Cooter, 1979; Jensen, 1956; Wortmann and Zarnack, 1993), hawkmoths (Willmott and Ellington, 1997), butterflies (Wootton, 1993), crane flies, hoverflies and bees (Ellington, 1984b) (as cited in Walker et al, 2009). However, the role of twist and camber in the force production of insect flight were not fully understood due to the complexity of the structural deformations and the qualitative nature of the observation methods. Wang et al (2002) described a new method based on a projected comb-fringe technique to acquire wing kinematics, deformations, body position and attitude of a free-flying dragonfly. Their measurements revealed that both forewing and hindwing have positive camber during the downstroke, whereas negative camber is present during the upstroke for a short duration. In order to investigate the effect of camber on force generation, they conducted a two-dimensional numerical simulation of a single airfoil undergoing the measured kinematics of the dragonfly's forewing in the forward flight configuration. These simulations revealed that the flexible airfoil with the time-varying camber generates higher forces both in lift and drag than a rigid wing in contrast to some previous studies which reported that camber deformation has a minor effect on aerodynamic forces at high angles of attack (Dickinson and Götz, 1993; Sunada et al, 1993). A similar numerical study by Du and Sun (2008) showed that twist has a marginal influence on the force generation whereas camber deformation has a significant effect. A flapping wing with 6 % camber and 20° twist produces 10 %-20 % more force and has approximately 10 % higher lift to drag ratio compared to a rigid flat-plate wing. Moreover, the power required to drive the wings is reduced by 16 %. Walker et al (2009) used photogrammetic techniques to reconstruct the deforming wing surface topologies of tethered locusts (*Schistocerca gregaria*) and free-flying hoverflies (*Eristalis tenax*). They used four high-speed digital cameras to film the insects and then digitized several natural features and marked points on the wings. Compared to the comb-fringe technique, which is limited in terms of the maximum number of lines projected on a wing due to the practical difficulty of generating a fine and bright enough laser grid and lacks the ability of tracking a certain point on the wing surface, the photogrammetry methods allowed them to reconstruct the wing surfaces with very high spatial resolution and fairly low measurement error level (0.11 mm for the locust and 0.03 mm for the hoverfly). They stated that variable spanwise twist and camber are two outstanding features in the wingbeats of both species. Further investigation of the wing kinematics and deformations of a number of locusts by tracking more than 100 identified points of the hindwings and 15 natural features of the forewings in a manual and semi-automatic manner revealed that although the hindwing dynamics are very similar within and between the individuals, the forewing motions display significant variation (Walker et al, 2010). During the downstroke, both wings are positively cambered at the 50 % wing position (reaching approximately a maximum camber value of 8 %). At an intermediate time step during the downstroke, they found that the camber decreases from root to tip. During the upstroke, the hindwing has a negative camber (with a minimum value of −4 %), while the forewing preserves a positive camber in most of the individuals. They also stated that the linear decrease of the incidence angle in the spanwise direction toward the tip of the hindwing counterbalances the increase of effective angle of attack (calculated by considering the stroke velocity and the forward flight velocity) that would otherwise occur for an untwisted configuration during the downstroke. This causes each section to operate

at a unique angle of attack that maximizes lift to drag ratio. Young et al (2009) explored the consequences of the wing deformations of the locusts by use of three-dimensional numerical simulations, which were complemented and validated by smoke flow visualizations and digital particle image velocimetry measurements on real locusts. In addition to the simulations of full wing kinematics and deformations, they also performed numerical solutions by first removing the camber while preserving temporal variation of twist and second by excluding the camber and spanwise twist. They reported that during the downstroke, when the actual wings have a positive camber, the computations of the uncambered wing displays less lift and thrust compared to full-fidelity wing model computations. They concluded that the insect wing topography and deformation are key elements in terms of aerodynamic force generation. Similar experimental studies were performed on free-flying dragonflies (Koehler et al, 2012), bats (Tian et al, 2006) and a free-flying barn owl (Wolf and Konrath, 2015).

The relationship between the structural deformation of the flapping flexible wings and aerodynamic forces has been investigated also by use of mechanical flapping-wing systems and flapping-wing MAVs. Wu et al (2010) tested four flexible membrane wings with different stiffness characteristics by measuring structural deformations and unsteady forces in hovering configuration. The three-dimensional coordinates of a random speckle pattern on the wing was measured by stereo triangulation using four cameras. They reported that wings with stronger skeletal reinforcement produce higher thrust (corresponding to lift or X-force in hovering configuration) at relatively high frequencies (e.g., above 25 Hz) and the inverse at lower flapping frequencies. They noted that thrust increases quadratically with flapping frequency, however this increase is degraded to a linear trend in case extreme twisting deformations occur. They also stated that the chordwise stiffness should be orders of magnitude lower than the spanwise stiffness in order to achieve greater performance in terms of efficiency and thrust effectiveness. Nakata et al (2011) used two high-speed cameras to trace the markers on the flexible wings of a hummingbird-inspired flapping-wing MAV with a mean chord length of 23.6 mm tethered on a balance mechanism positioned in a uniform flow with a position tracking resolution of 5 mm. They tested both mono-plane and bi-plane configurations in the wind tunnel and confirmed the benefit of the clap-and-fling mechanism in terms of force generation. The measured wing deformations were then used to define the unsteady wing geometry in the three-dimensional numerical simulations. Passive wing deformations of the DelFly II flapping wings have been subject to a number of experimental studies (de Clercq et al, 2009; Groen et al, 2010). The wing shape was obtained from the images of PIV measurements conducted at a certain spanwise location so that no information on spanwise variation was available for further analysis. Nevertheless, these planar observations revealed the wing deformation history over the cycle, in particular the occurrence of the clap-and-peel mechanism, leading and trailing edge paths, the presence of a significant wing camber (de Clercq et al, 2009) and difference between the deformation-wise behaviours of the original and improved DelFly wings (Groen et al, 2010). The observed wing deformation profiles were subsequently digitized to be used in a two-dimensional unsteady numerical simulations of the DelFly flapping wings (Gillebaart, 2011).

It is clear that variation of the wing shape during a flapping cycle is a prominent feature in flapping-wing aerodynamics. Notwithstanding the number of studies aiming to

assess wing deformations on biological flyers, the relation between the wing shape and unsteady forces in flapping-wing MAVs, particularly in the biplane configuration where wing-wing interaction further complicates the fluid-structure interaction, is not fully resolved. In this regard, the main objective of this study is to characterize the time-varying three-dimensional passive structural deformations of the DelFly II flapping wings in hover configuration at a high temporal and spatial resolution. In this context, different wing configurations (viz., wings with different Mylar foil thickness, stiffener orientation, aspect ratio) were tested for varying flapping frequencies. Also, simultaneous force measurements were carried out in order to assess the relation between the unsteady forces and the structural deformation characteristics.

3.4.2. Experimental setup and visual detection methods

The experiments were performed on a full-scale DelFly model without a tail, which was mounted on the balance system (see sections 3.1.2 and 3.2.2) in an quiescent environment (viz. simulating the hovering flight configuration) as shown in Fig. 3.27. The FPGA and the microcontroller systems were utilized in these measurements not only to perform aforementioned tasks (see sections 3.1.2 and 3.3.1) and data acquisition at 12.5 kHz recording frequency but also to synchronize the high-speed imaging system with the force measurements and the flapping motion.

The structural deformations of six different wing configurations, properties of which are given in 3.3, were measured in a flapping frequency range of 7 – 13 Hz. However the discussion in this section is limited to three cases which have considerable differences in terms of temporal variation of lift, drag and power consumption so that it is expected to observe significant differences between the structural deformations. These cases are: (1) Ref10 wing flapping at 7.5 Hz; (2) Ref10 wing flapping at 12 Hz; (3) Ref5 wing flapping at 12 Hz. For each case, the three-dimensional wing geometry was reconstructed for twenty phases in the flapping cycle. The marker positions one time step (i.e., 1/image recording frequency) before and after a given phase were also reconstructed to determine the velocity of the markers at that instant. A two-point central difference scheme was then used with the position data to calculate the velocity values.

A structured grid of circular dots with an approximate diameter of 1 mm were marked on the Mylar surface of the right upper wing during the manufacture process. Structural deformations of only the upper wing were captured in these measurements assuming that the lower wing displays similar deformation characteristics in the hover condition. The distance between the markers is 5 mm in the chordwise direction and 10 mm in the spanwise direction (see Fig. 3.28). The first horizontal line of markers is positioned at 5 mm distance from the leading edge, whereas the distance between the outermost vertical line and the wing tip is 10 mm. This gives a total number of 200 markers on the present wing configurations. Nevertheless, the innermost line of markers had to be omitted from the detection process due to their proximity to the DelFly body, which results in the loss of these markers from the vision of the cameras at numerous phases of the flapping motion.

The images of the markers were captured with two CMOS cameras with a maximum resolution of 1024 × 1024 pixels and a pixel pitch of 20 μm. The cameras were arranged at an angle of 30° with respect to each other (Fig. 3.29a). Each camera was equipped with a Nikon lens (with an objective focal length of 60 mm for the Camera 1 and 50 mm

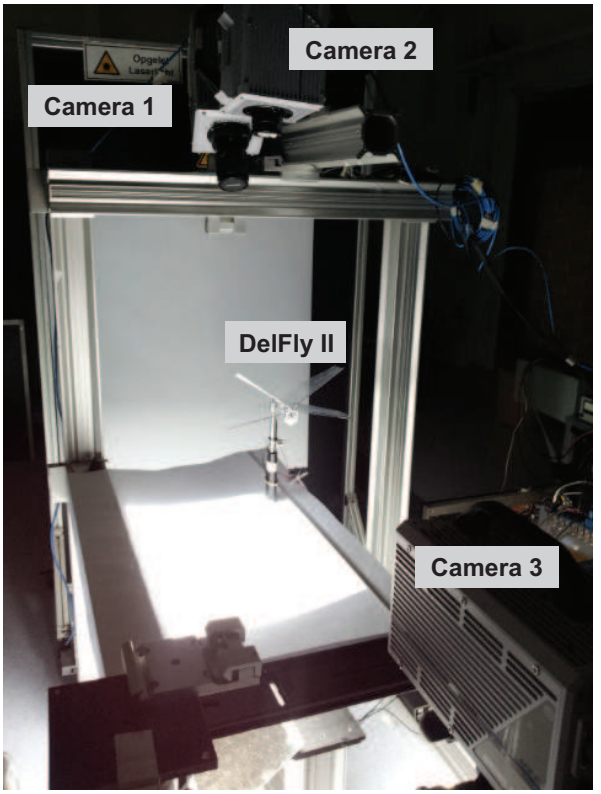

Figure 3.27: Experimental setup for the wing structural deformation measurements

for the Camera 2) with a numerical aperture of $f\# = 16$. A Scheimpflug adapter was used on the Camera 1 to align the mid-plane of the measurement volume with the focal plane. The digital resolution is approximately 7.5 pixels/mm. A measurement volume of 150 × 150 × 140 mm in size was positioned with its lowermost plane at the same height with the DelFly body so as to cover the complete stroke of the upper wing (see Fig. 3.29a and b). In order to provide a clear image of the markers and improve the detectability, a back-lighting illumination technique was used. For this purpose, a sheet of white paper was laid underneath the DelFly model, onto which the light beam produced by an HMI spotlight (JB System FSP 757 MSR Followspot) was reflected to generate a white diffusive background in a dark environment. Simultaneously, a third camera, which was placed normal to the flapping wings in front view (see Figs. 3.27 and 3.29a), captured the motion of the leading edges of the left upper and lower wings in order to determine the stroke angle. The images of the markers and the leading edges were acquired in an image recording frequency range of 1-2 kHz.

Image acquisition, volume calibration and image preprocessing were performed in the PIV software LaVision DaVis 8.1.6. The measurement volume was calibrated by scanning a three-dimensional plate through the volume in depth of 140 mm with steps of 20 mm. The

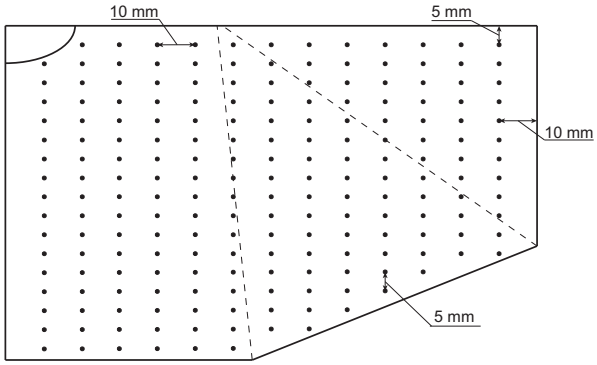

Figure 3.28: Sketch of the Ref wing layout with circular markers

calibration plate has two planes with an in-depth distance of 2 mm. Each plane consists of a structured grid of 2 mm diameter dots with an in-plane distance of 22.5 mm. These grids are positioned with an offset of 11.25 mm on the two planes providing fine spatial information in both in-plane and in-depth directions. In each calibration plane, the relation between the physical coordinates and the image coordinates is described by a 3rd order polynomial fit. Linear interpolation is then used to find corresponding image coordinates at intermediate z locations. Finally, the mapping information between the image coordinates and the physical coordinates for each camera was exported from DaVis 8.1.6 with a resolution of 1.3 mm in each direction. The black and white images were inverted in colour and preprocessed with background intensity removal and a Gaussian smooth with 9×9 kernel size.

An in-house developed Matlab code was used for the detection of the markers and the reconstruction of their three-dimensional coordinates. The circular Hough transform technique was utilized for the initial detection of the wing markers in both images. Then, the positioning of the image coordinates of the marker centers were further improved by calculating the centroid of the intensity distribution for each detected marker. Subsequently, the matching process between the detected markers in the two images was performed based on the known structural grid properties and three reference points defined in the both camera images at the beginning of the process. The image coordinates of the markers were then triangulated by use of the mapping information of the cameras to acquire the three-dimensional coordinates. A mid-point triangulation technique was used and the closest distance between projection lines for each marker was defined as a measure of uncertainty. The reconstructed markers with more than 1.4 mm distance between the projection lines are detected as outliers and excluded from the further analysis. The average uncertainty in the detection and triangulation of the resultant marker coordinates is about 0.1 mm for the cases considered in this study. The three-dimensional coordinates of the markers acquired in the global camera coordinate system (x_d, y_d, z_d) are transformed into the wing coordinate system (x_w, y_w, z_w with x_w oriented parallel to the leading edge), see Fig. 3.29b, in order to calculate the wing profile properties, i.e., camber, angle of attack, trailing edge deformation and the width of the suction column at a given spanwise location. The deformed wing profiles at different phases of the wingbeat cycle are depicted

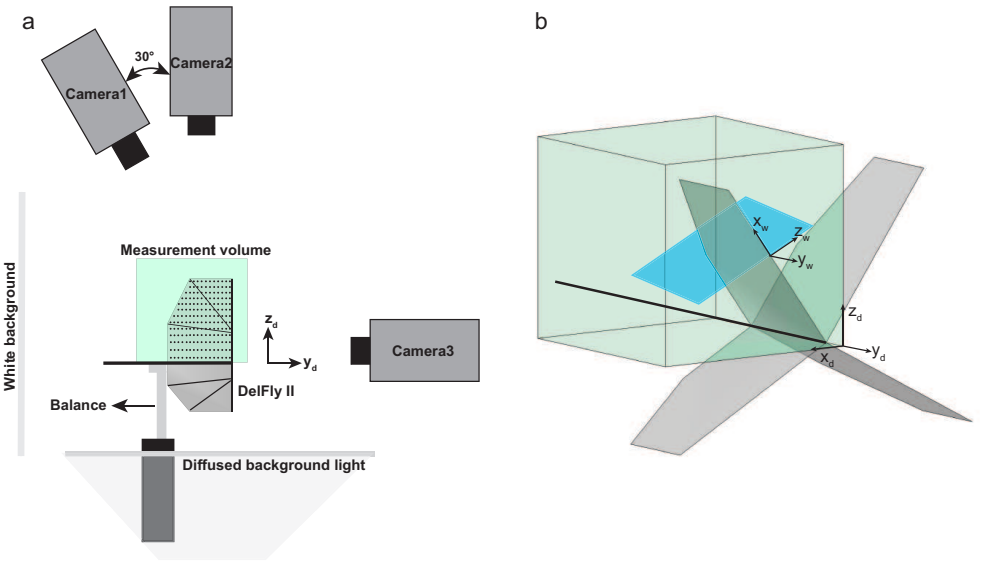

Figure 3.29: **a** Sketch of the side view of the experimental setup for the wing deformation measurements; **b** schematic representation of the measurement volume (*in green*), the global coordinate system for the reconstruction of the three-dimensional marker coordinates (x_d, y_d, z_d), the wing coordinate system for the calculation of wing profile shape at a given spanwise location (x_w, y_w, z_w), the $y_w - z_w$ plane in which the wing deformations are depicted (*in blue*)

in a sectional $z_w - y_w$ plane (blue plane in Fig. 3.29b). Although Fig. 3.29 indicates the origin of the wing coordinate system to lie on the wing leading edge, in the following wing representations the reference position $z_w = 0$ is relocated to the dihedral plane in order to visualize the wing motion in the stroke plane.

Figure 3.30a shows the reconstructed wing geometry in the non-dimensional global coordinate system (x_d^*, y_d^*, z_d^*), where dimensions have been normalized by the wing mean chord length ($\overline{c}$ = 80 mm), at t^* = 0.75 (corresponding approximately to the half of the outstroke, see Fig. 3.5a) for the case of the Ref10 wing flapping at 12 Hz. The images of the markers that were captured by the first and the second camera are shown in Fig. 3.30b and c, respectively. For this three-dimensional representation, the leading edge spar and the stiffeners were also reconstructed, yet the further analysis is primarily based on the behaviour of the markers.

The first and last markers on the chord line are used to represent the leading and trailing edges and to calculate their kinematics, respectively. At a given instant of the flapping motion, the chord line is defined as the straight line connecting the leading edge and trailing edge markers for a specified spanwise position (Fig. 3.31). The camber of the wing profile is defined as the maximum distance between the chord line and the markers along the profile. The geometric angle of attack (α) is the angle between the chord line and the stroke velocity vector of the leading edge marker ($\vec{U}_{\mathrm{LE}}$). The maximum horizontal suction column width is defined as the maximum horizontal distance between the leading edge marker and the other detected markers. This property is indicative of the extent of the area

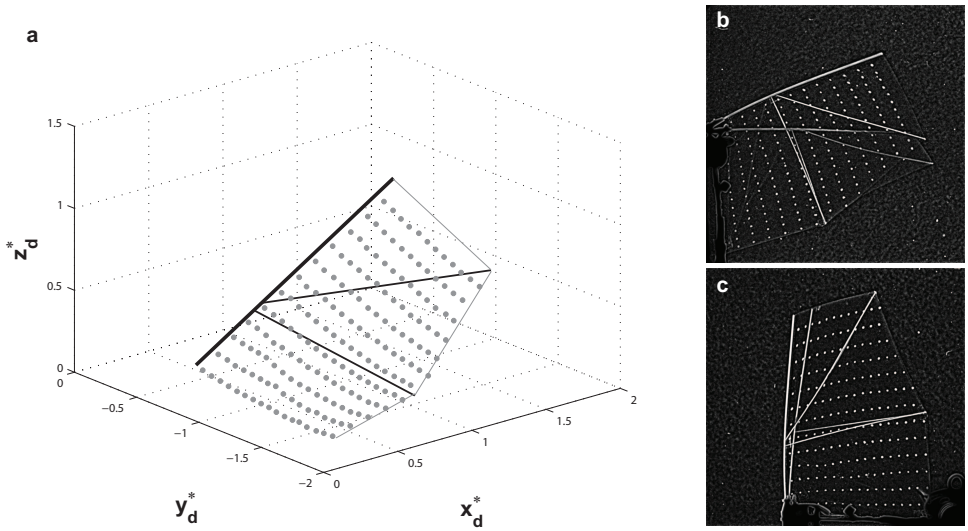

Figure 3.30: **a** Three-dimensional reconstructed wing geometry in the non-dimensional global coordinate system (x_d^*, y_d^*, z_d^*) at the phase of $t^* = 0.75$ for the Ref10 wing flapping at 12 Hz; images of the wing markers recorded by **b** the first and **c** the second camera

over which the wing section can generate a force in the (vertical) x_b direction. The trailing edge deformation (d_{TE}) is defined as the horizontal distance between the leading edge and the trailing edge markers. All parameters with the dimension of length are normalized by the mean chord length of the wing and denoted with superscript "*".

3.4.3. Results

In this section, deformation variations of the DelFly's flexible wings during the flapping motion are presented. The three selected cases are compared to investigate the effects of flapping frequency and the membrane foil thickness on the deformation characteristics. The comparative analysis is performed based on the wing section properties (i.e, angle of attack, camber, maximum suction column width) at a number of spanwise locations and behaviour of the leading and trailing edge markers during the flapping motion. Moreover, the relation between the deformation characteristics and the force histories is examined.

Structural deformations of the Ref10 wing for different flapping frequencies

Wing profiles throughout a flapping cycle at three different spanwise locations (i.e., $0.5R$, $0.71R$ and $0.93R$) of the Ref10 wing for the flapping frequencies of 7.5 and 12 Hz are shown in Fig. 3.32. Note that the colour of the wing profile changes from black to light gray as the wing proceeds in motion starting from the beginning of the instroke. The red curve indicates the leading edge trajectory. To generate these representations of the wing profiles during the flapping cycle, they have been translated from the $z_w^* = 0$ position (dihedral plane section, see Fig. 3.31) based on the distance between the leading edge and the dihedral plane at a given stroke angle and spanwise location. For this reason, the stroke amplitude in z_w^* direction increases in the spanwise direction toward the wing tip.

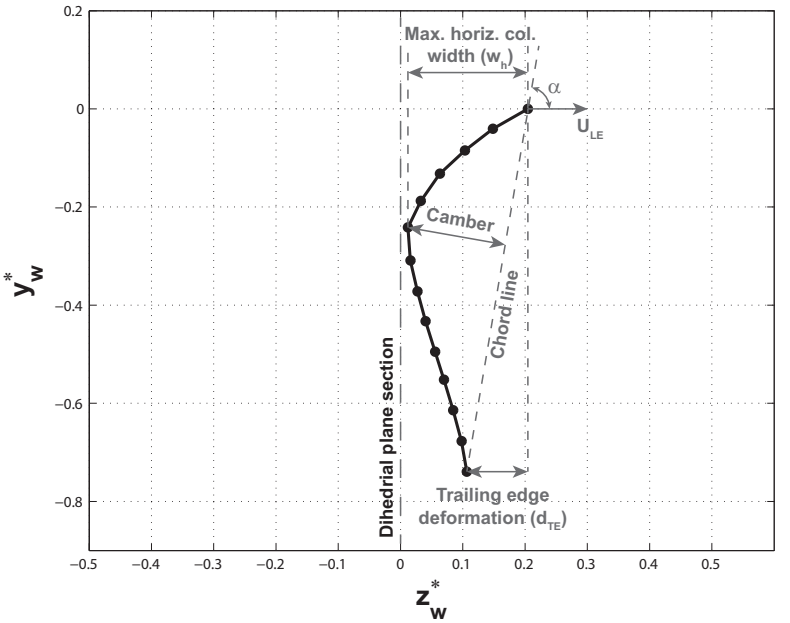

Figure 3.31: Wing profile definitions depicted on the wing profile at 70 % spanwise position of the Ref10 wing flapping at 12 Hz at the phase of $t^* = 0.65$ plotted in the non-dimensional wing coordinate system x^*_w, y^*_w, z^*_w (normalized by the mean chord length, $\overline{c} = 80$ mm)

It is clear that in addition to the sweeping (driven by the flapping system) and pitching (occurs passively due to combination of aerodynamic, inertial and elastic forces) motion, the wings also undergo a heaving motion, which becomes more pronounced closer to the wing tip (see the spanwise position of $0.93R$ in Fig. 3.32). As discussed earlier, the heaving motion kinematics in combination with the sweeping motion determines the trajectory of the leading edge, which plays an important role in the generation of forces by changing the effective angle of attack of the wing during the sweeping motion. For instance at this spanwise position, the downward motion of the wing in the $-y^*_w$ direction increases the angle of attack which can promote the formation of LEV circulation and thus force generation. The amplitude of the heaving motion is approximately $0.07\overline{c}$ and $0.085\overline{c}$ for the flapping frequencies of 7.5 and 12 Hz, respectively. For the low flapping frequency case, the leading edge marker heaves downwards (for $0.08\overline{c}$) until $t^* = 0.25$ and then start moving upwards (for $0.14\overline{c}$), which lasts until the stroke reversal. In combination with the decreasing sweeping velocity of the wing (see Fig. 3.3), this upward heaving motion during the second half of the instroke further decreases the effective angle of attack. During the outstroke, the wing first heaves down for $0.1\overline{c}$ during the first $t^* = 0.15 - 0.20$ and subsequently moves upwards for $0.05\overline{c}$ in the remaining part of the outstroke. The high flapping frequency case mostly differs in terms of heaving amplitudes and kinematics in the second half of the instroke. Similar to the low frequency case, the wing heaves downwards until

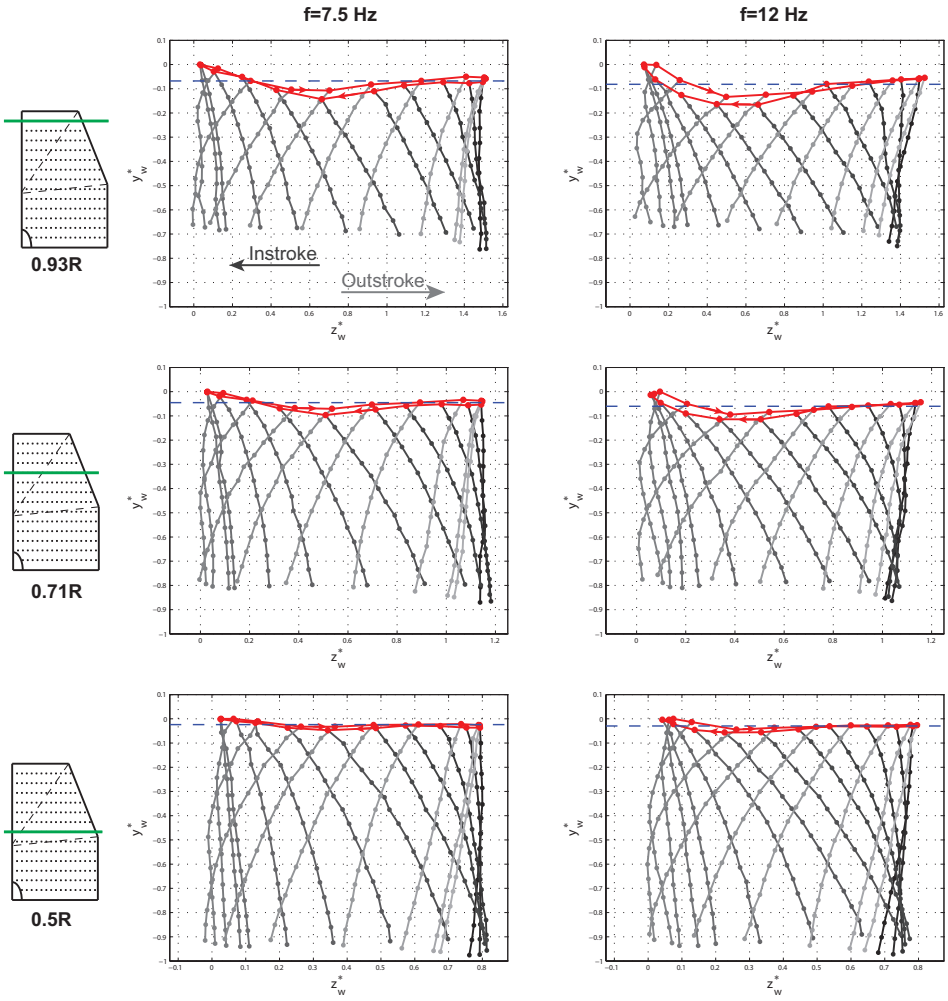

Figure 3.32: Wing profiles throughout the flapping cycle for the case of Ref10 wing flapping at 7.5 Hz (*left*) and 12 Hz (*right*) at three different spanwise locations: 0.93R (*first row*); 0.71R (*second row*); 0.5R (*third row*). Note that the colour of the wing profile changes from black to light gray as the wing proceeds in motion starting from the beginning of the instroke. The leading edge and its trajectory is depicted in red, whereas the mean stroke plane is represented with blue dashed line.

$t^* = 0.25$ during the instroke but then follows an exponential curve upwards rather than a linear path. Such a pattern is more favourable because most of the vertical motion occurs toward the end of the stroke when the sweeping velocity is rather low so that the force generation is small as well. In this way, the negative effect of the upward heaving motion is excluded from the energetic part of the instroke. This is the underlying strategy behind the idealized figure-of-eight pattern in which the wing heaves downwards during both strokes and performs the upward heaving movements only during the stroke reversals. It should also be noted that the leading edge trajectory is rather flat about the stroke reversal from

outstroke to instroke. Evidently, the heaving motion works in favour of increasing the effective angle of attack during the first half of both instroke and outstroke phases for this case together with the increasing stroke (sweeping) velocity at the outer sections of the wing. However, the amplitude of the heaving motion decreases down to $0.02\overline{c}$ and $0.03\overline{c}$ already at $0.5R$ position for the flapping frequencies of 7.5 and 12 Hz, respectively.

Another prominent feature that comes out from the comparison of the two cases is the difference between the deformation characteristics of the wing around the two stroke reversals. At the beginning of the instroke, it is clear that the profile is mostly non-deformed and displays some waviness particularly at the outer spanwise position. In this period, the trailing edge moves more outwards in the low flapping frequency case. This can be attributed to relatively small chordwise deformation of the wing compared to the high flapping frequency case and as a result changing balance between the aerodynamic, inertial and elastic forces. On the other hand, at the start of the outstroke, the wing displays a significantly different deformation behaviour due to the wing-wing interaction (clap-and-peel motion) occurring during this phase: the wing starts moving outwards at the leading edge side, whereas the lower-chord side of the wing is being attracted toward the mirror wing due to the formation of a low-pressure region between the wings. This interaction results in a peel-like deformation that increases the effective horizontal column width as well as forming a cambered wing profile.

It is of importance to assess the influence of these observed differences of the wing deformation characteristics in relation to the resultant forces to gain a better understanding of the DelFly force generation mechanisms. In Fig. 3.33, the X-force variation during a flapping period is plotted for the two cases considered in the deformation measurements. Clearly, the higher flapping frequency case produces a higher X-force during the complete flap cycle. The comparison also reveals that there is a phase difference in the production of the forces such that the low flapping frequency case precedes high frequency case by a non-dimensional time difference of $t^* = 0.05$.

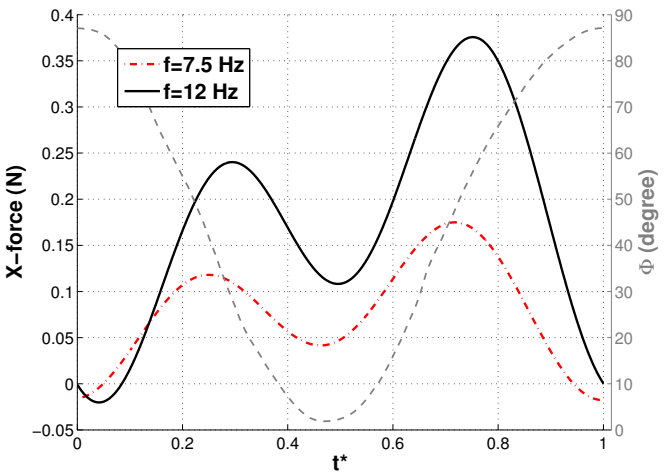

Figure 3.33: Temporal variation of the X-force component complemented with the variations of the upper wing angle (*dashed gray*) during a wing-beat cycle for the flapping frequencies of 7.5 and 12 Hz

In order to connect the wing deformation to the observed X-force history, the angle of attack and horizontal suction column width variations of the two cases at the spanwise location of $0.71R$ are plotted in Fig. 3.34. The angle of attack values greater than 90° occur during the stroke reversals and indicate the existence of a reverse flow on the wing profile, which is detrimental in terms of force generation. The average uncertainties in the reported angle of attack and suction column width values are $\delta\alpha = 0.3°$ and $\delta w^* = 0.4$ %, respectively, with 95 % confidence level. The comparison of the angle of attack variations reveals that the wing orients itself such that it attains a positive angle of attack in the upcoming stroke faster for each of the stroke reversals in the low flapping frequency case, which means that the wing profile at this location experiences reverse flow for a longer period of time in the high frequency case. In other words, the wing performs a delayed rotation during stroke reversals in both cases but a larger phase delay in the high flapping frequency case. As the wing accelerates in sweeping motion both during the instroke and the outstroke, the wing deforms more in the high frequency case due to relatively higher fluid forces, resulting in lower angle of attack values than for the low frequency case. The higher deformation at high flapping frequency also brings in a larger suction width throughout most of the flapping cycle (Fig. 3.34b). The phases of the occurrences of the maximum suction areas during the flapping cycle show a good correlation with those of the X-force in both cases. There is 4 and 7 % of $\overline{c}$ difference between the maximum suction column widths of the two cases during the instroke and outstroke, respectively. The phase difference between the X-force variations of the two cases is also present in the angle of attack and suction column width variations. Apparently, the delay in the reorientation of the wing surface during the stroke reversals retards the progress of the wing profile parameters and hence the X-force generation.

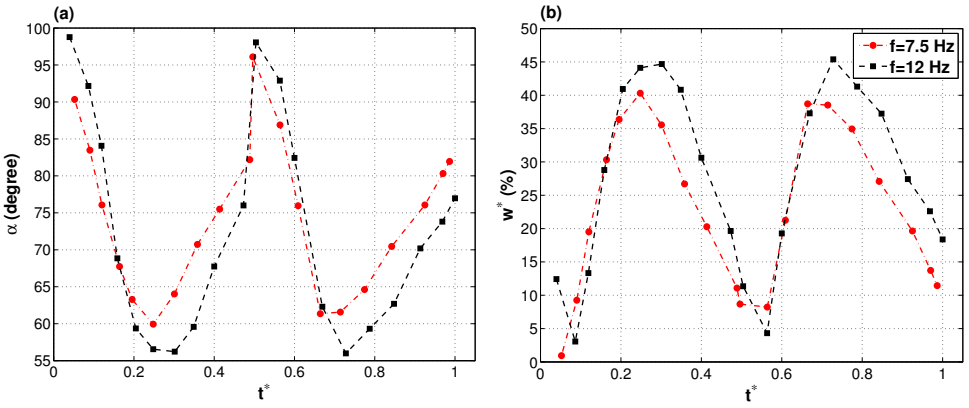

Figure 3.34: Comparison of temporal variations of the **a** angle of attack (α) and **b** horizontal suction column width (w^*) of the upper wing during a flapping cycle for the flapping frequencies of 7.5 and 12 Hz

Another important wing profile property that influences the force generation is the wing camber, variation of which at the $0.71R$ spanwise location during a flapping cycle for the two flapping frequency cases is shown in Fig. 3.35a. For a given flapping frequency, the wing camber peaks twice during a flapping period both happening at the early stages

of the instroke ($t^* = 0.10 - 0.20$) and the outstroke ($t^* = 0.60$). Due to the wing-wing interaction and related pressure fields, the camber during the outstroke reaches significantly higher values than those during the instroke. The wing profile has a maximum camber value (defined relative to the local chord length c) of 11 % at the $0.54c$ chord location ($c = 0.75\overline{c}$) during the instroke, whereas it is 21 % with the camber location of $0.35c$ ($c = 0.79\overline{c}$) during the outstroke. Apparently, the clap-and-fling motion with flexible wings results in the formation of a wing profile with a significant camber, which is reported to be favourable in terms of force generation (Du and Sun, 2008; Young et al, 2009), and hence boosts its aforementioned benefits on the force generation mechanisms.

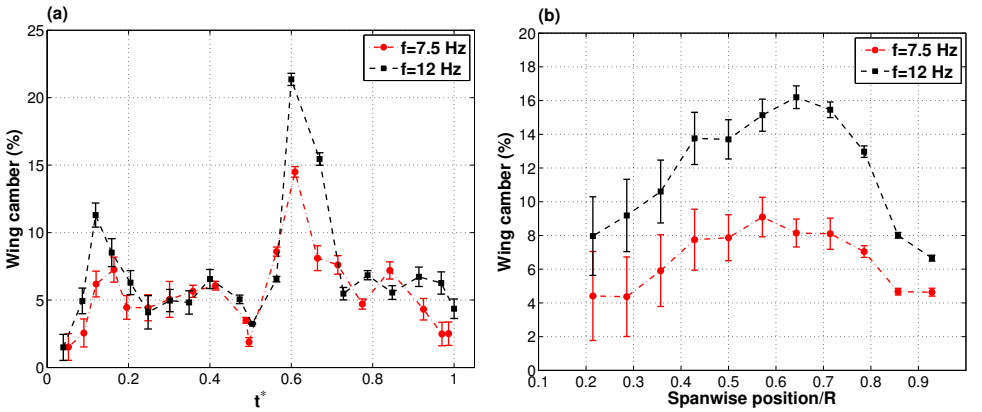

Figure 3.35: **a** Temporal variation of the wing camber during a flapping cycle at the $0.71R$ spanwise location, **b** spanwise variation of the wing camber at $t^* = 0.67$ for the flapping frequencies of 7.5 and 12 Hz

Spanwise variation of the camber along the wing span at the time instant of $t^* = 0.67$ is shown in Fig. 3.35b. This particular moment in the cycle is selected for the representation due to its proximity to the maximum X-force generation phases (see Fig. 3.33) while having relatively large camber values. The wing camber follows an increasing trend starting from the wing root until approximately $0.55R - 0.65R$ spanwise location, after which the values decrease toward the wing tip in both cases. Smaller camber values toward the wing root can be attributed to the relatively small stroke velocities due to the nature of the curvilinear motion and the wing displaying more rigid characteristics in the chordwise direction as it is constrained both at the leading and trailing edges at the wing root. It is important to note that the inner stiffener is positioned with its leading edge at the $0.4R$ spanwise location and the trailing edge at the $0.46R$ position intersecting with the taper corner (see Fig. 3.20b). In accordance with this, the wing camber has a change in trend in the region between $0.3R$ and $0.42R$ locations and the profiles at $0.43R$ and $0.5R$ positions have equivalent wing camber for both flapping frequencies under the influence of the chord-wise oriented inner stiffener. The outer stiffener, that is oriented diagonally from the leading edge at the $0.4R$ spanwise position to the trailing edge at the wing tip, results in a variation of camber as evident in the high flapping-frequency case such that it first increases until the $0.65R$ position and then decreases onwards toward the wing tip. This is mainly due to the effect of the deflected outwards stiffener on the wing profile depending on its chordwise

location in the given spanwise station: in case the stiffener passes through a point close to the leading edge, it induces a wing profile with a camber; in case the stiffener is close to the trailing edge, as is the case for the spanwise stations close to the wingtip, it results in the deflection of the trailing edge with the upper chord part flexing about the leading edge similar to pitching down in the direction of lowering the angle of attack. Therefore, the effect of the outward stiffener is twofold: it adds a camber to the profile and it decreases angle of attack by promoting the trailing edge deformation. The balance between these two effects depends on the chordwise position at which the chord-line at a given spanwise position and the stiffener intersects.

The spanwise variation of the angle of attack also supports the previous discussion regarding the effect of the outward stiffener. Figure 3.36a shows the angle of attack distribution over the span length at a number of time steps. In general, the angle of attack decreases toward the wing tip indicating existence of torsion and wing twist. There are two main reasons for the torsion: (1) increasing sweeping velocity toward the wing tip and thus increased fluid forces; (2) aforementioned changing stiffness characteristics of the wing structure in the spanwise direction. It is also important to note that the angle of attack variation for the flapping frequency of 7.5 Hz at $t^* = 0.67$ shows a better agreement with that for the frequency of 12 Hz at $t^* = 0.73$ in terms of trend. Likewise, the variation at $t^* = 0.6$ of 7.5 Hz case displays a similar trend with that at $t^* = 0.67$ of the 12 Hz case. This also substantiates the presence of a phase lag between the two cases in terms of the temporal evolution of the wing profile's angle of attack.

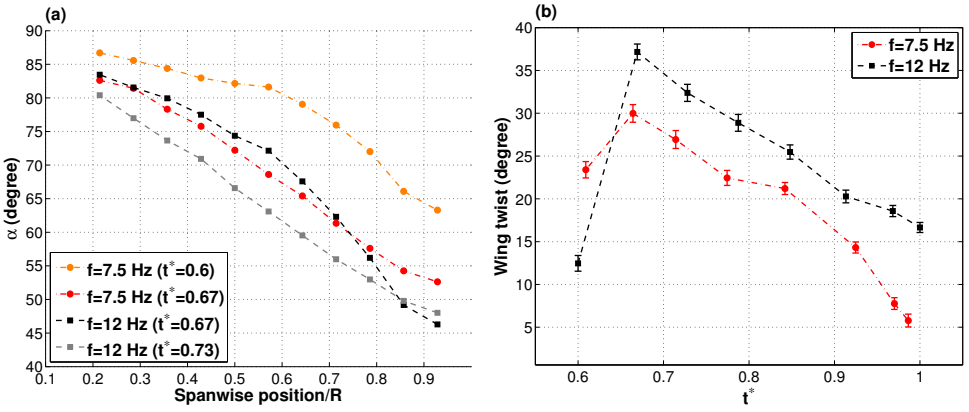

Figure 3.36: **a** Spanwise variation of the angle of attack at $t^* = 0.67$, which is complemented with the data at $t^* = 0.6$ for the flapping frequency of 7.5 Hz and the data at $t^* = 0.73$ for the flapping frequency of 12 Hz to show the phase difference between the cases, **b** temporal variation of the wing twist angle in the time period of $t^* = 0.6 - 1$ during the outstroke for the flapping frequencies of 7.5 and 12 Hz

The effect of flapping frequency on the wing twist is also important as the angle of attack has a direct effect on the force generation mechanisms. In Figure 3.36b, the wing twist angle is plotted for the time period between $t^* = 0.6$ and the end of the outstroke. The initial part of the outstroke ($t^* = 0.5 - 0.6$) is not included in this analysis as the wing still performs stroke reversal and experiences reverse flow during most of this time period.

The instroke phase is also not considered due to poor imaging conditions at the inner spanwise locations of the wing close to the root and hence high uncertainties in the marker detection. The twist angle is calculated as the difference between the angles of attack of $0.21R$ and $0.93R$ spanwise positions. As a result, it is clear that the wing performing high frequency flapping motion undergoes a greater torsional motion in the spanwise direction than the low flapping frequency case, which results in a higher wing twist angle during the most part of the outstroke. As expected, the twist angle decreases toward the end of the outstroke as the stroke velocity and fluid forces becomes smaller.

When a single flexible wing is considered, the resultant force acting on the wing can be decomposed into two main components: first, the component in the y_w direction (vertical force which is normal to the sweeping velocity); second, the force in the z_w direction (parallel to the sweeping velocity, acting as a resisting force to the motion). The wing flexibility modulates these force components and subsequently the driving power requirements of the flapping motion in several ways; either indirectly by changing the wing morphology (i.e. adding camber or twist) that results in a different flow topology around the wings which alter the fluid forces (Du and Sun, 2008, 2010; Thielicke and Stamhuis, 2015; Vanella et al, 2009; Young et al, 2009; Zhao et al, 2009), or directly by storing and releasing elastic potential energy such that elastic forces come into play (Lehmann et al, 2011; Miller and Peskin, 2009). In the present case, the wing flexibility effects on the force component in the y_w direction for the single wing can be assessed from the measurements of the X-force on the complete MAV, because this force component is essentially the summation of the vertical forces of four wings undergoing a similar flapping motion. On the other hand, the influence of elastic deformations on the resisting force cannot be assessed from the force measurements on the DelFly due to the configuration with counter-moving wings, which essentially cancels the forces in the z_b direction. However, this can be related the power consumption of the motor during the flapping motion. In theory, the power required to flap the wing can be calculated by multiplying the velocity of the motion and the resisting force. In the case of the DelFly, the wings are driven in a reciprocating flapping motion at the leading edges so that the power requirement for a single wing is simply the velocity of the leading edge and the resisting force exerted at this point (note that this calculation excludes the energy losses in the driving mechanism). The force and the stroke velocity vary within a flapping cycle and so does the power consumption. One can expect to observe in-phase variations of these three parameters, which will happen for a rigid wing undergoing a constant-velocity motion. However, in the case of flexible wings driven in unsteady motion, in which considerable accelerations are present, the interactions become more complicated which makes the phenomenon more difficult to explain.

Fig. 3.37 shows the power consumption oscillations within a flapping cycle with the stroke angle and angular velocity variations. Clearly, the flapping motion consumes more power during the outstroke than the instroke, which is in accordance with the generation of the X-force. It is important to note that for this case (the Ref10 wing flapping at $f = 12$ Hz), the flapping wings generate 75 % more mean X-force during the outstroke than during the instroke at the expense of only 6 % more power consumption. The trend of the power consumption variation seems to be similar to the magnitude of the leading edge velocity (Fig. 3.37) and the X-force oscillations (Fig. 3.12) albeit having a different phase. Previously in Section 3.1.3, it was asserted that the trend of the power consumption vari-

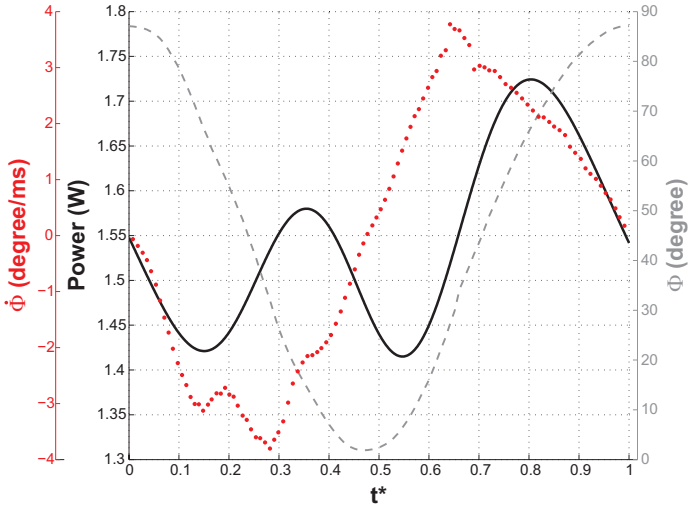

Figure 3.37: Temporal variation of the power consumption complemented with the variations of the upper wing angle (*dashed gray*) and stroke velocity (*red dots*) during a wing-beat cycle for the flapping frequency of 12 Hz

ation is probably related to the wing deformation characteristics. This was qualitatively supported with the high-speed images of the flapping wings. However, the availability of the quantitative wing deformation data can facilitate the verification of this hypothesis. In this respect, the velocity of the leading and trailing edge markers in the z_w direction is plotted in Fig. 3.38a for the spanwise location of $0.71R$. Additionally, the temporal evolution of the trailing-edge deformation for the same spanwise location is shown in Fig. 3.38b.

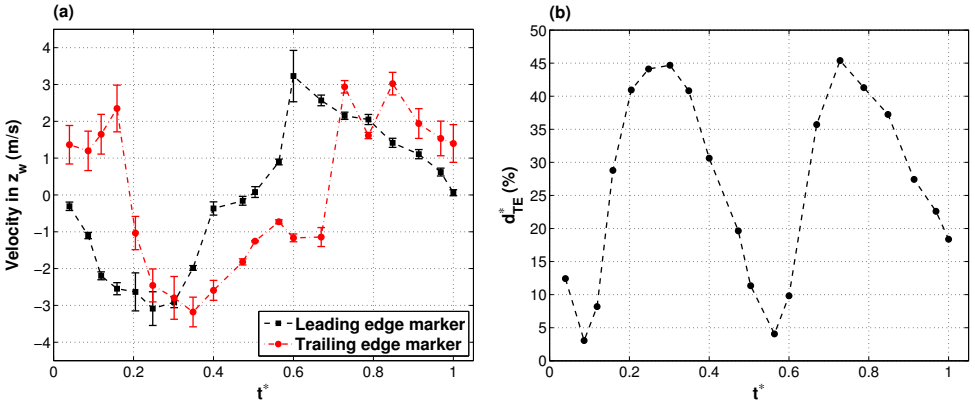

Figure 3.38: Temporal variation of **a** the velocity of the leading edge (*black squares*) and the trailing edge (*red circles*) markers, and **b** the trailing edge deformation (d^*_{TE}) of the upper wing at the spanwise location of $0.71R$ during a wing-beat cycle for the flapping frequency of 12 Hz

Despite the fact that the leading edge marker does not coincide with the leading edge spar, the temporal evolution of its velocity shows a good agreement with the angular velocity of the leading edge (see Fig. 3.5) for this spanwise position. The comparison of the leading and trailing edge marker velocities reveals that it takes at least a time period of $t^* = 0.20$ before the trailing edge reverses direction and starts moving in the same direction as the leading edge after the stroke reversals. For instance, the first time instant when the trailing edge is observed to perform an instroke motion is $t^* = 0.20$. From $t^* = 0.15$ to 0.20, the wing surface is apparently exposed to relatively high forces resulting in a strong negative acceleration such that the trailing edge marker abruptly changes direction and at about $t^* = 0.25$, it reaches comparable velocities to the leading edge marker. The same takes place at the beginning of the outstroke at about $t^* = 0.70$. Once this delayed stroke reversal occurs for the trailing edge, it follows a similar trend with the leading edge marker in the remaining part of the stroke but with a phase lag. As expected, the maximum trailing edge deformations during both instroke and outstroke occur just before the trailing edge starts moving at a higher speed than the leading edge ($t^* = 0.30$ and $t^* = 0.73$ for the instroke and the outstroke, respectively). Evidently, the flexible nature of the wings and the associated elastic forces have a considerable influence on the wing surface kinematics and accordingly on the forces, which will modulate the power consumption characteristics of the flapping motion. In order to further investigate this relation, a simplified mass-spring-damper (MSD) analogy was utilized (Fig. 3.39).

Mass-spring-damper analogy

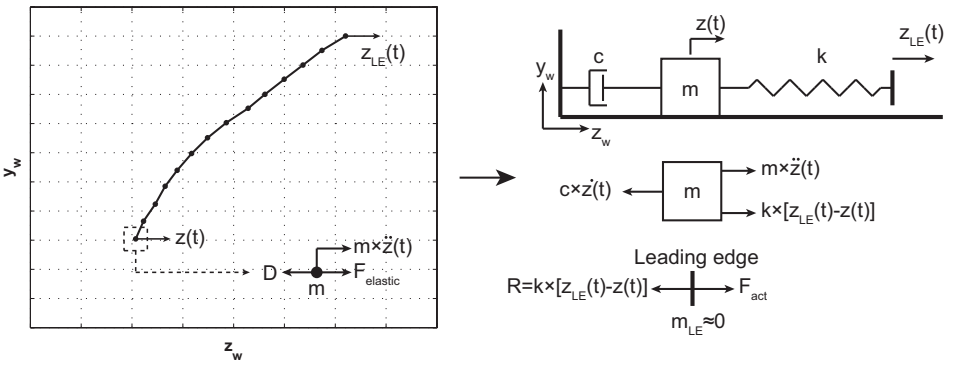

Figure 3.39: The deformed wing profile at the spanwise position of $0.71R$ at an instant during the outstroke with the schematic of the forces exerting on a specific segment of it with a mass m taken at an arbitrary chordwise position (trailing edge segment is considered for the current simulations) under the prescribed leading edge motion kinematics (*left*); a mass-spring-damper (MSD) system used to simulate the actual dynamics of the wing segment of mass m and to assess the required actuating force (F_{act}) to perform the prescribed kinematics at the leading edge due to dynamics of the wing segment and flexibility of the wing (*right*). Note that schematic of the MSD system represents a certain moment during the outstroke and should be considered to be a system in which the leading edge and the wing segment can pass over each other as in the case of actual flapping motion.

In the simplified MSD analogy, the main objective is to determine the resisting force (R) acting on the leading edge and calculate the power consumption for the prescribed

motion kinematics of the leading edge, by putting it in relation to the wing dynamics, considering a segment with a mass m. Essentially, the forces applied on this wing segment are the inertial force ($m \times \ddot{z}(t)$), the fluid force (viz. drag) (F_{fluid}) and the elastic force due to structural deformations ($F_{elastic}$). In the MSD system, the wing segment of mass m is connected to a damper on one side, that represents the aerodynamic drag (see Fig. 3.39). The amount of force applied by the damper is proportional to the velocity ($\dot{z}(t)$) multiplied by the damping constant (c). This clearly does not represent the actual phenomenon, where the aerodynamic force is closer to being proportional to the square of the velocity, yet it is a plausible assumption considering the simplified nature of the analogy (viz. use of a lumped mass system and simulating the chordwise deformation of the wing in a one-dimensional system). The flexibility of the wing is represented with a spring connected to the opposite site of the mass with a spring constant of k. The spring is connected to the so-called leading edge on the other side, which is taken as massless and actuated to perform the flapping motion kinematics ($z_{LE}(t)$). For the flexible wing scenario, the resisting force is basically the spring force ($k[z_{LE}(t) - z(t)]$), whereas in the case of the rigid wing, there is no spring force in the system so that the mass undergoes the leading edge motion kinematics. In this case, R is simply the difference between the fluid forces and the inertial forces acting on the mass. The power consumption for both flexible and rigid wing cases were calculated by multiplying the leading edge velocity ($\dot{z}_{LE}(t)$) and the resisting force exerted at this point. The displacement of the spring in time in the case of flexible wing is acquired by solving the equations of motion for the wing segment:

$$m\ddot{z}(t) = k[z_{LE}(t) - z(t)] - c\dot{z}(t) \tag{3.12}$$

Introducing the natural frequency of the system ($\omega_n = \sqrt{k/m}$), the damping ratio ($\zeta = c/(2\sqrt{km})$ and the leading edge motion kinematics, which was considered as pure sinusoidal motion for the sake of simplicity ($z_{LE}(t) = A\cos\omega t$, where A is the amplitude and ω is the circular frequency of the motion), into the Eq. 3.12 and rearranging the terms:

$$\ddot{z}(t) + 2\zeta\omega_n\dot{z}(t) + \omega_n^2 z(t) = A\omega_n^2\cos\omega t \tag{3.13}$$

The solution representing the periodic response to the excitation is given by:

$$\ddot{z}_p(t) = c_1\cos\omega t + c_2\sin\omega t \tag{3.14}$$

where c_1 and c_2 are:

$$c_1 = \frac{A}{\left(1 - \frac{\omega^2}{\omega_n^2} + \frac{4\zeta^2\omega^2}{\omega_n^2 - \omega^2}\right)} \tag{3.15a}$$

$$c_2 = c_1\frac{2\zeta\omega_n\omega}{\omega_n^2 - \omega^2} \tag{3.15b}$$

The above analytical solution was then used to simulate the dynamics of the wing segment. The solution was performed for the parameter values of $\omega_n = 3.2$ rad/s, $\zeta = 1.56$ and $\omega = 0.8$ rad/s. Although the selection of these particular values is mainly out of simplicity and does not reflect the actual flapping wing motion and structural properties, some

physical observations were still taken into account. In this respect, the circular flapping frequency was selected to be a quarter of the natural frequency of the system ($\omega = 0.25\omega_n$) based on the observation in the comparison of the power spectral densities of in-air and in-vacuum X-force measurements that the fourth and the sixth harmonics of the flapping motion are dampened in-air conditions and probably associated to the wing structural modes. Secondly, the system was designed to be slightly over-damped ($\zeta > 1$) based on the observations that the trailing edge of the wing lags behind the leading edge and it does not overpass the maximum position the leading edge reaches at the end of the outstroke. Nevertheless, as the main objective of the use of the analogy is to assess the general behaviour of the wing surface and its influence on the power consumption in a simplified setup, the coarse assumptions made on the determination of the parameters should not affect the main conclusions of this analysis. Before proceeding with the further analysis of the MSD analogy, it should be noted that all the results presented are in a non-dimensional form: the displacement data are normalized by the amplitude of the leading edge motion ($z^*(t) = z(t)/A$), whereas the velocity data are normalized by the maximum velocity of the leading edge ($\dot{z}^*(t) = \dot{z}(t)/(A\omega)$). Forces and power values are scaled with $mA\omega^2$ and $mA^2\omega^3$, respectively.

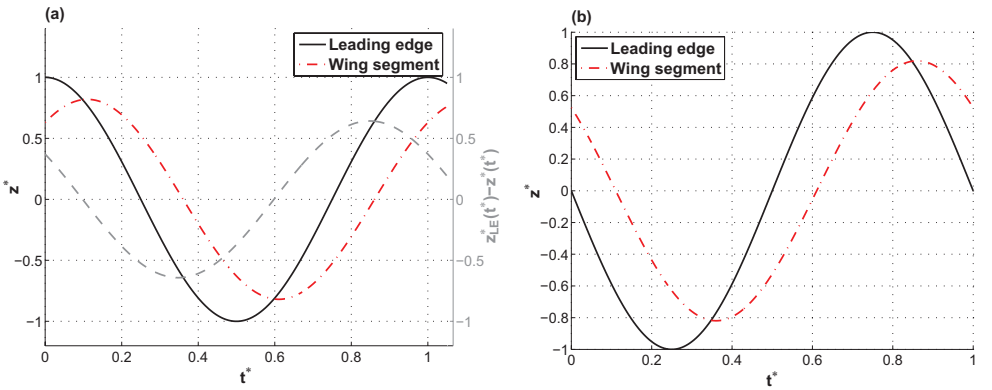

Figure 3.40: **a** Non-dimensional displacements of the leading edge and the wing segment in time complemented with the relative position of the wing segment with respect to the leading edge (deformation at the wing segment location, shown in *dashed gray*), **b** non-dimensional velocities of the leading edge and the wing segment in time

Figure 3.40a displays the displacement of the leading edge and the wing segment (henceforth, it is also referred to as the trailing edge) in time, which is complemented with the difference between the z coordinates of the two, that is equivalent to the extension of the spring or in other words, the deformation of the wing at the position of the wing segment. The trajectories have a phase difference such that the trailing edge follows after the leading edge throughout the motion, as is in the actual case. The trend of the trailing edge deformation has a good agreement with the actual case for the instroke phase (see $t^* < 0.5$ in Fig. 3.38b) such that the maximum deformation occurs at a later phase than the instant when the leading edge moves at the maximum velocity. Due to symmetric nature of the leading edge motion prescribed in the MSD model, the wing deformations are the same both during instroke and the outstroke, whereas in the actual case, there is a significant

difference due to the wing-wing interaction taking place at the onset of the outstroke. As expected, the trailing edge velocity changes sign after the leading edge (Fig. 3.40b) and the wing deforms until it reaches the velocity of the leading edge following the stroke reversal. Subsequently, the trailing edge moves faster than the leading edge resulting in the decrease of the trailing edge deformations toward the end of the stroke.

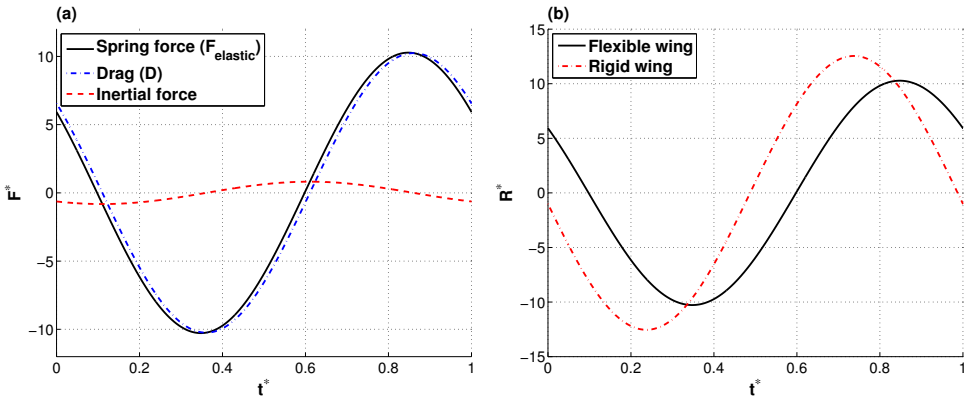

Figure 3.41: **a** Variation of non-dimensional elastic ($F_{elastic}$), drag (D) and inertial force acting on the wing segment within a cycle of the motion, **b** variation of the non-dimensional resisting force (R) exerting at the leading edge within a cycle of the motion for the flexible and rigid wing scenarios

The lagged motion of the wing segment with respect to the leading edge is a natural result of the spring forces coming into play (Fig. 3.41a). For instance at the beginning of the instroke phase (i.e., the phase the leading edge moves in the negative z direction in the MSD system), the trailing edge still moves outwards in the positive z while decelerating under the effects of: (1) the spring restoring force, as the spring is still slightly elongated (see the relative wing segment position in Fig. 3.40a, which is essentially the spring displacement); (2) the aerodynamic damping force, which is dominant over the former, as the mass still has an outwards velocity. As the motion of the leading edge progresses in the instroke direction, the elastic force component vanishes with the spring reaching its relaxed condition at around $t^* \simeq 0.098$, and while the outward motion of the wing segment continues until $t^* \simeq 0.11$ so does the effect of the aerodynamic force. Between these two time stages, the elastic and the aerodynamic forces act in the same direction (i.e., in the negative z direction), which causes the wing segment to accelerate in the instroke direction. Under the effect of the dominant elastic force component, the wing segment reaches the velocity of the leading edge ($t^* \simeq 0.35$), after which the balance between the forces changes in favour of the aerodynamic forces due to the reversed motion of the leading edge and hence decrease of the spring displacement. In consequence, the delayed motion of the wing segment clearly stems from the flexible structure storing the kinetic energy imposed by the leading edge as elastic potential energy and its release afterwards. This mechanism also affects the resisting force acting on the leading edge in terms of peak values and phase of the temporal evolution compared to the rigid wing case (Fig. 3.41b). As the resisting force experienced at the leading edge is essentially the spring restoration force in the case of the flexible wing motion, it peaks when the maximum spring extension

occurs (i.e. the time the maximum wing deformation occurs) rather than at the time of the maximum leading edge velocity as is the case for the rigid wing. This consequence is an important aspect regarding the power consumption of the motion (Fig. 3.42). Once multiplied with the leading edge velocity, the resisting force acting on the leading edge of the rigid wing results in significantly higher values of the power consumption when compared to that of the flexible wing case, which is basically multiplication of two off-phase oscillations with a phase difference of approximately $\phi \simeq 40^\circ$. As a result, the calculated power consumption oscillations are also off-phase ($\phi \simeq 22^\circ$) with respect to the leading edge velocity, which agrees with the phase difference observed in the actual MAV measurements (see Fig. 3.12). Moreover, the comparison of the flexible and rigid wing cases for the current set of parameters reveals that the flexible wing requires 32 % less power with respect to the rigid wing to perform the simulated reciprocating motion.

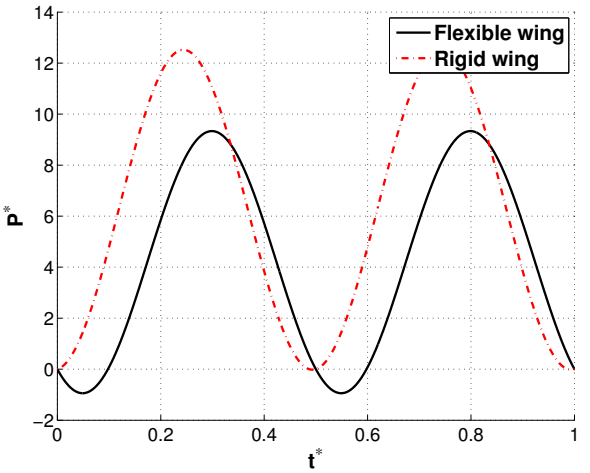

Figure 3.42: Variation of non-dimensional mechanical power requirement within a cycle of the motion for the flexible and rigid wing scenarios

Structural deformations of the Ref5 wing

In order to explore the effect of the Mylar foil thickness on the structural deformations, the case of the Ref5 wing with a flapping frequency of 12 Hz is considered in this section. The wing section profiles at two different spanwise location (i.e., $0.71R$ and $0.93R$) within a complete flapping cycle are shown in Fig. 3.43.

In general, the structural features of the Ref5 wing are similar to those of the Ref10 wing at the same flapping frequency (see Fig. 3.32). The most prominent difference between the Ref5 and Ref10 wing cases is a slight difference in the leading edge trajectories that is apparent particularly at the $0.93R$ spanwise location with a mean stroke amplitude of the heaving motion being $0.095\overline{c}$. The Ref5 wing performs a higher amplitude heaving motion than the Ref10 wing; however, its effect on the force generation mechanisms is disputable due to a non-ideal figure-of-eight-like trajectory of the leading edge. It is favourable that the Ref5 wing plunges down for a larger distance ($0.15\overline{c}$) than the Ref10 wing ($0.1\overline{c}$) in the

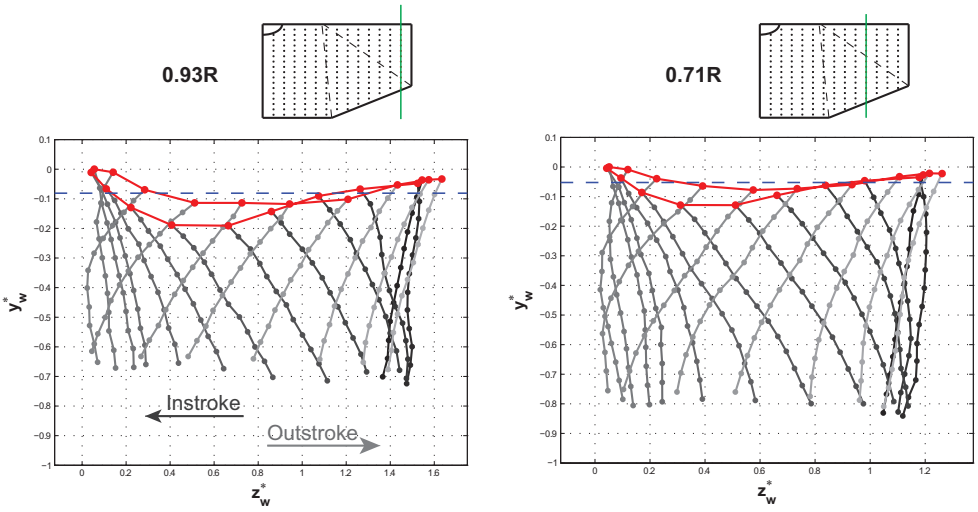

Figure 3.43: Wing profiles throughout the flapping cycle for the case of Ref5 wing flapping at 12 Hz at two different locations: 0.93R (*left*); 0.71R (*right*). Note that the colour of the wing profile changes from black to light gray as the wing proceeds in motion starting from the beginning of the instroke. The leading edge and its trajectory is depicted in red, whereas the mean stroke plane is represented with blue dashed line.

first part of the instroke (until $t^* = 0.25$) yet it also heaves up for more (heaving distance of $0.18\overline{c}$ and $0.15\overline{c}$ for the Ref5 and Ref10 wings, respectively) until the end of instroke, which is detrimental in terms of the effective angle of attack. The heaving kinematics are more-or-less similar during the outstroke for both wings. Apparently, the relatively flexible surface of the Ref5 wing yields larger amplitude motion in the heaving direction but its influence on the force generation is uncertain.

The angle of attack of the Ref5 wing shows a similar variation during a flapping period with that of the Ref10 wing as shown in Fig. 3.44a (note that the average uncertainty in the reported angle of attack for the Ref5 wing is $\delta\alpha = 0.7°$). In general, the Ref10 wing has marginally larger angle of attack than the Ref5 wing, which can be attributed to the relatively stiffer structure of the Ref10 wing. In other words, the Ref5 wing deforms more reducing the angle of attack, while also generating a slightly larger suction column width than the Ref10 wing in most part of the flapping cycle (Fig. 3.44b). The effects of these two parameters (i.e., angle of attack and suction column width) essentially counter-act each other in terms of force generation and it is difficult to determine their quantitative contribution for the cases of Ref5 and Ref10 wings to explain the difference in the X-force generation of the two wings (Fig. 3.25). Nevertheless, it is clear that the difference between the two cases is rather small and even in the uncertainty range of the measurements for some time instants.

In addition to these observations, the camber of the wing profile at the 0.71R position of the Ref5 wing during the flapping period is very similar to that of the Ref10 wing both in terms of amplitude and phase (Fig. 3.45a). It indeed supports the statement that the wing camber is mostly determined by the structural deformation of the stiffener particularly at this spanwise location, where the outer stiffener passes through the upper-half-chord of

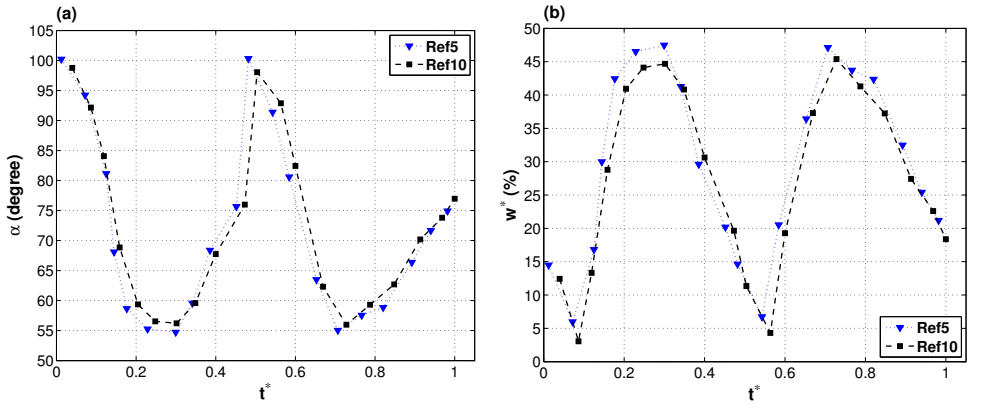

Figure 3.44: Comparison of temporal variations of the **a** angle of attack (α) and **b** horizontal suction column width (w^*) of the upper wing during a flapping cycle for the Ref5 and Ref10 wings flapping at 12 Hz

the section. The wing twist angle variation during the outstroke also shows very similar characteristics for the two cases. All these results eventually suggest that the wing deformation properties are more dependent on the stiffeners than on the surface foil thickness. However, it is possible that the thin Mylar wing has slightly different local deformations at the locations where the stiffeners are less effective. These differences are not completely revealed in the reported wing profile parameters, which are defined based on the relatively coarse tracking marker positions.

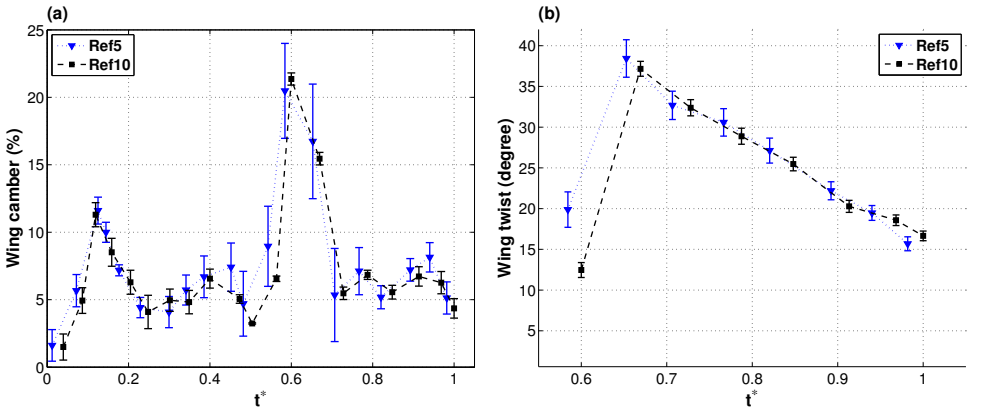

Figure 3.45: a Temporal variation of the camber of the wing profile at $0.71R$ spanwise position during a wingbeat cycle of the Ref5 and Ref10 wings flapping at 12 Hz, b temporal variation of the wing twist angle in the time period of $t^* = 0.65 - 1$ during the outstroke for the Ref5 and Ref10 wings flapping at 12 Hz

Still, compared to Ref10 wing, the Ref5 wing produces lower X-force (10 % less force with respect to the Ref10 wing) and also consumes less power (11 % less power consumption). However, these differences are rather small compared to the those discussed in the

previous section, where significantly different structural deformation characteristics are observed for different flapping frequencies. For the present case, the smaller force production of the Ref5 wing is probably caused by slight modifications in the force generation mechanisms due to unsubstantial differences in the wing structure.

3.5. Conclusions

In this chapter, the aerodynamics of the DelFly II flapping-wing motion have been explored by means of force, power consumption and structural deformation measurements. Moreover, the validity of the force measurements on the flapping-wing MAV by means of conventional methods (balance-mounted wind tunnel measurements) is examined by comparing the measured forces to free-flight estimated forces.

First, experiments were performed under in-air and in-vacuum conditions to identify aerodynamic and inertial force components. It is shown that the first two harmonics in the X-force (corresponding to lift in the hover configuration) spectrum are certainly associated to the aerodynamic forces. High-speed imaging of the flapping wings reveals that the motion of the wing surface is rather dampened in-air conditions, whereas in vacuum it performs excessive stroke behaviour compared to the leading edge, that is driven by the flapping mechanism. Comparison of the power consumption in the two measurement conditions shows that $64-74$ % of the total consumption is due to aerodynamic effects, while the power required to overcome the elastic and the inertial forces reaches maximum 20 % of the total consumption. Further inspection on the X-force oscillations in combination with the high-speed images clarifies that the first (fundamental) harmonic is related to the clap-and-peel mechanism that takes place once during a flapping cycle, whereas the second harmonic is most likely associated to the leading edge vortex (delayed stall) mechanism, which occurs twice in a cycle, both during the instroke and the outstroke. It is shown that mean X-force generated during the outstroke is 75 % more than that of the instroke due to the force-enhancing effect of the clap-and-peel effect. The power consumption in a wing-beat cycle shows a similar variation as the X-force generation yet with a phase lag.

Second, the force measurements performed by use of a force sensor have been compared to the aerodynamic forces which are calculated from the position data obtained in free-flight visual tracking experiments at identical flight conditions. For the latter, the general aircraft equations of motion were utilized to calculate the aerodynamic forces. Several factors affecting the two force determination methods are reported. Calculations from free-flight position data relies on derivation of velocities and accelerations by use of numerical differentiation algorithms, which have two major impacts: (1) smoothing of the data due to a low-pass filtering effect; (2) magnification of the position measurement error. Considering the low data sampling rates of the visual tracking systems, this is the main limiting factor in the reconstruction of the unsteady flap-cycle resolved forces. Regarding the balance-mounted wind tunnel measurements, it is shown that the clamping point on the ornithopter has a non-negligible effect on the measurements of the Z-force component by modifying the structural dynamics of the flexible body. For long body lengths between the clamping point and the exertion point of the unsteady forces, the natural frequency of the structure falls into the frequency range of the forces, that results in vibrations with comparable amplitudes with the forces of interest. Nevertheless, the structural

dynamics only interferes with the measurement of the Z-force component, while X-force is rather insensitive to the clamping point. Comparison of the forces acquired from both methods at different flight conditions reveals that there is a good agreement for the X-force component, whereas the Z-force component from both methods still displays some deviations depending on the flapping frequency. Further sources for this discrepancy are reported as structural resonance of the tail-side of the DelFly body and the absence of motion-induced forces in the case of wind tunnel measurements. As a result of this study, the reliability of the balance-mounted force measurements for the determination of the X-force component in hovering condition is justified.

Third, a parametric study is performed to investigate the effects of the flapping frequency, stiffener orientation, wing surface thickness and span length on the X-force generation and power consumption characteristics of the DelFly II in hover condition. It is shown that the force generation and power consumption increases with the flapping frequency. However, instead of a quadratic relation between the frequency and the force, a quasi-linear variation is observed in the nominal flapping frequency range of the DelFly. It is also observed that increasing the flapping frequency introduces a phase shift in the time-variation of the forces. Increasing Mylar foil thickness results in the elevation of the X-force, yet also the power consumption increases, such that the X-force to power ratio decreases. The most dominant effect is observed in the case of the span length study: increasing total span length by 4 cm results in an approximately 28 % increase in X-force with respect to the standard DelFly wing. This wing is also favourable in terms of X/P by scoring the best among all the tested wings.

Last, structural deformations of the flapping wings were measured by tracking markers on the wing surface. The reconstruction of the wing surface is performed for three different cases to focus on the effects of two parameters: the flapping frequency and the Mylar foil thickness. Firstly, it is shown that the wing performs a delayed rotation at the stroke reversals for all of the cases considered. This delay is further increased when increasing the flapping frequency, which also explains the phase shift between the force generations of different flapping frequency cases. The wing profile at $0.71R$ spanwise location was selected to compare the temporal variations of wing profile properties (viz., wing camber, angle of attack, horizontal suction column width) for the different parameters tested. It is shown that the clap-and-peel motion promotes camber formation (11 % and 21 % wing camber at the beginning of the instroke and outstroke, respectively). The higher flapping frequency case generates higher camber and has a higher suction column width due to an increased chordwise flexure. Moreover, increasing frequency results in a spanwise distortion of the wing, forming a relatively high wing twist angle, which may explain the less-than-quadratic increase of the forces with the flapping frequency. The delayed motion of the wing surface due to the elastic behaviour of the wing results in the phase difference between the maximum power consumption and the maximum wing velocity, which is also simulated by means of a simplified mass-spring-damper system. The wing with the thinner surface membrane displays very similar characteristics to the baseline wing, which implies the dominance of the stiffeners in terms of providing rigidity to the wing. On the other hand, slightly smaller X-force generation of the thinner wing can be attributed to small differences in the wing profile properties.

4

Flow Visualization in the Wake and Around the Flapping Wings of the DelFly II in Hovering Flight Configuration

This chapter focuses on the experimental investigation of the vortical structures around and in the wake of the flapping wings of the DelFly II in hovering flight configuration employing two- and three-component (stereoscopic) planar particle image velocimetry measurements. The effects of flapping frequency and wing span length on the flow structures are analyzed by means of time-resolved flow fields acquired in two different experimental configurations.

4.1. Introduction

In the previous chapter, force generation and power consumption characteristics of the DelFly II flapping-wing motion have been analyzed by means of dedicated experiments. Furthermore, effects of some flapping and wing structural parameters, viz., wing-beat frequency, wing aspect ratio, wing surface thickness and stiffener orientation, on the force production of the flapping-wing motion were investigated. As a first step to explain the differences in the force generation in the aforementioned test cases, wing structural deformations were acquired during the time course of the flapping motion and differences in the wing profile properties were analyzed in a quantitative manner. However, to understand how these kinematics and deformation characteristics can be related to the aerodynamic force generation, it is required to acquire the unsteady flow fields around the wings and assess the effectiveness of the force generation mechanisms, particularly the leading edge vortex (LEV) and clap-and-peel motion.

The presence, benefits and stability of the LEV phenomenon have been investigated in many experimental studies on biological flyers and dynamically scaled robotic models, as discussed in Section 2.2.1. A number of different qualitative and quantitative flow measurement techniques were employed to visualize and analyze the LEV in these studies. It has been always challenging to perform accurate flow measurements in the vicinity of the flapping wings due to the unsteady nature of the phenomenon, which is further enhanced by three main factors in the case of the DelFly II flapping flight: (1) the shiny wing surface which is built from Mylar foil and causes significant reflections and glare once the vicinity of the wing is illuminated to perform PIV measurements; (2) the considerable amount of unsteady wing deformation that results in the time-variation of light blockage and reflection in the flow field; (3) the presence of two wings on each side of the fuselage that also interact with each other. All these factors can result in optical obstructions and saturation of the images in the vicinity of the wing due to glare and reflections, that may hinder the visualization of the LEV, as reported by de Clercq (2009). She performed time-resolved stereo-PIV measurements around the wings of DelFly II flapping at 13 Hz in hover configuration and showed that there is a strong influx into the gap between the wings during the peel phase, whereas there is no downward expelling jet during the clap. Although she was not able to provide a clear picture of the LEV during most part of the flapping motion due to optical obstruction, they supported its occurrence by the significant augmentation in lift generation. Later, Groen (2010) performed phase-locked stereo-PIV measurements to capture the flow fields in the vicinity of the flapping wings. In order to reduce the effects of the optical obscurities and laser-induced reflections, the illumination plane was aligned normal to the upper wing surface for a given phase of the flapping motion. By thus approach, the existence of an LEV during the flapping motion of the DelFly was revealed explicitly for the first time. The measurements were done also at different spanwise positions and it was shown that the LEV has a conical shape increasing in size from root to tip, up to approximately 86 % of the wing span. It was speculated that at this location, the LEV tube connects to the tip vortex and is bent toward the trailing edge. Moreover, the comparison of the flow fields around the original and improved wing configurations showed that the LEV stays closer to the wing surface for the improved wing, which was attributed to the increased suction during the peeling phase of the motion.

In addition to aforementioned experimental researches performed on the DelFly II

flapping-wing MAV, there are also other studies in the literature that aimed to explore the flow structures around flapping wings. Generally, the flapping motion is achieved by use of robotic models with MAV-scaled wings, which cannot fly by themselves but can mimic complex insect-based wing kinematics and operate at similar Reynolds numbers with the MAVs. Tarascio et al (2005) performed a flow-visualization study on a flapping rigid rectangular wing driven by such a mechanism. They coated the wings and driving mechanism with a thin black coating material (~ 0.02 mm) in order to reduce laser-induced reflections and glare. Consequently, they reported the presence of multiple vortices on the top surface of the wing during the translation phase of the motion. They showed that the LEV grows in the spanwise direction and the flow is rather separated at the outboard sections of the wing. Seshadri et al (2013) conducted an experimental study employing a rigid rectangular wing driven by a mechanism that is capable of emulating complex insect wing flapping kinematics. As a result of PIV and force measurements, they identified a strong LEV responsible for the significant increase in forces. They also pointed out that the strength of the LEV varies during the flapping cycle.

Evidently, the formation and behaviour of the LEV have a great influence on the generation of aerodynamic forces in flapping-wing flight. In the case of the DelFly II flapping motion, the presence of the mirror wing and wing-wing interaction occurring during the stroke reversal from instroke to outstroke (clap-and-peel motion) promotes the formation of the LEV as well as presumably generating a jet-flow structure as a result of the clapping motion. In this respect, it is aimed to explore the evolution of unsteady flow structures in the vicinity and wake of the DelFly II flapping wings in hover configuration via PIV measurements. Different from previous investigations on the DelFly, the wings were sprayed with a mat black paint to avoid excessive reflection caused by the Mylar foils. The PIV measurements were performed in two different configurations to capture the flow fields both around the wings and in the wake.

4.2. Experimental setup and data processing

4.2.1. Experimental setup

The experiments were performed in a quiescent environment by use of the balance mechanism with the ATI Nano-17 Titanium force sensor (see sections 3.1.2 and 3.2.2 for detailed information). A full-scale DelFly II model without a tail was used as an experimental model. The FPGA and the microcontroller systems were used in combination in order to acquire voltage and current fed to the motor, the Hall sensor output and the motor phase information, six components of forces and moments at a recording rate of 10 kHz. The flapping frequency was varied in the range of 9-12 Hz by use of the microcontroller system that was also utilized for the phase determination of the wings and synchronization of the PIV acquisition. A Chebyshev II low-pass filter with -80 dB attenuation of the stop-band was used to filter the raw force data in MATLAB (note that the forward-backward filtering technique was used to prevent time shift of data). The cut-off frequency was selected based on the flapping frequency to preserve only the first two harmonics of the X-force.

4.2.2. Time-resolved particle image velocimetry

Two different PIV measurement configurations were used in order to obtain the evolution of flow structures around and in the wake of the flapping wings. Three high-speed cameras (Photron FASTCAM, SA 1.1) were employed equipped with 60 mm Nikon lenses mounted on Scheimpflug adapters where required. The flow region under investigation was illuminated by a double- pulsed Nd:YFL laser (Quantronix Darwin Duo, wavelength, 527 nm). The laser sheet thickness was set around 2 mm. A SAFEX fog generator (DANTEC DYNAMICS Inc.) was used to generate a water-glycol based fog of droplets with a mean diameter of 1 µm. The measurement room was filled with the particles to achieve a homogenous seeding scenario. Double-frame images of tracer particles were captured at a recording rate of 200 Hz. A total of 200 to 600 images were taken for each measurement condition, such that in each case at least 10 flapping cycles are captured. By doing so, images from different flapping cycles with the same wing-beat frequency can be used to resolve one period with more non-dimensional time instants.

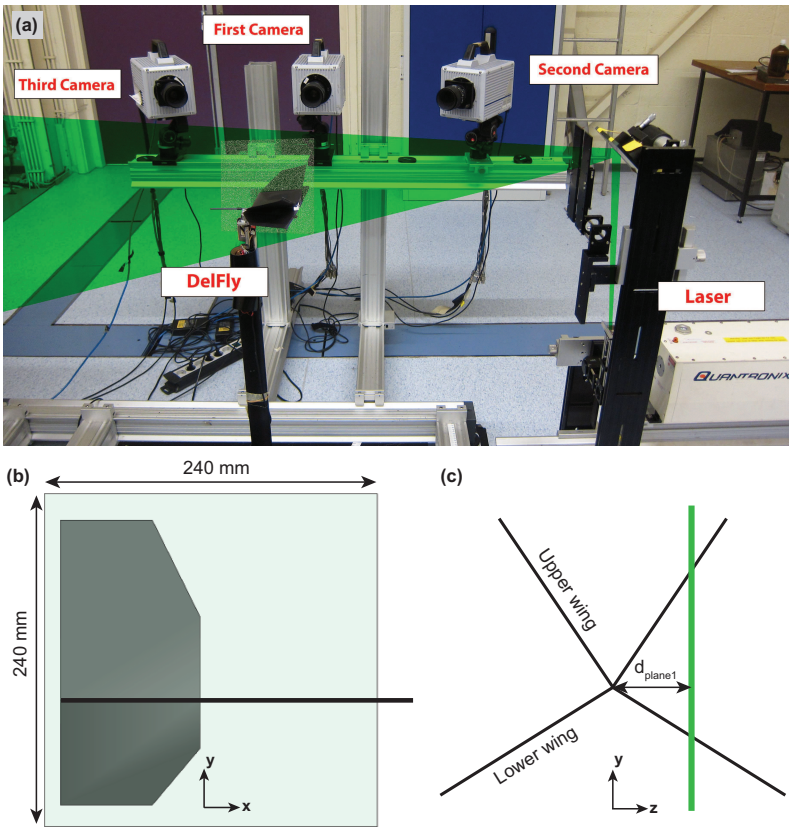

Figure 4.1: **a** First experimental setup to acquire time-resolved velocity fields in the vicinity of the flapping wings, **b** sketch of the side view of the DelFly II model with the measurement plane for the planar-PIV measurements, **c** sketch of the front view of the DelFly II model with the orientation of the measurement plane

The first setup was configured to acquire time-resolved flow fields around the wings on one side of the ornithopter. In this configuration, the measurement plane (laser plane) was oriented in the chordwise direction as illustrated in Fig. 4.1a. The cameras were arranged in the same horizontal plane as the experimental model at an angle of 40° with respect to each other. The three-camera setup was configured primarily for the stereo-PIV measurements. However, excessive reflections from the wing surface (particularly for the second camera as it was in the forward scattering mode) and optical obstruction (particularly for the third camera, vision of which was blocked by the wings) made it difficult to perform accurate stereoscopic calculations out of the three camera images for most phases of the flapping motion. Therefore, a planar-PIV approach was then followed by use of the images from the first camera, which was aligned normal to the laser plane. In this case, the field of view is 240 × 240 mm^2 (Fig. 4.1b) that was captured with a magnification factor of 0.85 at a digital resolution of 4.2 pixels/mm. The measurements were performed at 8 spanwise positions in a range from 40 to 180 mm distance from the wing root (d_{plane1}, see Fig. 4.1c). The laser plane was kept fixed and the complete balance mechanism was shifted for 20 mm to perform the measurements at different spanwise locations.

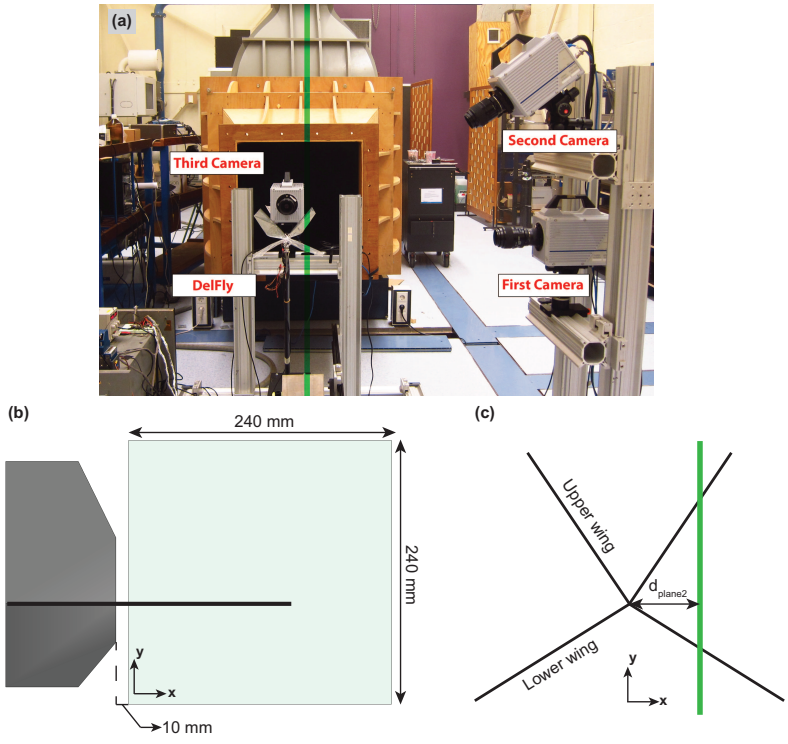

Figure 4.2: **a** Second experimental setup to acquire time-resolved velocity fields in the wake of the flapping wings in the chordwise oriented measurement planes, **b** sketch of the side view of the DelFly II model with the measurement plane for the stereo-PIV measurements, **c** sketch of the front view of the DelFly II model with the orientation of the measurement plane

In the second arrangement, the laser plane was aligned in the chordwise direction to capture the evolution of the spanwise oriented vortical structures (i.e., leading and trailing edge vortices) in the wake of the of the flapping wings (Fig. 4.2a). The measurement region was a square plane with the dimensions of 240×240 mm^2 (Fig. 4.2b) that was captured at a magnification factor of approximately 0.85. The measurement region was centered about an axis slightly above the fuselage of the DelFly model to cover the complete stroke amplitude of the wings and located at 10 mm downstream position from the trailing edge of the wings. The stereo-PIV measurements were performed at 10 spanwise positions by use of 2 high-speed cameras. The first measurement plane was aligned at 20 mm distance from the wing root (d_{plane2}, see Fig. 4.2c) on the right hand side of the model and the complete setup was shifted with an increments of 20 mm up to 200 mm from the wing root while keeping the laser plane fixed fo perform the measurements at different spanwise positions. The first camera was positioned at the same horizontal plane with the DelFly model, whereas the second camera was located above the model at 40° angle with respect to the first camera. The third camera was aligned at a normal view to the flapping wings in order to acquire phase angle of the wings at the PIV image acquisition instants.

The commercial software Davis 8.1.6 (LaVision) was used in data acquisition, image pre-processing, stereoscopic and planar correlation of the images, and further vector post-processing. For around-wing planar-PIV measurements, the pre-processed double frame images were interrogated using windows of final size of 64×64 pixels with two refinement step and an overlap factor of 75 % resulting in approximately 4096 vectors with a spacing of 3.8 mm in each direction.

4.3. Results and discussion

In this section, the results of the flow field measurements around the DelFly II model in hovering flight conditions are presented. First, the formation of the dominant flow structures are discussed based on the planar-PIV measurements performed around the flapping wings.

4.3.1. Flow structures around the flapping wings

The aim of the around-wing measurements is threefold: (1) to reveal the formation and subsequent behaviour of the spanwise oriented vortical structures (i.e., LEVs and TEVs); (2) to relate the vortex dynamics to the X-force generation; (3) to compare aforementioned formations between the cases with different flapping frequencies or different wing configurations (HAR10 and LAR10, see Fig. 3.21).

The resultant vector fields were overlapped with the corresponding image recordings of the camera to provide a combined view of the vortical structures and the position and shape of the wings at the same time. In these images, the black bands are used to mask the regions, which suffer from lack of illumination due to blockage of the wings or excessive reflection of the laser light. The vortices are labeled in order to better follow their behaviour throughout the images: each label reports the typology (LEV or TEV), the stroke phase (in and out for instroke and outstroke, respectively) and the wing to which they belong to (u and l for upper and lower, respectively).

Before proceeding to further discussion, there are some points that should be men-

tioned to facilitate interpretation of the results. The planar-PIV measurements in this case are used to visualize the vortical structures rather than providing a quantitative information due to two reasons: (1) the fixed vertical measurement plane does not intersect the wings at the same nominal spanwise position and at a right angle during the wing-beat cycle due to the curvilinear nature of the flapping motion; (2) the reflection of the laser light prevents proper measurements close to the wing surface. Due to the former, the angle between the transverse vortical structures and the measurement plane varies in time which results in the sampling of a vortex in sectional planes that are not parallel to the main axis of the vortex at a given spanwise location. Furthermore, due to dihedral angle of the wings, the relative orientation of the upper and lower wings with respect to the measurement plane is different at a given phase of the flapping motion. This hinders the comparison of vortical structures of the two wings in terms of their strength at a certain measurement instant.

Contours of non-dimensional out-of-plane vorticity (ω_z/f) are plotted in a plane that is located at 100 mm from the fuselage of the DelFly (d_{plane1} = 100 mm) for six instants of the flapping motion at 11.2 Hz (Fig. 4.3). The measurement plane position corresponds to approximately $0.73R$ when the stroke angle is zero (i.e., when the wings are fully closed at the end of instroke). At the flapping instant A (t^* = 0.13 and $\Phi = 53.8°$), the wings are moving in the instroke direction with the leading edge vortices ($\text{LEV}_{\text{in-u}}$ and $\text{LEV}_{\text{in-l}}$) apparent in the vicinity of the wing leading edges. The trailing edge vortices of the previous instroke ($\text{TEV}_{\text{in-u}}$ and $\text{TEV}_{\text{in-l}}$) are still present in the far wake. There are also relatively small-scale vorticity contours in the near wake, which are probably the LEVs and TEVs of the outstroke phase. The time stage B (t^* = 0.28 and $\Phi = 28.9°$) corresponds to the maximum X-force generation instant of the instroke phase. The LEVs are now more elongated along the surface of the wings. A close inspection on the lower wing, which is oriented almost perpendicular to the measurement plane at this time instant, reveals that the positive vorticity contours cover the complete wing surface and there is another blob of vorticity close to the trailing edge, which indicates a formation of multiple LEVs at the early phases of the instroke. At the start of the outstroke (C, t^* = 0.49 and $\Phi = 1.0°$), the wings are nearly in their non-deformed state and parallel to each other. At this stage of the motion, the X-force generation is at the local minimum level between the force peaks of the instroke and the outstroke. This can be attributed to the wings being relatively stationary and their small surface area oriented in the streamwise direction, which also results in better illumination conditions in the wake and provide a clear picture of the wake structures. The LEVs generated during the instroke ($\text{LEV}_{\text{in-u}}$ and $\text{LEV}_{\text{in-l}}$) are shed and moved upstream with their induced velocities in the form of a vortex pair. The trailing edge vortices generated during the instroke phase ($\text{TEV}_{\text{in-u}}$ and $\text{TEV}_{\text{in-l}}$) are present in the wake forming a horizontally-oriented mushroom-type vortical structure. This vortical formation in combination with the clapping motion of the wings induces a positive streamwise velocity and generates a momentum-surfeit wake velocity profile, which is evident from the contours of positive non-dimensional streamwise velocity ($V_x/V_{m,tip}$) in the near wake of the wings as shown in Fig. 4.4. On the other hand, the LEV pair induces a negative streamwise velocity which results in a slight momentum-deficiency at the upstream conditions. This momentum increase is essentially indicative of force generation in the negative x direction (i.e., positive X-force in the DelFly body coordinate system in hovering configuration).

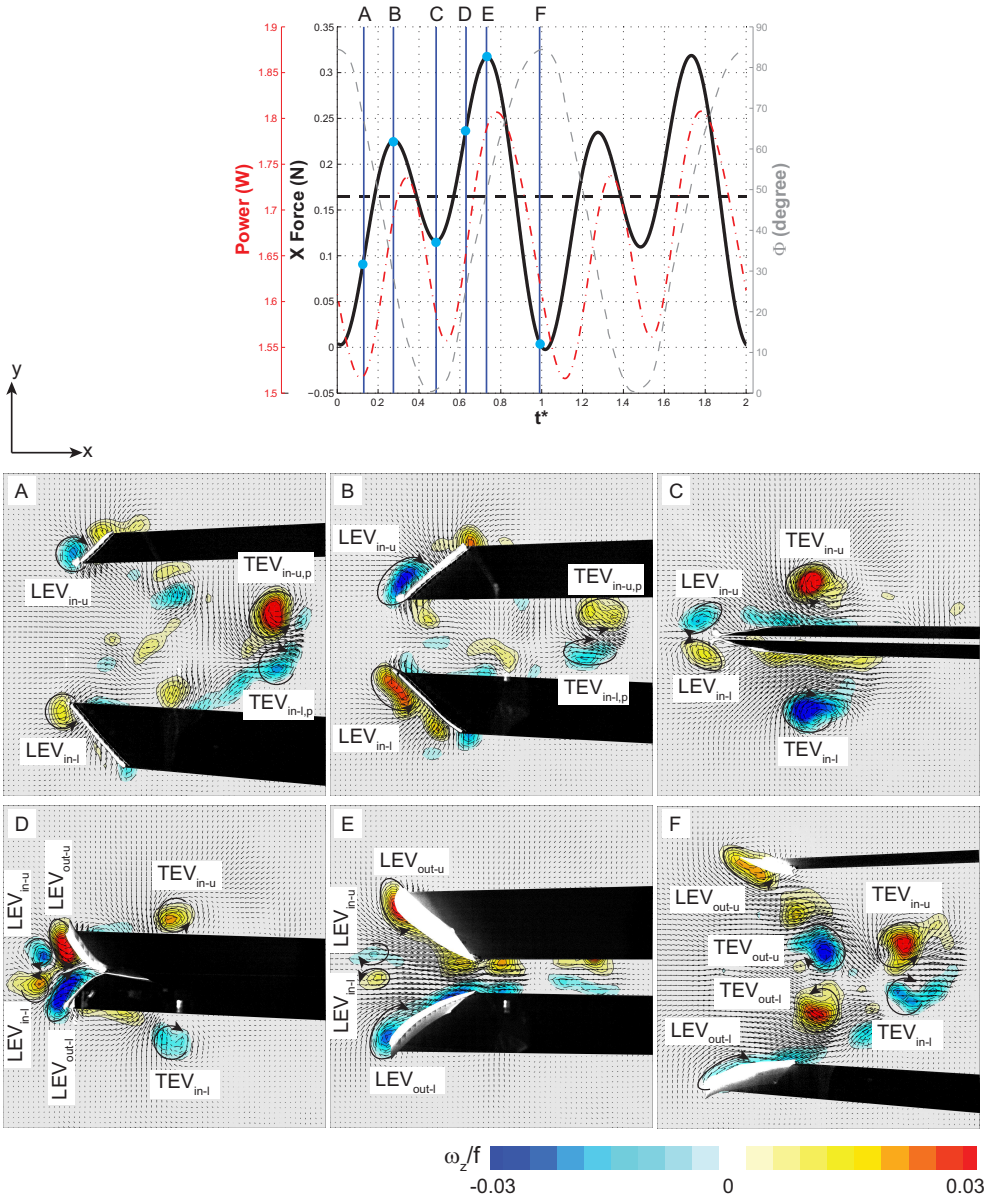

Figure 4.3: Temporal variations of the X-force (*black line*) and power consumption (*dash-dot red*) plotted for two periods of the flapping motion for the flapping frequency of 11.2 Hz in hover configuration of the DelFly with Ref10 wings complemented with the variation of the stroke angle (Φ, *dashed gray*) and the flap-averaged X-force value (*dashed black*)(*top*); contour plots of the non-dimensional out-of-plane vorticity (ω_z / f) in a chordwise oriented plane at 100 mm distance from the fuselage (d_{plane1} = 100 mm, see Fig.4.1c) at six instants of the flapping cycle

Indeed, the comparison of the force generation levels of the flapping motion at the two stroke reversals shows that the X-force is significantly higher while turning from instroke to outstroke. This can be explained by the formation of a streamwise momentum jet (i.e., downward momentum jet in the case of actual hovering condition) by the wing-wing interaction (clapping motion) and the interaction between the flow structures of the upper and lower wings. As the motion progresses in the peeling phase (D, $t^* = 0.63$ and $\Phi = 27°$), two massive LEVs ($LEV_{out\text{-}u}$ and $LEV_{out\text{-}l}$) appear in the gap between the two wings, which occupy the peeled wing surface regions of both wings completely (note that the lower wing intersects the measurement plane at nearly a right angle also at this phase of the flapping motion so that presumably the $LEV_{out\text{-}l}$ is also cut off at a right angle). The rapid build-up of circulation for the LEVs can be attributed to the inrush of the surrounding fluid to the low-pressure region in the cleft formed between the two wings as they peel apart (see the corresponding plot in Fig. 4.4). The LEVs of the instroke interact with the newly formed LEVs of the outstroke and generates a dynamic region ahead of the flapping wings. First, the LEVs of the instroke and outstroke for both wing induce a velocity component directed toward the cleft between the wings. Second, the vortex pairs of the two strokes induce velocities in the opposite direction along the mid-line of the wings: the $LEV_{in\text{-}u}$ and $LEV_{in\text{-}l}$ induce a negative V_x velocity in the region between them, whereas those generated at the beginning of the outstroke induce a positive V_x velocity, which results in the formation of a small region where two velocity components cancel each other out. As a result, these two effects form a tilted v-shaped streamwise velocity pattern that elongates into the gap between the wings (see Fig. 4.4-D).

The influence of the instroke LEVs on the force production at the beginning of the outstroke can be evaluated in different aspects. First, the presence of a counter-rotating vortex in the vicinity of the wing may inhibit the growth of the new LEV and may cause a delay in the production of forces, analogous to the Wagner effect. On the other hand, the resultant induced velocity region may also create relatively favourable conditions in terms of force generation by aligning the entrained velocity vector with the wings and preventing excessive decrease of the effective angle of attack of the wings in the stroke direction (i.e., y direction). The relation between the behaviour of the instroke LEVs and the X-force production can be intepreted by use of the vorticity moment theory (Wu, 1981), which calculates the force exerted on a body based on the time rate of change of the total first moment of the vorticity field in the complete fluid domain (for a thin body) in an inertial coordinate system. In this respect, an LEV that is attached to the wing (so that the moment arm is increasing in time as it moves with the wing) with its circulation increasing in time will have a constructive effect on the force generation since the moment of vorticity has an increasing trend. When a single flapping wing is considered with the associated vortical formations at the beginning of the outstroke, it is obvious that the effect of the instroke LEV would be destructive (opposite to the effect of the outstroke LEV) if it moved with the wing or increased in strength. However, looking at the consecutive time instants of the outstroke phase (Fig. 4.3 C, D and E), the LEVs of the instroke phase stay rather stationary in front of the flapping wings. Although it is difficult to interpret the change of their circulation levels accurately in time, it is plausible to presume that they get weaker during the outstroke. It can be concluded that their presence does not cause significant reduction or change in the forces based on the vorticity moment theory, yet their indirect

effect on the forces by affecting the formation and growth of the other flow structures is not completely resolved. The maximum force generation occurs at the instant E (t^* = 0.73 and Φ = 51°). The LEVs of the instroke are still situated in front of the flapping wings but their vorticity levels are clearly reduced at this stage. In relation to this, the negative velocity region induced by this vortex pair has also vanished, which is evident in Fig. 4.4. There is a strong inflow pattern toward the gap between the wings with magnitudes reaching the mean wing-tip velocity, which generates low pressure on the inner surface of the wings and enhancing the force production. There are two concentrated vorticity contours in the vicinity of the leading edges of the both wings representing the LEVs, but it is also evident that the associated vorticity contours elongate toward the trailing edge and even to the near wake. Probably, some amount of LEV vorticity, which is rapidly built up at the beginning of the outstroke, advects along the wing surface and sheds into the wake due to the strong flow pattern between the wings. Close to the end of the outstroke (F, t^* = 0.98 and Φ = 85°), the X-force decreases to the minimum of the complete flapping cycle in correlation with the wings slowing down and reaching their non-deformed state. It is difficult to comment on the LEV formations at this instant due to the oblique orientation of the wings with respect to the measurement plane. However, the wake velocity field reveals that prominent TEVs form and shed during the outstroke contrary to what is hypothesized in the literature regarding the benefits of the clap-and-fling motion. It is possible that the formation of TEVs is delayed with respect to LEVs because of the fact that the trailing edges of the wings completes stroke reversal later than the leading edges as discussed in Section 3.4. This essentially means that the lower-chord region of the wings performs a clapping motion while the leading edges move in the peeling phase.

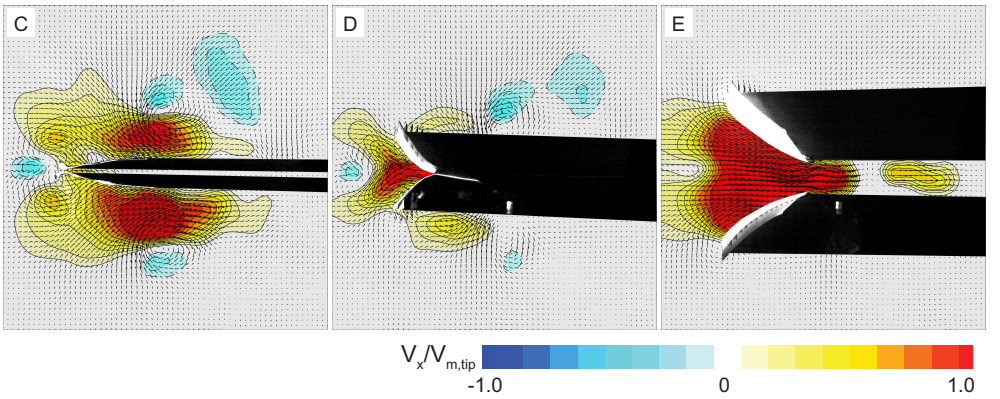

Figure 4.4: Contour plots of the non-dimensional streamwise velocity ($V_x/V_{m,tip}$) in a chordwise oriented plane at 100 mm distance from the fuselage (d_{plane1} = 100 mm, see Fig.4.1c) at three instants of the clap-and-fling phase for the DelFly with Ref10 wings flapping at 11.2 Hz

In order to assess the spanwise variation of the flow structures, contours of non-dimensional out-of-plane vorticity are plotted in chordwise oriented planes at three different spanwise locations for t^* = 0.28 in Fig. 4.5. This time instant corresponds to the maximum X-force generation point of the instroke phase (B, see Fig. 4.3) and it is selected deliberately since the lower wing is oriented normal to the measurement plane, which will

allow to assess spanwise characteristics of $LEV_{in\text{-}l}$ more accurately. It is clear that at the inner measurement plane location (d_{plane1} = 60 mm), the LEV appears rather small both in size and strength. Moreover, there is a clear evidence that the LEVs of the outstroke ($LEV_{out\text{-}u}$ and $LEV_{out\text{-}l}$) are shed and advect downstream in the region between the wings contrary to the LEVs of the instroke, which move upstream with their induced velocities at the end of the instroke. Moving toward the wing-tip, the size and circulation level of the LEV increases such that the LEV covers the complete wing surface at the outer measurement plane location, that corresponds to $0.86R$ position of the lower wing at this instant. This indicates a conical LEV structure as also reported by Groen et al (2010).

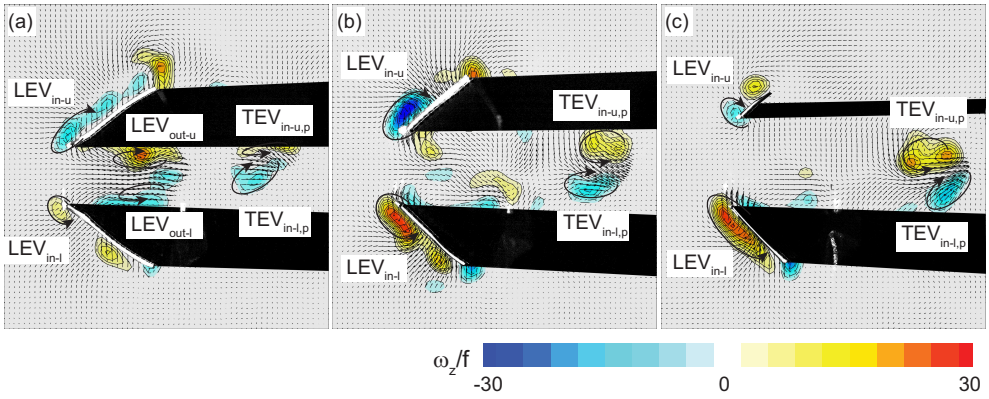

Figure 4.5: Contour plots of the non-dimensional out-of-plane vorticity (ω_z/f) in chordwise oriented planes at three different spanwise positions: **a** 60 mm distance from the fuselage (d_{plane1} = 60 mm), **b** 100 mm distance from the fuselage (d_{plane1} = 100 mm), **c** 120 mm distance from the fuselage (d_{plane1} = 120 mm) at t^* = 0.28 for the DelFly with Ref10 wings flapping at 11.2 Hz

Comparison of the measurements at different spanwise positions at t^* = 0.63 (i.e., the other time instant when the lower wing is oriented normal to the measurement plane during the outstroke) reveals that there are prominent differences in the formation of the flow structures (Fig. 4.6).

First, different TEV shedding characteristics can be observed at different measurement planes such that there are two discrete vortex structures at the innermost spanwise position (d_{plane1} = 60 mm) and no out-of-plane vorticity contours representing the TEVs at the outer spanwise position (d_{plane1} = 120 mm). The large shadow region in the wake and the three-dimensional nature of the flow structures, while the measurement technique is limited to acquire velocity components in a two-dimensional plane makes it difficult to interpret this vortex shedding behaviour. Second, the LEVs of the instroke phase are found in front of the flapping wings at the first two measurements planes (viz., d_{plane1} = 60 mm and 100 mm) and interact with the newly formed outstroke LEVs, whereas they are not present in the outer measurement plane. Indeed, similar to the inner measurements planes, the instroke LEVs are shed and advected upstream at the previous time steps in this measurement plane, yet probably they tilt into a different direction and cannot be captured by means of ω_z contour plots. The vortex tilting affects the streamwise flow pattern toward the gap between the wings as shown in Fig. 4.7c.

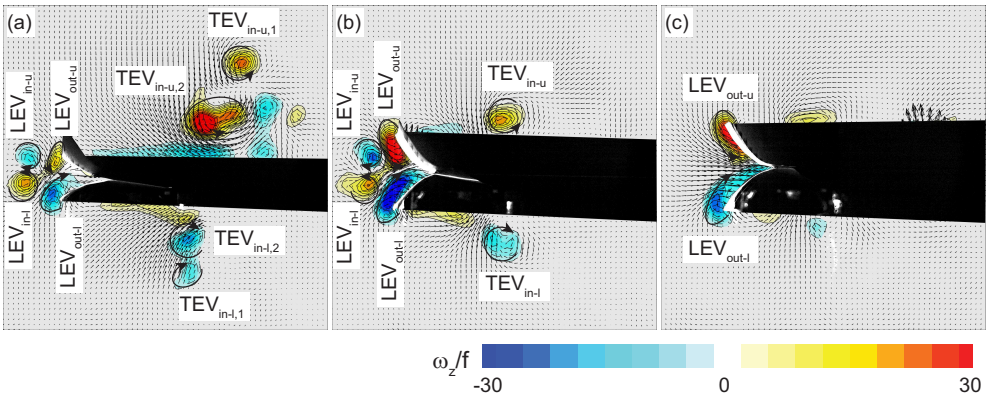

Figure 4.6: Contour plots of the non-dimensional out-of-plane vorticity (ω_z/f) in chordwise oriented planes at three different spanwise positions: **a** 60 mm distance from the fuselage (d_{plane1} = 60 mm), **b** 100 mm distance from the fuselage (d_{plane1} = 100 mm), **c** 120 mm distance from the fuselage (d_{plane1} = 120 mm) at t^* = 0.63 for the DelFly with Ref10 wings flapping at 11.2 Hz

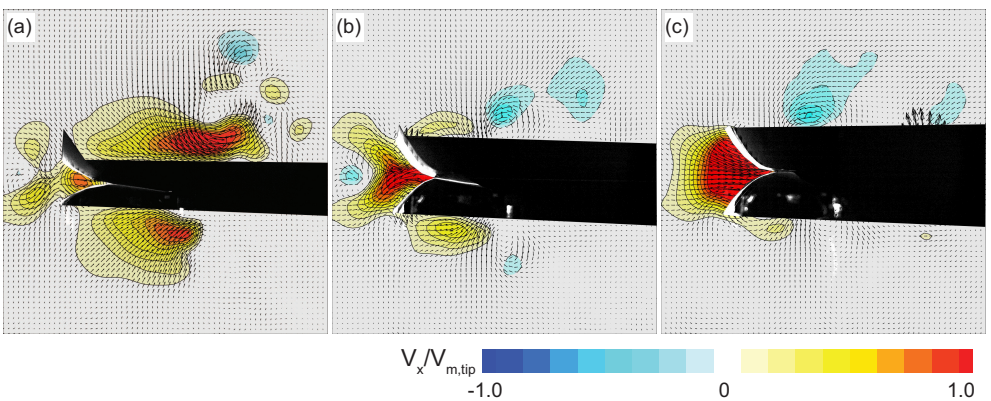

Figure 4.7: Contour plots of the non-dimensional streamwise velocity ($V_x/V_{m,tip}$) in chordwise oriented planes at three different spanwise positions: **a** 60 mm distance from the fuselage (d_{plane1} = 60 mm), **b** 100 mm distance from the fuselage (d_{plane1} = 100 mm), **c** 120 mm distance from the fuselage (d_{plane1} = 120 mm) at t^* = 0.63 for the DelFly with Ref10 wings flapping at 11.2 Hz

The flow pattern toward the cleft between the wing is clearly influenced by the presence and the strength of the instroke LEVs. Relatively weak instroke LEVs at the inner spanwise position cannot induce a negative velocity in the x direction. On the other hand, the absence of the counter-rotating instroke LEV pair at the outer position results in a fairly uniform flow pattern upstream of the peeling wings. The increased velocity levels between the wings is basically beneficial in terms of force generation; however, this pattern probably decreases the effective angle of attack of the wings and brings about slightly decreased amount of circulation accumulated in the LEV (see $\text{LEV}_{\text{out-l}}$ in Fig. 4.6b and c).

Flapping at a lower frequency (9.2 Hz) does not cause prominent differences in the vortex formations in the measurement plane located at d_{plane1} = 100 mm (Fig. 4.8). Obviously,

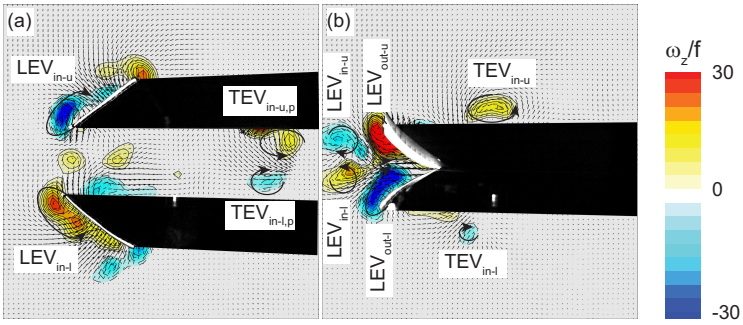

Figure 4.8: Contour plots of the non-dimensional out-of-plane vorticity (ω_z/f) in a chordwise oriented planes a 100 mm distance from the fuselage (d_{plane1} = 100 mm) at **a** t^* = 0.28 and **b** t^* = 0.63 for the DelFly with Ref10 wings flapping at 9.2 Hz

a smaller amount of vorticity is generated, which scales more-or-less with the flapping frequency, as evident from the similarities between the non-dimensional vorticity contours of 9.2 and 11.2 Hz flapping frequency cases (see corresponding phases in Figs. 4.8 and 4.3).

It was shown in Fig. 3.26 that the HAR10 wings generate significantly higher force than the Ref10 wings at a given flapping frequency albeit with a phase delay. Visualization of the flow features of the HAR10 wings flapping at 11 Hz at a plane that is located 120 mm from the fuselage (corresponding to 0.76R position when the stroke angle is zero) at two different instants of the flapping motion (i.e., t^* = 0.28 and 0.63) reveals that qualitatively similar vortical structures are generated during the flapping motion (Fig. 4.9). During the instroke (Fig. 4.9a), prominent LEVs with comparable magnitudes to those in the Ref10 case are present near the wing surfaces. On the other hand, the instroke structures appear slightly weaker (Fig. 4.9b). This can be perhaps due to delayed build-up of the circulation levels, which can be inferred from the time shift in the variation of the forces (Fig. 3.26a).

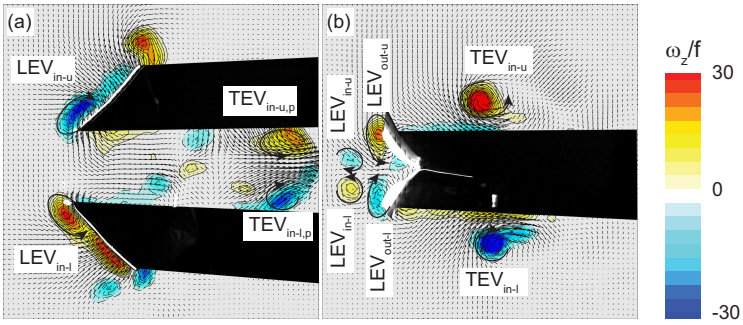

Figure 4.9: Contour plots of the non-dimensional out-of-plane vorticity (ω_z/f) in a chordwise oriented plane at 120 mm distance from the fuselage (d_{plane1} = 120 mm) at **a** t^* = 0.28 and **b** t^* = 0.63 for the DelFly with HAR10 wings flapping at 11 Hz

4.3.2. Flow field in the wake of the flapping wings

Aerodynamic mechanisms in flapping-wing flight, determined by different aspects of the flapping motion such as sweeping, pitching and clap-and-peel, leave their footprints in the form of structures that are shed into the wake. In this context, the wake formations can deliver important clues about the force production characteristics of the flapping motion. This section presents the results for the wake flow field measurements that were performed for a selection of parameters.

Figure 4.10 illustrates the evolution of wake flow structures in a chordwise oriented plane at 100 mm distance from the fuselage (d_{plane2} = 100 mm, see Fig. 4.2c) for the flapping frequency of 11 Hz at four time instants in the flapping cycle (t^* = 0.28, 0.49, 0.73 and 0.98, corresponding to B, C, E and F in Fig. 4.3)). In order to provide a clear representation of the wake velocity profiles, velocity vectors are plotted once at every six streamwise measurement points. The region with poor imaging conditions and hence less reliable velocity vectors due to presence of the balance system is covered with a gray band in the vector fields.

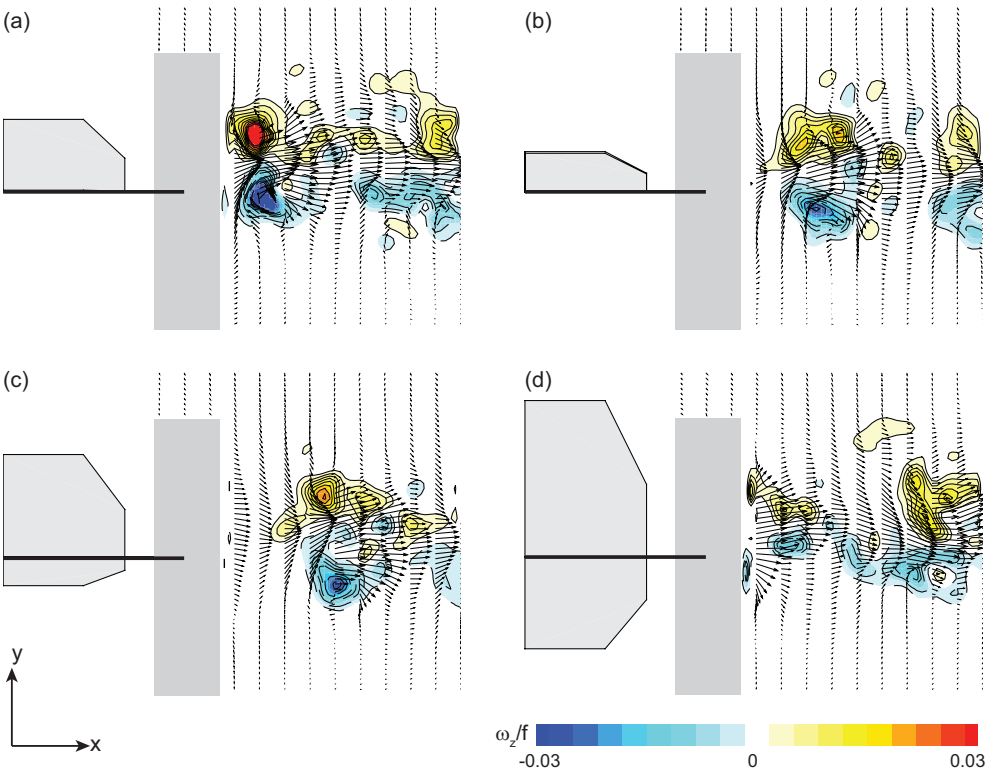

Figure 4.10: Contour plots of the non-dimensional out-of-plane vorticity (ω_z/f) in a chordwise oriented plane at 100 mm distance from the fuselage (d_{plane2} = 100 mm) at **a** t^* = 0.28, **b** t^* = 0.49, **c** t^* = 0.73 and **b** t^* = 0.98 for the DelFly with Ref10 wings flapping at 11 Hz

In this measurement plane, there are two major flow structures present throughout the flapping motion. These are the trailing edge vortices of the upper and lower wings that are formed during the instroke and shed during the clapping phase. They convect downstream as a counter-rotating vortex couple and induce a prominent positive streamwise velocity (x-velocity) in the region between them. Their projection views on the chordwise plane grow larger and become more fragmented (compared to their coherent views at $t^* = 0.28$ as shown in Fig. 4.10a) while moving downstream and their spanwise vorticity (ω_z) levels decrease, which can be attributed to the diffusion and tilting of the vortices. In addition to these vortex formations, the clapping motion of the wings also induces a streamwise velocity in the form of a jet velocity profile. It is better visible at the time step of $t^* = 0.98$ (Fig. 4.10d) when the counter-rotating TEV couple is not still in the field of view but the clapping-induced velocity profile is apparent in the first vector column after the gray region. The induced streamwise velocities in this measurement plane reach approximately 1.6 times the mean wing-tip velocity during a flapping cycle at $1\overline{c}$ distance downstream from the trailing edges of the wings (Fig. 4.11). The maximum velocity is achieved during the passage of the counter-rotating vortex pair so that it occurs with a phase delay at further downstream locations. In correlation with the decrease of the vorticity levels, the amplitude of the oscillations also decay in the downstream direction. For all three positions, the streamwise velocity shows a periodic variation indicating periodic behaviour of the wake flow structures. The main frequency component is the one at the frequency of the flapping motion (associated to the shedding of the instroke TEVs once in every flapping cycle) yet there is also secondary humps which are more evident at further downstream locations.

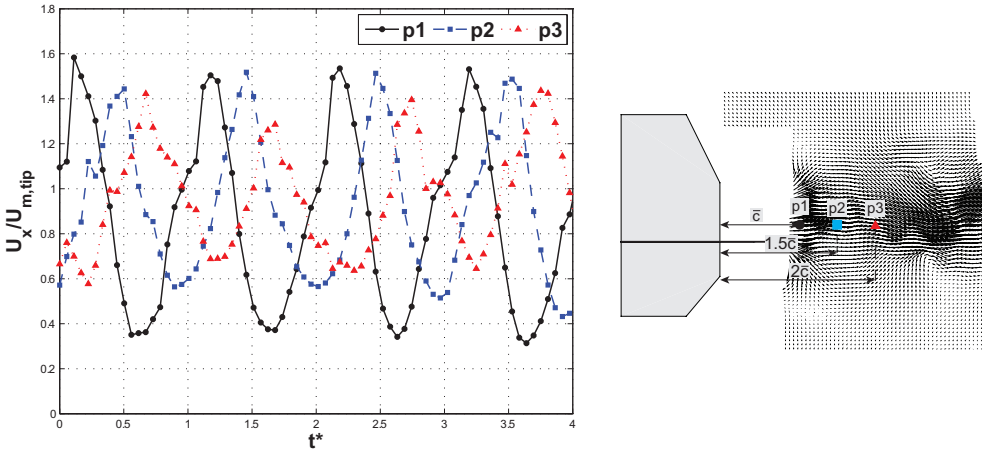

Figure 4.11: Temporal variation of the nondimensional x-velocity component ($U_x/U_{m,tip}$) measured at three different streamwise positions aligned with the bisector of the wings plotted for four periods of the Ref10 wings flapping at 11 Hz (*left*); streamwise positions of the probe points (*right*)

In order to better visualize the wake flow structures, three-dimensional wake of the flapping wings is reconstructed by use of the experimental data that were captured at the measurement planes positioned at a number of spanwise locations ($d_{\text{plane2}} = 20$ to

200 mm). Then, a modified Kriging regression technique (see Section 5.2.3) is utilized in order to reconstruct the three-dimensional wake structures with a spanwise spatial resolution that is higher than that of the PIV measurements. Wake formations for two instants of the flapping motion are shown in Fig. 4.12. Three-dimensional wake reconstruction results also confirm the presence of a counter-rotating vortex couple that is shed at the end of the instroke. This vortical formation is slightly tilted with respect to the z axis and aligned with the dihedral of the wings. In addition to these vortices, there is another vortical structure that is aligned rather vertically and shed at the end of the outstroke. This arrow-shaped structure is comprised of mainly y-vorticity, thus it does not emerge in the chordwise oriented measurement planes.

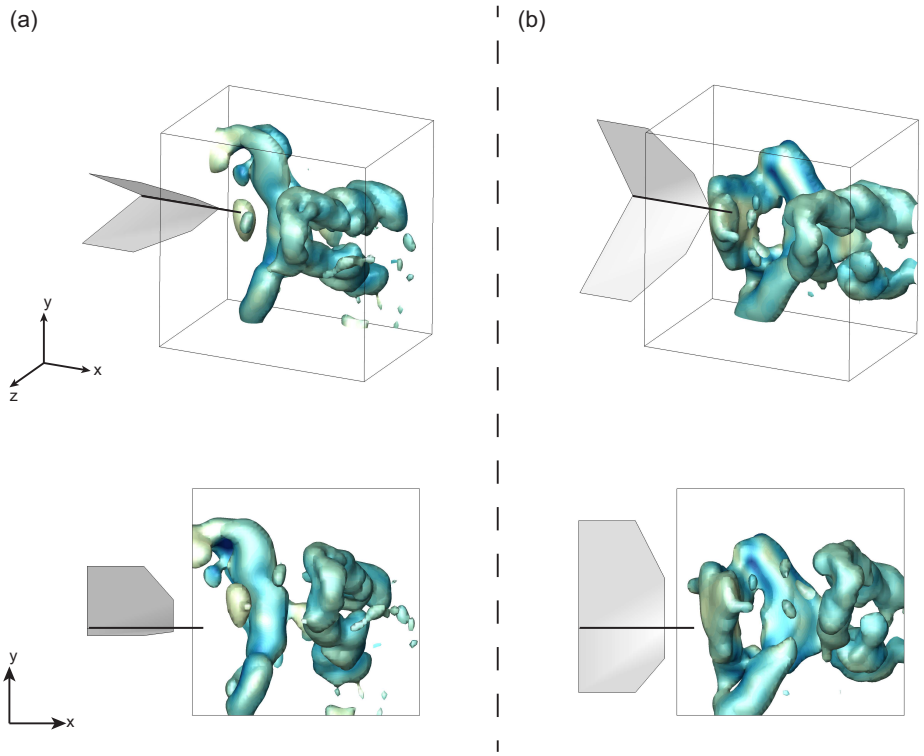

Figure 4.12: Perspective (*top*) and side view (*bottom*) of the wake structures visualized by isosurfaces of $Q/f^2 = 8$ and coloured by vorticity magnitude for the DelFly with Ref10 wings flapping at 11 Hz at two instants of the flapping motion: **a** $t^* = 0.6$ and **b** $t^* = 0.98$

The wake velocity information is also utilized in an attempt to estimate the aerodynamic X-force by means of a momentum-based approach. In this process, a control volume is defined (Fig. 4.13a) such that the upstream and downstream boundaries are assumed to be far enough to have the static pressure being equal to ambient pressure. The upstream boundary is positioned at an arbitrary location with a zero-inflow assumption

in the hovering flight configuration. The downstream boundary is located at $2.5\overline{c}$ distance from the wing trailing edge. The upper and lower boundaries of the control volume coincides with the boundaries of the measurement region where velocities are negligibly small. The right and left control surfaces are determined by the first and the last measurement plane in the spanwise direction (d_{plane2} = 20 and 200 or 220 mm for the close-root and outer-most measurement planes, respectively) and in these locations it is assumed that the effect of the flapping motion is significantly reduced. The internal boundary of the control volume, on the other hand, encompasses the flapping wings.

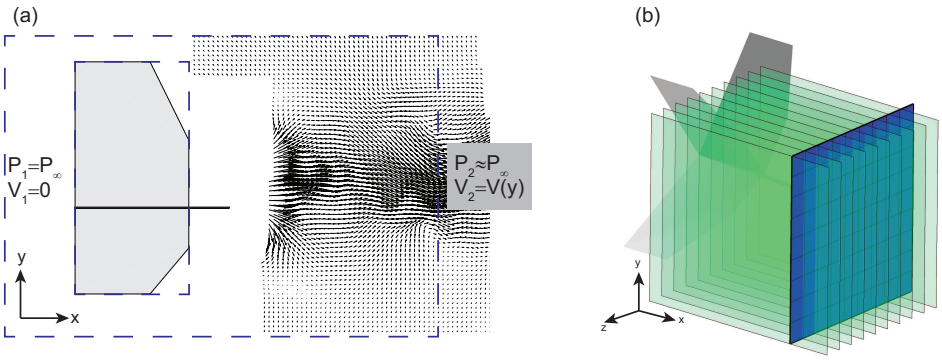

Figure 4.13: a Boundaries of the control volume (*dashed blue*) used for the estimation of the aerodynamic forces in a side view, b streamwise oriented measurement planes (*green*) and downstream surface of the control volume (*blue*) formed from the velocity vectors of the measurement planes at $2.5\overline{c}$ streamwise distance from the trailing edge

Velocity vectors at the downstream control surface are acquired from the chordwise oriented measurement planes. The momentum equation applied to the fluid flow in the fixed control volume reads:

$$\frac{\partial}{\partial t}\iiint_{\mathcal{V}} \rho\vec{V}\,\mathrm{d}\mathcal{V} + \oiint_{S} \rho\vec{V}\left(\vec{V}.\vec{n}\right)\mathrm{d}S = -\oiint_{S} p\vec{n}\mathrm{d}S + \vec{\mathrm{F}}_{\text{body}} + \vec{\mathrm{F}}_{\text{viscous}} \tag{4.1}$$

where ρ is the fluid density, $\vec{V}$ is the velocity, $\mathcal{V}$ stands for the control volume, S for the control surface and $\vec{n}$ is the normal vector to the control surface. A number of assumptions and simplifications are made for the calculation of the X-force. Since it is assumed that pressure is equal to the ambient pressure, the first term on the right side of Eq. 4.1 drops out around the outer control surface. The viscous effects are also neglected for the outer boundary. Pressure and viscous forces around the inner control surface gives the total force applied to the fluid by the flapping wings. Here, the main focus of interest is the X-force component of the total force experienced by the wings, which is equal and opposite to that exerted on the fluid in regard to Newton's third law. It is now necessary to calculate the left hand side of the equation, where unsteady and flux terms are present, respectively. It is clear that the unsteady term requires the knowledge of the complete velocity field (particularly V_x for the calculation of the X-force) and its temporal evolution

inside the control volume. As it is not available from the present measurements, another simplification is made to exclude the unsteady term. The flapping wings are replaced with an imaginary thin body rotating at a constant speed, which is essentially analogous to the actuator disk theory. It is clear after this assumption that it is not possible to obtain the time-history of the forces within a flapping cycle yet it is aimed to calculate the flap-averaged aerodynamic X-force. Taking into account there is no body force applying in the x direction, Eq. 4.1 simplifies to:

$$\mathrm{X} = \oiint_S \rho \left(V_{2,x}\right)^2 \mathrm{d}S \tag{4.2}$$

where $V_{2,x}$ is velocity in the x direction measured in the downstream control surface. Note that X stands for the X-force applied on the DelFly, which is defined in the DelFly body axis (i.e., opposite to the x axis of the flow coordinate system). The X-force that is calculated by use of wake velocity profiles on one side of the DelFly is multiplied by two to account for the other half of the wake. The resultant flap-averaged X-force values for different wings used in the wake measurements are shown in Fig. 4.14 (red). They are compared to the mean X-force values measured with the force sensor. In general, there is a good agreement in the trends, albeit that the control volume approach results in an under-estimation of the forces. The maximum error is 15 %, which occurs for the HAR10 wing. The error decreases down to 6 % of the sensor-measured values for the LAR10 wing. The larger error in the case of the HAR10 wing can be attributed to lack of measurement planes outwards from the wing tip. The last measurement plane was positioned at 220 mm from the wing root while half-span length of the HAR10 wing is $R = 160\ mm$. This implies that the momentum flux through the left-hand-side (i.e., wing-tip-side) control surface should be taken into account for a more accurate calculation. On the other hand, the outwards measurement plane distance is 180 mm for the LAR10 wing (R = 120 mm), which may account for the better correspondence in this case. In general, the momentum-based approach in a control volume for the estimation of the X-force shows a good performance so that it can serve as an alternative method for the determination of aerodynamic forces in flapping wing applications when direct measurements with a force sensor is not feasible (e.g., in free-flight or in cases when the sensor measurements are interfered by strong inertial components or structural vibrations).

4.4. Conclusions

The temporal evolution of vortical structures around the wings and in the wake of the flapping-wing MAV DelFly II has been investigated by means of two- and three-component planar PIV measurements. Experiments were performed in two different configurations, which were realized to acquire time-resolved flow fields around the flapping wings and in the wake, respectively. Simultaneous force measurements were conducted in order to obtain the relation between the flow structures and unsteady forces.

Flow visualizations around the flapping wings reveal the presence of conical LEVs on both wings during the instroke and outstroke. The LEV that is formed during the outstroke forms and grows rapidly at the onset of this phase. They interact with the LEVs of the previous instroke that are shed and advected upstream with their induced velocities. This

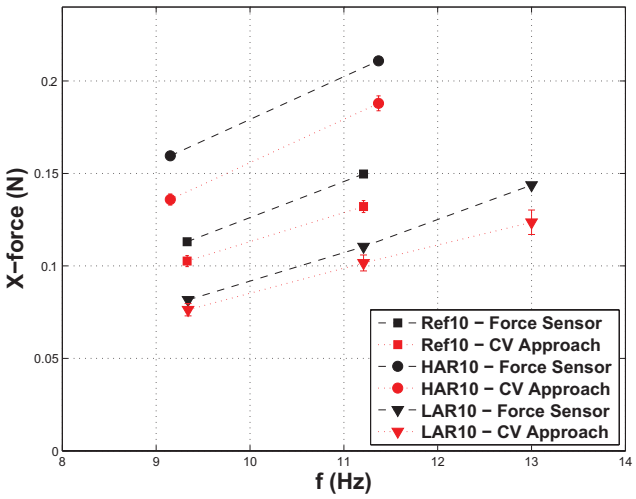

Figure 4.14: Flap-averaged X-force measured with the force sensor (*black*) and estimated with the momentum-based approach in a control volume (*red*) for the Ref10, HAR10 and LAR10 wings at different flapping frequencies

vortex behaviour results in the modification in the streamwise velocity profile (V_x) that is generated at the beginning of the peeling phase and directed toward the cleft between the wings. This velocity component reaches to a level as much as the mean wing tip velocity in the region between the wings, whereas its magnitude is significantly lowered upstream of the wings due to the induced velocities of the instroke LEVs. It is hypothesized that the particular vortex shedding behaviour and interaction between the LEVs of the instroke and outstroke prevents reduction of the effective angle of attack in the stroke direction (i.e., sweeping motion direction). The low pressure region formed between the wings and the rapid growth of the LEVs during the peeling phase are likely reasons for the elevated forces of the outstroke. On the other hand, the formation of a momentum jet due to the clapping motion and the velocity pattern induced by the instroke TEV couple result in the generation of a momentum surfeit wake, that accounts for the higher X-force generated at the end of the instroke compared to that of the outstroke. Flapping at a lower frequency does not cause significant differences in the vortex behaviour yet less amount of vorticity is generated, which scales with the flapping frequency. For the HAR10 wing, the growth of the LEV is delayed compared to the Ref10 wing in correlation with the phase delay between the force histories of the two cases.

Flow field measurements in the chordwise oriented measurement planes in the wake show that there are two major structures, i.e., TEVs shed from both wings during the instroke phase. They convect downstream as a counter-rotating vortex couple and induce a positive streamwise velocity in the wake. The wake velocity information is also utilized to estimate the aerodynamic X-force generated by the flapping wings. A momentum-based approach is used in a control volume that encompasses the flapping-wing pair on one side of the DelFly. The estimated forces are compared to those measured with the force sensor. It is shown that there is a reasonable agreement in the observed trends, although the

momentum-based approach underestimates the X-force with a maximum error of 15 %, which occurs for the HAR10 wing. This is attributed to insufficient lateral size of the control volume, which is determined by the number and position of the measurement planes, for the assumptions to hold in the case of the HAR10 wing which has a larger span. On the other hand, the method estimates the forces for the Ref10 and LAR10 wings in an error range of 5 - 10 %. In this respect, the momentum-based approach for the estimated on forces by use of wake velocity information offers good potential such that it can be used in free-flight conditions or it can be utilized when the force sensor measurements are not feasible or reliable.

5

Flow Visualization in the Wake of the DelFly II in Forward Flight Configuration

This chapter investigates the formation and evolution of the unsteady three-dimensional wake structures generated by the flapping wings of the DelFly II Micro Aerial Vehicle (MAV) in forward flight configuration. Time-resolved stereoscopic particle image velocimetry (stereo-PIV) measurements were carried out at several spanwise-aligned planes in the wake, to allow a reconstruction of the temporal development of the wake of the flapping wings throughout the complete flapping cycle. Simultaneous thrust-force measurements were performed to explore the relation between the wake formation and the aerodynamic force generation mechanisms. The three-dimensional wake configuration was subsequently reconstructed from the planar PIV measurements by two different approaches: 1) a spatio-temporal wake reconstruction obtained by convecting the time-resolved three-component velocity field data of a single measurement plane with the free-stream velocity; 2) for selected phases in the flapping cycle a direct three-dimensional spatial wake reconstruction is obtained from an interpolation of the data of different measurement planes, using a Kriging regression technique.

Parts of this chapter have been published in Experiments in Fluids **55(9)** (Percin et al, 2014a) and in Experiments in Fluids **55(1)** (de Baar et al, 2014).

5.1. Introduction

In the previous chapters, the discussion has been mostly limited to the DelFly in hovering flight configuration with a particular focus on the force generation, deformation and flow structures of the flapping wings, as the main objective was to identify the underlying mechanisms behind the flapping-wing flight of the DelFly in a simplified configuration. However, the DelFly does not only hover but also performs forward flight. Moreover, in the forward flight configuration, the downstream evolution of the flapping wing vortical structures is of vital importance due to possible interaction of these with the tail that is situated in the wake. Accordingly, this chapter focuses on the temporal evolution of the flow structures in the wake of the DelFly flapping wings in forward flight configuration.

One of the few reported attempts to visualize the near wake region of a flapping-wing MAV was made by Ren et al (2012). They performed PIV measurements in the wake of flapping wings of an MAV that was designed at Wright State University, in chordwise planes at four different spanwise positions. From their observations they concluded that a vortex ring is shed into the wake during the fling phase. They also described the three-dimensional character of the vortex ring based on the interpretation of the data from the planar velocity fields acquired at different spanwise locations. Ghosh et al (2012) performed Stereo-PIV measurements in a chordwise plane located in the near wake of a flapping butterfly-shaped wing model which was driven by a 4-bar linkage system. They captured the evolution of flow structures and the spanwise flow at different stroke angles and they reported the dependence of ejected trailing edge vorticity on the flapping frequency.

The wake structure behind the flapping wings of MAVs can be expected to bear similarities to the wake of flapping animal species. The three-dimensional characteristics of the wake structure have been investigated in several studies, by their reconstruction from time-resolved planar PIV measurements, using a convection model (Taylor's hypothesis). Experiments performed in the wake of different species of birds revealed relatively simple structures: a compact starting vortex at the start of the downstroke and more diffuse stop vortices (Hedenström et al, 2006; Spedding et al, 2003). It was also shown that during the slow flight of birds, most vortical structures are generated during the downstroke whereas the upstroke is almost aerodynamically unemployed. Contrary to birds, experiments on bats suggest a fairly complicated wake structure. Hedenström et al (2007) studied wakes of *G. soricina* bats via the PIV technique. They showed that separate vortex loops are generated by each wing that consists of the starting vortex, the tip vortex and root vortex, in which the bat wake differs from the bird wake. Moreover, it was observed that, during the end of upstroke at medium and high flight speeds, the outer part of the wing generates a vortex dipole structure with opposite sense to the main vortex. This reversed vortex dipole, which is actually a part of the vortex loop, generates an upwash which in turn produces a negative lift (Muijres et al, 2011). This negative lift can be regarded as one of the reasons why birds, which retract their wings to make them aerodynamically inactive during the upstroke, outperform bats in terms of span efficiency and flight efficiency (Muijres et al, 2012a). The vortex loops are also observed at smaller length scales. Flow visualizations around and in the near wake of free-flying bumblebees revealed that each wing generates a separate vortex loop that is comprised of LEV, TV and RV with no linkage between the left and right wing structures (Bomphrey et al, 2009). On the other hand, PIV measurements in the near-wake of a Hawkmoth (*Manduca Sexta*) exhibited great resemblance

to the elliptical vortex loops (Bomphrey et al, 2006). Recently, volumetric flow field measurements (Tomographic PIV) were performed in the wake of desert locusts in a volume of $60 \times 80 \times 4$ mm^3 (Bomphrey et al, 2012). The three-dimensional wake was visualized in substantial detail, which showed that animal wakes can deform which cannot be detected by use of planar measurement techniques in combination with the convection model, pointing out the importance of a true volumetric visualization of the wake structures.

It is clear that the wake structure of flapping wings, which contains information about the time history of aerodynamic structures and generated forces, requires a detailed investigation, especially for the case of multi-wing MAVs. For example in the specific case of the DelFly under study in the present investigation, the wake structure is even more compelling as it has two wing pairs and a tail that is presumably interacting with the vortical structures leaving the wings. At these conditions, the size of the wake makes application of regular tomographic PIV not feasible (Scarano, 2013). Therefore, in the present investigation the flow in the wake of the flapping wings of the DelFly was captured at several streamwise positions via time-resolved Stereo-PIV measurements. The three-dimensional wake was subsequently reconstructed by use of two different approaches. Firstly, the time-resolved three-component velocity field data of a single measurement plane is convected with the free-stream velocity to yield a spatio-temporal wake reconstruction. Secondly, a Kriging regression technique with a local error estimate was used to generate an instantaneous volumetric representation of the wake structure on a spatial grid that is finer than the spacing between the measurement planes (de Baar et al, 2014). The specific objective of this wake study is: 1) to investigate the influence of the reduced frequency on the wake structure and 2) to compare the two different approaches, in order to estimate the importance of self-induced wake deformation.

5.2. Experimental setup and data processing

5.2.1. Experimental setup

The experiments were performed in a low-speed wind tunnel at the Aerodynamic Laboratory of TU Delft. The wind tunnel has an open test section with cross-section dimensions of 600×600 mm^2. The measurements were performed for free-stream velocities U_∞ in the range of 2 to 6 m/s. The corresponding Reynolds number based on the mean wing chord-length ($\overline{c} = 80$ mm) and (U_∞) ranges from 10,000 to 30,000.

A complete DelFly II model was used as the experimental object in the present study. The DelFly model was positioned in the test section of the wind tunnel in a forward flight configuration at 0° angle of attack and attached to the balance mechanism (Fig. 5.1). The forces and moments were captured by use of a six-component force sensor (ATI Nano-17 with a maximum sensing value of 25 N in x, y and 35 N in z direction with a resolution of 1/160 N) that is attached to the balance mechanism, at a recording rate of 25 kHz. The raw force and moment data then were filtered to remove noise and vibration components in the signal, by means of a Chebyshev Type II low-pass filter with -80 dB attenuation of the stop-band. A forward-backward filtering technique was used in order to prevent time-shift of the data. The cut-off frequency was selected based on the flapping frequency to allow the first two harmonics of the force oscillations to be present in the resultant data as these modes were found to be related to aerodynamic forces.

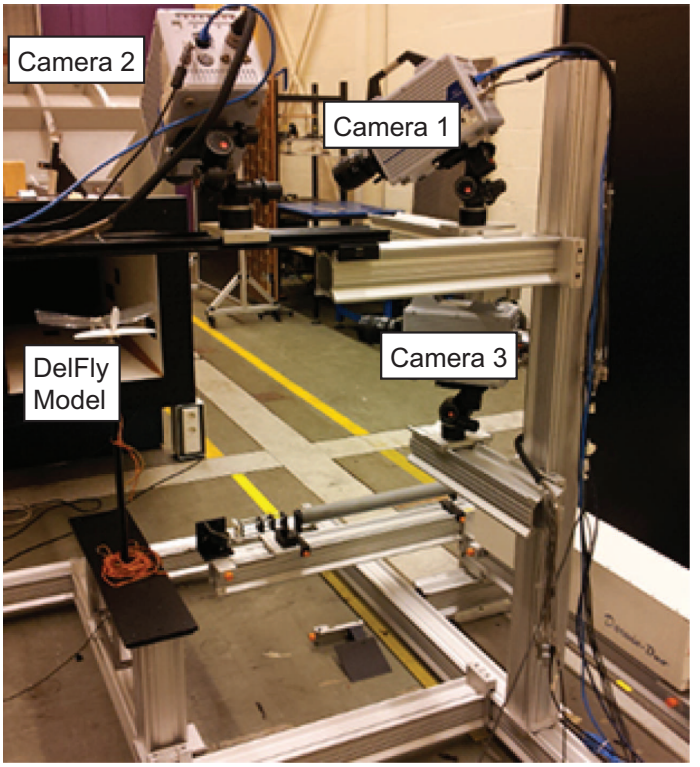

Figure 5.1: Experimental setup for the wake reconstruction study

In addition to the free-stream velocity, also the flapping frequency (f) of the DelFly wings was varied, in the range of 5.7-11 Hz by use of the microcontroller system that was also utilized for the phase determination of the wings and synchronization of the PIV acquisition.

5.2.2. Time-resolved stereoscopic-PIV

High-speed Stereo-PIV measurements were performed at 12 consecutive spanwise planes with a distance of 10 mm between each other (Fig. 5.2). The first measurement plane was positioned 10 mm downstream from the trailing edge of the wings. Note that only one side of the wake was imaged, due to field of view size restrictions and imaging blockage by the DelFly structure, however, the wake is assumed to be nominally symmetric with respect to the center plane. The flow was illuminated with a double pulse Nd:YLF laser (Quantronix Darwin Duo) with a wavelength of 527 nm. The laser sheet with a thickness of 4 mm was kept at a fixed position and the complete balance mechanism was shifted in order to perform measurement on a plane at a different streamwise position relative to the model. The flow was seeded with a water-glycol based fog of droplets with a mean diameter of 1 μm, which is produced by a SAFEX fog generator. The complete measurement room was filled with the fog beforehand in order to achieve a homogeneous seeding of the flow. Images

of tracer particles were captured with three CMOS cameras with a maximum resolution of 1024 × 1024 pixels at a data rate of 5.4 kHz. Each camera was equipped with a Nikon 60 mm focal objective with numerical aperture 4 for the first two cameras and 2.8 for the last camera and mounted with Scheimpflug adapters. It should be noted that the first two cameras, which were placed above the test section with an angle of 40° with respect to each other (Fig. 5.1), were primarily used for the measurements. The third camera, which was positioned at the same horizontal plane with the DelFly model, was only used when the tail caused substantial amount of blockage in the view of the second camera. In that case, the first and the third cameras were used for image acquisition, which were also oriented at an angle of 40° with respect to each other.

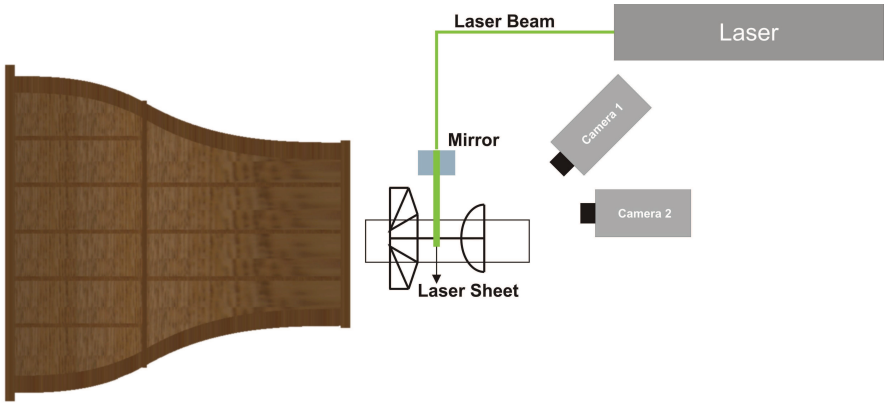

Figure 5.2: Sketch of the top view of the experimental setup for the wake reconstruction study

A field of view of 200 × 200 mm^2 was captured at each streamwise position with a magnification factor of approximately 0.1 at a digital resolution of 5 pixels/mm. Double-frame images were recorded at a rate of 250 Hz for a time duration of one second. This allows for a time-resolved measurement of the flow field, as the flapping frequency ranges between 6 and 12 Hz. The commercial software Davis 8.0 (LaVision) was used in data acquisition, image pre-processing, stereoscopic correlation of the images, and further vector post-processing. The pre-processed double frame images were interrogated using windows of final size of 64 × 64 pixels with two refinement steps and an overlap factor of 75 % resulting in approximately 5000 vectors with a spacing of 3 mm in each direction.

5.2.3. Wake reconstruction

As mentioned earlier, two different methods were used to reconstruct a three-dimensional representation of the wake of the flapping wings. First, a spatio-temporal reconstruction was performed for the initial interpretation of the physical phenomenon. For this purpose, time-series measurements in a single measurement plane (i.c., 40 mm downstream of the trailing edge of the wings) were employed to generate a three-dimensional representation of the wake structures by using a convection model (Taylor's hypothesis). This implies that the data of the measurement plane is translated with the free-stream velocity (with an assumption of a non-deforming wake and neglecting the induced velocities), which

results in spatial resolution of 8 - 24 mm in the streamwise direction for the given image recording rate of 250 Hz and for the considered free-stream velocity range (2 - 6 m/s).

Secondly, a Kriging regression technique was applied to the flow fields from consecutive measurement planes in order to reconstruct a true spatial representation of the instantaneous three-dimensional wake of the flapping DelFly wings, for specific phases in the flapping cycle (de Baar et al, 2014). In this procedure two equi-distant planes are interpolated between each of the measurement planes resulting in a spatial resolution of 3.33 mm in the streamwise direction (which is then comparable to the in-plane resolution). The implemented Kriging technique can be regarded as an improved version of the ordinary Kriging interpolation, in that it is modified to take into account the local measurement uncertainty in the regression process. A short description and performance assessment of the technique are given subsequently. For a detailed explanation and discussion, the reader is referred to (de Baar et al, 2014).

Kriging regression of the PIV data by use of a local error estimate

The Kriging predictor is a tool that can provide a single-step prediction of the flow field at any set of grid points and it generally operates as a regressor rather than an exact interpolator. To do this, it uses a number of observations of a physical quantity (i.e., velocity) sampled at discrete locations X_{PIV} and based on these data, it predicts the values of the physical quantity at any (new or existing) set of locations X. In the current study, it is aimed to predict the complete flow field U in the wake of the flapping wings conditional on the measured velocity data U_{PIV}. The PIV measurement of the velocity data can be considered as:

$$U_{\mathrm{PIV}} = HU + e_{\mathrm{PIV}} \tag{5.1}$$

where H is the observation matrix that contains only ones and zeros to select the PIV data locations from the larger discrete set of locations where the true flow field U is defined and e_{PIV} is the measurement error that is assumed to be nonsystematic and normally distributed according to the measurement error covariance matrix R. Given the velocity field data $U_{\mathrm{PIV}} = (u_{\mathrm{PIV}}, v_{\mathrm{PIV}}, w_{\mathrm{PIV}})$, the Kriging predictor for the velocity component u is given by the estimated mean (Wikle and Berliner, 2007):

$$E(u|u_{\mathrm{PIV}}) = \mu_u + PH'\left(R + HPH'\right)^{-1}\left(u_{\mathrm{PIV}} - H\mu_u\right) \tag{5.2}$$

and the estimated variance (Wikle and Berliner, 2007):

$$\mathrm{var}(u|u_{\mathrm{PIV}}) = \left[I - PH'\left(R + HPH'\right)^{-1}H\right]P \tag{5.3}$$

which are based on linear and Gaussian assumption. In these formulae, the observation matrix H selects the PIV data positions from the complete flow field locations ($X_{\mathrm{PIV}} = HX$), E is the expectation operator, P is the flow-field covariance matrix and μ is the velocity mean, which is considered as the statistical mean of the PIV data such that it can be interpreted as an approximation to the free-stream velocity. The elements of the covariance matrix P are obtained from a Gaussian covariance kernel:

$$P_{i,j} = \sigma^2 \exp\left(-\sum_d \frac{\left|X_i - X_j\right|_d^2}{2\theta_d^2}\right) \tag{5.4}$$

which contains a summation over the dimensions d. The performance of the Gaussian covariance kernel was assessed and it was found to perform well in similar flow cases with relatively low gappiness (Gunes and Rist, 2007, 2008; Gunes et al, 2006). The correlation range θ can be determined by use of maximum likelihood estimate (MLE) optimization (Kitanidis, 1986; Kitanidis and Lane, 1985; Mardia, 1989; Mardia and Marshall, 1984). However, in this study, a frequency-domain sample variogram (FSV) optimization was used to reduce computational cost (de Baar et al, 2013).

Generally, the Kriging predictor is used without an error estimate ($R = 0$), which results in Kriging acting as an exact interpolator (Kriging NE). However, in order to ensure numerical stability, a small matrix regulation term is used ($R_{NE} = \varsigma I$ with ς being at the order of machine precision). In the case of working with experimental data, which are likely to contain a certain level of measurement error, it is not very desirable to utilize the Kriging predictor as an exact interpolator. Therefore it is convenient to introduce some level of Gaussian noise in the Kriging predictor allowing for regression instead of exact interpolation of the experimental velocity values. In this case, the global error covariance matrix $R_{GE} = \epsilon_0^2 I$, where ϵ_0 is the global measurement uncertainty. This represents an uncorrelated white noise measurement error with the same value for the entire flow field. However, in general, the measurement error is not constant over the domain; particularly in the case of PIV measurements, regions of insufficient seeding or imperfect illumination can lead to a local increase in the measurement uncertainty. In this case, the measurement error covariance matrix is taken as $R_{LE} = \mathrm{diag}(\epsilon^2)$, where ϵ is a vector of local measurement uncertainties ϵ_i such that each $e_i = \mathcal{N}(0, \epsilon_i^2)$ is an Gaussian error estimate for each individual velocity vector (Kriging LE). In this study, a low fidelity uncertainty model is employed, which is primarily based on the first peak to second peak ratio (PPR) of the stereo-PIV cross-correlation map. The PPR of the correlation map can also be considered as a measure of detectability of the true displacement (Adrian and Westerweel, 2010; Keane and Adrian, 1992; Raffel et al, 2007).

In order to assess the performance of the Kriging LE based on PPR values of the stereo-PIV data, it is first compared to a direct interpolation technique, i.c., cubic spline interpolation (after validation and smoothing of the velocity vectors). In Fig. 5.3, iso-surfaces of two helicity values for the case of $k = 0.5$ ($f = 6$ Hz and $U_\infty = 3$ m/s) are plotted for cubic spline interpolation (left) and Kriging interpolation with local error estimate (right). It should be noted that with both interpolation methods, two equi-distant planes are interpolated between each measurement plane resulting in a spatial resolution of 3.33 mm in the streamwise direction. For this particular phase of the flapping motion (end of outstroke), it is expected to capture counter-rotating root and tip vortex pairs of each wing. Comparison of the effectiveness of the two interpolation techniques is performed on the basis of possible appearance and plausible physical behaviour of these wake structures.

Spatial derivative based values are naturally more sensitive to the performance of the interpolation technique, thus comparison of helicity iso-surfaces reveals substantial differences. For the case of cubic spline interpolation, one can observe a large amount of spurious helicity packets. The appearance of these structures can be attributed to sev-

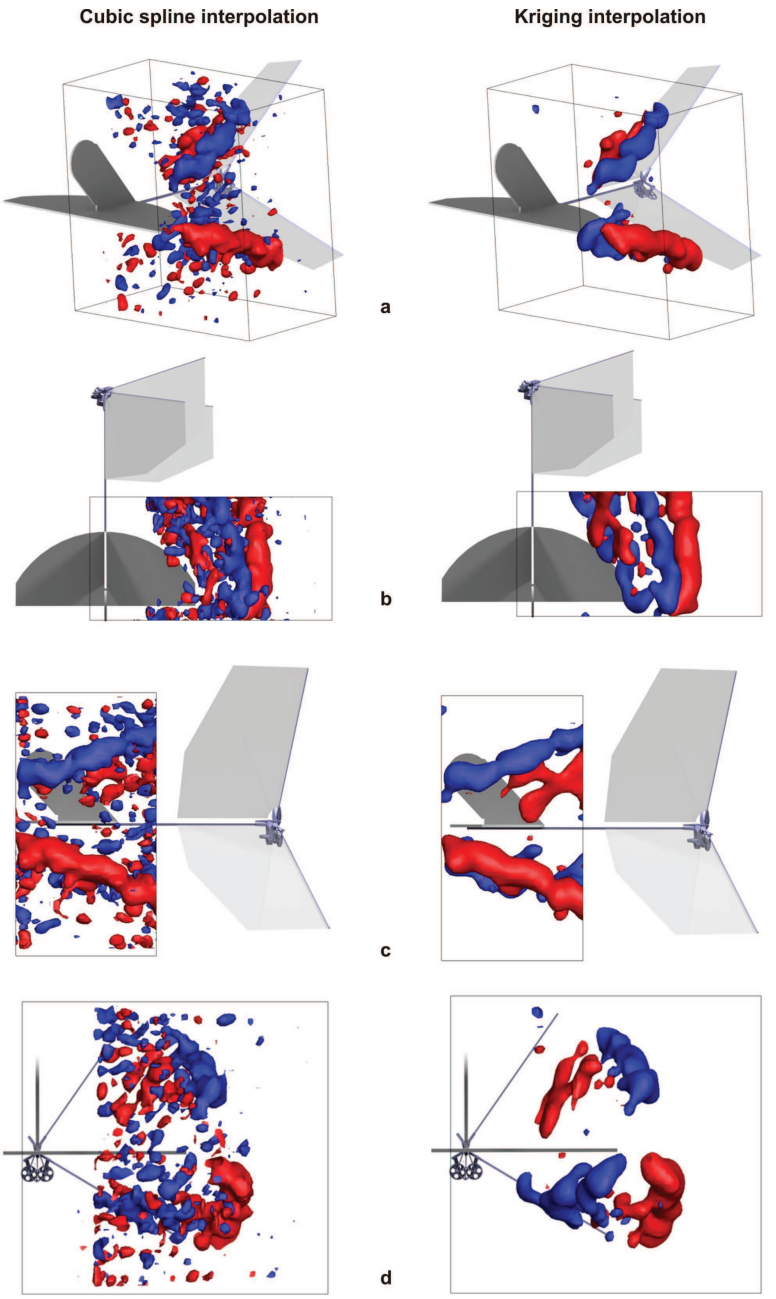

Figure 5.3: The wake of the DelFly II during outstroke: isosurfaces of helicity, where *blue* is clockwise and *red* is counter-clockwise. The results were obtained using cubic spline interpolation (*left*) and Kriging LE regression (*right*). **a** Perspective view, **b** top view, **c** side view, **d** rear view

eral different sources: 1) spatial variation of image quality in the measurement planes due to lower seeding density closer to the fuselage of the DelFly and regions of shadows and severe reflections; 2) lower spatial resolution in the out-of-plane direction with respect to in-plane resolution; 3) mismatch of velocity fluctuations due to the fact that measurements of the same flapping phase in different planes were not performed simultaneously; 4) unstructured and different measurement grids for each measurement plane; 5) cubic spline interpolation does not take into account the error of the measured velocity vectors. However for the case of Kriging interpolation, the PPR values, which can be regarded as a measure of reliability of the vector (Westerweel, 1994), are implemented to provide an estimation of the measurement error. This implementation adequately restricts the influence of the vectors calculated in the regions of relatively bad PIV conditions on the interpolated data points. As a result, spurious and non-physical structures are, to a large extent, removed from the flow field.

One should be aware that (in general) the PPR solely is not necessarily sufficient to provide an accurate model of the local PIV measurement uncertainty. However, it is quite efficient in modeling the error resulting from regions of shadow, severe reflection, and low seeding quality. This can be regarded as the reason why the error model based on PPR values works effectively for the DelFly measurements. For PIV measurements with proper seeding and illumination, it is more likely that a PPR based error model is not appropriate and another error model should be utilized.

The success of the regression technique was also evaluated by comparing the flow fields predicted by the Kriging LE method with the measurement data. For this purpose, a particular data set with 24 measurement planes with a distance of 5 mm between each other was used. Initially, the complete wake of the flapping wings was reconstructed from these 24 available measurement planes. The Kriging regression technique was utilized at this stage only to fill the gaps in the individual measurement planes, which originate from masked regions in the PIV data. On the other hand, the same wake was reconstructed again from a down-sampled data set, by using every other measurement plane (12 measurement planes), and with the Kriging LE regression technique used to interpolate one plane in between the measurement planes, which results in the same spatial resolution in the streamwise direction as in the original data set. The resultant wake structures for both cases are visualized with isosurfaces of the Q criterion coloured by the vorticity component parallel with the free-stream (ω_x) in Fig. 5.4. It is clear that the Kriging regression technique performs well in this case and apart from the small scale details, the most prominent features of the vortical structures are captured.

In order to quantify the accuracy of the Kriging LE regression technique, Fig. 5.5 shows the root-mean-square (RMS) error of the out-of-plane vorticity (ω_x) on the predicted intermediate streamwise planes for a complete flapping cycle. The RMS error is computed by comparing the interpolated field with the smoothed data planes, while the reference is the RMS error of the raw data plane compared with the smoothed data plane. It is clear that the RMS error during the instroke phases is lower than that of outstroke phases for both reconstruction techniques. It can be attributed to the relatively more complicated vortex interactions happening during the outstroke of the flapping motion. Throughout the flapping cycle, the Kriging LE vorticity is more accurate than the cubic spline vorticity.

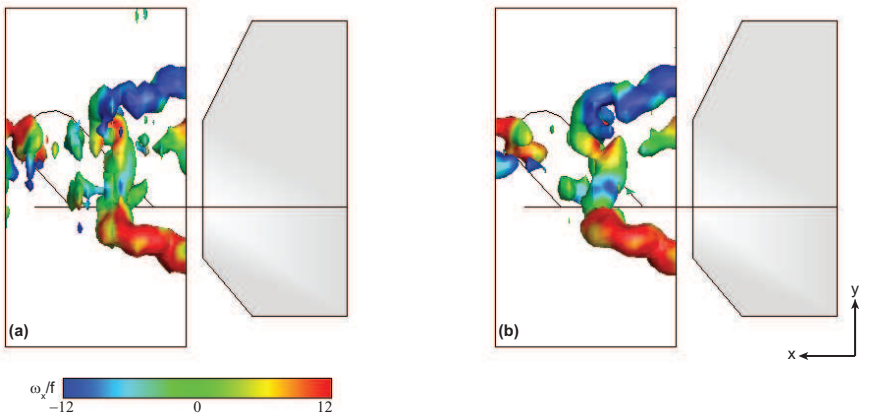

Figure 5.4: Isosurfaces of $Q/f^2 = 20$ coloured by ω_x at the end of outstroke for the case of $f = 10$ Hz and $U_\infty = 3$ m/s (side view). **a** Wake reconstruction by use of 24 measurement planes with 5 mm spatial resolution in the streamwise (x) direction; **b** Wake reconstruction by use of every other plane with 10 mm distance and Kriging regression technique with local error estimate to interpolate one plane in between to achieve 5 mm spatial resolution in x direction

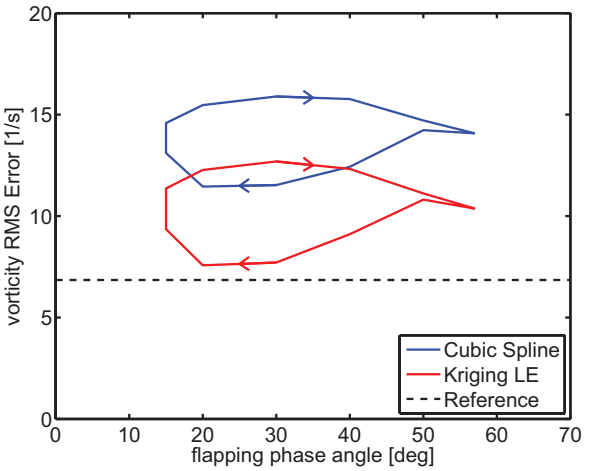

Figure 5.5: Validation of vorticity for different phase angles. Computed from regression of original 12-plane data to intermediate planes of 24-plane data

5.3. Results

In this section, the reconstructed wakes are compared and analyzed for a variety of experimental parameters. First, spatiotemporal wake reconstruction results are discussed for different reduced frequencies in conjunction with the aerodynamic forces generated. Sec-

ond, spatial reconstruction results are used in order to describe the true instantaneous wake structures in more detail. Before proceeding to a comprehensive analysis of the results, it is necessary to mention some issues regarding the visualization of the results, which may impact the interpretation of the physical phenomena. First, it should be noted that only one half of the wake was visualized (as the wake is assumed to be nominally symmetrical) and that the region in the vicinity of the tail is masked during PIV processing due to intensive reflections underneath the tail and lack of illumination above it. Additionally, to assist the interpretation of the results, the DelFly wings are schematically displayed in the images as an indication of the flapping phase (particularly in the case of the spatial wake reconstruction); however, they are represented here as rigid bodies, whereas in reality there is a significant amount of deformation of the wings during the flapping motion (maximum trailing edge deformation with respect to rigid leading edge is 60 % of the mean chord length, see de Clercq et al (2009)). Therefore, this may cause that the position of vortical structures may occasionally seem to be uncorrelated with the indicated position of the wings. Finally, for the sake of eliminating random noise and thus to provide a better visualization of the wake structures, ensemble averaging has been performed for both spatiotemporal and spatial wake reconstructions. For the former, the number of cycles used in averaging varies between 4 and 8 depending on the flapping frequency. For the latter, ensemble averaging of five vector fields for each phase of the flapping motion in each measurement plane is performed before the wake reconstruction step.

5.3.1. Spatiotemporal wake reconstruction

A perspective view of the wake structures is shown in Fig. 5.6 for the case of a reduced frequency of 0.47 (corresponding to a free-stream velocity of U_∞ = 3 m/s and flapping frequency of 5.7 Hz). Side and bottom views of the vortical structures for a selection of parameters with corresponding reduced frequencies ranging from 0.47 to 1.17 are shown in Figs. 5.7 and 5.8 (cases a–d correspond to a free-stream velocity of U_∞ = 3 m/s and flapping frequency of 5.7, 7.4, 9.4, and 11 Hz, respectively; e and f are for U_∞ = 2 m/s and 7.5 and 9.3 Hz, respectively). Two periods of the flapping motion are depicted, visualized by means of isosurfaces of the Q criterion (Jeong and Hussain, 1995) which is non-dimensionalized by the square of the flapping frequency. The isosurfaces of dimensionless Q criterion (Q/f^2) are coloured by the dimensionless vorticity component parallel with the freestream (ω_x/f) in the side and perspective views and by the dimensionless spanwise vorticity component (ω_z/f) in the bottom views.

It can be observed that the wake of the flapping wings is composed of well-organized vortical structures and is dominated by the counter-rotating tip vortices of upper and lower wings (Fig. 5.6). The instroke starts with the formation of starting vortices (Fig. 5.6; 1 and 2) linked to the tip vortices of both upper and lower wings (Fig. 5.6; 3 and 4). During the outstroke, similarly the wings shed coherent tip vortices (Fig. 5.6; 5 and 6) of the opposite sense. For the lowest reduced frequency, the vortical structures of the instroke and outstroke phases are clearly separated (see also Fig. 5.7a), indicating that little vortex activity occurs during the stroke reversal moments. During the instroke phase of the flapping motion, both the upper and the lower wings form symmetrical tip vortices (Fig. 5.7a–f; 1 and 2, respectively) about an axis situated slightly above the centerline of the DelFly (i.e., the fuselage of the DelFly which is depicted as a horizontal line in the DelFly drawings in

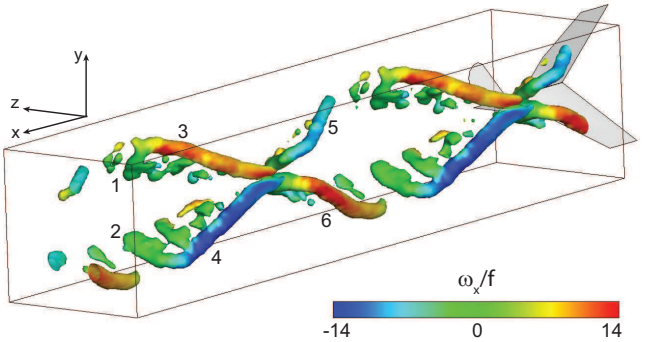

Figure 5.6: Perspective view of the wake structures visualized by isosurfaces of $Q/f^2 = 10$ and coloured by ω_x/f for two periods of the flapping motion (flow is the positive x direction) for the case of $k = 0.47$ ($U_\infty = 3$ m/s and $f = 5.7$ Hz)

Fig. 5.7) due to the 12° dihedral angle of the DelFly wings. Tip vortices shed during the outstroke also show a similar behaviour in terms of symmetry in general (Fig. 5.7a–f; 3 and 4); however, for the lowest reduced frequencies (Fig. 5.7a, b), relatively weaker vortical wake structures occur. Also, the inclination of the tip vortices differs, as indicated in the figure, being larger for the outstroke than for the instroke. These difference between the vortical structures of in- and outstroke can be explained by the different wing kinematics during the in-and-out stroke, which is presumably a direct result of the wing–wing interaction occurring at the onset of the outstroke (viz. clap-and-peel) together with the asymmetry in the flapping motion profile (Fig. 3.5).

The most obvious effect of the reduced frequency reflected in the visualizations of Figs. 5.7 and 5.8 is the wave length of the wake being inversely proportional to k. This is a logical outcome, as the reduced frequency is, by its definition, proportional to the ratio of the wavelength of the vortex wake U_∞/f to the characteristic length of the flapping wings ($\bar{c}$).

Another prominent difference between the considered cases of reduced frequencies is the time shift in the appearance of vortical structures in the reconstructed wakes. As mentioned earlier, the Hall sensor input is used for zero-referencing between the measurements; thus, all wake reconstructions are synchronized with respect to the stroke angle of the flapping wings. Therefore, the phase lag suggests different formation and convection times of the wake structures for different reduced frequencies. This implies that the convection time of the vortices from the vicinity of the flapping wings to the measurement plane that is used for the spatiotemporal reconstruction is not only determined by the free-stream velocity but might also be affected by these structures' own induced velocities as well as flapping-wing induced velocities [e.g., the momentum jet during the clap phase (de Clercq et al, 2009)]. The formation time of these structures, on the other hand, is a more complex and difficult-to-estimate parameter as it might depend on a number of interrelated variables (fluid-deforming structure interactions, wing–wing interactions, wing kinematics, fluid dynamics effects, etc.). In this regard, earlier flow visualization stud-

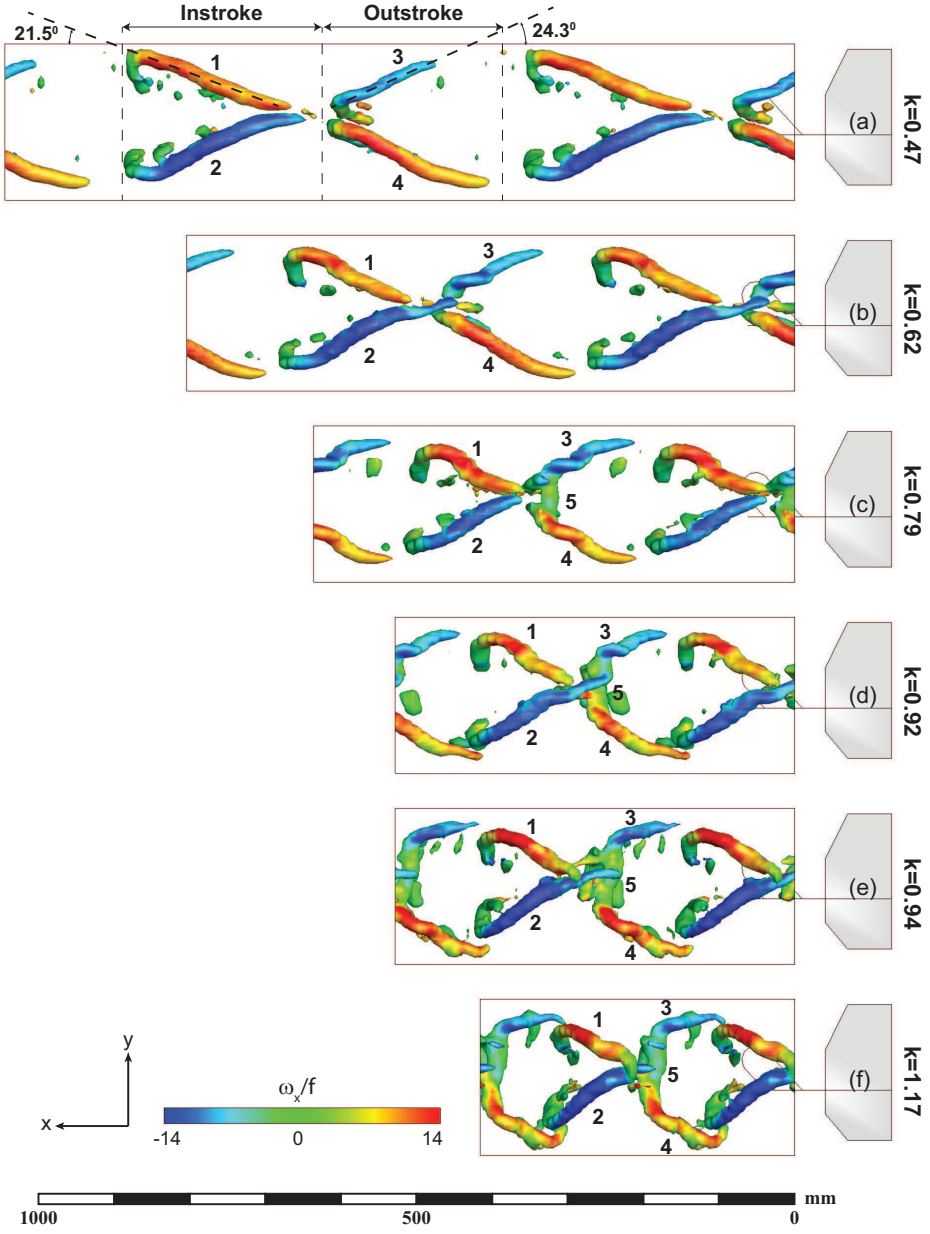

Figure 5.7: Side view of the wake structures visualized by isosurfaces of $Q/f^2 = 15$ and coloured by ω_x/f for two periods of the flapping motion (flow is the positive x direction). **a** $k = 0.47$ ($U_\infty = 3$ m/s and $f = 5.7$ Hz). **b** $k = 0.62$ ($U_\infty = 3$ m/s and $f = 7.4$ Hz). **c** $k = 0.79$ ($U_\infty = 3$ m/s and $f = 9.4$ Hz). **d** $k = 0.92$ ($U_\infty = 3$ m/s and $f = 11$ Hz). **e** $k = 0.94$ ($U_\infty = 2$ m/s and $f = 7.5$ Hz). **f** $k = 1.17$ ($U_\infty = 2$ m/s and $f = 9.3$ Hz).

ies around the flapping wings of the DelFly (Groen, 2010) indeed reported different TEV developments at different flapping frequencies. It was shown that increasing flapping frequency delays the formation of the TEV as well as increasing its circulation.

Therefore, the observed phase lag can be explained by the formation time of vortical structures that changes with varying flapping frequency and finds its likely origin in wing deformation characteristics. The structural dynamics of equivalent DelFly wings have been analyzed by the use of a simplified analytical model (see Chapters 3 and 6) which showed that the wing inertia term has a considerable effect on the resultant wing deformation especially at the stroke reversals. Whereas the leading edge spars are directly driven by the gear and hinge mechanism and thus have a defined kinematics for different parameters of the flapping motion, the passive behaviour of the flexible wing surface and the wing stiffeners alters significantly due to wing inertia. At stroke reversal, the wing body continues moving with its inertia and changes direction in motion later than the leading edge spars. The delay and amount of deformation are enhanced by the flapping frequency and free-stream velocity which results in the formation of vortical structures with a time shift. In this context, comparison of thrust profiles (Fig. 5.9) also displays a lag in the non-dimensional times at which the peak forces are generated. Figure 5.10 displays the relative time delays with respect to the lowest reduced frequency case. It is clear that during both instroke and outstroke phases, generation of maximum forces delays with increasing k at a constant U_∞ (viz. increasing f) and smaller lag is observed at lower U_∞ cases.

A distinct feature that comes out of the comparison of the spatiotemporal wake reconstructions is the changing interaction characteristics between the vortical structures. The interaction takes place between the formations of the instroke and outstroke phases as well as vortical structures of the upper and lower wings within a single stoke. The former emerges for the cases of k greater than 0.47 (Fig. 5.7b–f). For these cases, tip vortices of the instroke (1 and 2) and the outstroke (3 and 4), respectively, are situated close to each other and co-rotating vortices of these strokes even interact with each other. On the other hand, the lowest k case (Fig. 5.7a) displays individual structures of different strokes with no interaction observed with the current Q isovalue. Furthermore, gaps between the consecutive strokes with no prominent wake structures can be observed for this case. The other type of interaction mostly occurs during the outstroke as the wing–wing interaction takes place at the onset of this phase. For the cases of k greater than 0.62, tip vortices of the upper and the lower wings are linked to each other and form an arrow-shaped vortex loop (Fig. 5.7c–f; 5), whereas for the two lowest k cases, this interaction is absent or only weak. The presence of such a vortex formation is also correlated with the thrust generation mechanism of the flapping motion (Fig. 5.9). For the lowest k case, higher thrust is produced during the instroke than for the outstroke (relative difference of 28 %). The relative strength of the instroke and outstroke vortical structures is also in accordance with this behaviour. This result, on the other hand, contradicts the previous studies on the hovering DelFly (de Clercq et al, 2009; Groen et al, 2010), which reported larger force generation during the outstroke thanks to the enhancing effect of the peel motion. Equivalent thrust is generated for the case of $k = 0.62$ during both the instroke and the outstroke. This contradiction vanishes at larger values of k, where considerably greater thrust is generated during the outstroke with footprints of wing–wing interaction in the wake. Apparently, the clap-and-peel mechanism that is prominent in hovering flight is active in the forward

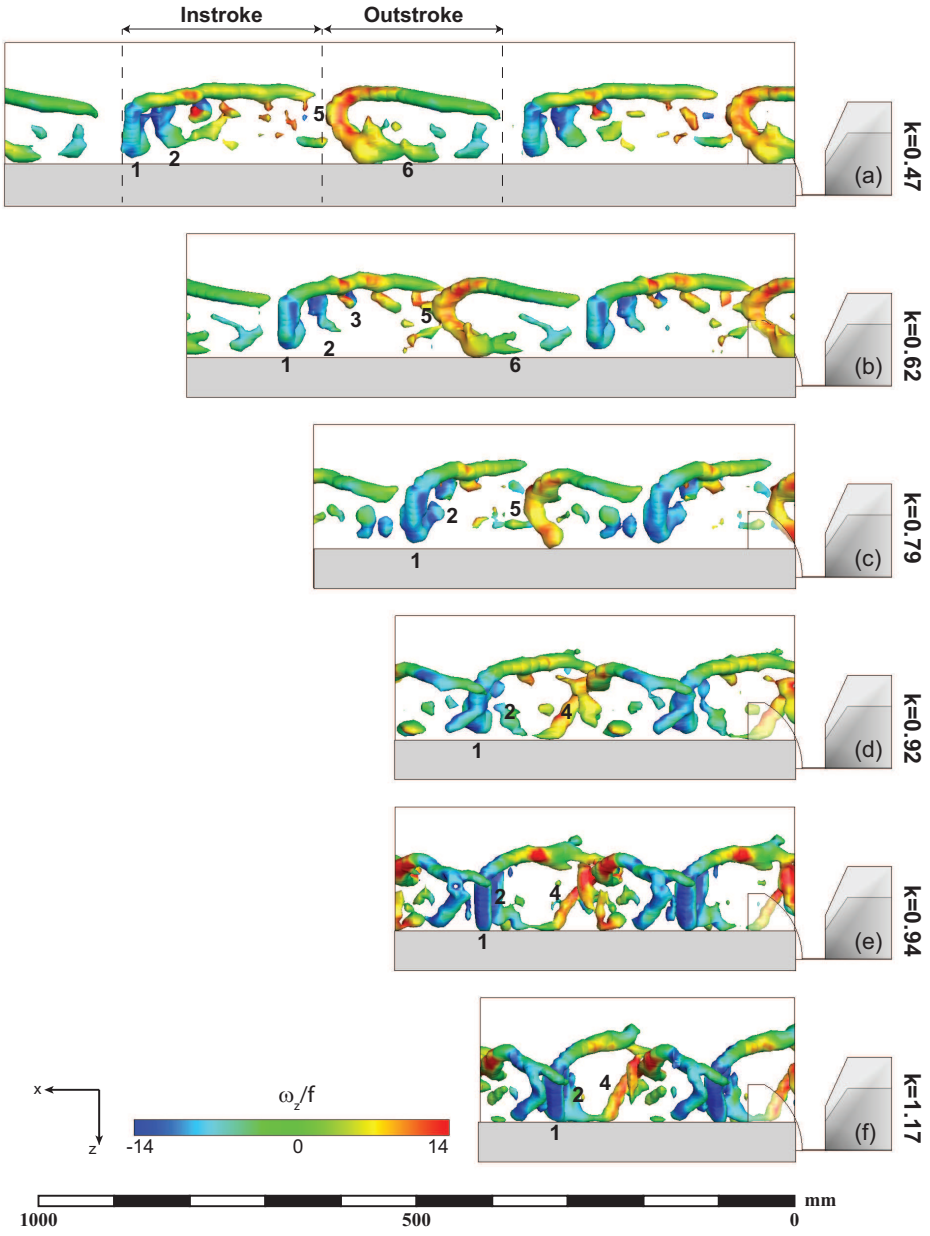

Figure 5.8: Bottom view of the wake structures visualized by isosurfaces of $Q/f^2 = 8$ and coloured by ω_z/f for two periods of the flapping motion (flow is the positive x direction, and only lower half of the wake is visualized). **a** $k = 0.47$ ($U_\infty = 3$ m/s and $f = 5.7$ Hz). **b** $k = 0.62$ ($U_\infty = 3$ m/s and $f = 7.4$ Hz). **c** $k = 0.79$ ($U_\infty = 3$ m/s and $f = 9.4$ Hz). **d** $k = 0.92$ ($U_\infty = 3$ m/s and $f = 11$ Hz). **e** $k = 0.94$ ($U_\infty = 2$ m/s and $f = 7.5$ Hz). **f** $k = 1.17$ ($U_\infty = 2$ m/s and $f = 9.3$ Hz).

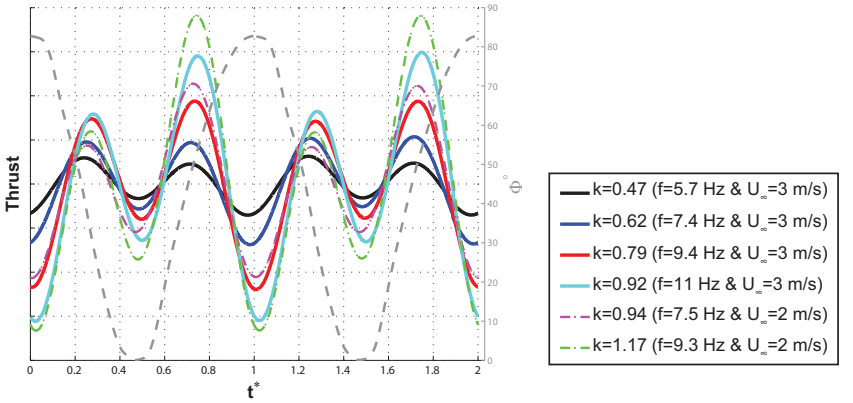

Figure 5.9: Time variation of thrust plotted for two periods of the flapping motion for difference reduced frequencies (mean force is subtracted from the measured forces for a better comparison) complemented with the variation of stroke angle (gray dashed line)

flight condition only for a sufficiently high value of the flapping frequency, but becomes deactivated at low values of the reduced frequency (low frequency or high free-stream velocity).

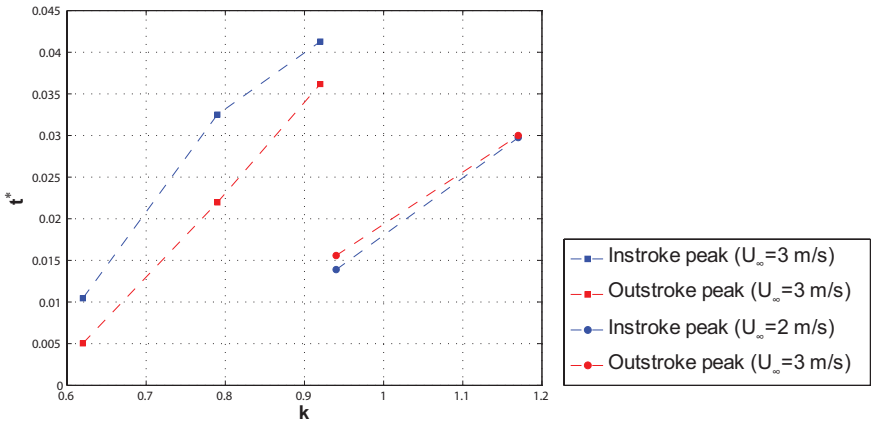

Figure 5.10: Relative time shift of the maximum force generation instants of the instroke and the outstroke with respect to that of the case $k = 0.47$

Comparison of the transverse wake structures (viz. leading and trailing edge vortices) exhibits more complex interaction characteristics as shown in Fig. 5.8. Note that the region where there is no reliable data due to reflection and shadow of the tail is covered with a gray band and only the wake structures of the lower wing are visualized for ease of comparison. Common to all cases, the instroke starts with the formation of starting vortices

(Fig. 5.8a–f; 1) of both wings. The starting vortex is then followed by the shedding of a secondary trailing edge vortex (2). There is a weak trace of leading edge vorticity for the case of $k = 0.62$ (Fig. 5.8b; 3). The LEV of the instroke sheds at the end of the instroke and appears as a prominent structure in the wake as a part of a vortex loop with the root vortex which looms for the cases of k greater than 0.79 (Fig. 5.8d–f; 4). In the other cases, presumably it sheds and interacts with the starting vortex of the outstroke and appears as a single structure in the wake. A starting vortex forms at the beginning of the outstroke clearly for the cases of $k = 0.47 - 0.79$ (Fig. 5.8a–c; 5) contrary to the theory of Weis-Fogh (1973) which postulates annihilation or absence of the starting vortex at the onset of the outstroke due to opposite bound circulations of the wings. Moreover, there are indications of root vortices forming during the outstroke for the two lowest k cases which are linked to the starting vortices (Fig. 5.8a, b; 6). On the other hand, less coherent trailing edge formations are present for the higher k values mostly closer to the wing tips at the onset of the outstroke which is intuitive as the outer parts of the wings move away initially. However, for these cases, there is no sign of a root vortex of the outstroke interacting with the starting vortex. Instead, as shown earlier, vortices of upper and lower wings interact and form a vortex loop.

5.3.2. Spatial wake reconstruction

Spatial reconstruction results are presented in this section for a selection of reduced frequencies (i.e., $k = 0.47$, 0.62, and 0.92) and phases of the flapping motion. The phases have been selected so as to capture the most prominent vortical structures of the strokes in the field of view.

Figure 5.11 displays the three-dimensional wake formations in the case of a reduced frequency of $k = 0.47$ ($U_\infty = 3$ m/s and $f = 5.7$ Hz) at a time instant close to the end of the instroke ($t^* = 0.335$ and $\phi = 15.5°$), when most of the vortical structures generated during the instroke appear in the observed region of the wake. In general, the reconstructed wake displays similar characteristics as the spatiotemporal reconstruction of the wake (Figs. 5.7a, 5.8a): no prominent vortex activity between the outstroke and the instroke phases (Fig. 5.11b, c); no interaction between the formations of the upper and lower wings; and a tip vortex formation symmetrical about the dihedral axis (Fig. 5.11b; 1 and 2). Furthermore, the inclination angle of the upper wing's tip vortex tube for the spatiotemporal reconstruction and the spatial reconstruction shows a good agreement (see Figs. 5.7a, 5.11b, 5.12b). This similarity validates the assumptions underlying the spatiotemporal wake reconstruction (i.e., non-deforming wake and free-stream velocity as the convection velocity) for this particular case.

Examination of transverse vortical structures also indicates similar behaviour with the spatiotemporal wake reconstruction results, but with more details thanks to a better resolution in the streamwise direction and more information in the region closer to the wing roots provided by the upstream measurement planes. The bottom view of the three-dimensional vortical structures (Fig. 5.11) is complemented with the contours of the out-of-plane vorticity in an x-plane that is positioned at 70 % of the span length (Fig. 5.11d). It should be noted that this section cut is not normal to the chordwise-oriented vortical structures and only used for visualization purposes. The instroke starts with the shedding of a clockwise rotating starting vortex for the lower wing (Fig. 5.11c and d; 3) that is then

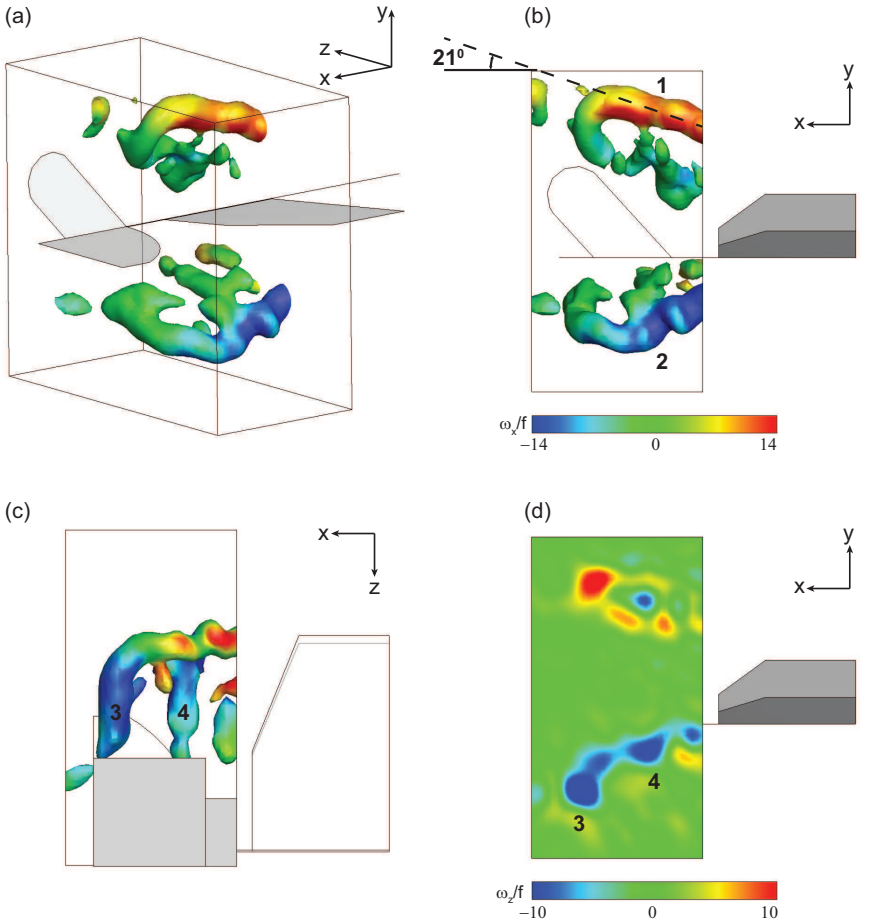

Figure 5.11: Wake structures for the case of $k = 0.47$ ($U_\infty = 3$ m/s and $f = 5.7$ Hz) at $t^* = 0.335$ ($\phi = 15.5°$). **a** Perspective view of the isosurfaces of $Q/f^2 = 10$ coloured by ω_z/f. **b** Side view of the isosurfaces of Q/f^2 coloured by ω_z/f. **c** Bottom view of the isosurfaces of Q/f^2 coloured by ω_x/f (note that only lower half of the wake is visualized). **d** Contours of the out-of-plane vorticity ω_x/f in an x-plane positioned at 70 % of the span length

followed by continuous trailing edge vorticity and secondary trailing edge vortex shedding (Fig. 5.11c, d; 4). The upper wing displays an identical vortex shedding mechanism, although it is not properly visualized in Fig. 5.11d because the structures of the upper wing have a larger angle with the x-plane with respect to that of the lower wing for this phase.

In Fig. 5.12, the three-dimensional wake is depicted at approximately the end of the outstroke ($t^* = 0.91$ and $\phi = 79°$). At this time instant, vortex structures formed during the outstroke appear in the field of view. As discussed earlier in the spatiotemporal reconstruction results, tip vortices of upper and lower wings are present in the wake (Fig. 5.12b; 1 and 2) linked to the starting vortices of the outstroke (Fig. 5.12d; 4 and 5). Similar to the

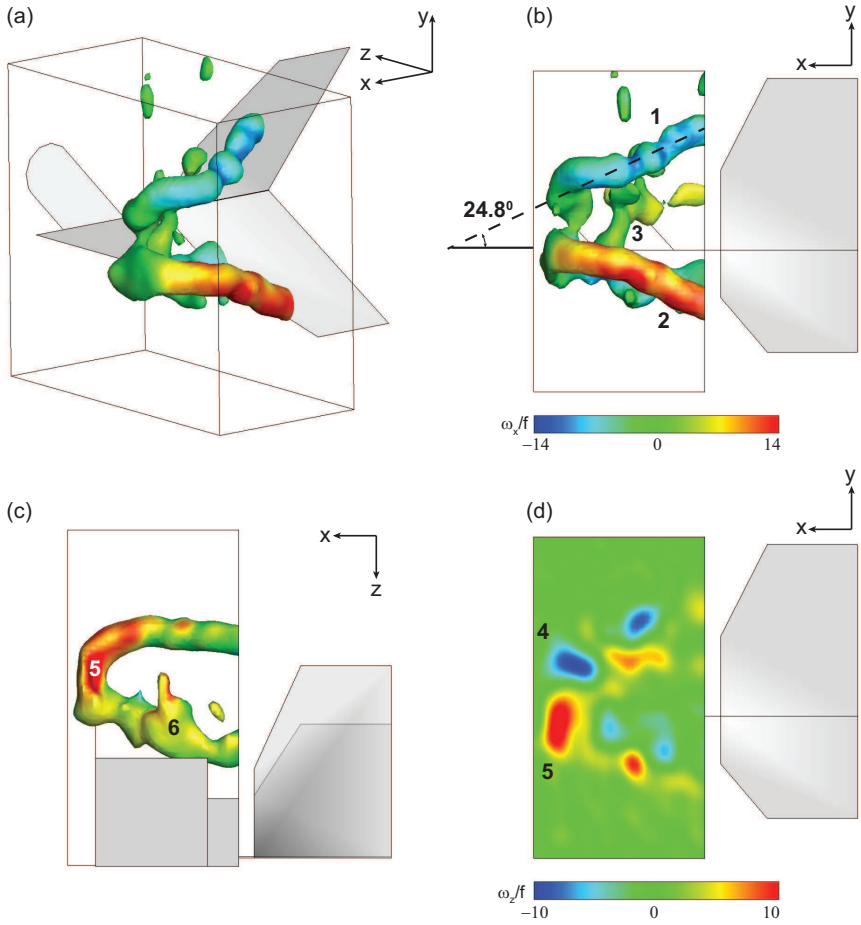

Figure 5.12: Wake structures for the case of $k = 0.47$ ($U_\infty = 3$ m/s and $f = 5.7$ Hz) at $t^* = 0.91$ ($\phi = 79°$). **a** Perspective view of the isosurfaces of $Q/f^2 = 10$ coloured by ω_x/f. **b** Side view of the isosurfaces of Q/f^2 coloured by ω_x/f. **c** Bottom view of the isosurfaces of Q/f^2 coloured by ω_z/f (note that only lower half of the wake is visualized). **d** Contours of the out-of-plane vorticity ω_z/f in an x-plane positioned at 70 % of the span length

structure shown in Fig. 5.7a, the starting vortex and the root vortex of the outstroke phase are present in the wake (Fig. 5.12c; 5 and 6). No interaction takes place between the tip vortices of upper and lower wings, but there is an indication of interaction between the root vortices of both wings (Fig. 5.12b; 3).

In Fig. 5.13, the wakes of the flapping wings are compared for different reduced frequencies ($k = 0.47$, 0.62, and 0.92) at the same phase of the flapping motion ($t^* = 0.335$ and $\phi = 15.5°$). The comparison reveals and confirms two features of the wake of the flapping wings that were assessed as a result of spatiotemporal wake analysis. Firstly, there is the phase lag in the appearance of the structures for the lowest flapping frequency case (Fig. 5.13a), the vortices of the instroke are already formed and convected more than half

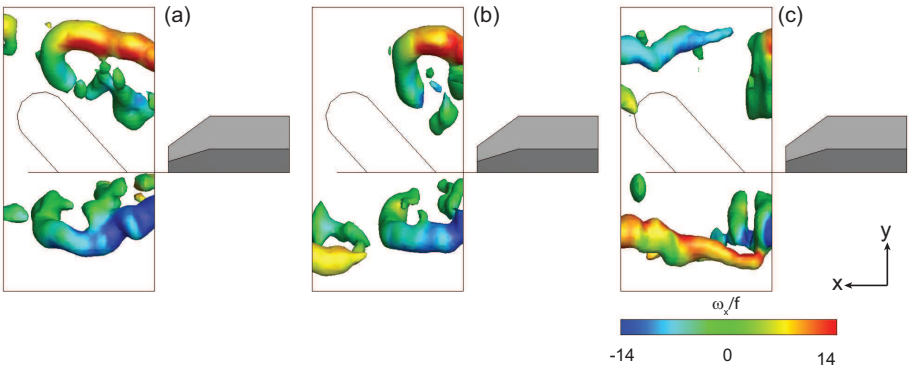

Figure 5.13: Side view of the wake structures visualized by isosurfaces of $Q/f^2 = 10$ and coloured by ω_x/f (flow is the positive x-direction) at $t^* = 0.335$ ($\phi = 15.5°$). **a** $k = 0.47$ ($U_\infty = 3$ m/s and $f = 5.7$ Hz). **b** $k = 0.62$ ($U_\infty = 3$ m/s and $f = 7.4$ Hz). **c** $k = 0.92$ ($U_\infty = 3$ m/s and $f = 11$ Hz)

of the reconstruction length in the streamwise direction, whereas for the highest flapping frequency case, the tip vortices of the previous outstroke are still in the wake and starting vortices of the instroke are newly formed (Fig. 5.13c). Secondly, changing interaction characteristics between the formations of consecutive strokes are observed. In the view of the latter, no prominent vortex activity during the stroke reversal case at the lowest reduced frequency case evolves into a more complex vortex interaction with increasing flapping frequency.

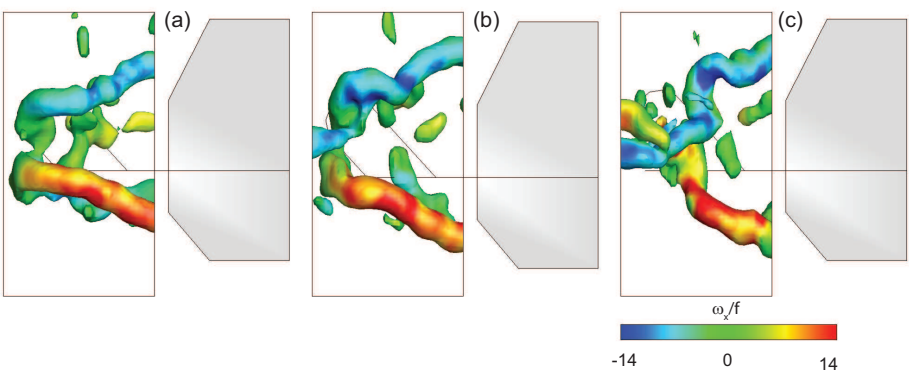

Figure 5.14: Side view of the wake structures visualized by isosurfaces of $Q/f^2 = 6$ and coloured by ω_x/f (flow is the positive x-direction). **a** $k = 0.47$ ($U_\infty = 3$ m/s and $f = 5.7$ Hz) at $t^* = 0.91$ ($\phi = 79°$). **b** $k = 0.62$ ($U_\infty = 3$ m/s and $f = 7.4$ Hz) at $t^* = 1.0$ ($\phi = 82°$). **c** $k = 0.92$ ($U_\infty = 3$ m/s and $f = 11$ Hz) at $t^* = 1.08$ ($\phi = 79°$)

To compensate for the phase lag to achieve a clearer comparison of the outstroke wake

structures, slightly shifted phases of the flapping cycle were reconstructed for increasing flapping frequency (Fig. 5.14). The comparison of the outstroke structures shows the evolution of wake structures from non-interacting upper and lower wing case to fully interacting cases. Moreover, it is clear that the structures of the instroke and the outstroke have a linkage in between for the higher flapping frequency cases (Fig. 5.14b, c). In addition to the arrow-shaped vortex loop that is formed as a result of clap-and-fling motion being dominant for the highest flapping frequency case, there is a less coherent structure present formed by the root vortices.

5.4. Conclusions

Unsteady three-dimensional wake structures generated by the flapping wings of the DelFly II MAV in forward flight condition have been explored in this study. Time-resolved three-component velocity fields were acquired at a number of consecutive spanwise-oriented planes via stereo-PIV measurements. Simultaneous thrust-force measurements were carried out to obtain insight into the correlation of the wake structures with force generation mechanisms. First, a spatiotemporal reconstruction of the wake was performed, in which three-component vector field data of a single measurement plane (positioned at 4 cm downstream of the trailing edges) were convected with the free-stream velocity. Second, a Kriging regression technique was used in order to execute a three-dimensional spatial reconstruction, interpolating two additional planes between the measurement planes and thus achieving similar in-plane and streamwise resolutions.

Comparison of spatiotemporal reconstruction of the wakes for different reduced frequencies revealed the effects of the flapping frequency on the wake formation and force generation mechanisms. First, various interaction forms are observed and described in the compared cases. For the lowest reduced frequency case (k = 0.47), there is no interaction observed between the wake structures of the consecutive strokes and there are gaps with no vortex activities in between. The situation changes with increasing reduced frequency with the appearance of interacting and coupled structures of the successive strokes. A more important interaction takes place between the upper and lower wings at the start of the outstroke (i.e., clap-and-peel motion) that affects the thrust generation mechanism significantly. Analysis of the results reveals that this mechanism is inactive at the reduced frequencies smaller than 0.62, which reflects in a higher thrust generation during the instroke phase of the flapping motion, in contradiction to what is generally reported for the clap-and-fling phenomenon in hovering flight condition (de Clercq et al, 2009; Groen et al, 2010; Lehmann et al, 2005), and individual vortex formations of the upper and lower wings. For the reduced frequencies greater than 0.62, however, this wing interaction mechanism becomes more dominant and generates greater thrust during the outstroke in combination with the arrow-shaped vortex loop that is formed by the tip vortices of both wings. Secondly, increasing flapping frequency for a given freestream velocity introduces a time shift in the appearance of vortical structures in the wake that is also correlated with the lag in the generation of the maximum thrust during both the instroke and the outstroke. This time shift is associated with the changing wing deformation characteristics, especially at the stroke reversals due to significant contribution of the wing inertia.

Analysis of the spanwise-oriented vortical structures (i.e., leading and trailing edge vortices) was made based on both spatiotemporal and spatial reconstruction results. In

the case of the spatial reconstruction method, it was observed that these structures are visualized more clearly due to the increased resolution in the streamwise direction and more data points closer to the wing roots that are available thanks to the use of upstream measurement planes with respect to the plane used in the spatiotemporal reconstruction.

It was shown that there are multiple trailing edge vortex shedding events during the instroke in all cases. A starting trailing edge vortex connected to the tip vortex also forms during the outstroke for both wings mostly closer to the wing tips and links to the root vortex which is clearly visible for the reduced frequencies smaller than 0.79. For greater values of k, trailing edge vortex shedding is less coherent. Instead, as mentioned earlier, tip vortices of upper and lower wings form a vortex loop.

Similar wake characteristics during the outstroke and the instroke are also acquired with the spatial reconstruction method but with more details. For the lowest reduced frequency case, it was shown that the orientation angle of the upper wing's tip vortices during both phases is similar in the spatiotemporal and the spatial reconstruction cases. Moreover, comparison of different flapping frequencies at the same phase of the flapping motion exposes a time shift in the appearance of the structures in accordance with the spatiotemporal reconstruction results. This coherence validates the assumption of a non-deforming wake and the use of free-stream velocity as the convection velocity and asserts the possible use of spatiotemporal reconstruction technique to assess general characteristics of the three-dimensional wake for this particular case.

II

Fundamental Research in Flapping-Wing Aerodynamics

6

Wing Flexibility Effects in Clap-and-Fling

The work described in this chapter explores the use of time-resolved tomographic PIV measurements to study a flapping-wing model, the related vortex generation mechanisms and the effect of wing flexibility on the clap-and-fling movement in particular. An experimental setup is designed and realized in a water tank by use of a single wing model and a mirror plate to simulate the wing interaction that is involved in the clap-and-fling motion. The wing model used in the experiments has the same planform as the DelFly II wings and consists of a rigid leading edge and an isotropic polyester sheet as wing surface. The thickness of the polyester sheet was varied in order to investigate the influence of flexibility. A similarity analysis based on the two-dimensional dynamic beam equation was performed to compare aeroelastic characteristics of flapping-wing motion under in-air and in-water conditions. Based on the experimental results, the evolution of vortical structures during the clap-and-peel motion is explained. General effects of the wing flexibility on the vortex formations and interactions are discussed. It was observed that the flexibility influences the behavior and the orientation of the vortices in relation to the deformation of the wing and interaction with the mirror plate.

Parts of this chapter have been published in the International Journal of Micro Air Vehicles **3(4)** (Percin et al, 2011)

6.1. Introduction

The phenomenon of force production as a result of flapping motion has been studied extensively in the literature originating from the pioneering studies of (Knoller, 1909) and (Betz, 1912), who pointed out that flapping wing motion generates an effective angle-of-attack that results in lift production with a thrust component, which is known as Knoller-Betz effect. Thenceforward, further investigations have clarified the underlying aerodynamic mechanisms, different flow topologies, and effective parameters for simplified two-dimensional flapping rigid wing motions, i.e. pitching, plunging or combined pitching-plunging (Anderson et al, 1998; Lai and Platzer, 1999; Platzer et al, 2008; Tuncer and Kaya, 2005; Young and Lai, 2007a,b; Young and S. Lai, 2004). However, the understanding of the underlying physics of the actual flapping-wing flight undoubtedly requires consideration of three-dimensional effects, as also discussed previously in Chapter 2.

It has been shown that the majority of flapping-wing studies focus on the flapping motion of rigid wings and the effect of flexibility has received relatively little attention. However, studies on the mechanical properties of insect wings report complicated variations in their stiffness and identify them definitely flexible (Combes and Daniel, 2003a; Wootton, 1981). Although aerodynamic benefits of flexibility for the insect are not completely clear (Heathcote and Gursul, 2007), there is a growing evidence that wing deformation during the flapping motion boosts thrust and lift production considerably (Gopalakrishnan and Tafti, 2010). Vanella et al (2009) carried out a computational study on a hovering two-dimensional flexible wing model for Reynolds numbers ranging from 75 to 1000. They concluded that flexibility can enhance the aerodynamic performance and the best performance was achieved when the wing was flapped at 1/3 of the natural frequency. Heathcote and Gursul (2007) performed water tunnel experiments to investigate the effect of chordwise flexibility on the propulsive efficiency of a heaving airfoil for Re of 9000 to 27000. They concluded that a certain degree of flexibility enhances the thrust coefficient and propulsive efficiency. Heathcote et al (2008) also studied the influence of spanwise flexibility and they found out that introducing a degree of spanwise flexibility affects the vortex mechanism and increases the thrust efficiency. They added that the range of Strouhal number in which spanwise flexibility was beneficial overlaps with the range observed in nature ($0.2 < Sr < 0.4$). Based on the above discussion, it can be inferred that MAVs might benefit from aerodynamic contributions of flexibility, in addition to the intrinsic low weight of flexible structures.

The clap-and-fling mechanism is the particular research interest for the present study because of its relevance to the DelFly II flapping-wing MAV. From a design optimization point of view, it is important to obtain a better understanding of the effect of flexibility on the clap-and-fling motion. Notwithstanding the extensive measurements performed on the DelFly wings, it proved difficult to link the effect of flexibility to the flow field characteristics and performance improvements, due to the anisotropic characteristics of the DelFly wings and the associated complicated aeroelastic behavior. Based on these considerations, in this chapter it is aimed to investigate the influence of wing flexibility in a more generic configuration. The experiments were performed in a water tank to permit high-quality and time-resolved three-dimensional flow field measurements via time-resolved tomographic particle image velocimetry (tomo-PIV) (Elsinga et al, 2006; Scarano, 2013). The wing model used in the experiments consists of a rigid leading edge and an isotropic

flexible wing surface made from polyester sheet; therefore it is assumed that the wing is flexible in only the chordwise direction. The flexibility was varied in the experiments by changing the thickness of the polyester sheet.

6.2. Similarity analysis

The determination of scaling laws is an important step in order to identify characteristic properties of the system under consideration and to establish which combination of parameters is of importance for the given conditions. In the current study, analysis of structural dynamics as well as fluid dynamics becomes necessary, because of the different deformation characteristics of a flapping flexible wing for in-air and in-water conditions. The Euler-Bernoulli dynamic beam equation was utilized for the analysis of similarity parameters. The general form of the equation after neglecting the rotary inertia and deformations due to shear is shown below.

$$m\frac{\partial^2 w}{\partial t^2} + EI\frac{\partial^4 w}{\partial x^4} = f(x,t) \tag{6.1}$$

It should be noted that deformation only in the chordwise direction x is considered, in accordance with the model wing used in the experiments. In Eq. 6.1, w is the deformation in the direction normal to the wing chord, m is the mass per unit chord length, E is the Young's modulus, and I is the moment of inertia. The term $f(x,t)$ on the right hand side is the forcing function, consisting of aerodynamic and inertial contributions, as given in Eq. 6.2, for a sinusoidally heaving motion of the leading edge.

$$f(x,t) = -C_{aero}\left|\omega\overline{h}\sin(\omega t)\right|\left(-\omega\overline{h}\sin(\omega t)\right) - m\left(\omega^2\overline{h}\cos(\omega t)\right) \tag{6.2}$$

Here C_{aero} is the aerodynamic multiplication factor ($C_{aero} = 0.5\rho_f\overline{c}$, where $\overline{c}$ is the mean chord length and ρ_f the fluid density), ω is the circular frequency ($\omega = 2\pi f$ with f the flapping frequency), and $\overline{h}$ is the amplitude of the heaving motion. Dimensional analysis of Eqs. 6.1 and 6.2 yields two similarity parameters, which are the ratio of elastic to aerodynamic forces (bending stiffness parameter, Eq. 6.3) and the ratio of inertial to aerodynamic forces (Eq. 6.4), reinterpreted here in relation to the flapping wing geometry.

$$\lambda = \frac{EI}{\rho_f f^2 \phi^2 R^3 c^3} \tag{6.3}$$

$$\tau = \frac{\rho_w t_w}{\rho_f R\phi} \tag{6.4}$$

In this, ϕ is the angular flapping amplitude, R the half-span length, c the chord length (taken as the mean chord in the present calculations), ρ_w the density of the wing material and t_w the thickness of the wing. It should be noted that for the dimensional analysis m is taken as $\rho_w t_w$ and $\overline{h}$ as $R\phi$.

In addition to the derivation of similarity parameters, analytical solutions of the dynamic beam equation were used for comparison of the deformation characteristics for in-air and in-water conditions. The solution was performed for a sinusoidally plunging

airfoil which is assumed to represent the cross-section of the flapping wing. Firstly, a wing of isotropic flexibility was defined as an equivalent-DelFly-wing. Secondly, a model wing for in-water conditions was defined, operating at the same order of the Reynolds number and with similar flexibility as the (equivalent) DelFly wing.

Assumptions involved in the definition of the equivalent DelFly wing are: (1) it has the same geometry ($R = 0.14$ m, $\overline{c} = 0.08$ m) and mass (88 mg for a single wing excluding the rigid leading edge) as the DelFly wing; (2) it has isotropic structural characteristics; (3) it flaps in air at 13 Hz and (4) the maximum deformation (trailing edge displacement with respect to leading edge) it experiences is equal to that of the DelFly wing. The maximum deformation for the reference case was observed to be approximately 60 % of the chord length at $0.71R$ spanwise location, based on the wing shape visualization performed by Groen (2010).

The analytical solution was then used to determine the required flexural stiffness of the equivalent-DelFly-wing. The maximum deformation of 60 % of the chord length is achieved at a flexural stiffness value of 1.06×10^{-4} Nm^2. The order of flexural stiffness agrees with the study of Combes and Daniel (2003a) who measured the flexural stiffness (both in spanwise and chordwise directions) of 16 different insect wings. Based on their correlation, the chordwise flexural stiffness for the chord length of 8 cm is estimated as approximately 10^{-4} Nm^2.

Deformation characteristics for in-water conditions were acquired for a scaled down model-wing ($R = 0.1$ m and $\overline{c} = 0.057$ m). Polyester sheet was used as a wing material and apart from reproducing the order of Reynolds number, it was aimed to satisfy two constraints: first to have approximately the same amount of maximum deformation during the flapping motion for in-air and in-water conditions; second to keep the bending stiffness parameters of the equivalent-DelFly-wing and the model-wing as close as possible. These conditions were satisfied for the case of a model wing with a thickness of 100 μm flapping at 0.75 Hz in water. The resultant bending stiffness parameters were calculated as 2.13 for equivalent-DelFly-wing and 1.63 for the model-wing. Deformations for a flapping period are compared in Fig. 6.1a. It should be noted that although it might be possible to satisfy the above-mentioned conditions with a different flapping frequency and wing thickness, current values were selected based on the limitations regarding to the experimental setup and material availability.

It is clear that the deformation characteristics in air and water are different, as already expected. The major difference can be approximated by a phase shift of 10 % of the flapping period. In order to clarify the reason of this difference, the deformation contributions of the aerodynamic and inertial effects are shown separately in Figure 6.1b. It is obvious that inertial forces are substantially diminished when conducting the experiments in water rather than air, as also evident from Eq. 6.4. It can be concluded that the effect associated to the wing-inertia term is largely reduced when the wing flaps in water, which has similar density. As a result, it is difficult to achieve the same deformation characteristics for air and water experiments. Therefore, in the current study it is only aimed to achieve order of scales of deformation and flexural bending stiffness as similar as possible to the equivalent-DelFly-wing. On the other hand, this simplified analysis reveals that for the DelFly flapping-wing motion in air, the wing inertia term may be notably influential on the wing deformation characteristics. However, it is difficult to quantify its contribution in the

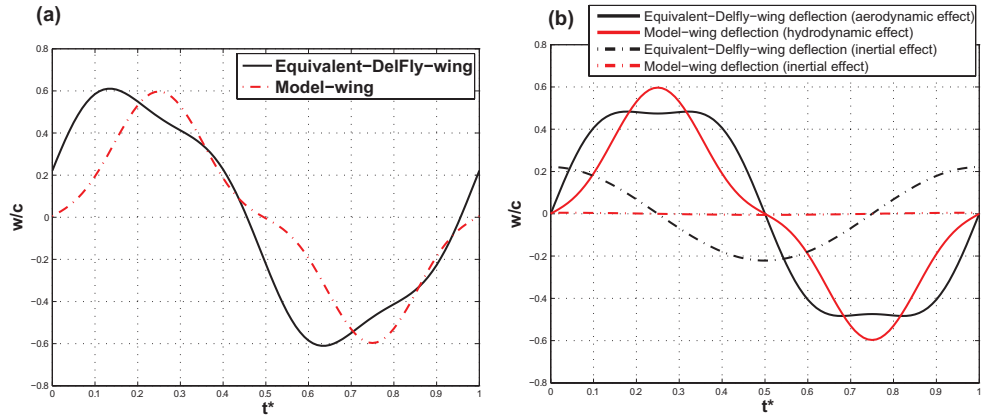

Figure 6.1: **a** Comparison of total deformations (trailing edge displacement with respect to leading edge) for the equivalent-DelFly wing flapping in air (*black*) and model-wing flapping in water (*dashed-dot red*); **b** comparison of deformations due to aerodynamic/hydrodynamic and inertial forces separately for the equivalent-DelFly-wing flapping in air and model-wing flapping in-water

actual flapping-wing situation based on the above-mentioned two-dimensional analytical solution, in view of all the simplifying assumptions regarding the structural characteristics of the wings and the calculation of the forcing function terms.

6.3. Experimental setup

6.3.1. Wing model and setup

The experiments were conducted in a water tank (Fig. 6.2a) at the Aerodynamic Laboratory of Delft University of Technology (TUDelft). A single actuated wing was used in combination with a mirror plate to simulate the clap-and-fling motion of DelFly II in hovering flight. The wing model consists of a rigid leading edge and a flexible wing surface. The leading edge is made of two D-shape carbon rods of 4 mm diameter and the wing is manufactured from transparent polyester film (see Fig. 6.2b). Four different polyester wings with thickness of 50, 100, 175 and 250 µm were used to investigate the effect of flexibility.

As shown in Fig. 6.2a, a stainless steel rod with a diameter of 15 mm, connecting with the wing model, is positioned vertically in the octagonal water tank (600 mm of diameter and 600 mm of height). The water tank is made of Plexiglass allowing full optical access for illumination and tomographic imaging, and was originally constructed to study turbulent jets (Violato and Scarano, 2011). The distance between the rod axis and the surface of the mirror plate is 10 mm. When the motor actuates the crank-arm mechanism, it drives the rod in a reciprocating rotational motion, which makes the wing flap with a total amplitude (peak-to-peak) of 50° and a frequency of 0.75 Hz. Based on the mean wing tip velocity and the mean chord length, the Reynolds number for the experimental model (Ellington, 1999) is 7500.

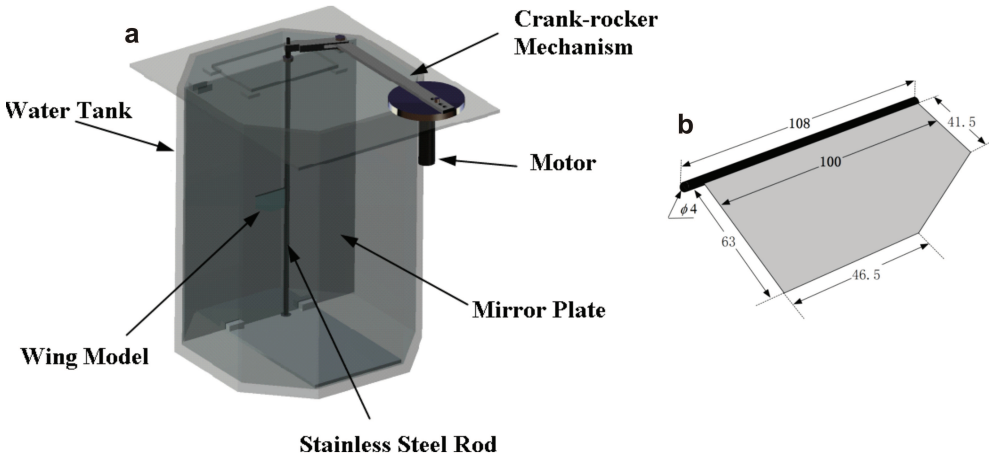

Figure 6.2: **a** Schematic representation of experimental set-up, **b** dimensions of the wing model

6.3.2. Time-resolved tomographic-PIV

High-speed tomographic-PIV measurements were carried out to acquire time-resolved three-dimensional quantitative information of the flow around the wing model. Polyamide spherical particles of 56 μm diameter were employed as tracer particles at a concentration of 0.04 particles/mm^3. An alternative method to laser was applied for volume illumination, using the light beam from a normal projector, Acer PD125D DLP, which is converged by a convex lens. Position, colour and size of the beam could be modified easily by Microsoft PowerPoint software on the computer. The light from the projector with lumen of 2000 ANSI is adequate to collect sufficient light scattered by the particles. The measurement volume of $100 \times 100 \times 40$ mm^3 in size, oriented as indicated in Fig. 6.3b where the distance $D = 70$ mm, is captured by three high-speed cameras arranged along different azimuthal directions in a horizontal plane as shown in Figure Fig. 6.3.

The digital resolution is 10 pixels/mm and the average particle image density is approximately 0.015 particles per pixel (ppp). The tomographic recording system is composed of three CMOS cameras with a resolution of 1024×1024 pixels at 5.4 kHz. The pixel pitch of the cameras is 20 μm. Each camera is equipped with a Nikon 60 mm focal objective with numerical aperture $f\# = 11$. Scheimpflug adapters are used on two cameras to align the mid-plane of the measurement volume with the focal plane. Image sequences of tracer particles are recorded with a recording frequency of 250 Hz (exposure time is 1/300 s).

6.3.3. Tomographic reconstruction

Besides synchronization of the cameras and image acquisition, DaVis 7.4 (LaVision) was also used in the image pre-processing, volume calibration, self-calibration (Wieneke, 2008), reconstruction, and three-dimensional cross-correlation based interrogation that yields the velocity vector fields.

In this experiment, the measurement volume is calibrated by scanning a plate with 9×10 dots through the volume in depth of 20 mm with steps of 5 mm. In each of the

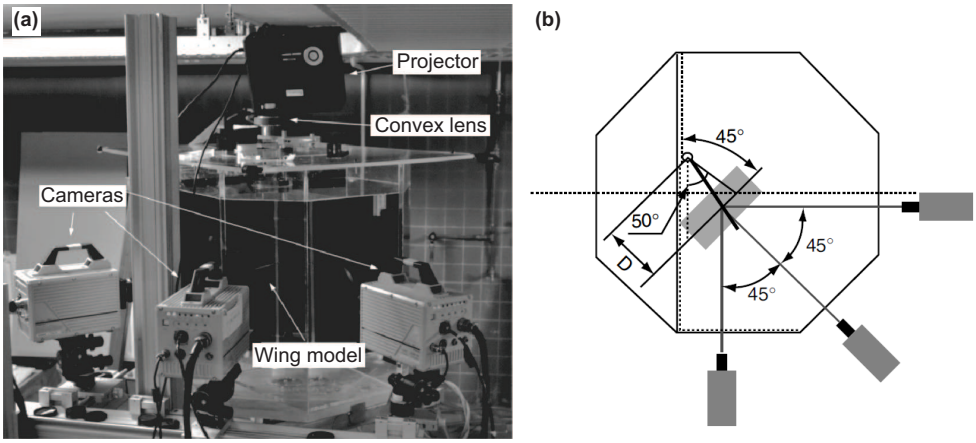

Figure 6.3: Optical arrangement for the tomographic-PIV experiments: **a** experimental arrangement in the water tank, **b** schematic representation of top view

calibration planes, the relation between the physical coordinates (x, y, z) and image coordinates is described by a 3rd order polynomial fit. Linear interpolation is used to find the corresponding image coordinates at intermediate z-locations.

The reconstruction process is improved by means of image pre-processing with background intensity removal, particle intensity equalization and a Gaussian smooth (3×3 kernel size). Reconstructed volumes are discretized at 103 voxels per mm^3. The particle images are interrogated using windows of final size $64 \times 64 \times 64$ voxels with an overlap factor of 75 %, resulting in a vector spacing of about 1.6 mm in each direction. A dataset of order $62 \times 62 \times 25$ velocity vector volumes is acquired in each region.

6.4. Results

Four polyester wings with different thickness (ranging from 50 to 250 μm) were used to investigate the effect of flexibility. In this section, the evolution of vortical structures at the clap-and-peel phase of the flapping motion is discussed. For brevity, only the cases of 100 and 250 μm wings flapping at 0.75 Hz are presented here.

In Fig. 6.4, iso-surfaces of vorticity magnitude during the clap-and-peel phase are shown for the wing with a thickness of 100 μm. The end of clap, when the wing leading edge is closest to the mirror plate, is labeled as $t = 0$ and the rear surface of the illumination volume is represented with a green slice. The wing position with respect to the symmetry plane is schematized on the left corner of each phase. The vortex formation mechanism can be explained as follows: After the onset of instroke, the wing starts to move toward the wall with the formation of leading end trailing edge vortices (LEV1 and TEV1 at $t = -0.12T$). The separating shear layer from the trailing edge forms into a discrete trailing edge vortex. Trailing and leading edge vortices grow in size as the rotation progresses ($t = -0.06T$). At the end of instroke, the trailing edge vortex sheds into the wake of the wing, whereas the leading edge vortex stretches downward behind the wing ($t = 0$). After the stroke reversal ($t = 0.06T$), the stretched leading edge vortex moves to-

ward the tapered part of the wing and interacts with the newly formed trailing edge vortex ($t = 0.12T$). The outstroke continues with the formation of a massive leading edge vortex (LEV2 at $t = 0.18T$)

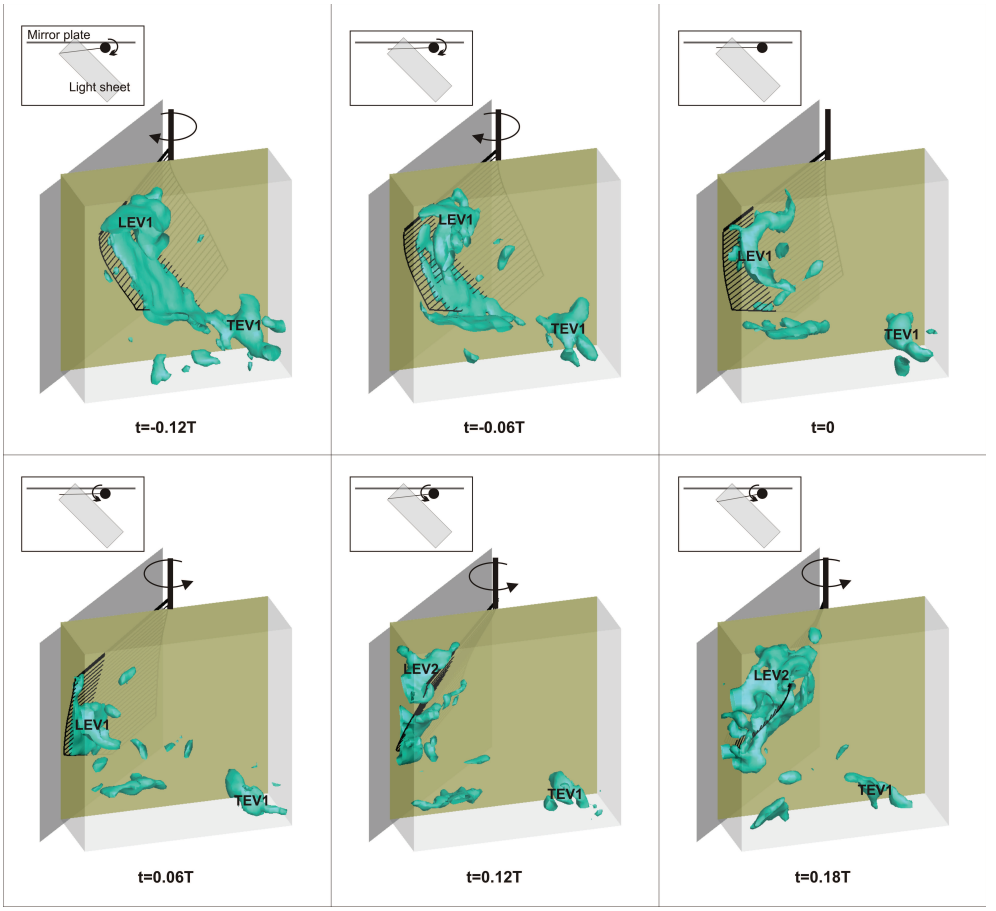

Figure 6.4: Isosurfaces of vorticity magnitude during the clap-and-fling phase ($t_w = 100\ \mu$m, $f = 0.75$ Hz)

The wing flexibility manifests its effects in the deformation of the wing during the flapping motion as well as in the related formation and generation of the vortical structures. In Fig. 6.5, contours of z-vorticity (ω_z) are plotted in the cross section plane at 70 % of the span at the early clap phase ($t = -0.12T$), comparing the wings with thickness of 100 and 250 µm.

It is clear that the flexible wing curves toward its own wake, whereas the other wing behaves as almost rigid. In the case of the rigid wing, a stronger leading edge vortex is present but rather detached from the wing surface. It is possible to indicate that this condition will result in lower lift generation than the flexible wing case where the leading edge vortex stays near the curved surface of the wing and creates a suction that works in favour of lift generation. On the other hand, the separating shear layer of the rigid wing trailing edge is

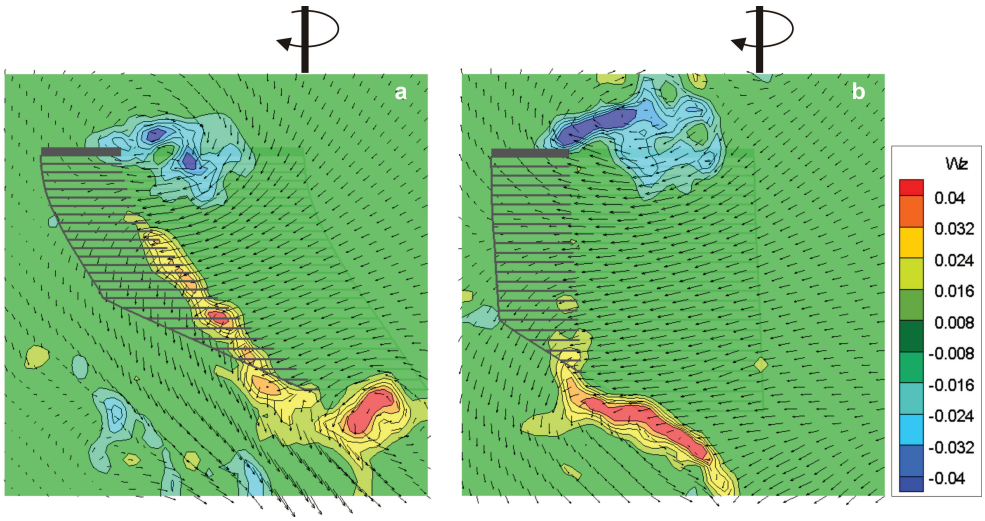

Figure 6.5: Contour plots of z-vorticity (ω_z) at 70 % of the spanwise locations of the wings with thicknesses of **a** 100 μm and **b** 250 μm at $t = -0.12T$

curved downwards, while for the flexible wing, the trailing edge vortex remains inside the wake.

The vortical formations for the rigid and flexible wings are compared at the end of the clap ($t = 0$) in Fig. 6.6. It is evident that due to the rigidity of the wing, the interaction with the wall results in stronger downwash and upwash (due to the finite distance between the rigid leading edge and the wall) which in turn cause the vortices formed during the previous instroke to convect downward and upward, respectively. As noted earlier, contrary to the rigid wing case, the leading edge vortex in the case of flexible wing stays in the wake.

The comparison of z-vorticity contours at the late peel phase (Fig. 6.7) reveals the fact that the rigid wing supinates into relatively low-velocity fluid region in comparison to the flexible wing case for which there is a stronger downwash due to the deflection of the wing. It can be speculated that this condition will result in an increase of the power requirement to fling the wing apart.

6.5. Conclusion

The applicability of time-resolved tomographic PIV for the experimental investigation of vortical structures and effects of flexibility for the clap-and-fling type flapping motion was studied in this investigation. Experiments were performed in a water tank with a model wing that consists of a rigid leading edge and an isotropic flexible polyester film. The thickness of the polyester film was changed to investigate the influence of flexibility. A similarity analysis was performed by use of the two-dimensional dynamic beam equation. This revealed the different deformation characteristics for in-air and in-water conditions. Experimental results obtained with the tomographic PIV technique allow to characterize the three-dimensional structure of the flow field around the flapping wing model. The gen-

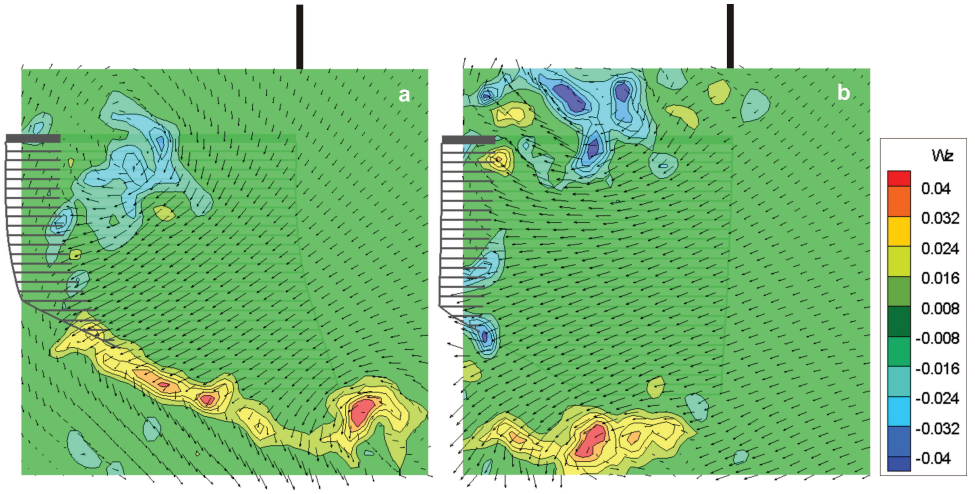

Figure 6.6: Contour plots of z-vorticity (ω_z) at 70 % of the spanwise locations of the wings with thicknesses of **a** 100 μm and **b** 250 μm at $t = 0$

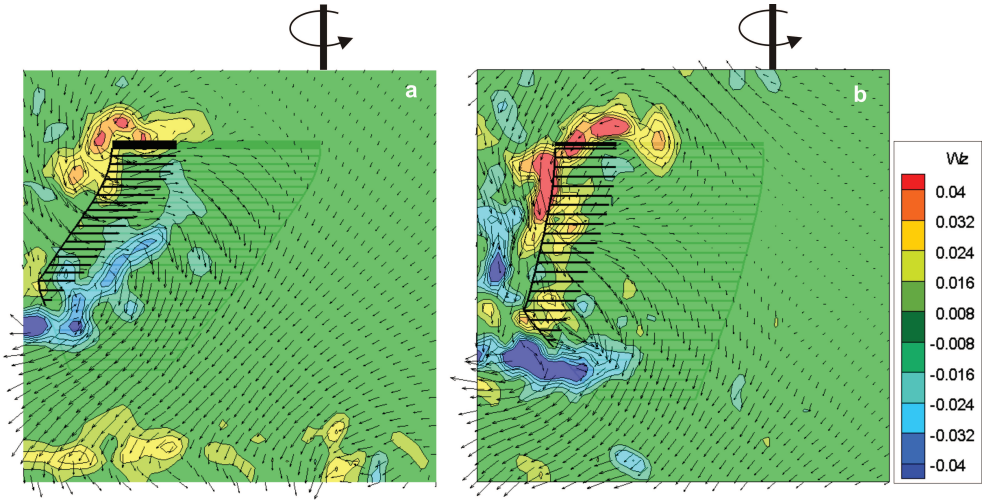

Figure 6.7: Contour plots of z-vorticity (ω_z) at 70 % of the spanwise locations of the wings with thicknesses of **a** 100 μm and **b** 250 μm at $t = 0.18T$

eral vortex formation and interaction mechanisms during the clap-and-peel phase of the flapping motion are demonstrated. It was shown that in the case of more rigid wing case, leading and trailing edge vortices stay detached from the surface of the wing and they convect upwards and downwards due to relatively strong up-downwash generated as a result of interaction with the mirror wall. Therefore, at the stroke reversal, the more rigid wing cannot benefit from the phenomenon of the wake capture. However, in the more flexible wing case, vortices from the previous stroke interact with the wing and newly generated

vortices.

Despite the fact that the wing with a thickness of 100 μm under in-water conditions was shown to correspond to the actual DelFly flapping wings in terms of bending stiffness parameter, there are obviously significant differences between the deformation characteristics of the two cases. In the DelFly flapping motion in air, the wings have a positive camber after the stroke reversals (see Chapters 3), whereas the equivalent-DelFly wing has a negative wing camber during the flapping motion under in-water conditions. Moreover, the behaviour of the vortical structures also differ between the in-air and in-water cases, resulting in different interaction characteristics between the vortices of instroke and outstroke phases. It has been shown in Chapter 4 that the LEVs that are formed during the instroke phase convects upstream with their induced velocities in the hovering flight of the DelFly. On the other hand, in the case of the equivalent-DelFly-wings flapping in water, the LEV of the instroke phase convects downwards during the stroke reversal from instroke to outstroke. This behaviour may be attributed to the absence of a mirror wing (that is simulated by a mirror plate), and hence the lack of a counter-rotating LEV, which would otherwise induce an upward directed convective velocity.

7

Three-Dimensional Flow Structures and Unsteady Forces on Pitching and Surging Revolving Flat Plates

In this chapter, the evolution of three-dimensional flow structures of revolving low-aspect-ratio flat plates is explored by means of tomographic particle image velocimetry measurements in combination with force measurements at a Reynolds number of $10,000$. *In particular, two motion kinematics are compared that result in the same terminal condition (revolution with constant angular velocity and* $45°$ *angle of attack) but which differ in the motion during the build-up phase: pitching while revolving at a constant angular velocity; or surging with a constant acceleration at a fixed angle of attack. A quasi-steady model is used in order to estimate the unsteady forces particularly in the build-up phases of the two motion kinematics. The vorticity moment theory is employed in order to assess the relation between the vortical structures and the force histories.*

Parts of this chapter have been published in Experiments in Fluids **56(2)** (Percin and van Oudheusden, 2015b)

7.1. Introduction

The flapping flight of insects and birds is a three-dimensional unsteady phenomenon, which combines pitch, plunge and sweeping motions of the wing, with three-dimensional effects being further enhanced by low values of the wing aspect ratio. This challenging phenomenon has been subject of many studies aiming to characterize the flow structures and force generation on wings undergoing aforementioned motions, especially for the low Reynolds number conditions typical of animal flight (see Lehmann, 2004; Sane, 2003, and references therein). Among these, the pitch motion of the wing to high angle of attack has received a special attention as it was shown to enhance the aerodynamic performance by the formation of additional circulation.

One of the earlier studies to investigate the effect of wing rotation on the generation of forces was reported by Dickinson (1994). He performed experiments on a two-dimensional wing model to investigate the effect of wing rotation during the stroke reversal and showed that the formation of vortical structures in the rotation phase of the motion increases forces considerably. Hamdani and Sun (2000) studied the fast pitching motion of a two-dimensional airfoil in a constant free-stream by Navier-Stokes simulations. They reported that large aerodynamic forces are generated during the rapid pitch-up which they associated with the formation and motion of new vorticity layers in addition to the previously existing thick vorticity layers. More recently, loading on a rapidly pitching nominally two-dimensional flat plate was studied by Granlund et al (2013). They investigated the effects of the pitch rate and the pitch pivot point location on the time history of lift and drag in conjunction with the flow field evolution. They found that, similar to unsteady wing theory, the pitch contribution to lift is proportional to the pitch rate and to the distance from the pivot point to the 0.75 chord point. The latter is also in agreement with the results of Sane and Dickinson (2002).

To include three-dimensional effects, Yilmaz and Rockwell (2011) explored the flow structures around a low-aspect-ratio wing with rectangular and elliptical planforms undergoing a pitch-up motion from 0° to 45° in a constant free-stream. Flow visualization with particle image velocimetry (PIV) revealed the formation of a significantly three-dimensional LEV structure. They reported a spanwise flow component with magnitudes larger than the free-stream velocity and which is directed away from the symmetry plane near the leading edge and toward the symmetry plane near the trailing edge in the fully developed state. They also observed distortion of the LEV, which is less pronounced for the elliptical wing associated with different spanwise flow structures. More recently, Hartloper and Rival (2013) studied development of forces and three-dimensional flow fields on pitching rectangular, lunate and truncate planforms of aspect ratio four placed in a free-stream flow. They reported that the LEV on the rectangular plate is compressed while it grows and consequently an arch-shaped vortex is formed. On the other hand, the formation of this structure is suppressed due to outboard convection of vorticity (rather than vortex stretching) on lunate and truncate planforms.

The aforementioned studies considered the pitch-up motion of a translating wing, yet the natural flapping flight is represented more realistically with revolving motion with the associated occurrence of spanwise variation of the flow. Moreover, Lentink and Dickinson (2009) point to the rotational inertial mechanisms (i.e. centripetal and Coriolis accelerations) in combination with the spanwise flow (Ellington et al, 1996), which are present in

the case of revolving wings, as the responsible mechanism for stabilizing the LEV and thus augmenting force generation. Recently, Jardin and David (2014) showed that the spanwise gradient of the local wing speed by itself leads to stabilization of the LEV but not to enhanced lift; the latter is observed when including the rotational inertial effects.

The flow and the aerodynamic loading on revolving wings at a constant angle of attack or with combined revolving and pitching motions, particularly in a reciprocating manner with rotation of the wings at the stroke reversals, have been studied extensively in the literature (Ozen and Rockwell, 2012, and references therein). Ozen and Rockwell (2012) investigated the flow field around a revolving low-aspect-ratio flat plate experimentally, excluding the transient phase at the start of the motion. They reported a stable LEV for angles of attack from 30° to 75° and added that the sectional structure of the LEV at the midplane is not affected by the Reynolds number in the range from 3,600 to 14,500 (based on the velocity at the radius of gyration).Venkata and Jones (2013) conducted flow visualizations and force measurements on a revolving wing in the Reynolds number range of 5,000 to 25,000 based on the velocity at 75 % span position. They showed that following the initial non-circulatory peak at the onset of the motion, the forces reach a local maximum after approximately four chords of travel and decrease to steady-state values of the first revolution. Flow visualizations revealed the burst of the LEV at the outboard section of the wing span. Furthermore, Garmann et al (2013) performed high fidelity implicit large eddy simulations to resolve the flow around a revolving low-aspect-ratio wing at a constant angle of attack. Their results revealed a coherent vortex system that is generated after the onset of the motion and which stays attached to the wing during the motion. Correspondingly, following the initial fast increase in the wing loading due to the angular acceleration of the flat plate, forces grow gradually with the settlement and strengthening of the vortical structures. However, increasing Reynolds number causes vortex breakdown in these structures, in the sense that large scale coherence gradually gives way to fragmentation and formation of vortical substructures. Nevertheless, the force generation mechanisms appear not to be adversely affected by this loss of coherence of the vortex system and on the contrary, wing loading is observed to moderately increase with increasing Reynolds number. They indicated that the reversal of the outwards spanwise flow in the core of the LEV is correlated with the vortex breakdown and formation of the unsteady substructures. Their analysis further showed that the spanwise pressure gradient and centrifugal forces are the dominant mechanisms in the generation of spanwise flow, whereas Coriolis force is not contributing to the stability of the LEV in their case. They also compared revolving and translating wings and reported that although similar patterns are present at the onset of the motion, the following period of the two motions generate significantly different flow fields. The lift-off and the subsequent breakdown of the LEV was also reported by Carr et al (2013). They investigated the effect of aspect ratio on the three-dimensional flow structures of revolving wings at 45° angle of attack. Phase-locked, phase-averaged Stereo-PIV measurements were performed on aspect ratio 2 and 4 flat plates at the Reynolds number of 5,000 based on the tip velocity. They showed that for both aspect ratios, the LEV lifts off from the wing surface and forms an arch-shaped structure in the outer-span region after 20° rotation. For the aspect ratio 2 plate, breakdown of the outboard LEV and the TV occurs around the rotation angle of 70°. They observed a stable LEV up to approximately 60 % span for the complete motion and outwards of this position, the TV and the LEV are

indistinguishable. Garmann and Visbal (2014) conducted high fidelity numerical simulations in order to investigate the flow around revolving wings at different aspect ratios. They mentioned that the chordwise growth of the LEV along the span is physically limited by the trailing edge therefore the aerodynamic forces saturate with increasing aspect ratio. They also confirmed the importance of the centrifugal forces on the LEV attachment by adding a source term in the governing equations to cancel out centrifugal forces near the wing surface resulting in the propagation of outboard LEV lift-off inwards. Recently, Bross and Rockwell (2014) reported flow field measurements on a simultaneously pitching and revolving wing and discussed the presence of distinctive vortical structures in comparison to translating-pitching and pure revolving wing cases. They showed that the vortex system involving the LEV and the TV preserves its coherence in the case of the revolving-pitching wing, while it is degraded in the case of a pure revolving wing. It is also revealed that compared to the translating-pitching wing case, in which the LEV moves away from the leading edge region relatively quickly, a more stable vortex structure is present in the revolving-pitching motion.

Whereas previous studies on plates accelerated from rest have extensively documented the aerodynamics and force generation characteristics of both translating pitching plates and revolving wings at a constant pitch angle, relatively little attention has been paid so far to the comparison with pitching revolving wings. The specific aim of the current study is therefore to experimentally explore flow characteristics of pitching/surging revolving wings, in particular regarding the impact of the wing kinematics in the build-up phase on the vortex formation and time history of the forces for a revolving wing ultimately rotating with constant angular velocity at 45° angle of attack. In the first case, indicated as revolving-pitch, the wing first accelerates up to the terminal velocity while at zero angle of attack and subsequently pitches to 45°. For the second case, referred to as revolving-surge, the wing accelerates from rest while at constant angle of attack. Thus, two wing motions result such that the two have the same terminal condition, but with a different transient behaviour in the motion build-up phase. The particular objective of the study is to characterize the initial formation, stability and the integrity of the flow structures in conjunction with the variation of the forces and to assess the impact of the build-up phase.

7.2. Experimental setup and methods

The experiments were performed in a water tank at the Aerodynamics Laboratory of Delft University of Technology (TUDelft). The octagonal water tank (600 mm of diameter and 600 mm of height) is made of Plexiglass allowing full access for illumination and optical imaging (Fig. 7.1a). A Plexiglass flat plate with sharp edges and a thickness of 3 mm was used as the rectangular wing model. It has chord length (c) of 50 mm, a span length (b) of 100 mm, resulting in an aspect ratio of 2 (Fig. 7.1b). The wing model was positioned at approximately $5c$ distance from the water surface, $7c$ distance from the bottom wall and $4.2c$ (wing tip to wall) distance from the side wall and tests were carried out to verify that with these settings the results are not affected by wall or free-surface interference effects. A brushed DC motor with a gearbox (gear ratio of 132:1) that was connected to the main vertical axis (y axis) of the setup drove the wing in revolution. The wing model was pitched about its leading edge (z axis) by a waterproof servo motor that was placed in the servo box which also contains the force sensor.

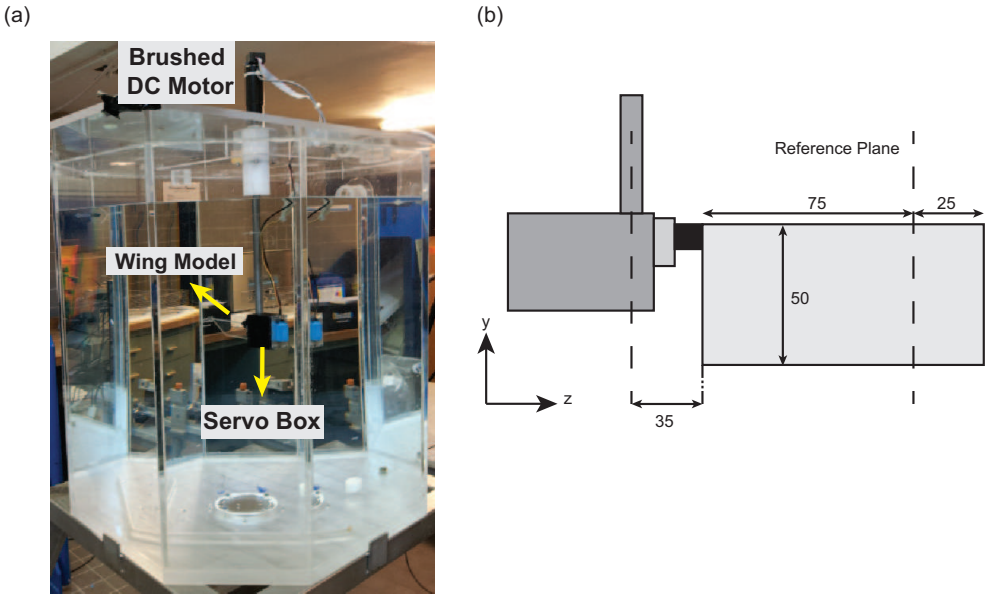

Figure 7.1: **a** Experimental arrangement in the water tank, **b** dimensions of the wing model

7.2.1. Motion kinematics

The three-quarter span length of the wing model was taken as the reference position for defining the terminal velocity (V_t) and non-dimensional parameters, such as the convective time ($t^* = t \times V_t/c$) and chords traveled ($d^* = d/c$ where d is the wing displacement at the reference position). The distance between the root chord and the rotation axis is 35 mm and the radius of gyration is 90 mm, resulting in a Rossby number of 1.8. The revolving-pitching motion kinematics used in the experiments can be described as follows (Fig. 7.2a): the motion is initiated by a constant acceleration from rest to $V_t = 0.2$ m/s (corresponding to a Reynolds number of 10,000 based on the wing chord length) at an angle of attack (α) of 0° over $t^* = 2$ ($d^* = 1$ and the revolution angle $\phi = 25.8°$); this is then followed by a period in which the wing pitches up to $\alpha = 45°$ over $t^* = 1$ ($d^* = 1$) at a constant pitch rate ($\dot{\alpha} = 3.14$ rad/s corresponding to a non-dimensional pitching rate of $k = \dot{\alpha}c/(2V_t) = 0.39$); and the wing continues to revolve at a constant rate at $\alpha = 45°$. On the other hand, in the revolving-surging motion (Fig. 7.2b), the wing motion is initiated at 45° angle of attack with an acceleration period from rest to $V_t = 0.2$ m/s over $t^* = 2$ ($d^* = 1$) after which the wing remains to revolve at a constant angle of attack and constant rate. During the measurements, real time position and rotational velocity information was acquired from the motor encoder at 33 Hz data acquisition frequency to check the motion kinematics. The accuracy of the brushed DC motor is $0.018c$ (corresponding to 0.46°) in position and $0.0125V_t$ in velocity. In all experiments, the entire travel distance is $14c$ ($d^* = 14$) corresponding to one full revolution. Although the forces were captured for the full motion, flow field measurements were limited to the first $7c$ of travel.

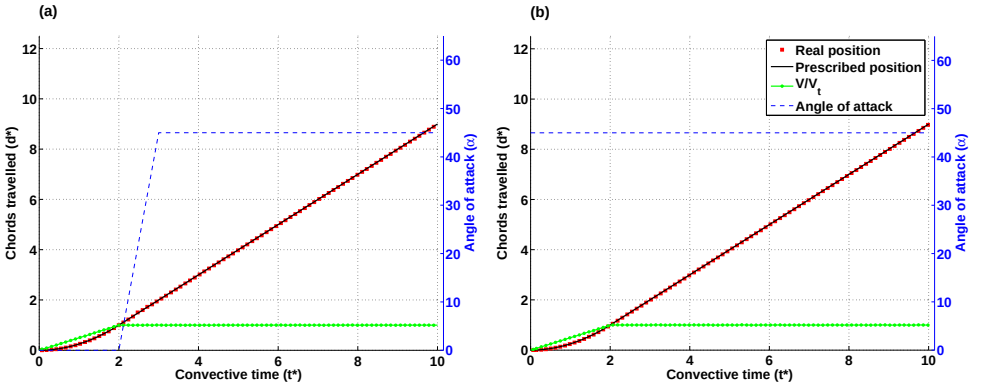

Figure 7.2: Kinematics of the **a** revolving-pitching and **b** revolving-surging motions

7.2.2. Measurement and estimation of the unsteady forces

Six components of forces and moments were measured by use of a water-submergible ATI Nano17/IP68 force sensor. Force signals were acquired at 2 kHz data acquisition frequency via an in-house developed LabVIEW code that also controls the motors and synchronizes the wing motion with the force data acquisition and the PIV measurements. Ensemble averaging of forces and moments was performed over 20 repetitions of the experiments for the pitching case and 50 repetitions for the surging case. The averaged force and moment data were then filtered to remove electrical noise and mechanical vibrations of the driving system as well as the natural frequency of the test rig (16.6 Hz) in the signal, by means of a Chebyshev Type II low-pass filter with a cut-off frequency of 15 Hz. A forward-backward filtering technique was used in order to prevent time-shift of the data. Lift and drag are normalized by use of the terminal velocity V_t and wing surface area, in order to produce force coefficients (c_L and c_D, respectively). When calculating the measurement uncertainty from the raw unfiltered data and number of repetitions of the experiments, the average uncertainty in the calculated force coefficients is 6 % of the steady-state mean values for the surging case and 12 % for the pitching case with 95 % confidence interval. The increased level of uncertainty in the revolving-pitching motion is caused by the smaller number of repetitions and increased level of vibrations during the pitch-up. However, this calculation of the uncertainty based on the raw signal also includes the contribution of the structural resonance of the test rig due to impulsive start of the motion as well as the sensor noise. Therefore, the uncertainty in the measurements was also calculated based on the 15 Hz low-pass filtered signal which results in 0.5 % and 1.5 % average uncertainties in the revolving-surging and revolving-pitching cases, respectively. These values are considered to be representative for the reported measurement data.

In addition to the measurements, a quasi-steady model (Sane and Dickinson, 2002) was used to estimate the evolution of the unsteady forces for the given kinematics. In this model, the instantaneous force is composed of three main contributions:

$$F_i = F_{\text{revolution}} + F_{\text{inertial}} + F_{\text{rotation}} \tag{7.1}$$

The first term on the right hand side of Eq. 7.1 stands for the force component due to

circulatory effects as a result of the revolving (curvilinear) motion of the wing at a certain angle of attack. Normal and tangential force components were approximated based on steady-state mean values measured on the revolving wing at various angles of attack and Re. Steady-state mean values of force measurements at different angles of attack were interpolated to estimate revolution related forces during the pitch-up motion. A similar approach was employed for the estimation of the revolving motion component during the acceleration phase of the surging case by use of force measurements performed on a revolving-surging wing at various Re at 45° angle of attack.

The second term is the force due to inertia of the added mass of the fluid acting normal to the wing surface. It is estimated by use of an approximation derived for an infinitesimally thin two-dimensional plate moving in an inviscid fluid (Sedov, 1965) and integrating the sectional values over the spanwise direction. For the rectangular wing model, the equation is simplified as follows:

$$F_{\text{inertial}} = \rho \frac{\pi}{4} c^2 \ddot{\phi} \sin\alpha \int_{r_{root}}^{r_{tip}} r\, dr + \rho \ddot{\alpha} \frac{\pi}{8} c^3 b \tag{7.2}$$

where ρ is the fluid density, $\ddot{\phi}$ is the angular acceleration of the revolving motion, r is the spanwise distance from the revolution axis and $\ddot{\alpha}$ is the angular acceleration of the pitch-up motion.

The last term in Eq. 7.1 is the contribution due to the pitch-up motion of the wing which also acts in the wing-normal direction. The pitching motion results in varying local velocities in the chordwise direction which in turn generates a varying effective angle of attack distribution along the chord. Similar as in the unsteady airfoil theory, this effect can be considered equivalent to adding camber to a non-pitching airfoil such that it imparts an equivalent downwash distribution along the plate. Likewise, the motion can be decomposed into two parts with regard to the mid-chord position: (1) a uniform motion of the plate at a velocity that is proportional to the pitch rate and the distance between the mid-chord position and the pitching pivot point; (2) a rotational motion of the plate about the mid-chord point. The former generates a uniform downwash distribution along the chordline, the value of which is constant for a constant pitch rate and fixed pitching point. This component can, hence, be interpreted as a dynamic angle of attack effect. The latter motion component induces a downwash that varies linearly with respect to mid-chord point, so that it can be considered as a dynamic camber effect.

Following thin airfoil theory and integrating the sectional contribution over the span of the wing, the theoretical estimation of this circulatory force component is given as (Ellington, 1984c; Granlund et al, 2013; Sane and Dickinson, 2002):

$$F_{\text{rotation}} = \rho \pi c^2 \dot{\phi} \dot{\alpha} (0.75 - \hat{x}_0) \int_{r_{root}}^{r_{tip}} r\, dr \tag{7.3}$$

where $\dot{\phi}$ is the angular velocity of the revolving motion, $\dot{\alpha}$ is the angular velocity of the pitch-up motion and $\hat{x}_0$ is the non-dimensional distance of the pitching pivot point from the leading edge.

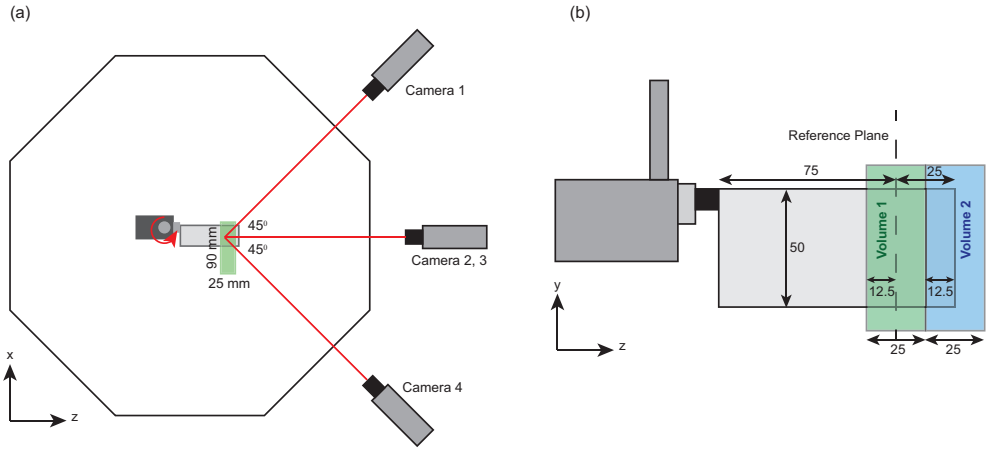

Figure 7.3: **a** Sketch of the top view of the experimental setup with camera arrangement, **b** wing model and measurement volume arrangement

7.2.3. Tomographic particle image velocimetry

Three-dimensional quantitative information of the flow around the outboard section of the wing model was acquired via phase-locked tomographic PIV (Tomo-PIV) measurements (Scarano, 2013). At each run, a double-frame image was captured at a specific phase of the wing motion. Repeated runs were performed with sufficient time intervals to restore quiescent conditions in the water tank. The measurement volume of $90 \times 70 \times 25$ mm^3 in size (Fig. 7.3a) was positioned at two different spanwise locations side by side as shown in Fig. 7.3b. Then, a Kriging regression technique (de Baar et al, 2014) with a correlating length of 2 mm in all directions was used in order to combine the two measurement volumes and to provide a complete visualization of the flow field. The starting position of the wing was adjusted based on the desired measurement phase so as to have the wing oriented normal to the measurement volume during image acquisition. For each measurement phase, the experiments were repeated for three times and vector fields are ensemble-averaged in order to improve signal-to-noise ratio. The volume was illuminated by a double-pulsed Nd:Yag laser at a wavelength of 532 nm. Polyamide spherical particles of 56 μm diameter were employed as tracers at a concentration of 0.4 particles/mm^3. The motion of tracer particles was captured by four 12 bit CCD cameras with a resolution of 1376×1040 pixels and a pixel pitch of 6.45 μm. Three cameras were arranged along different azimuthal directions in a horizontal plane at an angle of 45° with respect to each other while the fourth camera was positioned above the mid-camera in a vertical plane at an angle of 30° with respect to the horizontal plane (Fig. 7.3a). Each camera was equipped with a Nikon 60 mm focal length objective with numerical aperture $f\# = 11$. Scheimpflug adapters were used on the three off-axis cameras to align the mid-plane of the measurement volume with the focal plane. The digital resolution is 15 pixels/mm and the average particle image density is approximately 0.04 particles per pixel (ppp). Image preprocessing, volume calibration, self-calibration, reconstruction, and three-dimensional cross-correlation based interrogation were performed in LaVision DaVis 8.1.5. The mea-

surement volume was calibrated by scanning a plate with 9 × 10 dots through the volume in depth of 25 mm with steps of 5 mm. In each calibration plane, the relation between the physical coordinates and image coordinates is described by a 3^{rd} order polynomial fit. Linear interpolation is then used to find corresponding image coordinates at intermediate z locations. Image pre-processing with background intensity removal, particle intensity normalization and a Gaussian smooth with 3 × 3 kernel size was performed in order to improve the volume reconstruction process. Particle images were interrogated using windows of final size 32 × 32 × 32 voxels with an overlap factor of 50 %. The resultant vector spacing is 1.0 mm in each direction forming a dataset of 87 × 68 × 24 velocity vectors in the measurement volume.

7.3. Results

7.3.1. Evolution of unsteady forces

Figure 7.4 represents the time variation of lift and drag coefficients for both revolving-pitching and revolving-surging motions. Note that for sake of comparison, the origin for the horizontal axis, which expresses the elapsed time in terms of chords traveled (d^*), has been defined such that the start of the pitch-up phase for the pitching wing and the start of the acceleration phase for the surging wing (i.e. the two build-up phases) match and that for both cases the terminal condition is reached at $d^* = 1$.

In the case of the revolving-pitching wing motion, during the acceleration phase that precedes the pitch-up, the model experiences very low forces: nominally zero lift due to its zero angle of attack and a slight drag ($c_D = 0.08$) which is attributed to added mass and skin friction contributions. This phase is then followed by the pitch-up motion, which is characterized by four prominent features: initial strong rise of the lift coefficient due to non-circulatory effects resulting from the rotational acceleration at the onset of this phase; persistent and high lift coefficient values which also have an increasing trend during the period of constant pitch rate following the initial non-circulatory peak; nearly linear increase of the drag coefficient as the pitch angle increases; secondary non-circulatory peak in the opposite sense at the end of the motion due to the rotational deceleration of the model. The growth of lift and drag coefficients in this phase of the motion basically originates from the increasing angle of attack which has twofold effects on the force components: it promotes flow separation and growth of the LEV circulation which in turn enhance the circulatory force component; secondly it results in the tilting of the wing-normal vector toward the horizontal direction so that the drag component of the normal force increases gradually with increasing angle of attack. These features are captured fairly well by the quasi-steady model albeit with a slight over-prediction of the magnitudes. Also, the added mass peaks due to acceleration and deceleration of the wing during the pitch-up motion are not reproduced precisely because the rotational acceleration of the waterproof servo motor is not a controllable and well-defined parameter and it was estimated roughly for the calculations. A further source of discrepancy for the constant velocity pitch-up phase of the motion originates from the fact that the force component due to the revolving motion ($F_{\text{revolution}}$) is estimated based on the steady-state force values of experimental cases for wings undergoing revolving motion at various angles of attack. These steady-state values are reached approximately $4c$ of travel after the start of the motion in the experiments,

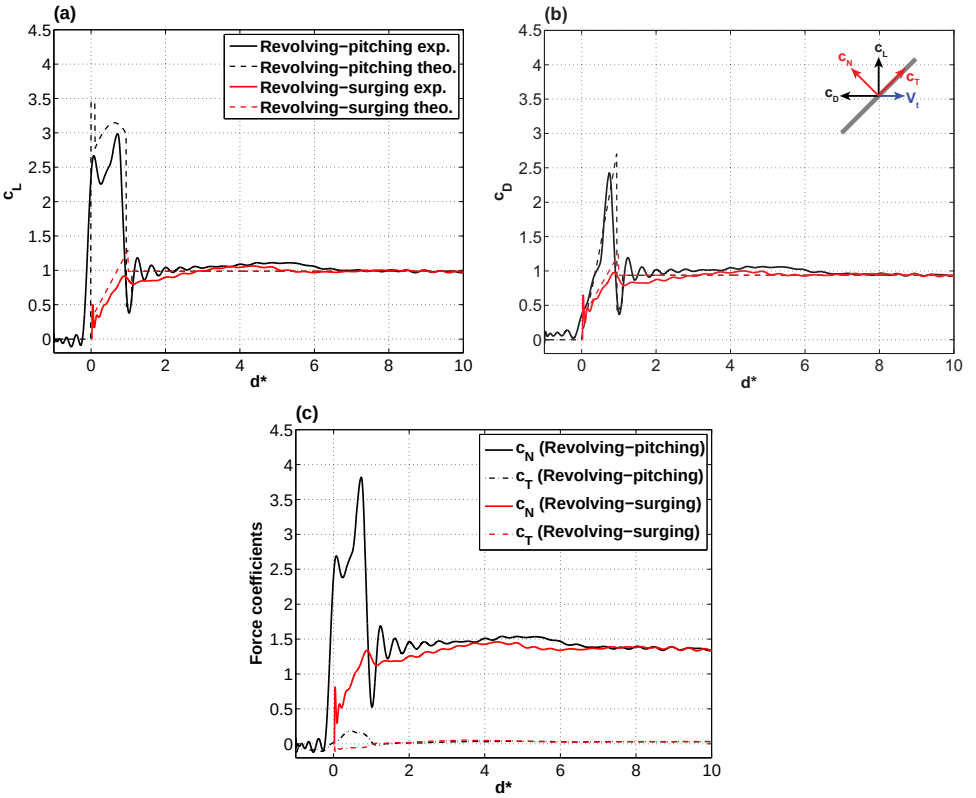

Figure 7.4: Temporal evolution of **a** lift and **b** drag coefficients for the wings undergoing revolving-pitching (*black*) and revolving-surging (*red*) motions with theoretical estimations based on the quasi-steady model (*dashed*), **c** normal (*full*) and tangential (*dashed*) force coefficients for the wings undergoing revolving-pitching (*black*) and revolving-surging motions (*red*)

whereas in the model it is assumed that the wing generates that level of circulatory force as soon as it reaches a certain angle of attack during the pitch-up motion. It takes a finite time for the growth of circulation so that the wing does not achieve such levels of forces for a given angle of attack immediately, however it is observed that force levels comparable to the steady state are reached already at the end of the transient phase, which is much faster than the build-up rate predicted by the Wagner theory. Furthermore, the theoretical estimation of the F_{rotation} is essentially based on the calculation of the bound circulation of a wing with an established Kutta condition during the pitching motion in the context of potential flow theory. However, in reality the wing does not reach that state in the pitch-up phase (i.e. it does not generate that amount of circulation nor does it fully establish the Kutta condition), which might be considered as another source for the overprediction of the forces. Subsequently, after completion of the pitch-up motion and with the model revolving at a constant rate at $\alpha = 45°$, force coefficients increase slightly, reaching a maximum at around $d^* = 5.4$ ($c_L = 1.10$ and $c_D = 1.07$). After a following decrease of the forces,

more-or-less steady-state values ($c_L = 0.98$ and $c_D = 0.96$) are reached at approximately $d^* = 7$.

In the revolving-surging wing case, the acceleration phase should in principle display a constant non-circulatory force contribution and gradually increasing circulatory force, while some spurious force peaks can be observed that are attributed to test rig vibrations as a result of the impulsive start of the motion. The force coefficients peak at the end of the acceleration phase, which is then followed by a slight decrease as the added mass contribution stops to be active, and a subsequent increase due to circulatory effects until they reach maximum values ($c_L = 1.07$ and $c_D = 0.99$) after 4.3 chord lengths of travel with respect to the start of the motion. Subsequently, forces decrease to steady state values which are equal to those of the revolving-pitching wing case. Theoretical estimation of the forces in the acceleration phase of the motion yields reasonable values also for this case. The added mass contribution evident at the very start of the motion is calculated in a reasonable approximation, while the contribution due to the revolving motion (i.e. circulatory component) is estimated less accurately due to the use of steady-state values of revolving wing experiments at different Re, which are higher than those of a wing during the build-up phase of the LEV and associated circulation. This results in overestimation of the lift and drag coefficients.

It is clear that in both cases mainly normal forces are generated throughout the complete motion whereas tangential forces remain insignificant (Fig. 7.4c). During the pitch-up period, the normal force can be considered as a superposition of the rotational contribution (calculated as approximately 2.6 by use of the quasi-steady model) and the increasing contribution of the circulatory component with increasing angle of attack. At smaller angles of attack, a small tangential force is generated (with a maximum of $c_T = 0.18$) but it vanishes with increasing angle of attack. This force most probably stems from a leading-edge suction effect: a positive tangential force is generated due to acceleration of the fluid around the sharp leading edge which transforms into a normal force component with the increase of angle of attack beyond the static stall limits and formation of the LEV (Gülçat, 2010), also known as Polhamus' leading edge suction analogy (Polhamus, 1971). In the case of the revolving-surging wing, mostly normal forces are generated which is in accordance with the findings of Birch et al (2004) who showed that even at relatively low Re, the force vector is normal to the wing surface indicating the dominance of pressure forces. In the post build-up phase of both motions, the pitching moment displays steady characteristics yielding a stationary center of pressure at approximately $0.4c$ chordwise position.

The most prominent difference between the force histories of the two cases is the substantially different force generation during the initial phases of both motions in which the pitching wing outperforms the surging wing, with the latter hardly reaching the level of steady-state values. In the subsequent phase of both motions, from $d^* = 1$ until $d^* = 7$, the two cases display slightly different force histories with the revolving-pitching wing producing higher lift and drag in general. There is a local maximum in the force histories of both cases, appearing earlier for the revolving-surging motion. Apparently, the different start-up of the motion and build-up of the forces affect the evolution of forces and accordingly flow structures at least until six chords of travel after the build-up phase has ended.

7.3.2. Three-dimensional flow fields

Three-dimensional flow structures around the outboard part of the revolving flat plate are visualized by means of isosurfaces of the non-dimensional Q criterion ($Q/(V_t/c)^2$) for both motions. Three-dimensional vortical structures are complemented with contour plots of non-dimensional out-of-plane vorticity ($\omega_z c/V_t$) and out-of-plane velocity (viz. spanwise velocity - V_z/V_t) in the reference plane at 75% wing span, to facilitate interpretation of the results. Only half of the flat plate model is depicted in the figures, whereas the spanwise extent of the flow measurement domain ranges from approximately 0.62 to 1.12 of the wing span (see Fig. 7.3). The start of the pitch-up phase of the revolving-pitching wing motion is defined as $d^* = 0$ to match motion kinematics for both cases, similar as in the representation of the force data. The pitch-up phase of the revolving-pitching wing motion is resolved by two instants that are the mid pitch-up ($d^* = 0.5$ and $\alpha = 22.5°$) and the end of the pitch-up ($d^* = 1$ and $\alpha = 45°$) in Fig. 7.5. The subsequent part of the motion is represented by four phases ($d^* = 2,3,4$ and 5) in Figs. 7.6 and 7.8. Likewise, the accelerating part of the revolving-surging case is investigated in two instants corresponding to half-way acceleration ($d^* = 0.5$, and wing speed $V = 0.71V_t$) and end of the acceleration ($d^* = 1$ and $V = V_t$) in Fig. 7.5, whereas, the ensuing period of the motion is captured at six consecutive instants ($d^* = 1.5,2,3,4,5$ and 6) in Figs. 7.6 and 7.8. Note that every chord of travel in the reference plane corresponds to $\phi = 25.8°$ of rotation and the wing completes one full revolution approximately at $d^* = 14$ so that the presented data are not affected by the interaction of the wing with its own wake.

In addition to the visualization of the flow structures, the position and cumulative circulation of the LEV (or LEVs in the case of presence of secondary LEVs) is calculated based on the spanwise component of vorticity ($\Gamma = \iint_A \omega_z \, dx \, dy$) in the reference plane and it is non-dimensionalized by V_t and c ($\Gamma^* = \Gamma/(V_t c)$). The center of the LEV is tracked by use of the γ_1 scheme, which is primarily based on the topology of the vector field (Graftieaux et al, 2001). As this algorithm is not Galilean invariant, the calculations were performed in a non-inertial coordinate system that is moving with the wing. In the case of multiple LEVs present in the flow field, the position of the initial most coherent vortex was registered. In order to define the calculation region for the LEV circulation, the vortex core detection algorithm is employed (γ_2) as described by Graftieaux et al (2001). Cumulative LEV circulation for each instant was calculated by integrating the spanwise component of vorticity within the $\gamma_2 = 2/\pi$ contours. Moreover, the flux of the spanwise component of vorticity ($q = \iint_A V_z \omega_z \, dx \, dy$) is calculated at several chordwise oriented planes in the first measurement volume and non-dimensionalized by $V_t^2 c$. The integration was performed on the data points which satisfy the criteria of $\omega_z c/V_t > 1.25$ and $|V_z/V_t| > 0.01$ (note that the selection of the precise threshold values is not critical and use of different values does not lead to significantly different results). The calculation region was defined as a rectangular zone that is limited by the leading edge and a half chord distance aft of the trailing edge in x direction. The lower edge in y direction is aligned with the trailing edge position whereas the upper edge coincides with the border of the field of view (see the spanwise vorticity plot at $d^* = 1$ of the revolving-surging case in Fig. 7.5).

Flow field structure

Temporal evolution of flow structures during the build-up phases of the motions (pitch-up phase in the pitching motion, acceleration phase in the surging motion) are shown in

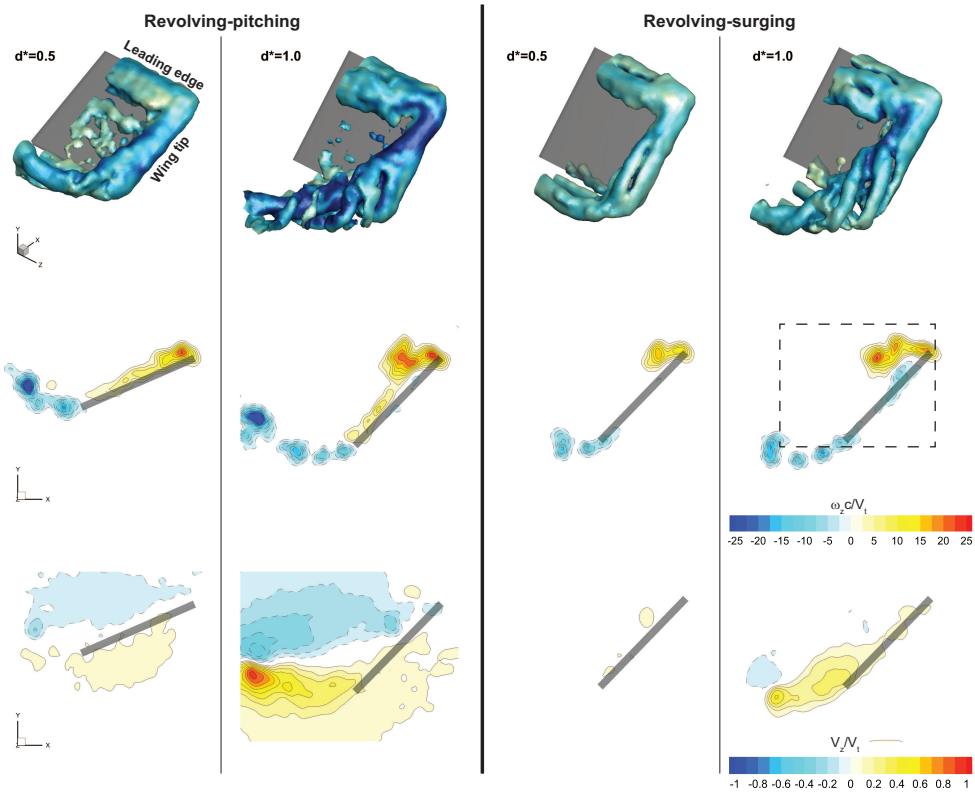

Figure 7.5: Isosurfaces of $Q/(V_t/c)^2 = 3.125$ coloured by vorticity magnitude (*first row*), contours of non-dimensional out-of-plane vorticity ($\omega_z c/V_t$) in the reference plane (*second row*) and contours of non-dimensional spanwise velocity (V_z/V_t) in the reference plane (*third row*) plotted in the build-up phase (the pitch-up phase of the revolving-pitching motion and the acceleration phase of the revolving-surging motion) for the revolving-pitching and revolving-surging cases (the rectangular zone that was used in the calculation of the spanwise vorticity flux is shown in the out-of-plane vorticity plot of the revolving-surging wing case at $d^* = 1$)

Fig. 7.5. The flow field around the pitching wing at the mid-pitch-up position ($d^* = 0.5$) stands out with well-defined and coherent vortical structures, i.e., a LEV, a TV and a TEV as the starting vortex of the motion. These initial structures are all connected to each other and have two-dimensional characteristics at the mid pitch-up phase with no appreciable spanwise flow pattern present in relation to the vortex positions (see bottom diagram). However, this scene has changed at the end of the pitch-up motion ($d^* = 1.0$): the TEV extends toward the wake of the wing model while sustaining its linkage to the TV; the TV has a conical shape with swirling features of small scale vortical structures which appear around the base of the conical formation and extend along the trailing edge as secondary TEVs (present as a train of vorticity structures in the contour plots of out-of-plane vorticity); the LEV is larger in size and slightly tilted downstream in the inward region of the wing. The vorticity patterns visualized in the reference plane bear a close resemblance to the measurements of a translating-pitching plate under similar conditions, as reported by

Yu and Bernal (2013). Although a similar vortex loop structure is observed in the revolving-surging wing motion case, these structures display different characteristics in terms of coherence. Clearly, at the position of $d^* = 0.5$, the TV already displays slightly fragmented formation which becomes more evident in the following instant ($d^* = 1$). The TV is divided into swirling features at the bottom side and these are all connected to a train of co-rotating trailing edge vortices as in the revolving-pitching wing case. Although both cases have similar morphology in terms of vortical structures, it may be observed that in the pitch case, the LEV is positioned closer to the wing surface and the TEV is stronger due to the high trailing edge velocity induced by the pitching motion. Moreover, the evolution of spanwise flow in the reference plane occurs differently. At the mid-pitch position, contours of positive spanwise flow (toward the wing tip) on the upstream side of the wing and negative spanwise flow (toward the wing root) on the downstream side of the wing are present while no considerable spanwise flow occurs around the wing in the reference plane in the middle of the acceleration phase in the revolving-surging motion. As the motion progresses for both cases, the positive spanwise flow pattern appears around the trailing edge on the downstream side of the wing in accordance with the evolution and positioning of the tip vortex.

At the position of $d^* = 2$, when the constant final motion has been established for one chord of travel (Fig. 7.6), in the revolving-pitching wing case, the LEV has burst into smaller structures and lifts off from the wing surface. The TV, on the other hand, loses its conical shape and starts segmenting into longitudinal structures extending along the tip. On the inner side of this segmented structure, there is still a coherent vortex formation extending into the wake and connecting to the starting vortex. Previously shed clockwise rotating secondary TEVs are coupled with counter-rotating vortical structures which are derived from counterclockwise vorticity formed during the pitch-up motion of the wing. The segmentation of the TV and the burst of the LEV become more significant in the following phase ($d^* = 3$). The initial LEV still stays in the vicinity of the wing but is located more downstream of the leading edge, whereas a large segment of the TV also unpins from the wing surface. A similar behaviour of the LEV is observed also in the revolving-surging wing case. At $d^* = 2$, the initial LEV is clearly detached from the wing surface and secondary small scale vortical structures emanate from the leading edge, which appear as individual blobs in the shear layer extending from the leading edge in the out-of-plane vorticity contours in the reference plane. The TV is more fragmented with respect to that of the revolving-pitching motion and a series of finger-like co-rotating TEVs are shed from the trailing edge. At the position of $d^* = 3$, the vortex formations display less coherent and more chaotic features. Notwithstanding significant differences in the spanwise flow patterns during the build-up phases of both cases, they now generate qualitatively similar flow fields in the reference plane albeit with different magnitudes. In both cases, at $d^* = 2$, the spanwise flow is confined within the LEV and TEV and it is directed toward the tip. The spanwise flow along the LEV is not observed in the previous stages of both motions. The existence of such a flow pattern can be explained by the three-dimensionality of the vortex system and the associated presence of a pressure gradient in the spanwise direction. As the motion continues and the LEV moves downstream, the spanwise flow pattern that is initially located near the leading edge starts to move along the wing chord toward the trailing edge.

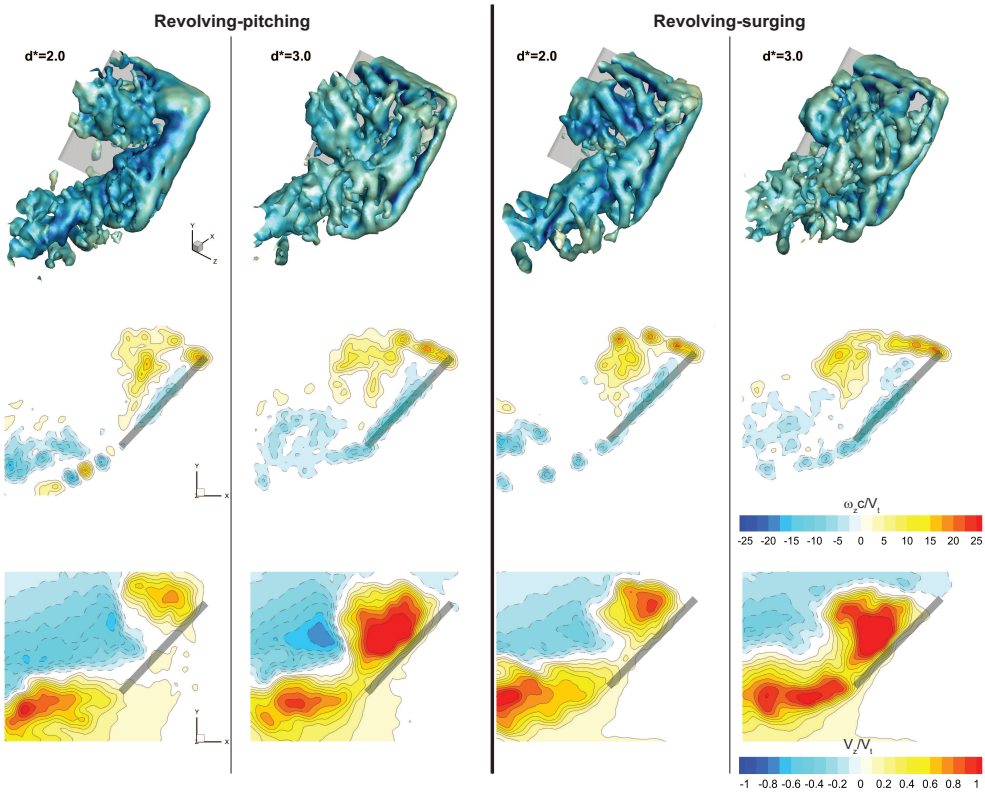

Figure 7.6: Isosurfaces of $Q/(V_t/c)^2 = 3.125$ coloured by vorticity magnitude (*first row*), contours of non-dimensional out-of-plane vorticity ($\omega_z c/V_t$) in the reference plane (*second row*) and contours of non-dimensional spanwise velocity (V_z/V_t) in the reference plane (*third row*) plotted at two instants ($d^* = 2$ and 3) for the revolving-pitching and revolving-surging cases

To better visualize the vortex formations at the phase of $d^* = 2$, when the departure of the initial LEV from the leading edge and instabilities at the substructure level are observed for the first time, close up views of isosurfaces of the Q criterion coloured by helicity density are shown in Fig. 7.7. Helicity density is the dot product of the velocity and vorticity vectors, integral of which is the helicity that is associated to the topology of the vortex lines in terms of having knots or linkages (Moffatt and Tsinober, 1992). Helicity density is also used for the detection of the vortex cores (Degani et al, 1990) and non-zero helicity indicates a helical vortex structure with an axial flow. In the case of the revolving-pitching motion, the LEV forms an arch-shaped structure with its outboard leg pinned around the wing tip corner. The inboard structure is not captured due to the limited extent of the measurement domain, but is presumed to display an inner leg reattachment inboards closer to the root. The revolving-surging wing has a similar arch-shaped structure, which was also reported by Garmann et al (2013) for a lower aspect ratio wing and different acceleration kinematics and by Carr et al (2013) for different acceleration kinematics. However, the outer leg of this structure does not attach to the wing surface at the front corner but

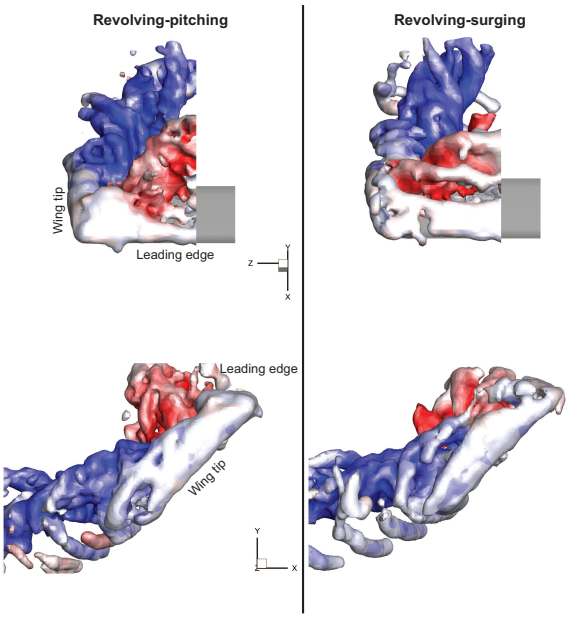

Figure 7.7: Isosurfaces of $Q/(V_t/c)^2 = 5$ coloured by helicity density (*red* positive, *blue* negative) plotted at the position of $d^* = 2$ for the revolving-pitching and -surging cases (*above* top view, *below* side view)

slightly more toward the trailing edge (near 0.4c). There are also secondary vortex formations rolling around the lifted-off LEV. In both cases, a helical LEV structure is present with a positive helicity density that is indicative of outwards spanwise flow aligned with the vorticity vector (as evident in Fig. 7.6). This implies flux of vorticity with the axial flow. The occurrence of counter-rotating vortical elements below the TEV in the pitch case and their absence for the surge case, as discussed in relation to Fig. 7.6, is also evident in the side-views of Fig. 7.7.

In the subsequent phases of the motion, the coherency of the initial vortex system is completely lost and there are small scale unsteady substructures spread over an increasing part of the measurement volume (Fig. 7.8). Notwithstanding the obscurity created by these incoherent structures (note that a slightly higher isovalue for the Q criterion is used in Fig. 7.8 in order to avoid overemphasis of these structures), there are still certain features similar to both cases: feeding of leading edge vorticity in the form of consecutive longitudinal structures extending along the leading edge; linkage between these secondary leading edge structures and the vortex formations of the wing tip, which are not attached to the wing surface all along the tip. The contour plots of out-of-plane vorticity in the reference plane show that vorticity layers in the case of revolving-pitching motion tend to be more curved toward the wing in the wake at both instances which can explain the generation of higher forces in this case. Arguably, the relative positioning of these vorticity layers will become virtually identical to that of the revolving-surging wing case after approximately $d^* = 7$ when the two cases display similar steady-state force generation. The spanwise velocity contours also reflect the phase difference between the two cases as

at the position of $d^* = 5$, the streamwise flow pattern is mostly concentrated around the trailing edge for the surging wing, whereas, strong spanwise flow is still present up to half of the chord length for the pitching wing. However, in general both cases display similar behaviour, which involves the translation of spanwise flow toward the trailing edge as the motion progresses such that there remains no significant spanwise flow pattern around the leading edge.

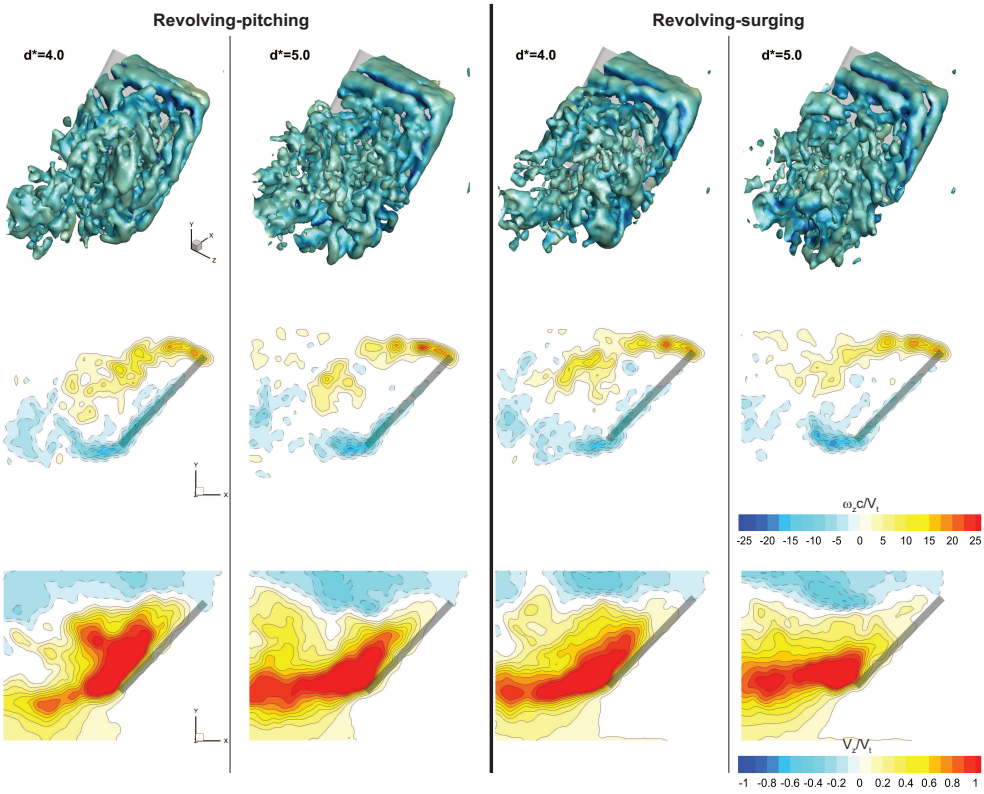

Figure 7.8: Isosurfaces of $Q/(V_t/c)^2 = 4.375$ coloured by vorticity magnitude (*first row*), contours of non-dimensional out-of-plane vorticity ($\omega_z c/V_t$) in the reference plane (*second row*) and contours of non-dimensional spanwise velocity (V_z/V_t) in the reference plane (*third row*) plotted at two instants ($d^* = 4$ and 5) for the revolving-pitching and revolving-surging cases

To complement the planar view of the spanwise flow patterns, a volumetric representation for the different phases is provided by means of isosurfaces of spanwise velocity ($V_z/V_t = -0.25$ (blue) and $V_z/V_t = 0.25$ (yellow)) in Fig. 7.9. It is evident that as a result of the higher pressure difference (as consistent with higher lift) between the pressure and suction sides of the wing during the pitching motion, a stronger spanwise flow pattern that is dominated by the tip vortex is formed in the pitch-up phase ($d^* = 0.5$ and 1). The region of strong spanwise flow in the case of the surging wing remains rather confined to the vicinity of the wing tip in accordance with the segmented structure of the tip vortex. At $d^* = 2$, in the revolving-pitching wing case, the tip vortex is still the dominant factor in the

formation of spanwise flow in most part of the measurement volume. However, there appears a flow pattern directed toward the tip in the inner side of the measurement volume around the leading edge, which is formed by the increasing effects of centrifugal forces and spanwise pressure gradient (Garmann et al, 2013), especially around the leading edge due to three-dimensional nature of the LEV. In the case of the revolving-surging wing, this outwards flow pattern overcomes the inward flow generated by the tip vortex and extends along the leading edge until the wing tip. As a consequence, the tip vortex loses its coherence and detaches from the wing tip corner. A similar state is achieved in the case of revolving-pitching wing case after one more chord length of travel ($d^* = 3$), which is in correlation with the lag in the temporal evolution of the forces. In the following instants of the motion, the spanwise flow pattern which is confined in the core of the LEV moves toward the trailing edge and secondary consecutive LEVs emanate from the leading edge in both cases. Comparison of figure 7.8 and figure 7.9 reveals that in the later phases of the motion, discrete tip vortex formations only emerge at the upper half-chord of the wing, where there is no pattern of outwards spanwise flow.

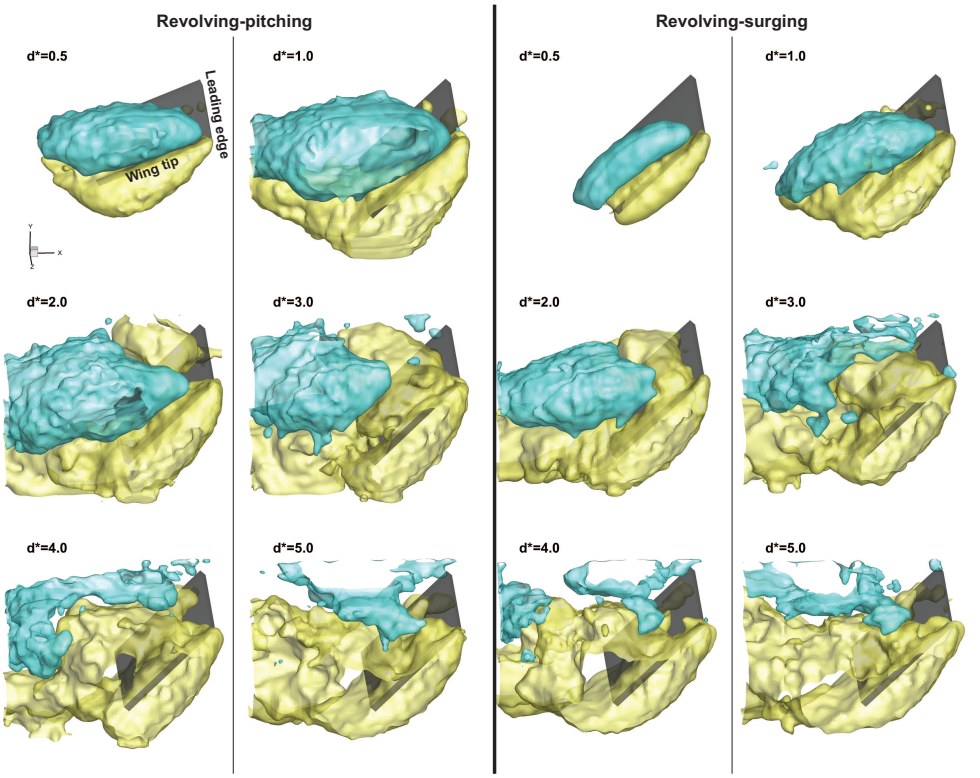

Figure 7.9: Isosurfaces of spanwise velocity ($V_z/V_t = -0.25$ (*blue*) and $V_z/V_t = 0.25$ (*yellow*) plotted throughout the motion for the revolving-pitching and revolving-surging cases

LEV circulation

Comparison of the temporal evolution of the LEV circulation (Fig. 7.10) reveals that the circulation increases rapidly in the build-up phases of both motions. Yet this increase has a higher pace in the revolving pitching case which results in a larger LEV circulation at the end of the build-up phase. The increasing trend of the circulation during the pitch-up motion is interrupted at the end of the build-up phase and at $d^* = 2$. This decline in the progression of the circulation for the revolving-pitching wing is correlated with termination of the pitching motion, the shedding of the counterclockwise leading edge vorticity from the trailing edge and the lift-off of the LEV at $d^* = 2$ (see Fig. 7.6). Once the final motion is settled, both cases display similar values until $d^* = 4$. The circulation level peaks at this position in the surging case in accordance with the position of the maximum force generation ($d^* = 4.3$). In a similar manner, the circulation continues to rise in the case of pitching motion as the maximum force is reached approximately at $d^* = 5.4$.

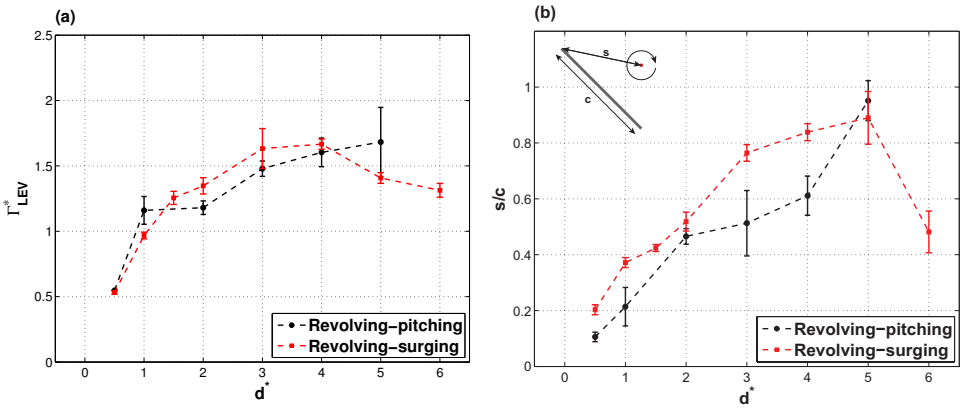

Figure 7.10: Temporal evolutions of **a** the LEV circulation and **b** the non-dimensional distance (s/c) between the leading edge corner and the core of the LEV

However, the differences in the temporal evolution of the LEV circulation by themselves are not sufficient to explain the differences in the resultant forces particularly for the build-up phase when significantly larger forces are produced in the revolving-pitching case. The relation between the vorticity (hence, circulation) and force generation can be interpreted by use of the vorticity moment theory described by Wu (1981), which reads for three-dimensional flows:

$$\vec{F} = -\frac{1}{2}\rho\frac{d}{dt}\int_{R_f+R_b}\vec{p}\times\vec{\omega}\,dR + \rho\frac{d}{dt}\int_{R_b}\vec{v}\,dR \tag{7.4}$$

where $\vec{p}$ is the position vector in a global reference frame, $\vec{\omega}$ is the vorticity vector, $\vec{v}$ is the body velocity, and R_f and R_b are the fluid volume and body volume, respectively. Eq. 7.4 states that the force exerted on the body can be calculated from the time rate of change of the total first moment of the vorticity field in the complete fluid domain including the body (first term) and the inertial force due to the mass of fluid displaced by the solid body (second term). For thin plates, the contributions from the body integrals can be neglected.

Thus it can be inferred from the first term that it is not only the temporal evolution of total amount of vorticity that affects the force generation, but also the temporal variation of its distribution in the flow field. Moreover, assessment of the resultant force requires consideration of the temporal variation of the moment of the complete vorticity field rather than that of the vorticity accumulated only in the LEV. For instance, in the build-up phases of both motions (Fig. 7.5), the TEVs are still partially moving with the wing (from $d^* = 0.5$ to $d^* = 1$, the starting vortex travels approximately $0.3c$ with the wing for the pitching case and $0.23c$ for the surging case in x direction as calculated in the reference plane) while also growing in strength. Therefore it is plausible to state that the moment of vorticity of the TEVs is changing in time so that it still contributes to the first term in Eq. 7.4, in an opposite sense with respect to the LEV in both cases. It should also be noted that the theorem can be applied to the experimental data correctly as long as the field of view of the measurements covers the entire generated vorticity.

In order to better evaluate the effect of the LEV on the force generation, its position is tracked throughout both motions and the diagonal distance between the leading edge corner and the core of the LEV (s) is determined (Fig. 7.10b). It is clear that for most part of the motion, the LEV stays relatively close to the leading edge in the revolving-pitching wing case. After $6c$ of travel in the revolving-surging motion, the initially coherent LEV cannot be captured in the reference plane anymore most probably due to bursting and inclination of the vortex structure with respect to the chordwise oriented reference plane so that the γ_1 algorithm detects secondary smaller scale LEVs emanating from the leading edge instead.

In order to estimate sectional lift forces from the flow data in the reference plane, the two-dimensional form of Eq. 7.4 is considered:

$$l = -\rho \frac{d}{dt} \int_{A_f + A_b} \omega_z x \, dA + \rho \frac{d}{dt} \int_{A_b} v \, dA \tag{7.5}$$

where x is the horizontal distance measured from the origin of the global coordinate system, A_f and A_b are the fluid and body areas, respectively. Obviously, such an analysis can only be performed in the build-up phases of both motions for the present study as these are the only stages of motions when the starting vortex and secondary TEVs could be captured mostly in the field of view. The moment of the spanwise component of vorticity ($|\omega_z c / V_t| > 1.25$) was calculated in the reference plane with respect to a global coordinate system that was positioned at $1c$ of distance from the leading edge at the start of both build-up phases. By use of the two available time instants during the build-up phases, the corresponding sectional lift coefficients are estimated as 3.38 and 1.15 for the pitching and surging cases, respectively. These values practically correspond to forces at approximately $d^* = 0.75$ of both motions, whereas the actual measured values are 2.8 and 0.78 for the pitching and surging wings, respectively. Overestimation of the forces is mainly attributed to the use of a two-dimensional approach to calculate sectional lift from the velocity fields in the reference plane which does not account for the three-dimensional effects present in the finite span wing. Additional sources of errors which may contribute to the discrepancy between the calculated and measured values are: (1) the low temporal resolution of tomographic-PIV data in the build-up phases of both motions in view of the discrete sampling of the motion, which results in a poor representation of the devel-

opment in the build-up phases when forces vary significantly in time; (2) not capturing a part of the wake and thus of the trailing edge vorticity at $d^* = 1$ stage of the pitching wing case (this is compensated for in the present analysis by use of Kelvin's circulation theorem and locating the "missing circulation" at the centroid of the wake vorticity); (3) incapability of the current tomographic-PIV setup in accurately resolving the velocity field in the close vicinity of the wing due to low effective spatial resolution (interrogation volume size of $2 \times 2 \times 2$ mm) when compared to the wing thickness (which is 3 mm). The last aspect is of particular importance to account for the bound circulation (in case generated throughout the motion) that can contribute substantially to the temporal variation of the vorticity moment (thus forces) as it translates with the wing. The presence of bound circulation and its contribution to the resultant forces in the build-up phases of both motions are addressed subsequently.

Rotational forces

The revolving-pitching wing generates significantly greater lift in the pitch-up phase with respect to the surging wing in the acceleration phase (approximately 3.6 times that of the surging wing at $d^* = 0.75$). However, there is not such a significant difference observed in the circulation and trajectory histories of the LEVs. In the above calculation of sectional lift, it was found that the contribution of the LEV to the time rate change of the moment of vorticity term in the pitching case is approximately 1.7 times that of the surging case. However, this ratio does not necessarily reflect directly in the forces because the contribution of negative vorticity emanating from the trailing edge (20 % higher in the pitching case) is also influential on the resultant force. Moreover, only $50-60$ % of the total positive circulation is accumulated in the LEV defined by the $\gamma_2 = 2/\pi$ contours for the pitching wing case, whereas it reaches 80 % for the revolving-surging wing in the build-up phase. These differences suggest the generation of bound circulation by the revolving-pitching wing. Bound circulation in the present discussion is understood as the vorticity accumulated in the close vicinity of the plate. This is verified by the use of two methods: (1) comparing the circulation of the LEV with the total circulation of the negative vorticity emanating from the trailing edge; (2) calculating the circulation in an arbitrary contour that includes the complete wing, the LEV and part of the trailing edge vorticity by means of the line integral of velocity along the contour, then subtracting the LEV and included negative circulation of the trailing edge region to obtain the bound circulation value (Fig. 7.11).

The first method is principally based on the application of the Kelvin's circulation theorem that implies conservation of angular momentum such that the total circulation of the flow is constant in time and equal to the initial value of zero as there is no net circulation when the fluid and the wing are at rest. Although the theorem is not strictly valid in a plane of a three-dimensional flow structure, the two dimensional nature of the vortical structures (i.e., LEV and TEVs) that carry majority of the spanwise vorticity at the early stages of the motion justify the application of the method in the reference plane in the present study. Furthermore, the second method, which is an application of the Stokes' theorem, is used as a means of verification.

According to Kelvin's circulation theorem, the circulation of the LEV should be equivalent to that of negative vorticity, in case of zero bound circulation and low levels of vorticity deposited in the feeding shear layer of the leading edge. Indeed for the revolving-surging wing case, both methods yield very small values of positive excessive circulation around

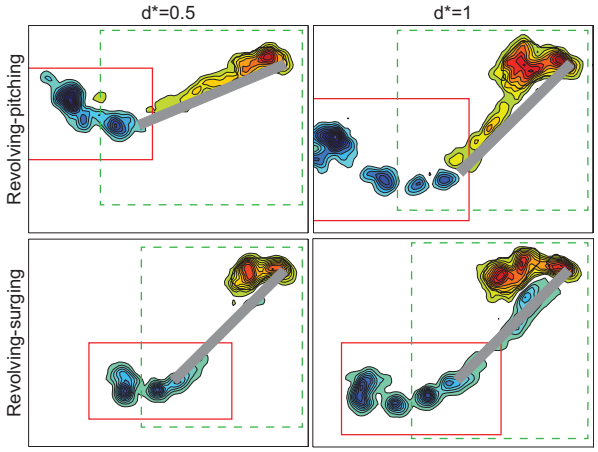

Figure 7.11: Regions of integration for the calculation of the bound circulation in the build-up phases of revolving pitching (*top*) and revolving surging (*bottom*) cases: (1) negative spanwise vorticity (*blue*) is integrated within the red rectangle with a threshold of $\omega_z c/V_t < -1.25$, whereas positive spanwise vorticity (*red*) is integrated within $\gamma_2 = 2/\pi$ contours (*black*) to calculate the LEV circulation; (2) the total circulation is calculated within an arbitrary rectangle (*dashed green*) by integrating the velocity around the edges

the wing ($\Gamma^* < 0.08$) at $d^* = 0.5$. At the stage of $d^* = 1$, this value of positive excessive non-dimensional circulation calculated by both methods is about 0.3. However, closer inspection reveals that this excessive part originates from the feeding shear layer between the two LEV contours and some layers of vorticity around the LEV contours defined by $\gamma_2 = 2/\pi$ at $d^* = 1$. Therefore, it is plausible to conclude that the surging wing does not generate appreciable bound circulation in the acceleration phase. This is in accordance with the findings of Pitt Ford and Babinsky (2013), who showed that for a translating wing at 15° angle of attack (impulsively accelerated from rest), bound circulation remains relatively small initially and most of the positive circulation is accumulated inside the LEV. Recently, they also showed that the bound circulation is negligible in the first chord and a half of travel after an impulsive start for a flat plate at both 15° and 45° angle of attack (Pitt Ford and Babinsky, 2014).

On the other hand, comparison of the LEV and negative trailing edge vorticity circulations at the mid-pitch-up phase of the revolving-pitching motion reveals that trailing edge vorticity circulation is roughly twice that of the LEV, whereas they are almost equal in the mid-acceleration phase of the revolving-surging motion. In physical terms, this can be understood as promotion of the trailing edge separation due to the higher trailing edge velocity induced by the pitching motion. Analysis of the flow field by both of the methods shows that the wing has a bound circulation at an equivalent value with the LEV at this instant ($\Gamma^*_{\mathrm{LEV}} \approx \Gamma^*_{\mathrm{bound}} = 0.5$). At $d^* = 1$, a slightly higher bound circulation value is found ($\Gamma^*_{\mathrm{bound}} = 0.6$), around 80 % of which is accumulated in the vorticity layer distributed along the chord. Although an accurate quantification is difficult due to the presence of the LEV and the feeding shear layer with positive vorticity (particularly at the end of the build-up phase) around the wing, there is a clear evidence that the pitching wing generates a bound circulation at least roughly at a value of $\Gamma^*_{\mathrm{bound}} = 0.48$. This can also be inferred from the

shedding of positive vorticity from the trailing edge after the pitching motion is over (see $d^* = 2$ of the revolving-pitching motion in Figs 7.6 and 7.7).

In the context of the unsteady thin airfoil theory, as discussed earlier, the prediction of the rotational force is based on the generation of additional bound circulation in order to establish the Kutta condition and can be interpreted as a consequence of dynamic angle of attack and dynamic camber effects. Under the current conditions, with large scale flow separation present, the increase in the LEV circulation is associated to the dynamic angle of attack effect, whereas the generation of bound circulation can likely be understood as an attempt to satisfy the Kutta condition during the pitching motion although the wing never reaches a fully-established state as evident from the continuous shedding of trailing edge vorticity. This may also explain why the theoretical estimation of the rotational circulation (Sane and Dickinson, 2002) is significantly higher ($\Gamma^*_{\text{rot,theo}} = 1.7$) than the bound circulation value measured in the experiments.

Clearly, the increased force generation of the pitching motion under the current conditions originates from relatively favourable characteristics of the LEV and TEV in addition to the generation of bound circulation. The contribution of the LEV is twofold: (1) the higher magnitude of circulation as well as higher growth rate ($d\Gamma^*_{\text{LEV,pitch}}/dt^* = 1.5$ and $d\Gamma^*_{\text{LEV,surge}}/dt^* = 0.8$); (2) the tendency of the LEV to remain closer to the wing. Contrary to the LEV, the starting vortex moves further from the wing in the pitching case (at $1.34c$ and $1.52c$ horizontal distance from the leading edge at $d^* = 0.5$ and 1, respectively) than in the surging case ($0.97c$ and $1.24c$, respectively), which reduces its negative effect on the resultant force and yields an enhanced lift. Furthermore, the contribution of the measured bound circulation based on the two-dimensional vorticity moment theory could reach approximately $\Delta c_l = 1$ in the ideal case (assuming that its counterpart with opposite circulation stays stationary at the starting position), which could then account for nearly 50 % of the difference between the pitching and surging cases. However, this is an optimistic assumption as the TEVs do not fully shed and stay stationary in the global coordinate system during the build-up phase, but rather translate with the wing while increasing in circulation.

Spanwise vorticity flux

Comparison of the flux of the spanwise vorticity component (Fig. 7.12) also reveals differences in the temporal progression of the flow in the two cases. At the initial stage of both motions ($d^* = 0.5$ and 1), there is negligible vorticity flux throughout the measurement volume. At $d^* = 2$ in both motions, the overall magnitude of the flux has increased with a significant spanwise variation. It should be noted that the gradient of the flux in the spanwise direction is the summation of vorticity advection term and stretching term. In the case of a positive spanwise gradient, it can be considered that positive spanwise vorticity is transported in the spanwise direction (Kim and Gharib, 2010). However, in the pitch-up case, there is a steep decrease of the flux in the spanwise direction. In the surge case, on the other hand, the flux value increases until 70 % span position and decreases afterwards at a relatively low rate. The negative gradient is an indication of vorticity accumulation in a given plane. However, this does not necessarily result in an increase in the circulation values as advection of the vorticity in the in-plane directions and the vortex tilting mechanisms also affect the resultant change of the vorticity in the plane. For instance, at

$d^* = 2$, the LEV is lifted off from the wing surface forming an arch-shaped structure (see Fig. 7.7) which contains x and y components in addition to the z component of vorticity. The tilting of the LEV results in the steep decrease of the flux in the spanwise direction. Subsequently, in the revolving-surging motion case, the magnitude of the vorticity flux decreases to a zero level gradually with no significant gradient in the spanwise direction. The revolving-pitching wing, on the other hand, displays different evolution also in terms of vorticity flux such that the magnitude of the flux remains relatively high with respect to the surging case at $d^* = 3$ and 4 while showing noticeable spanwise variation; at the last position ($d^* = 5$), although it levels at zero at the inwards stations, the flux value increases toward the tip with a significant gradient.

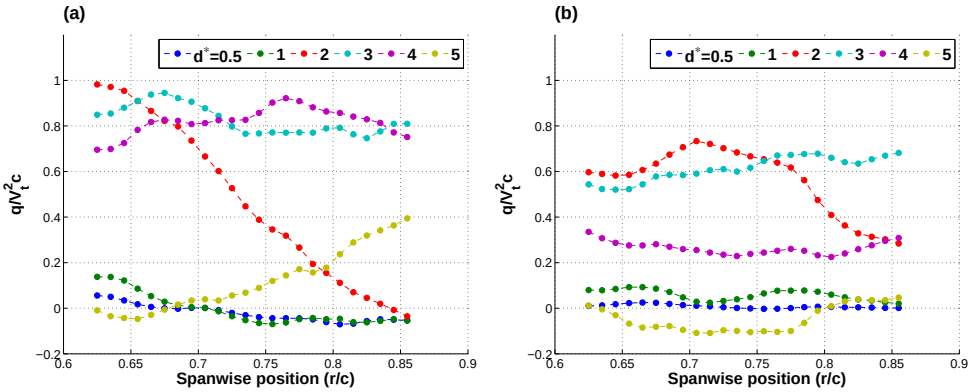

Figure 7.12: Spanwise vorticity flux calculated at different chordwise planes plotted at different phases of **a** revolving-pitching, **b** revolving-surging motions

7.4. Conclusions

The flow field around an accelerated revolving low-aspect-ratio flat-plate wing has been investigated experimentally via tomographic PIV. Two different motion kinematics were considered to transfer from rest to the final steady-state condition over one chord length of travel (based on the reference plane position at 75 % wing span): 1) the revolving-pitching motion, in which the wing first accelerates to the terminal velocity at 0° angle of attack, then pitches-up to 45° about its leading edge with a constant pitch rate (corresponding non-dimensional pitch rate $k = 0.39$); 2) the revolving-surging motion, in which the wing accelerates to the terminal velocity at a constant acceleration rate and at a constant angle of attack. Each motion then continues in revolution with a constant velocity at a fixed angle of attack. The reference terminal velocity is 0.2 m/s in both cases, corresponding to a Reynolds number of 10,000. Tomographic-PIV measurements were performed in two adjacent volumes, providing a total measurement volume of size $90 \times 70 \times 50$ mm^3 (chordwise × normal × spanwise). A water-submergible force sensor was used to measure the fluid forces on the wing model.

Comparison of force histories of both cases reveals that, as expected, the wing generates considerably higher lift and drag during the pitch-up motion when compared to

the acceleration phase of the revolving-surging motion. The lift coefficient reaches up to 2.5 times the steady-state value and drag displays a quasi-linear increase during the pitch-up phase. The quasi-steady model predicts the forces fairly well in terms of temporal variation and magnitude in the build-up phase of both cases. In the post-build-up phase, although the wing moves with the same kinematics in both cases, the revolving-pitching motion continues generating higher lift and drag coefficients until six chords of travel after the end of the pitch-up motion. During this period, both lift and drag peak and subsequently decrease to the steady-state values relatively later (difference of one chord length of travel) in the revolving-pitching wing case. Apparently, the build-up phase of the motion affects the following force evolution in terms of both amplitude and phase of the maximum force generation. Predominantly wing-normal forces are generated in the post-build-up phase of both motions.

In general, the flow fields during the build-up phases of both kinematics display a vortex system comprising an LEV, a TEV and a TV. This vortex system, especially the tip vortex, shows different characteristics in terms of integrity already in the middle of the build-up phases: the pitching wing generates a conical TV and a well defined LEV; the surging wing displays a TV with a fragmented structure at the lower half of the vortex. As the wing reaches the end of the acceleration phase, this fragmentation becomes more prominent with swirling features of vortical structures that are linked to secondary trailing edge vortices. The disintegration of the TV also occurs in the case of pitching wing with shedding of secondary trailing edge vortices during the build-up phase; however, it is not as severe as for the surging case. In accordance with what was reported by Carr et al (2013), the lift-off of the LEV is observed at $d^* = 1$ ($\phi = 25.8°$) for the first time in the surging case. As of $d^* = 2$, the flow fields display small scale substructures appearing in the vortex system in both cases. The arch-shaped LEV is clearly visible at $d^* = 2$ ($\phi = 51.6°$) for both cases. The outer leg of this structure is attached at the wing tip corner in the pitching wing case, whereas it is unpinned from the wing surface and attached back near 40 % of the chord length in the surging case. Seemingly, the surging wing precedes the pitching wing in terms of flow field evolution, which is also evident in the isosurfaces of spanwise velocity (Fig. 7.9): the state of dominant outwards spanwise flow driven by the centrifugal forces and pressure gradient in the core of the LEV is reached earlier in the surging wing case. In the following phases of both motions, the spanwise flow pattern which is confined in the core of the LEV moves toward the trailing edge and secondary consecutive LEVs emanate from the leading edge in both cases. In general, the flow fields have then become chaotic and populated with several substructures.

Apparently, the interaction between the tip vortex and the spanwise flow determines the coherence and the attachment of the tip vortex. The formation of a strong TV during the build-up phase of the revolving-pitching wing motion postpones the generation of outwards spanwise flow in the post-build-up period, which extends the period the TV stays attached to the wing surface and keeps its integrity. Correspondingly, the segmentation of the LEV occurs at a later phase in the pitching case; however, this does not cause a decrease in the force generation. Nevertheless, the delay in the formation of the spanwise flow affects the force histories such that steady-state values are reached at a later phase for the revolving-pitching wing. Furthermore, the local maxima in the force histories in the post-build-up phase of both motions are aligned with the translation of the spanwise flow

pattern toward the trailing edge such that in the period of steady-state force generation, the outward spanwise flow pattern is mostly accumulated around the trailing edge. This state is most probably due to the growth of the LEV toward the trailing edge and its inhibition by the trailing edge as recently investigated by Garmann and Visbal (2014). They showed that for revolving wings, the growth of the LEV is almost proportional to the distance from the root and it is constrained by the trailing edge for increasing aspect ratio such that once the LEV reaches the trailing edge and occupies the complete chord, forces level around the steady-state values.

The circulation of the LEV builds up rapidly in the transient phase of both motions. In the pitching wing case, this increasing trend is interrupted with the end of the pitch-up motion that is also correlated with the shedding of positive leading edge vorticity from the trailing edge and tilting of the LEV. Subsequently until $d^* = 5$, both motions generate similar amount of circulation which is altered by the decrease of the circulation level in the case of the revolving-surging motion in accordance with the decay of the forces to the steady-state values. The circulation of the LEV continues to increase in the revolving-pitching case similar to its force history. In order to assess the relation between the vortical structures and force generation, and to identify the phenomenon behind the greater performance of the pitching wing compared to surging wing in terms of force generation, the vorticity-moment theory (Wu, 1981) was applied on the flow fields in the reference plane during the build-up phase of both motions. It is found that the elevated force generation of the pitching motion originates from a number of consequences of the pitching motion: (1) increase in the magnitude and growth rate of the circulation accumulated in the LEV, (2) positioning of the LEV closer to the wing and the starting vortex further away from it; (3) generation of bound circulation.

Regarding the force prediction models, it is clear that the theoretical model inspired by the unsteady thin airfoil theory captures the general trend and the magnitude of the forces reasonably well despite its two major shortcomings. First, the model estimates the rotational forces due to pitch-up motion based on the generation of bound circulation of an amount that would establish the Kutta condition. However, this does not hold during the pitching motion as shown by the trailing edge vortex shedding observed in the experiments so that the model overestimates the bound circulation. Second, the steady-state values are used for the estimation of instantaneous circulatory forces during the build-up phases, whereas the formation of vortical structures and hence reaching the circulatory steady-state forces take a finite amount of time. This source of deficiency, however, can be scrutinized and possibly be corrected by adding a Wagner-function-like approach for the acceleration phase of the revolving-surging motion. The second theoretical model discussed in the study, based on the vorticity-moment theory provides a means of force prediction once the flow field information is available. Obviously, this model requires knowledge of the vortex behaviour, whereas the quasi-steady model attempts to provide a prediction based on the wing kinematics directly.

8

Parametric Investigation of Flow Fields and Unsteady Forces in Revolving Flat Plates

This chapter presents an extension of the work described in the previous chapter, by investigating the influence of the variation of different motion parameters. Like previously, the basic approach is again to study the evolution of the flow field structures and the forces of low-aspect-ratio flat plates subjected to two different motion kinematics: (1) an accelerated revolving motion starting from rest; (2) a simultaneous revolving and pitching motion. The measurements were performed in a water tank at angles of attack ranging from 15° *to* 75° *in a Reynolds number range of 5,000 – 25,000, based on the chord length and terminal velocity at the* 75 % *span position. The same experimental techniques were used, namely tomographic particle image velocimetry to capture three-dimensional velocity fields at different phases of the revolving motion, in combination with direct force measurements with a six-component water-submergible force sensor. In particular, the effects of the Reynolds number, angle of attack, acceleration period and number of revolutions were investigated with the revolving-surging wing. The pitch rate and the terminal velocity were varied in the revolving-pitching wing experiments to examine the influence of the non-dimensional pitch rate on the resultant force histories. The effects of the aforementioned parameters on the unsteady forces and the flow field characteristics are investigated by means of a comparative analysis of the different experimental cases.*

Parts of this chapter have been published in the proceedings of 17th International Symposium on Applications of Laser Techniques to Fluid Mechanics (Percin et al, 2014b) and 45th AIAA Fluid Dynamics Conference (Percin and van Oudheusden, 2015a)

8.1. Introduction

The evolution of three-dimensional flow fields and unsteady forces in revolving-surging and -pitching flat plates have been discussed in the previous chapter for a set of experimental parameters. As a result of the comparative analysis between the two canonical motions, main differences and their causes have been reported. This chapter, on the other hand, focuses on the effects of variations in the experimental parameters characterizing the motion kinematics and flow dynamics (viz., the Reynolds number, the acceleration period, the angle of attack and the pitching rate) on the flow field characteristics and the force generation mechanisms in revolving flat plates.

For the accelerating revolving flat plates, the Reynolds number (Re) is defined based on the terminal velocity of the motion measured at a specified spanwise location (usually at the 75 % span position) and its effects have been explored in a number of studies in the low-Re regime (i.e., Re $\approx 10^2$-10^5). Kim and Gharib (2010) investigated the three dimensional flow fields around low-aspect-ratio plates undergoing translational and revolving motions by use of a defocusing digital PIV technique. Comparison of the revolving motion measurements at different Reynolds numbers (viz., 60 and 8800 based on the wing-tip velocity) reveals that decreasing Re causes a decrease in the force generation due to the diffusive effects of viscosity. Jones and Babinsky (2011) captured the flow fields as well as unsteady forces generated by a waving wing in a Re range between 10,000 and 60,000 including both acceleration and deceleration phases of the motion. They reported a transient high-lift peak occurring in the early stage of the motion. Their flow visualizations and high speed PIV measurements revealed the development and the shedding of the LEV which occurs earlier at lower Re. On the other hand, Ozen and Rockwell (2012) observed a stable LEV for a range of Re between 3,600 and 14,500 in their experiments, which were performed with a revolving-surging wing at various angles of attack. They also added that the Reynolds number is not influential on the sectional structure of the LEV at the mid-plane position. Venkata and Jones (2013) performed an experimental study on a low-aspect-ratio wing that is set into a revolving motion at a constant velocity accelerating from rest. They conducted flow visualizations and force measurements in the Re range of 5,000-25,000 based on the velocity at the 75 % span position. Flow visualizations revealed the burst of the LEV at the outboard section of the wing span. They reported that the flow structures for the Re of 5,000 are similar to those at the Re=10,000 yet the LEV burst location is more inwards toward the wing root at the higher Re. They also showed that in the second revolution, forces decrease to approximately 78 % of those of the first revolution as the wing encounters its own wake. Garmann et al (2013) performed high fidelity implicit large eddy simulations to resolve the flow around a revolving low-aspect-ratio wing at a constant angle of attack. They reported a coherent vortex system that is generated after the start of the motion and that consists of an LEV, a tip vortex (TV), a trailing edge vortex (TEV) and a root vortex (RV). This vortex system stays attached to the wing throughout the motion. Correspondingly, following the initial fast increase in the wing loading due to the angular acceleration of the flat plate, forces grow gradually with the settlement and strengthening of the vortical structures. However, breakdown of these structures occurs with increasing Re such that the large scale coherence gradually gives way to fragmentation and formation of vortical substructures. Nonetheless, the loss of coherence of the vortex system does not affect the force generation mechanisms and contrarily wind load-

ing moderately increases with the increasing Reynolds number.

In addition to Reynolds number, flow field characteristics of the revolving-surging motion have been investigated at different angles of attack (α). Birch et al (2004) carried out an experimental study on the force generation and the flow structure characteristics of a dynamically scaled robotic insect wing undergoing a revolving-surging motion. They performed the measurements at two different Re (120 and 1400) and 12 different angles of attack in the range of -10° to 100°. They reported that the lift coefficients are higher for the high Re case for most of the angles. The net force coefficient increases with angle of attack and its direction reaches 90° (i.e., normal to the wing surface) at already about $\alpha = 20^\circ$ at the higher Re case. In their aforementioned study, Ozen and Rockwell (2012) varied also the angle of attack in the range from 30° to 75°. A stable LEV was observed for all cases and the dimensionless circulation of the LEV was found to be nearly proportional to the angle of attack. Beals and Jones (2015) conducted force measurements and dye flow visualizations to investigate the unsteady force on a revolving rigid wing and a chordwise flexible wing. The lift coefficient for both cases was shown to be a function of the angle of attack. The thin airfoil theory was used to estimate the steady-state force coefficients, which worked well up to 35° angle of attack. The maximum lift force was obtained at $\alpha = 45^\circ$, which is in accordance with the findings of Garmann et al (2013). They indicated that the lift increases gradually until an angle just above 45° and after this starts decreasing with a similar trend. On the other hand, drag increases monotonically with the angle of attack and the maximum is reached at $\alpha = 90^\circ$.

Parametric studies including combined revolving and pitching motion in the literature are scarce and rather limited to wings flapping in a reciprocative manner (Dickinson et al, 1999; Kweon and Choi, 2010; Lu and Shen, 2008; Poelma et al, 2006; Sane and Dickinson, 2001). The impulsive pitch-up movement during a steady motion, on the other hand, was studied mostly in the case of a translating wing. Granlund et al (2013) studied the unsteady loading on a rapidly pitching nominally two-dimensional flat plate. They found that the pitch contribution to the lift is proportional to the pitch rate and the distance from the pitch pivot point to the 0.75 chord point similar to the unsteady airfoil theory. The latter is also in agreement with the results of Sane and Dickinson (2002). Yilmaz and Rockwell (2011) investigated the flow around a low aspect ratio wing with rectangular and elliptical planforms undergoing a pitch-up motion from 0° to 45° in a constant free-stream. Flow visualization were performed with a PIV technique which revealed a significantly three-dimensional LEV structure. They reported a spanwise flow component with magnitudes larger than the free-stream velocity and it is directed away from the symmetry plane near the leading edge and toward the symmetry plane near the trailing edge in the fully evolved state. They also observed the distortion of the LEV, which is less pronounced for the elliptical wing associated with different spanwise flow structures. Recently, Bross and Rockwell (2015) investigated the effects of pitch rate on the flow structures of a revolving-pitching flat plate. They stated that the onset and the development of the vortex system components are affected by the pitch rate. Comparison of different cases at the same angle of attack revealed that vortex formation is delayed with increasing pitch rate. On the other hand, comparisons at the same revolution angle reveals similar flow structures, which is indicative of the predominant revolving motion effects.

In the context of the above discussion, the aim of the current study is to explore the

evolution of vortex formations and unsteady forces in revolving low-aspect-ratio flat plates in the Reynolds number range of 10,000 to 25,000 employing tomographic-PIV and simultaneous force measurements. Two main motion kinematics are considered: (1) a revolving-surging motion, where the wing starts from rest at a constant angle of attack and accelerate to a terminal velocity; (2) a revolving-pitching motion, in which the wing pitches up to 45° angle of attack at a constant pitch rate while revolving at a terminal velocity. The terminal velocity, acceleration, angle of attack and pitch rate were varied in the experiments in order to study their effect on the resultant flow fields and the unsteady forces. Thereby, it is particularly aimed to assess the factors affecting the initial formation, stability and integrity of the flow structures in conjunction with the variation of the forces.

8.2. Experimental setup and methods

The experiments were performed in the water tank facility at the Aerodynamic Laboratory of Delft University of Technology. The experimental facility, the model and the motion driving system are the same as those described in the previous chapter therefore the reader is referred to Section 7.2 for detailed information.

8.2.1. Motion kinematics

Similar to the study described in the previous chapter, three-quarters of the span length of the wing model was taken as the reference position and used for the definition of the terminal velocity (V_t) and non-dimensional parameters such as chords-traveled ($d^* = d/c$ where d is the wing displacement at the reference position) and convective time ($t^* = t \times V_t/c$). Note that in the current configuration, every chord length of travel in the reference plane ($d^* = 1.0$) corresponds to a rotation angle (ϕ) of 25.8°. The distance between the root chord and the rotation axis is 35 mm and the radius of gyration is 90 mm, resulting in a Rossby number of 1.8.

The revolving-surging motion kinematics used in the experiments can be described as follows: the motion is initiated by a constant acceleration of the wing model from rest to V_t over a defined d^* value at a fixed angle of attack (α), which is called as the build-up phase. Following to the build-up phase, the wing remains to revolve at a constant angle of attack and constant rate. On the other hand, in the revolving-pitching motion, the wing model accelerates to V_t at 0° angle of attack, then pitches up to $\alpha = 45°$ over a defined d^* at a constant pitch rate ($\dot{\alpha}$). Then it continues to revolve at a constant revolving velocity and at a fixed angle of attack. In this case, the build-up phase is the pitch-up period of the motion, when the major fluid forces start to grow up. Therefore, the two wing motions reach the same terminal condition but with a different transient in the build-up phase.

In order to assess the effect of the Reynolds number for the revolving-surging motion, the terminal velocity was varied in the range of 0.2 to 0.5 m/s corresponding to the Re range of 5,000 to 25,000 (based on the wing chord length) while fixing $\alpha = 45°$ and the acceleration period $d^* = 1$ ($t^* = 2.0$). The force measurements were performed for all cases; whereas the flow field measurements were conducted only for the cases of $V_t = 0.2$ and 0.4 m/s (Re = 10,000 and 20,000, respectively). Effects of the angle of attack were studied by performing the force measurements at $\alpha = 15°$, 30°, 45°, 60° and 75°, and flow field measurements at $\alpha = 30°$, 45° and 60° at $V_t = 0.4$ m/s (Re = 20,000) with an acceleration

period of $d^* = 1$. In addition to these, a test was carried out with an acceleration period of $d^* = 0.5$ ($t^* = 1.0$) at $V_t = 0.4$ m/s and $\alpha = 45°$ in order to investigate the influence of the acceleration on the flow fields and the unsteady forces.

On the other hand, for the revolving pitch motion, experiments were performed for $V_t = 0.2$ and 0.4 m/s and an acceleration period of $d^* = 1.0$. For the lower velocity case, pitch-up periods of $d^* = 1.0$ and 2.0 ($\dot{\alpha} = 3.14$ and 1.57 rad/s corresponding to non-dimensional pitching rates of $k = \dot{\alpha}c/(2V_t) = 0.39$ and 0.19, respectively) were considered, whereas for the $V_t = 0.4$ m/s case, a pitch-up period of $d^* = 2.0$ ($\dot{\alpha} = 3.14$ rad/s corresponding to $k = 19$) was achieved due to the angular rate limitation of the waterproof servo ($\dot{\alpha}_{\max} = 3.93$ rad/s).

Real time position and velocity information were acquired from the motor encoder at a data acquisition frequency of 33 Hz and logged during the measurements in order to verify the motion kinematics. In all experiments, the wing model performs approximately one full revolution, which corresponds to a travel distance of $14c$ ($d^* = 14$). Forces and moments were captured for the full rotation; however, flow field measurements were limited to the first $7c$ of travel. In addition to these experiments, force measurements were also performed on a revolving-surging wing performing three full revolutions at three different angles of attack ($\alpha = 30°$, $45°$ and $60°$).

8.2.2. Force measurements

Six components of forces and moments were captured by use of the water submergible ATI Nano17/IP68 force sensor. The reader is referred to Section 7.2.2 for the detailed explanation of the force measurement system.

The raw force and moment data are contaminated with an electrical noise as well as the mechanical vibrations of the test rig due to the impulsive start of the motion. Therefore, a number of post-processing steps were applied on the raw data. First, an ensemble averaging of forces and moments was performed over at least 20 repetitions of the experiments in order to eliminate random noise and to enhance the signal-to-noise ratio. The averaged force and moment data were then filtered to remove the effects of the mechanical vibrations of the driving system, by means of a Chebyshev Type II low-pass filter with a cut-off frequency of 15 Hz. A forward-backward filtering technique was used in order to prevent time-shift of the data. Lift and drag are normalized using the terminal velocity V_t and the wing surface area, in order to produce force coefficients (c_L and c_D, respectively).

8.2.3. Tomographic-PIV

The experimental setup for the phase-locked tomographic-PIV measurements have been explained in Section 7.2.3. Similar data processing procedures as described in the previous chapter have been applied to calculate the three-dimensional velocity fields from the particle images, yet an interrogation volume size of $48 \times 48 \times 48$ voxels was applied with an overlap factor of 75 %. Thus the resultant vector spacing for the results presented in this chapter is 0.8 mm in each direction forming a dataset of $117 \times 91 \times 32$ velocity vectors in each measurement volume. Then, a Kriging regression technique (de Baar et al, 2014) with a correlation length of 2 mm in each direction was employed to combine the two separate measurement volumes and to provide a complete visualization of the flow field.

8.3. Fidelity of the force and flow field measurements

8.3.1. Wall and free-surface interference effects

As mentioned in the previous chapter, the wing model was positioned at approximately $5c$ distance from the water surface, $7c$ distance from the bottom wall and $4.2c$ (wing tip to wall) distance from the side wall. In order to ensure that the results are not influenced by wall and free-surface interference effects, additional force measurements were carried out. In these measurements, first the closest distance between the wing tip and the water tank side wall (d_{wall}) was varied by moving the complete driving system. Second, the distance between the leading edge and the free-surface (d_{surface}) was varied by lowering the water height. For each different configuration, the wing was driven in a revolving-surging motion at a Re of 20,000 and $\alpha = 45^\circ$ with an acceleration period of $d^* = 1$. The measurements were repeated 5 times for each individual case and the resultant force histories were ensemble-averaged. In Fig. 8.1, mean lift and drag coefficients are plotted as a function of the non-dimensional wall distance (d^*_{wall}) and the free-surface distance (d^*_{surface}), both were normalized by the chord length. Note that in the investigation of the wall interference effects, force coefficients have been averaged over a relatively short period of revolution ($1 < d^* < 3.5$), which includes the stage when the wing was at its nearest position to the water tank wall.

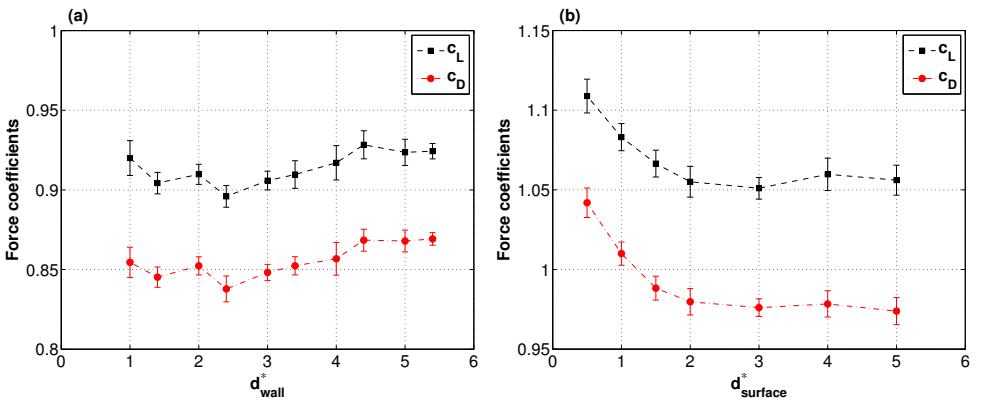

Figure 8.1: **a** Average force coefficients calculated in the motion range of $1 < d^* < 3.5$ ($25.8^\circ < \phi < 90.3^\circ$) as a function of non-dimensional wall distance (d^*_{wall}), **b** average force coefficients calculated in the motion range of $1 < d^* < 10$ ($25.8^\circ < \phi < 258^\circ$) as a function of non-dimensional free-surface distance (d^*_{surface})

It is clear that the force coefficients do not display a considerable variation or an asymptotic trend with respect to the wall distance (see Fig. 8.1a). This can be attributed to the fact that the wing experiences the reported smallest wall distance only momentarily during the revolving motion. Considering that the wing motion starts from rest and mostly the initial stages of the revolving motion are of interest in the current study, it is plausible to assume that the force and the flow field measurements are free of any wall interference effects when $d^*_{\text{wall}} = 4.2$, which was the configuration used in the actual measurements.

On the other hand, having the free-surface closer to the wing leading edge results in an increase in the measured forces (see Fig. 8.1b). However, this effect is considerably

diminished for distances larger than $d^*_{\text{surface}} = 2$ with the force coefficients presenting a nearly invariant behaviour. Obviously, with the free-surface distance of $5c$, as set in the actual measurements, the force histories and the flow structures presented in this study are free from free-surface effects.

8.3.2. Repeatability of the force and flow field measurements

In order to improve the signal-to-noise ratio in the resultant force histories and three-dimensional flow fields, the force data was ensemble-averaged over at least 20 repetitions of measurements for each individual case, whereas flow field measurements were limited to three repetitions. In this section, the repeatability of the physical phenomenon is assessed by means of a statistical analysis of the force data and a visual inspection of individual flow fields.

Figure 8.2 shows the force histories for a revolving-surging wing motion (Re=20,000, $\alpha = 45°$ and acceleration period of $d^* = 1$) as acquired in 20 different measurements (note that these plots contain 15-Hz low-pass filtered force signals for which the test-rig vibrations are eliminated). It is clear that the unsteady force generation mechanism and the force measurements are notably repeatable, which results in almost the same variations of the lift and drag coefficients for all cases. The average standard deviation of the force coefficients for this particular case with 20 repetitions is approximately 1 % of the steady-state mean values.

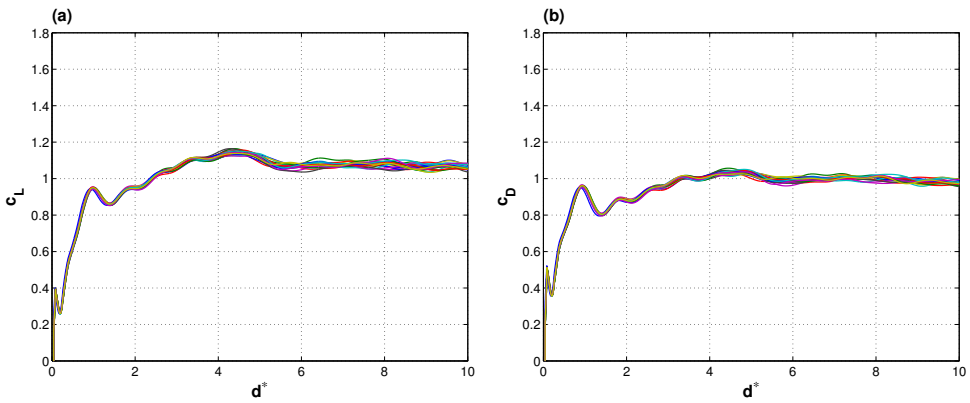

Figure 8.2: **a** Lift coefficient (c_L) and **b** drag coefficient (c_D) histories for 20 repetitions of the same experimental case — revolving-surging motion at Re=20,000, $\alpha = 45°$ and acceleration period of $d^* = 1$ — plotted in the same figure in different colours

Figure 8.3 shows the three-dimensional flow fields measured at three consecutive measurements of the same experimental case. It is clear that the physical phenomenon and flow field measurements are very consistent such that even the helical vortex patterns around the TV are captured at an identical position and phase. Although the shape of the LEV might slightly differ, as can be evidenced from the contour plots of $\omega_z c/V_t$, the general flow topology is obtained with a high degree of repeatability. This justifies the approach that the three-dimensional flow fields are ensemble-averaged over 3 repetitions for

the further analysis of the physical phenomenon without significant loss of information.

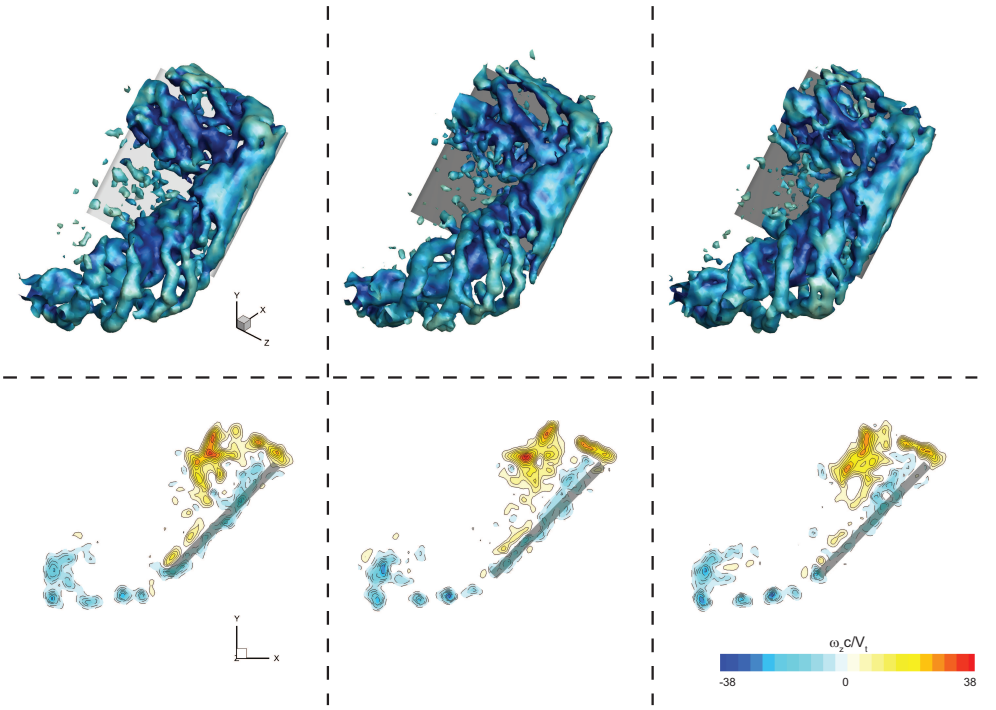

Figure 8.3: Isosurfaces of $Q/(V_t/c)^2 = 3.125$ coloured by vorticity magnitude (*first row*), contours of non-dimensional out-of-plane vorticity ($\omega_z c/V_t$) in the reference plane (*second row*) of the revolving-surging flat plate at Re=20,000 plotted at $d^* = 1.5$ for three consecutive repetitions of the same experiment

8.4. Results

In this section, results of the parametric study on the flow fields and force histories of the revolving-surging and revolving-pitching flat plates are presented. This section is divided into two main parts: (1) results for the revolving-surging motion in which effects of the Reynolds number, the angle of attack, the acceleration period and the multiple revolutions are investigated; (2) results for the revolving-pitching motion, in which the effects of the pitching rate are explored. In general, time histories of the lift and drag coefficients are plotted in addition to the mean force coefficients, which were calculated in the post-build-up period of the particular motion kinematics. Three-dimensional flow structures are visualized by means of isosurfaces of the Q criterion (Jeong and Hussain, 1995). For the sake of a better comparison of the different experimental cases, the Q criterion is non-dimensionalized by $(V_t/c)^2$. Moreover, three-dimensional vortical structures are complemented with contour plots of non-dimensional out-of-plane (viz. spanwise) vorticity $\omega_z c/V_t$ and non-dimensional spanwise velocity V_z/V_t in the reference plane to facilitate interpretation of the results. Only half of the flat plate model is depicted in the figures, whereas the spanwise extent of the flow measurement domain ranges from approximately

0.62 to 1.12 of the wing span (see Fig. 7.3).

In addition to the visualization of the flow structures, the cumulative circulation of the LEV (or LEVs in the case of presence of secondary LEVs) has been calculated based on the spanwise component of vorticity ($\Gamma = \iint \omega_z dxdy$) in the reference plane and it is normalized by V_t and c ($\Gamma^* = \Gamma/(V_t c)$). The center of the LEV is tracked by means of γ_1 scheme, which is essentially based on the topology of the vector field (Graftieaux et al, 2001). The position of the initial most coherent vortex structure was registered when there are multiple LEVs present in the flow field. The integration region for the calculation of the LEV circulation was determined by use of the γ_2 vortex core detection algorithm (Graftieaux et al, 2001). Cumulative LEV circulation for each instant of the revolving motion was calculated by integrating the spanwise component of vorticity within the $\gamma_2 = 2/\pi$ contours.

8.4.1. Revolving-surging motion

Effects of Reynolds number

The temporal evolution of the lift and drag coefficients for an angle of attack of 45° and different Re are plotted in Fig. 8.4a and b. Clearly, in all cases, a similar trend is observed: a sudden increase of the forces due to contributions of inertial effects stemming from the acceleration of the flat plate (i.e. non-circulatory added mass effect) and developing circulatory effects, with local maxima in lift and drag histories occurring at the end of the acceleration phase (at d*=1) and subsequent decrease due to the disappearance of the inertial effects for the motion at a constant speed. This is followed by a gradual increase of the forces until a maximum is reached near d*=4, with a subsequent decrease to more-or-less constant steady state values. Moreover, equivalent values of lift and drag coefficients indicate that the forces act predominantly normal to the wing. Notwithstanding similar variation in time, the force coefficients differ in magnitudes between different Re cases which can be clearly seen in Fig. 8.4c where mean lift and drag coefficients are plotted as function of Re. These mean values were calculated as the average between the end of the acceleration phase (d*=1) and 10 chord lengths of travel (d*=10), in order to eliminate starting and stopping transients of the motion. Force coefficients display an increasing trend with respect to Re. This trend flattens at higher Re such that the difference in the magnitudes of the forces between the cases of 20,000 and 25,000 is within the uncertainty range of the measurements. The relative difference between the maximum and the minimum mean values in the Re range of the measurements is 18 % and 10 % for the lift and drag coefficients, respectively.

For the sake of conciseness, vortical structures at two stages of the motion, $d^* = 1$ and 2, are shown in Fig. 8.5. Although the Reynolds number affects the magnitude of the forces slightly, the flow fields of different Re cases display similar characteristics in terms of behaviour of the vortical structures. At the end of the acceleration phase ($d^* = 1$), both cases have similar coherent structures: an LEV that is slightly lifted off from the wing surface, a conical tip vortex with swirling features of small scale vortical structures and a starting vortex that is linked to the tip vortex with secondary trailing edge vortices which are also connected to swirling features of the TV. In both cases, the formation of spiral patterns occurs at the bottom part of the TV, while the vortex is still intact at the top side. At d*=2, the LEV is greater in size and located more toward the trailing edge and there are secondary structures emanating from the leading edge in both cases. In general, the

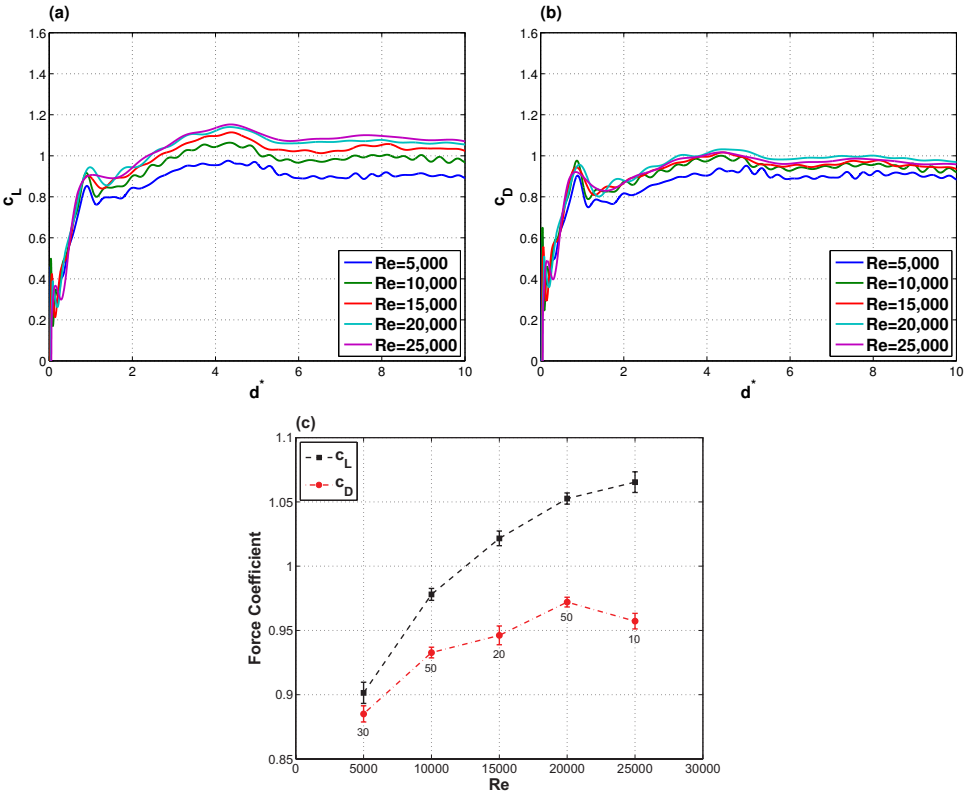

Figure 8.4: Temporal evolution of **a** lift and **b** drag coefficients for the wings undergoing revolving-surging motions at different Re; **c** mean lift and drag coefficients averaged between $d^* = 1$ (end of acceleration) and $d^* = 10$ with the numbers indicating the number of repetitions used in ensemble averaging of the forces

LEV structures are less clearly defined for the larger Re case, as can be evidenced from the out-of-plane vorticity plots in the reference plane.

The flow fields of the two cases are also considerably similar in term of the spanwise flow pattern. At the end of the build-up phase (i.e., end of the acceleration period, $d^* = 1$), there is no significant spanwise flow structure in the vicinity of the leading edge in the reference plane. Around the trailing edge, there is an outwards-directed spanwise flow pattern. As the motion progresses, another positive spanwise flow pattern (directed toward the wing tip) emerges around the leading edge, which is correlated with the growth and progression of the LEV. In order to examine the relation between the spanwise flow patterns and vortical structures, isosurfaces of Q criterion (transparent white isosurfaces) are displayed together with isosurfaces of spanwise velocity component (red isosurfaces) in Fig. 8.6. At $d^* = 1$, all visible positive spanwise flow patterns at the isovalue of $V_z/V_t = 0.5$ are generated by the tip vortex. It induces a positive flow on the pressure side of the flat plate along the tip. On the other hand, the positive spanwise flow pattern around the trailing edge is produced mainly due to tilted and fragmented formation of the TV at the

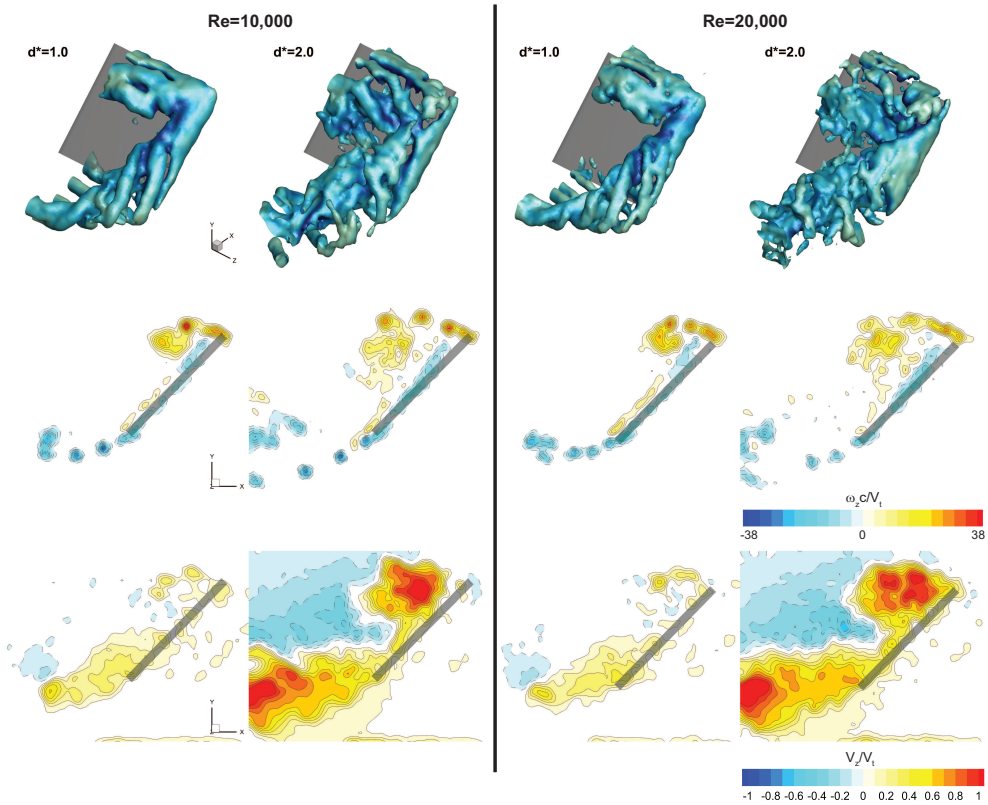

Figure 8.5: Isosurfaces of $Q/(V_t/c)^2 = 3.125$ coloured by vorticity magnitude (*first row*), contours of non-dimensional out-of-plane vorticity ($\omega_z c/V_t$) in the reference plane (*second row*) and contours of non-dimensional spanwise velocity (V_z/V_t) in the reference plane (*third row*) plotted at two instants ($d^* = 1$ and 2) for Re = 10,000 (*left*) and 20,000 (*right*)

bottom side. In this region, the TV is lifted off from the wing surface and broken into helical structures, which induce a positive spanwise flow. As the motion progresses, there appears a spanwise flow pattern around the leading edge gradually. The main sources of this formation are the centrifugal forces which arise from curvilinear motion dynamics and the spanwise pressure gradient that originates from the three-dimensional nature of the LEV. Moreover, it also seems that the tilted LEV structure with its secondary features also induce a flow with a spanwise velocity component.

The characteristics of the flow fields can be associated to the force generation by means of the vorticity moment theory (Eq. 7.4) as discussed in the previous chapter. The theory states that the force exerted on the body can be calculated from the time rate of change of the total first moment of the vorticity in the complete domain including the body and the inertial force due to mass of the fluid displaced by the solid body (Wu, 1981). For thin plates the contribution of the latter is marginal and can be neglected. Therefore, it allows to conclude that the distribution of the vortical structures in the flow field and its

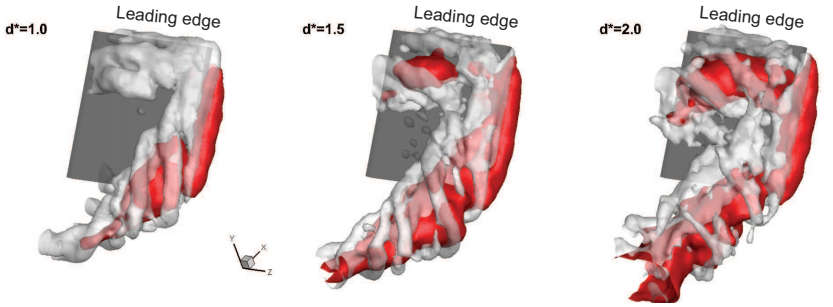

Figure 8.6: Isosurfaces of $Q/(V_t/c)^2 = 3.125$ (*transparent white*) and non-dimensional spanwise velocity $V_z/V_t = 0.5$ (*red*) plotted at three instants ($d^* = 1$, 1.5 and 2) for the revolving-surging motion at Re = 10,000

variation in time are as equally important as the total amount of vorticity accumulated in these structures. Furthermore, it is required to consider the complete vorticity field to assess the relationship between the flow fields and the unsteady forces. However, because of the limited field of view of the tomographic-PIV measurements, it is not possible to capture the evolution of all vortical structures throughout the revolving motion. For this reason, the analysis based on the vorticity moment theorem was limited to the build-up phases of the revolving-surging and revolving-pitching motions as explained in the previous chapter. In the current chapter, for the sake of conciseness, the comparison of the two Re cases is performed based on the two-dimensional characteristics of the LEV in the reference plane. This is a plausible approach because of two main reasons: (1) for the revolving-surging motion, it was shown that most of the circulation is accumulated in the LEV so that its characteristics are dominant in the determination of the forces (Percin and van Oudheusden, 2015b; Pitt Ford and Babinsky, 2013, 2014); (2) for these surging cases, it is assumed that the distribution and temporal evolution of the TEVs are similar. In this respect, the temporal variations of the non-dimensional LEV circulation (Γ^*_{LEV}) and the distance between the LEV core and the leading edge corner (s) are shown in Fig. 8.7. First, it is important to note the nearly identical development of the LEV characteristics for the two cases. In addition to showing that the flow field behaviour, at least regarding the LEV characteristics, is largely independent of the Reynolds number, the close agreement between the two cases also verifies the repeatability of the experiments even under different flow conditions. It is also clear that the cumulative circulation of the LEV scales with the terminal velocity as evident from the identical values for the non-dimensional circulation. For both cases, the cumulative circulation of the LEVs reaches a maximum value at about d*=4. During this time, the initial coherent LEV structure travels toward the trailing edge. With the vortex reaching the trailing edge and occupying the complete suction side of the wing, the LEV circulation decreases and levels at more-or-less steady state values. This observation is in accordance with the study of Garmann and Visbal (2014), who hypothesized that the growth of the LEV is proportional to the distance from the root and it is constrained by the trailing edge for increasing aspect ratio. They showed that once the LEV reaches the trailing edge, forces level around steady-state values. At $d^* = 6$, the initial LEV structure probably tilts and dissipates so that the γ_1 algorithm detects the core of the secondary LEVs emanating from the leading edge.

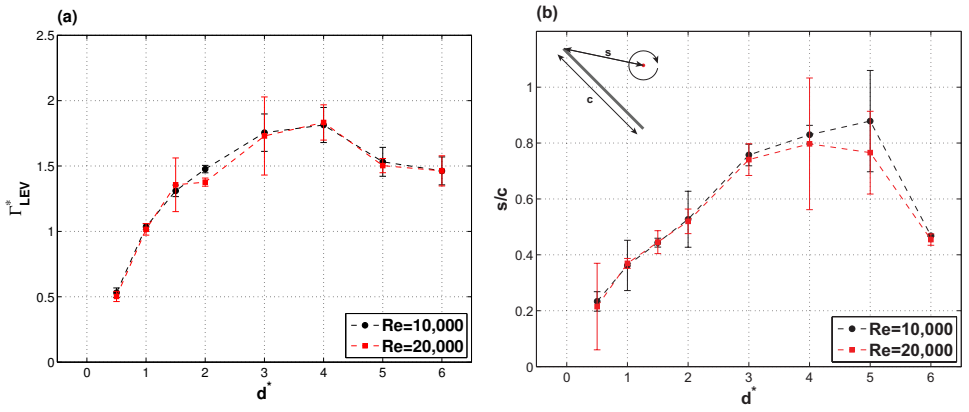

Figure 8.7: Temporal evolution of **a** non-dimensional LEV circulation (Γ^*_{LEV}) and **b** distance between the LEV core and the leading edge corner (s) for the Re=10,000 (*black circles*) and 20,000 (*red squares*)

Notwithstanding the similar evolution of flow structures throughout the revolving-surging motion for the two different Reynolds numbers, the force measurements reveal that the low Reynolds number case produces slightly lower force coefficients. This is likely to stem from the diffusive effects of viscosity, which may result in a different vorticity distribution in the flow field. This impacts the force generation in view of the vorticity moment theory (Kim and Gharib, 2010).

Effects of angle of attack

Performing surging motion at different angles of attack has a number of prominent effects on the force histories as well as the mean forces (Fig. 8.8a-c). Although the value of the acceleration is the same for all cases, the magnitude of the added mass force increases with increasing angle of attack as the surface area normal to the direction of the acceleration increases and thus more fluid is accelerated with the plate. In the post-build-up period, the most prominent difference between the force histories of different angle of attack cases is in the magnitudes of the forces: lift increases until 45° angle of attack and starts to decrease afterwards, whereas drag continuously increases with increasing angle of attack due to increasing wing surface area normal to the direction of motion. Representation of the mean forces in the wing-normal and -tangential directions reveals that the net force is almost normal to the wing in all cases (Fig. 8.8c). The mean normal force coefficient has an increasing trend with respect to the angle of attack. Another difference in the history of the forces is the phase at which the maximum force is generated. For instance, the lift peaks at $d^* = 3.2$, 4.3 and 3.6 for $\alpha = 30°$, 45° and 60°, respectively. Subsequently, the forces decrease to the steady-state values of the revolving motion.

In addition to the unsteady loads, the angle of attack has a considerable influence on the morphology of the vortical structures. The three dimensional flow fields for the angles of attack of $\alpha = 30°$, 45° and 60° at the end of the acceleration phase ($d^* = 1$) are depicted in Fig. 8.9. At this stage of the motion, the LEV displays fairly two-dimensional characteristics with its size increasing with the angle of attack. The prominent difference between

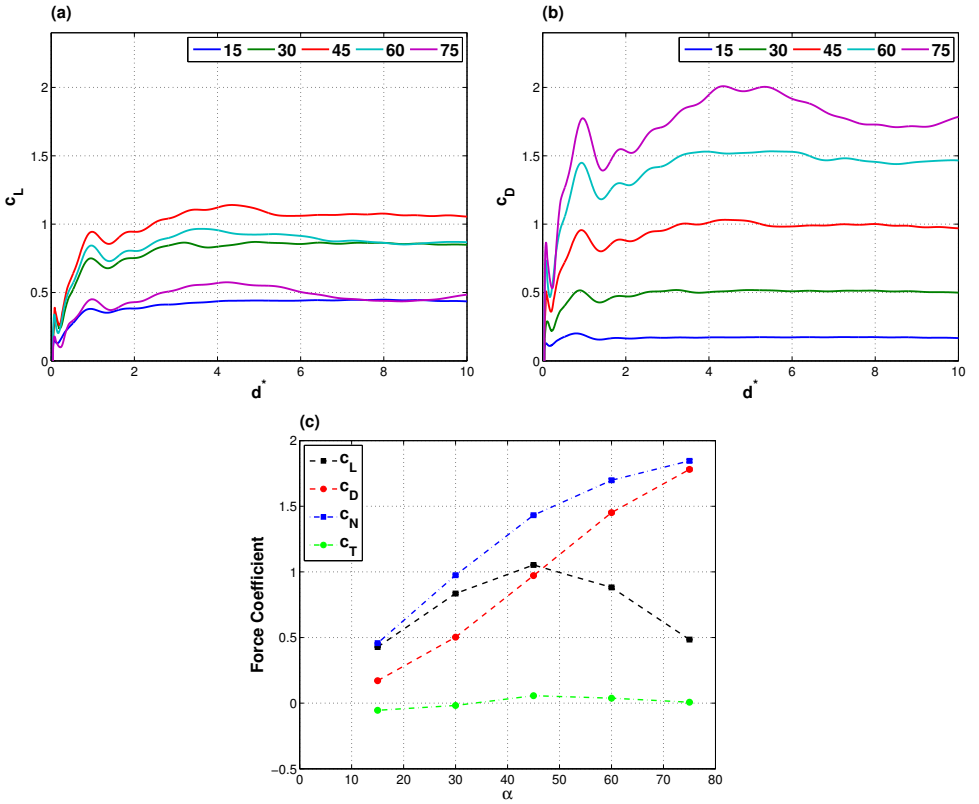

Figure 8.8: Temporal evolution of **a** lift and **b** drag coefficients for wings undergoing revolving-surging motions at different angles of attack at Re=20,000; **c** mean lift and drag coefficients averaged between $d^* = 1$ (end of acceleration) and $d^* = 10$

the flow field characteristics of the motions with different angles of attack is the morphology of the TV. For the smallest angle of attack, there is a coherent conical TV present at the wing tip, while as the angle of attack increases, this coherency is degraded with swirling features becoming apparent around the TV core. The chordwise location of the TV breakdown moves toward the leading edge with increasing angle of attack such that the vertically aligned helical features span until $0.3c$ chordwise position in the highest angle of attack case, whereas for $\alpha = 45°$ they start from approximately $0.4c$. The spanwise flow patterns are mostly similar in a qualitative sense for all cases such that the TV-induced spanwise flow exists around the trailing edge while no prominent flow pattern is apparent in the vicinity of the leading edge. The latter is in correlation with the two-dimensional nature of the LEV.

At $d^* = 2$ (Fig. 8.10), weaker vortical structures are present for $\alpha = 30°$ when compared to the case of $\alpha = 45°$. Still, the trend is similar such that the LEV is off the wing surface and it advects toward the trailing edge. Furthermore, in addition to the secondary TEVs, there are counter-rotating vortices shedding from the trailing edge. In this respect, the

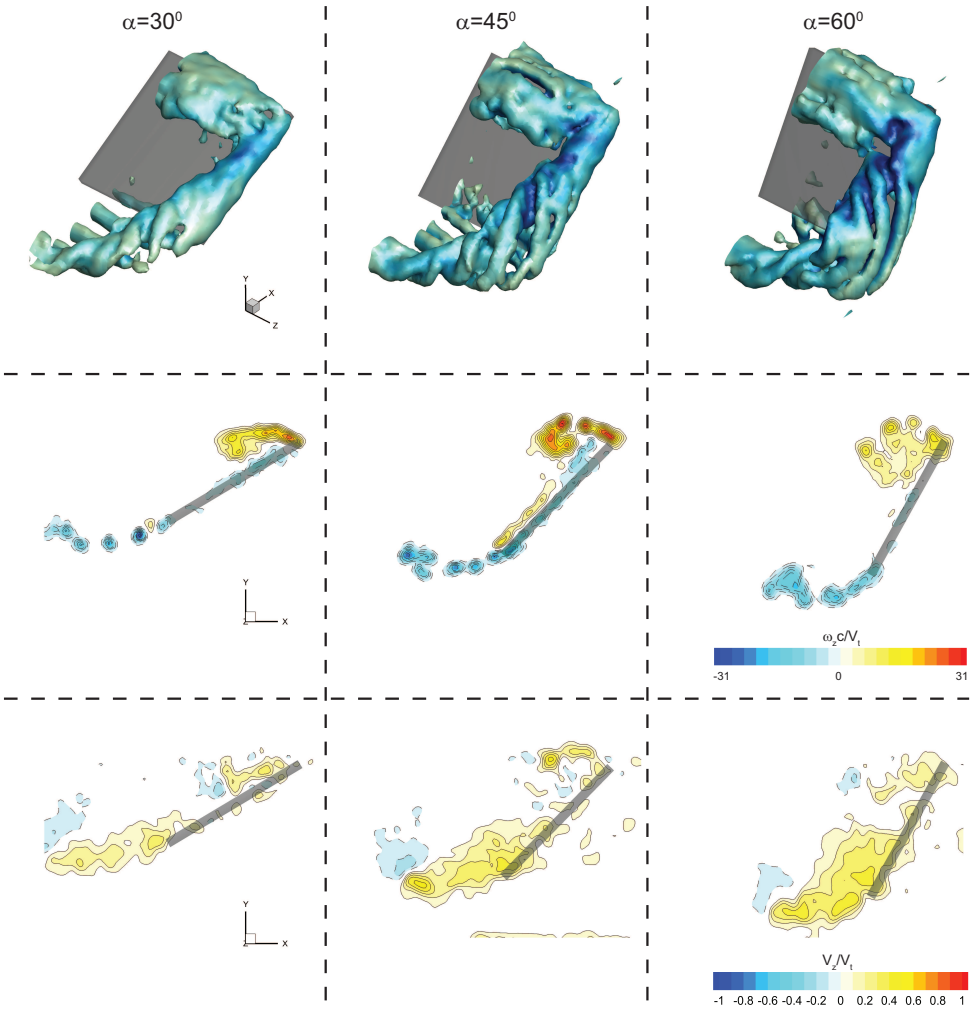

Figure 8.9: Isosurfaces of $Q/(V_t/c)^2 = 1.56$ coloured by vorticity magnitude (*first row*), contours of non-dimensional out-of-plane vorticity ($\omega_z c/V_t$) in the reference plane (*second row*) and contours of non-dimensional spanwise velocity (V_z/V_t) in the reference plane (*third row*) of the revolving-surging flat plate at Re=20,000 plotted at $d^* = 1$ for $\alpha = 30^\circ$ (*left*), $\alpha = 45^\circ$ (*middle*) and $\alpha = 60^\circ$ (*right*)

lowest angle of attack case bears similarity to the revolving-pitching wing as discussed in the previous chapter (see Fig. 7.6), which produces bound circulation during the pitching phase and some positive vorticity is shed after the pitching motion comes to the end. For the highest angle of attack case, on the other hand, the structures are more well-defined with swirling features of the TV aligned more vertically. Sure enough, the LEV is stronger in terms of spanwise vorticity for this case. In correlation with the growth of the LEV, a spanwise flow pattern emerges near the leading edge yet its strength decreases with decreasing angle of attack. In order to visualize the three-dimensional evolution of the spanwise flow,

isosurfaces of $V_z/V_t = \pm 0.25$ are shown in Fig. 8.11.

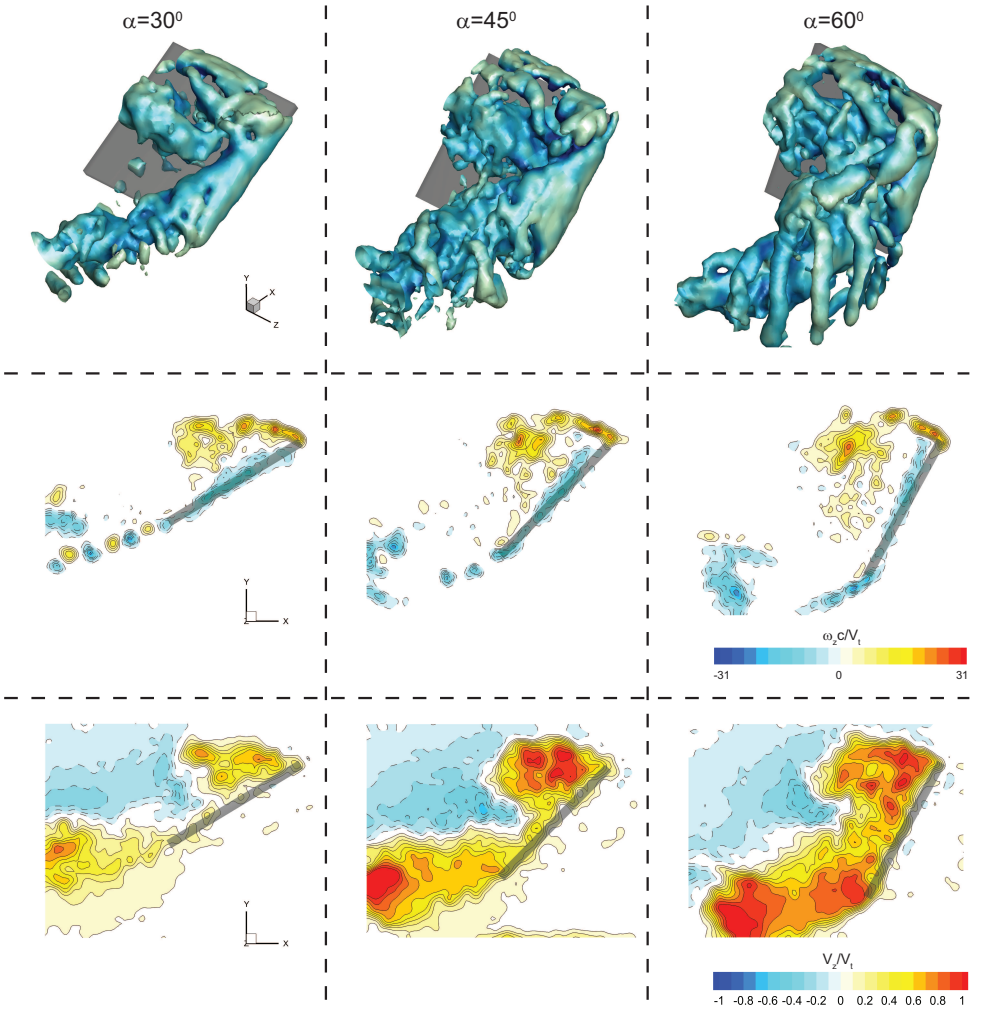

Figure 8.10: Isosurfaces of $Q/(V_t/c)^2 = 1.56$ coloured by vorticity magnitude (*first row*), contours of non-dimensional out-of-plane vorticity ($\omega_z c/V_t$) in the reference plane (*second row*) and contours of non-dimensional spanwise velocity (V_z/V_t) in the reference plane (*third row*) of the revolving-surging flat plate at Re=20,000 plotted at $d^* = 2$ for $\alpha = 30^\circ$ (*left*), $\alpha = 45^\circ$ (*middle*) and $\alpha = 60^\circ$ (*right*)

In relation to the characteristics of the TV, the three cases show differences in terms of spanwise flow patterns. At the end of the acceleration phase, the tip vortex is the dominant factor in the determination of the spanwise velocity profile such that there is a positive spanwise flow (toward the wing tip) at the pressure side and a negative flow (toward the wing root) at the suction side. The strength of this flow pattern is correlated with the angle of attack such that smaller velocities are present for the lowest angle of attack case. At the following stage of the motion, a positive spanwise flow pattern emerges on the suction

side for $\alpha = 45°$ and $60°$, while it is rather weak for $30°$. It has been stated that such a flow structure originates from centrifugal forces and spanwise pressure gradients. However, the difference between the strength of the positive spanwise flow patterns for the three cases at the same stage of the motion indicates the major influence of the spanwise pressure gradient. It is such that the promoted separation at the high angle of attack probably creates a larger spanwise pressure gradient and thus stronger spanwise flow.

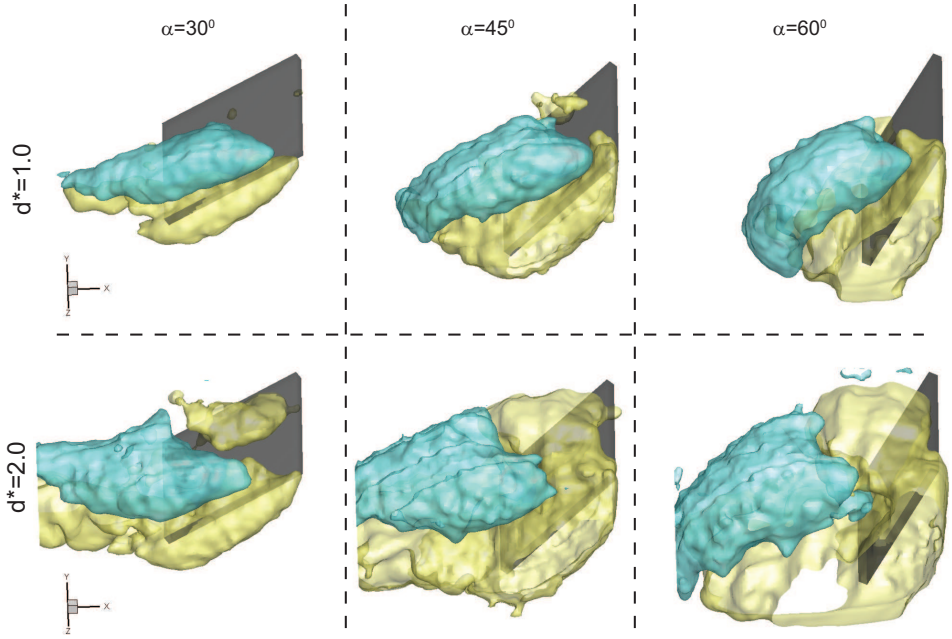

Figure 8.11: Isosurfaces of spanwise velocity ($V_z/V_t = -0.25$ (*blue*) and $V_z/V_t = 0.25$ (*yellow*) plotted for the cases of $\alpha = 30°$ (*left*), $\alpha = 45°$ (*middle*) and $\alpha = 60°$ (*right*) at $d^* = 1$ (*first row*) and $d^* = 2$ (*second row*) at Re=20,000

In order to evaluate the variation of the forces in relation to the vorticity dynamics, the circulation and position of the LEV for the cases of $\alpha = 30°$, $45°$ and $60°$ are plotted in Fig. 8.12. First, the increase of normal force with the angle of attack (see Fig. 8.8c) is in accordance with the increase of the LEV circulation (Fig. 8.12a). Apparently, the contribution of the LEV circulation is promoted by the augmentation of the vorticity generation at higher angles of attack. For all cases, the circulation of the LEV shows a rapid increasing trend in the first two chord lengths of travel (until $d^* = 2$). During this period, the position of the LEV with respect to the wing leading edge is also similar for the different angles of attack. Subsequently, the LEV reaches a maximum distance at $d^* \approx 3$ for the cases of $\alpha = 30°$ and $60°$, whereas the maximum distance is achieved at $d^* \approx 4$ for the case of $45°$. This is in agreement with the maximum force generation phases of these cases. Moreover, it was shown that for the cases of $\alpha = 30°$ and $60°$, the complete suction side of the plate is nearly covered with layers of (mostly) small scale structures emanating from the leading edge already at $d^* = 3$. Therefore, it supports the hypothesis that the force generation saturates once the LEV reaches the trailing edge and starts interacting with the TEV (Garmann and

Visbal, 2014).

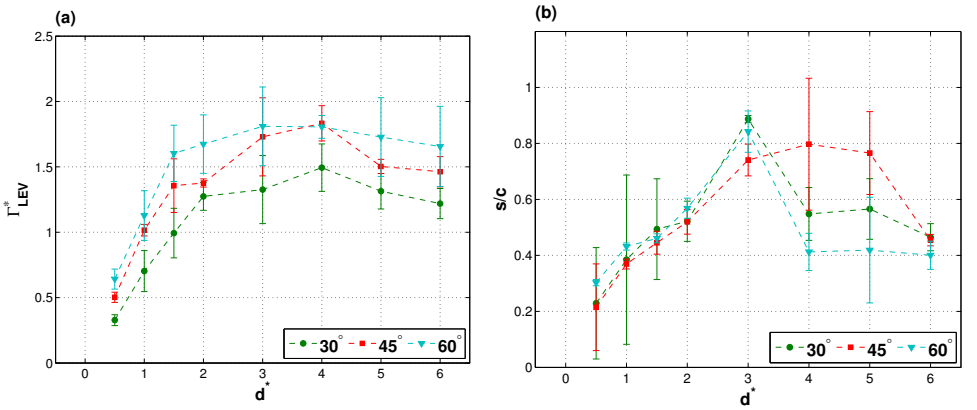

Figure 8.12: Temporal evolution of **a** non-dimensional LEV circulation (Γ^*_{LEV}) and **b** distance between the LEV core and the leading edge corner (s) at Re=20,000 for $\alpha = 30°$ (*green circles*), $\alpha = 45°$ (*red squares*) and $\alpha = 60°$ (*blue triangles*)

Effects of acceleration

Figure 8.13 shows the force histories for the revolving-surging wings which accelerate to the terminal velocity from rest over $d^* = 0.5$ (fast case, corresponding to acceleration value of $a = 3.2$ m/s^2 at the reference position) and $d^* = 1$ (slow case, $a = 1.6$ m/s^2). In relation to the different acceleration magnitudes, the wings experience different non-circulatory forces at the beginning of the motion. Although the acceleration of the fast case is twice that of the slow case, the ratio of the initial normal force peaks (Fig. 8.13c), which can be attributed to reaction force due to added mass acceleration, is approximately 1.8 (c_N = 1.12 and 0.63 for the fast and slow cases, respectively). By use of Eq. 7.2, the normal force coefficients associated with the accelerated fluid inertia are estimated as 0.8583 and 0.43, respectively. This disparity, on the other hand, may be associated with a faster acceleration of the wing than the prescribed value at the very beginning of the motion. This reasoning can be verified by the fact that the value of the dip ($c_N = 0.44$) following the initial peak in the normal force history of the slow case agrees well with the estimated value. The driving motor most likely started the motion with a relatively higher acceleration and then the integrated PID loop regulated the motion to the prescribed motion kinematics.

A striking result of this comparison is the good agreement between the two cases after the build-up phases are over. During the acceleration period, the fast case generates higher forces due to the increased non-circulatory force component and a relatively fast development of the circulatory effects. As the build-up period is over for the fast case at $d^* = 0.5$, both lift and drag coefficients initially decrease due to the vanishing of the added mass effect. Subsequently, they increase with the developing circulatory effects. The same also occurs for the slow case at $d^* = 1$. Following to this instant, force coefficients are quite similar except some variations due to the vibratory behaviour of the forces in the fast case. This behaviour is likely to stem from the test rig vibrations, which were more severe for the

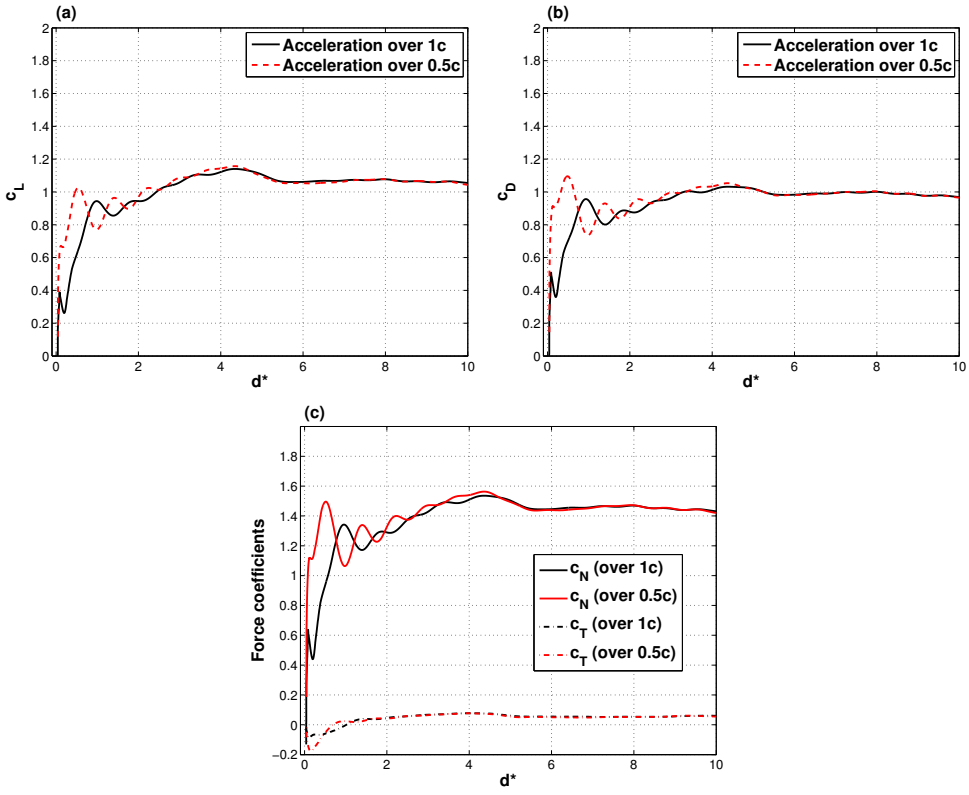

Figure 8.13: Temporal evolution of **a** lift, **b** drag and **c** normal and tangential force coefficients for the flat plates undergoing revolving-surging motions with acceleration periods of $d^* = 0.5$ (*red*) and $d^* = 1$ (*black*)

fast case and cannot be fully filtered. As these oscillations die out, force histories of the two cases become identical at about $d^* = 4$. This agreement implies that for the values considered here the amplitude of the acceleration in the build-up period has a negligible effect on the subsequent evolution of the circulatory forces for the revolving-surging motion.

Three-dimensional flow fields of the two cases compares similar to the force histories as shown in Fig. 8.14. At $d^* = 0.5$, the so-called fast wing reaches the terminal velocity while the slow wing is still accelerating ($V = 0.71V_t$). At this stage of the motion, both cases contain a vortex loop with intact topological characteristics. However, the vortical structures of the fast case are stronger in terms of vorticity magnitude in correlation with the generation of the elevated forces. As the wings reach the phase of $d^* = 1$, the breakdown of the TV into helical features occurs and the LEV lifts off from the wing surface while the shear layer emanating from the leading edge rolls into small-scale vortical structures in both cases. The vortices of the two cases at this phase are also similar in terms of strength, as can be evidenced from the colours of the Q criterion isosurfaces and contours of spanwise vorticity. It is also shown by means of the temporal evolution of the LEV circulation and its trajectory in Fig. 8.15. The LEV in the fast case initially has a higher value

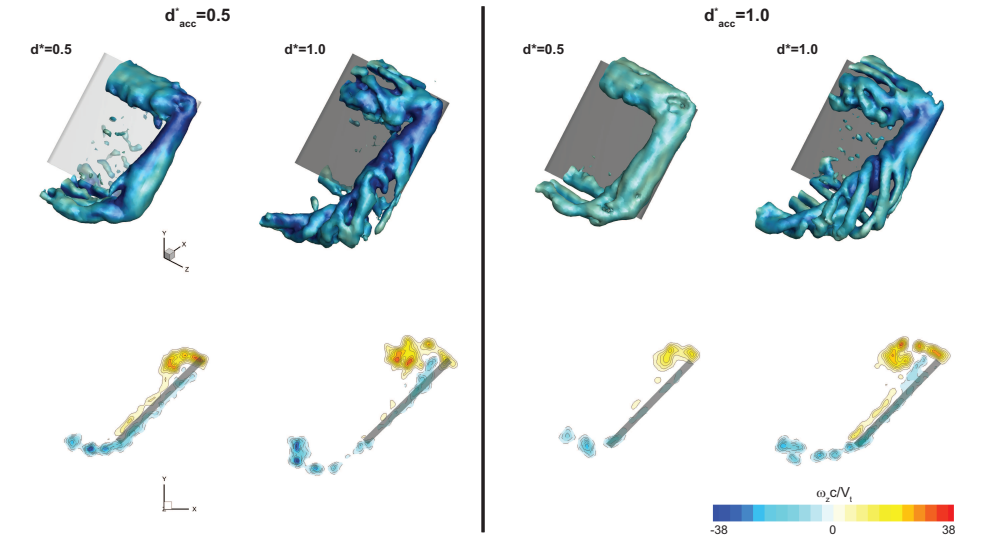

Figure 8.14: Isosurfaces of $Q/(V_t/c)^2 = 1.56$ coloured by vorticity magnitude (*first row*), contours of non-dimensional out-of-plane vorticity ($\omega_z c/V_t$) in the reference plane (*second row*) plotted at $d^* = 0.5$ and $d^* = 1$ for revolving-surging motions with acceleration periods of $d^* = 0.5$ (*left*) and $d^* = 1$ (*right*) at Re=20,000

of circulation yet at $d^* = 1$, when the slow case also reaches the same terminal velocity, the circulation values of the two cases have become identical. The LEV trajectories, on the other hand, displays a similar trend regardless of the different motion kinematics in the acceleration phase.

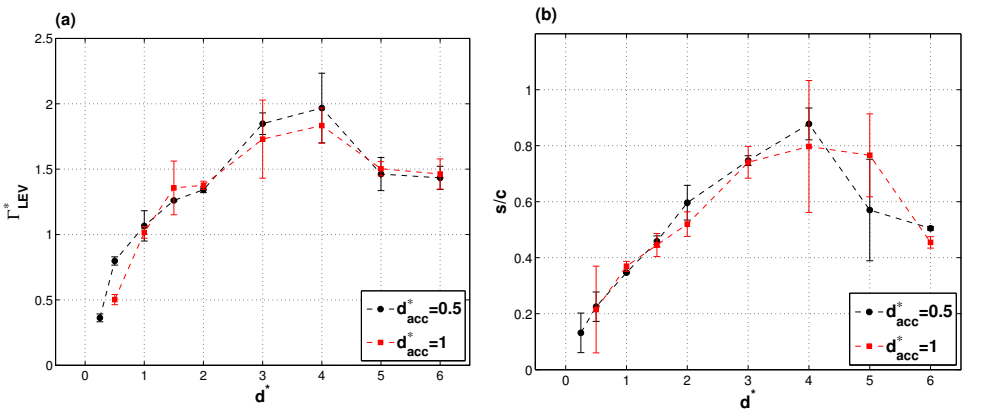

Figure 8.15: Temporal evolution of **a** non-dimensional LEV circulation (Γ^*_{LEV}) and **b** distance between the LEV core and the leading edge corner (s) for revolving-surging motions with acceleration periods of $d^* = 0.5$ (*black*) and $d^* = 1$ (*red*) at Re=20,000

Effects of multiple revolutions

In order to assess the effects of multiple revolutions, force measurements were done on a revolving-surging flat plate at three different angles of attack (α = 15°, 30° and 45°) performing three full revolutions (until d^* = 42). Corresponding lift and drag coefficients are presented in Fig. 8.16. In order to reveal the differences in force production between consecutive revolutions, steady-state mean values (i.e., the mean values that are attained close to the end of each revolution) are also indicated in the figure.

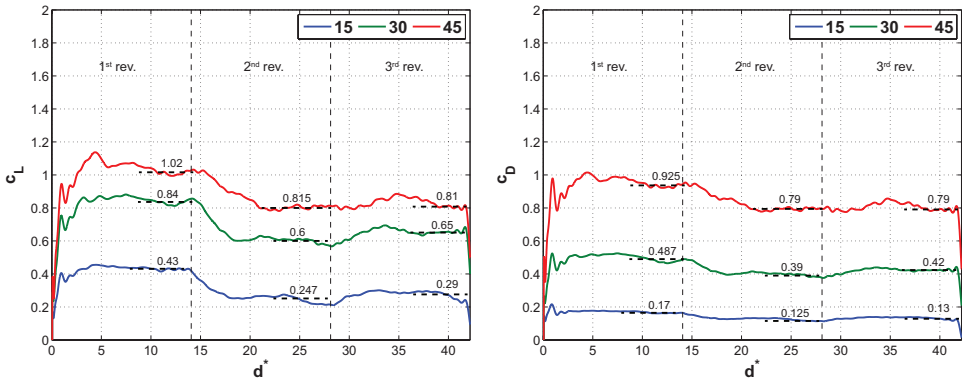

Figure 8.16: Temporal evolution of **a** lift and **b** drag coefficients for wings performing revolving-surging motions for three full revolutions at α = 15°, 30° and 45° at Re=20,000

In general, a similar trend is observed in all cases such that forces decrease as the wing starts moving into its own wake in the second revolution. The steady-state lift and drag coefficients of the second revolution are 80 % and 83 % of those of the first revolution for α = 45°, respectively. This variation is in a good agreement with the observations of Venkata and Jones (2013), who reported that in the second revolution force coefficients decline approximately to 80 % of their first revolution values. For smaller angles of attack, the decrease in lift is more severe, while drag coefficients still displays similar relative variation. At α = 30°, the decrease in lift coefficient is 30 %, and at α = 15° it is 43 %. As the wing starts moving in the third revolution, force coefficients increases slightly and subsequently decreases to a steady-state level, which is nearly equal to that of the previous revolution.

The decrease in the force production in the second revolution is a result of the wing encountering its own wake structures, which causes a reduction in the effective angle of attack. Apparently, the decay rate of these wake structures is higher at higher angles of attack, which results in a relatively small decrease in the forces in the second revolution.

For the results discussed previously, the main focus of interest was the initial stages of revolving motion starting from rest (generally first six chord lengths of travel, corresponding to a revolution angle of 154°) and the wall interference effects were shown to be negligible in Section 8.3.1. However, in case of multiple revolutions, the developing recirculating flow in the tank due to continuous revolution of the flat plate and interference effects may be significantly influential on the force histories. In their parametric study,

Manar et al (2014) showed that $5c$ tip clearance in a confined space is sufficient for experiments with revolving wings at Re=10,000 for up to at least two revolutions. In view of this, for the current case, the slight increase in the third revolution of the flat plate might be due to increasing wall interference and blockage effects in the water tank.

8.4.2. Revolving-pitching motion

Effects of pitch rate

Figure 8.17 illustrates lift and drag coefficients for three revolving-pitching cases with non-dimensional pitch rates of $k = 0.196$ and 0.39. The two $k = 0.196$ cases were attained by simultaneously varying the pitch rate and the terminal velocity (viz., $\dot{\alpha} = 1.57$ rad/s at $V_t = 0.2$ m/s and $\dot{\alpha} = 3.14$ rad/s at $V_t = 0.4$ m/s), whereas the $k = 0.39$ case corresponds to the revolving-pitching motion with $V_t = 0.2$ m/s and a pitch rate of $\dot{\alpha} = 3.14$ rad/s. The experimental results are complemented with the theoretical estimations based on the quasi-steady model (see Section 7.2.2). It should be noted that the two cases with the same normalized pitch rate only differ in Re. According to the theoretical model, the force generation does not depend on Re so that the estimated forces are identical for the two $k = 0.196$ cases.

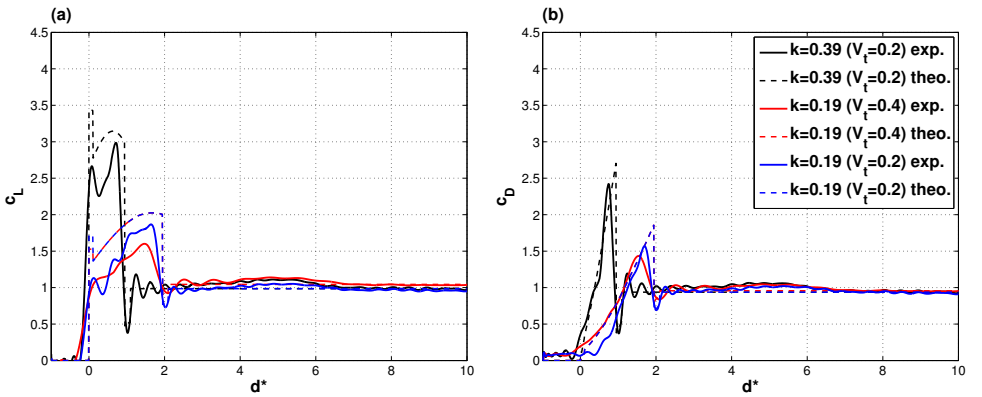

Figure 8.17: Temporal evolution of **a** lift and **b** drag coefficients for wings performing revolving-pitching motions with three different pitch rates corresponding to non-dimensional pitch rates of: $k = 0.39$ (pitching over $d^* = 1$ at $V_t = 0.2$ m/s and Re=10,000, *black*), $k = 0.19$ (pitching over $d^* = 2$ at $V_t = 0.4$ m/s and Re=20,000, *red*), $k = 0.19$ (pitching over $d^* = 2$ at $V_t = 0.2$ m/s and Re=10,000, *blue*) complemented with theoretical estimations based on quasi-steady model (*dashed*)

In the previous chapter, it was shown that the pitching motion results in the generation of elevated force coefficients compared to the surging motion (i.e., accelerating wing motion from rest at a constant angle of attack). The enhanced force production was shown to be a result of the formation of additional circulation (in the form of the bound and the LEV circulation) and modified trajectories of the LEV and TEV due to the pitching motion. Accordingly, the pitching motion at a lower pitch rate produces relatively lower forces as shown in Fig. 8.17. Still compared to the revolving-surging wing cases discussed in this chapter, the pitching motion provides high and persistent lift coefficients while the drag coefficient increases almost linearly due to changing orientation of the wing with respect

to the revolving motion direction.

Comparison of the revolving-pitching motions with the same non-dimensional pitch rate reveals that the motion at V_t = 0.2 m/s (Re=10,000) produces slightly higher forces during the course of the pitching motion, although the theoretical model estimates identical force histories for the two motion kinematics. The discrepancy between the two experimental results probably originates from the insufficiency of the pitching servo-motor in the faster revolving motion case in terms of actually achieving the prescribed pitching rates due to the higher hydrodynamic loads. After the pitching phase is over, the force coefficients of all cases overlap, suggesting that the forces and the flow fields at the terminal condition do not critically depend on the dynamics of the pitching phase.

8.5. Conclusions

The evolution of flow fields around revolving-surging and revolving-pitching low-aspect-ratio flat-plate wing has been investigated experimentally via Tomographic PIV. The measurements were performed in two adjacent volumes positioned at two different spanwise locations, providing a total measurement volume of size 90 mm × 70 mm × 50 mm (chordwise×normal×spanwise). A water-submergible force sensor was used to measure the forces exerted on the wing model. In order to investigate the effects of Reynolds number and angle of attack, the experiments were carried out in a Reynolds number range of 5,000 – 25,000 at 45° angle of attack; and at an angle of attack range of 15° - 75° for the Reynolds number of 20,000. Moreover, the effects of acceleration and multiple revolutions on the flow fields and unsteady forces of the revolving-surging wing have been explored. For the former, measurements were performed with the revolving-surging wing that accelerates from rest to the terminal velocity over d^* = 0.5 and 1. For the latter, the wing was set in motion for three revolutions in the surging configuration at α = 15°, 30° and 45°. Lastly, the pitch rate for the revolving-pitching wing was varied in order to assess its influence on the force histories. Three cases with two different non-dimensional pitch rates are considered in this study. The baseline case has a non-dimensional pitch rate of k = 0.39 (V_t = 0.2 m/s and $\dot{\alpha}$ = 3.14 rad/s, corresponding to a pitching period of d^* = 1), whereas the other cases both have k = 0.19, which was achieved either by changing the terminal velocity (V_t = 0.4 m/s and $\dot{\alpha}$ = 3.14 rad/s) or by changing the pitch rate (V_t = 0.2 m/s and $\dot{\alpha}$ = 1.57 rad/s), both cases corresponding to a pitching period of d^* = 2.

Comparison of force coefficient histories shows that force generation increases slightly with increasing Re. Calculation of mean values in the post-acceleration period for different Re reveals that force coefficients display an increasing trend with the curve flattening towards the higher end of the measurement Re range. Comparison of the LEV circulation for Re of 10,000 and 20,000 points out that a higher amount of vorticity is generated at higher Re, although normalized LEV circulations have almost the same magnitude and variation for both cases. Moreover, the LEV trajectories show a good agreement which, in the context of the vorticity moment theory (Wu, 1981), explains similar force coefficient histories with a small difference in the magnitude. This difference is likely to originate from the diffusive effects of viscosity that may result in a slightly different vorticity distribution. It is also shown that Re does not greatly influence the general behaviour of the flow structures.

Force histories at different angles of attack show that lift increases until 45° angle of at-

tack and starts to decrease for higher angles. Due to increase of the surface area normal to the direction of the motion and promoted flow separation at the leading and trailing edges, drag remains to increase for higher angles of attack. Mostly normal forces are generated in all cases. In addition to the amount of vorticity generated and circulation accumulated in the LEV, the angle of attack also affects the phase of the maxima in the force histories such that the 45° angle of attack case reaches the maximum the latest of the cases considered. This phase difference is shown to be in correlation with the trajectory of the LEV such that the LEV reaches the trailing edge and occupies to the complete suction side at a relatively early stage for the cases of $\alpha = 30°$ and 60°. The angle of attack of the surging motion also affects the morphology of the vortical structures around the wing. At the same stage of the motion, different spanwise flow patterns are observed around the wing. The positive spanwise flow strengthens with increasing angle of attack, which points to the considerable influence of spanwise pressure gradient that is enhanced by the promoted separation at high angles of attack.

Comparison of the unsteady forces for revolving-surging wings accelerating over $d^* = 0.5$ and 1 reveals that different motion kinematics during the build-up phase in terms of the acceleration amplitude does not have a significant influence on the subsequent force generation. The force histories of the two cases level just after the wings reach the terminal motion kinematics. Flow field characteristics support the observations from the force histories such that the LEV circulation is higher during the build-up period for the fast case due to the increased added mass reaction force and the faster development of circulatory effects. In the following stages, the two flow fields contain identical features with the LEV circulation and trajectory, as calculated in the reference plane, being unaffected from different start-up kinematics.

Performing multiple revolutions, on the other hand, results in a decrease in the forces due to wake interference effects. In the second revolution, lift and drag coefficients decline approximately by 20 % for the revolving-wing at $\alpha = 45°$. The relative decline of the forces increases with decreasing angle of attack, which is likely to be associated to the faster decay rate of the wake structures at high angles of attack.

The pitching motion results in the generation of relatively higher forces compared to the surging wing cases considered in this study. The elevated force coefficients are shown to be a function of the non-dimensional pitch rate, as also stated by the quasi-steady model. It is also shown that regardless of the pitching motion kinematics, force histories of all three cases coincide in the post-pitch-up period of the revolving motions.

9

Conclusions and Recommendations

In this chapter, the main results and the findings of the present dissertation on the aerodynamic mechanisms in flapping-wing flight are summarized, specifically in the context of the flapping-wing MAV DelFly II (Part I) and unsteady revolving (flexible) surging and pitching wings (Part II).

In Chapter 1, flapping-wing aerodynamics is compared to conventional means of force production (i.e., fixed and rotary wing) in the low-Reynolds number flight regimes, where small birds, insects and MAVs operate. The motivation for the present investigation is explained in relation to the comparative analysis performed between the aforementioned design concepts. Chapter 2 gives an overview of the major aerodynamic mechanisms that are responsible for the elevated force generation in flapping-wing flight. The following chapters of the thesis are organized in two parts.

The first part consists of studies performed with the flapping-wing MAV DelFly II. In Chapter 3, the aerodynamic performance of the DelFly II is assessed by means of extensive force, power consumption and wing deformation measurements. A special attention is given to the determination of aerodynamic force components from the force sensor measurements and the identification of the effects of the fixed-model force measurements, which restricts the dynamic body modes that exist in actual free-flight conditions. Chapter 4 includes flow field measurements around the flapping wings and in the wake of the DelFly II in hovering conditions. In Chapter 5, results of the three-dimensional wake reconstruction study are presented for the forward flight conditions of the DelFly. Furthermore, two wake reconstruction strategies are compared: (1) a spatio-temporal wake reconstruction based on the Taylor's hypothesis; (2) a spatial wake reconstruction by means of a modified Kriging regression technique, that was developed to take into account the measurement uncertainties.

In the second part, experimental studies concerning the fundamental research in flapping-wing flight are reported. In Chapter 6, effects of wing flexibility on the unsteady flow around a flexible wing undergoing a clap-and-fling type flapping motion are investigated by means of tomographic-PIV measurements. Chapter 7 focuses on the evolution of three-dimensional flow fields and unsteady forces in revolving surging and pitching flat plates. Subsequently, Chapter 8 reports the results of the experimental study exploring the effects of different parameters, viz., acceleration period, Reynolds number, angle of attack and pitch rate on the flow characteristics and force generation mechanisms in revolving wings.

9.1. Conclusions

The main conclusions of this study are presented as follows:

Significance of flapping-wing aerodynamics in the field of MAVs

Comparison of different design configurations (i.e., fixed-wing, rotary-wing and flapping-wing concepts) reveals that none of the MAVs currently available is able to fulfill the key design requirements (Chapter 1). Fixed-wing designs lack hovering capability which makes them unsuitable for indoor operations. Moreover, these designs are not aerodynamically efficient in the low Reynolds number regime (10^3-10^5) where most of the MAVs operate. Although rotary-wing designs are able to hover, their aerodynamic efficiency is also influenced by the detrimental effects of the low Reynolds number regime, which results in a shorter flight endurance in this class of MAVs. In contrast, flapping-wing configurations make use of unconventional force generation mechanisms peculiar to unsteady flows and outperforms the other design concepts in terms of force production in the intended flight regimes. This motivates utilization of flapping-wing phenomenon in the design of MAVs.

Part I: Experimental Investigation of the DelFly Flapping-Wing Aerodynamics

Identification of aerodynamic force components in the DelFly flapping-wing flight
Determination of aerodynamic forces generated by a flapping-wing MAV by means of balance-mounted wind tunnel measurements is a challenging procedure (Chapter 3). This is mainly due to the fact that the force sensor responds to inertial effects and structural vibrations in addition to the unsteady aerodynamic forces that are of primary interest. Therefore, complementary in-vacuum force measurements are required to isolate the aerodynamic force components. In the DelFly flapping-wing flight in hovering conditions, the first two harmonics in the X-force (i.e., the force component along the DelFly fuselage as defined in the body axis) are associated to the aerodynamic forces. The first (fundamental) harmonic is related to the clap-and-fling mechanism that occurs once in a flapping cycle and the second harmonic stems from the leading edge vortex (delayed stall) mechanism. Comparison of in-air and in-vacuum measurements also reveals that a large portion of the total power consumption (64-74 %) originates from the aerodynamic effects, whereas consumption due to mechanical effects is approximately (20 %). Considering that almost zero X-force is generated in vacuum conditions, the power consumed by these mechanical effects may considered to be lost. However, their indirect effects on the aerodynamic mechanisms should also be debated to comment on the contribution of the elastic-inertial effects. Due to the enhancing effect of the wing-wing interaction, flapping wings generate 75 % more mean force during the outstroke, which shows the effectiveness of the clap-and-peel mechanism.

Determination of forces in balance-mounted and free-flight conditions
Another effect of the balance-mounted force measurements is the restriction of the dynamic body modes which are present in actual free-flight conditions. A comparative analysis of the forces estimated from free-flight visual tracking measurements and acquired in balance-mounted wind tunnel experiments allows assessment of the body-restriction influence on the force mechanisms as well as revealing several factors that are effective on the force determination methods (Chapter 3). The main drawback of the free-flight force estimation method is the use of numerical differentiation algorithms to derive velocities and accelerations from position data. This results in a magnification of the measurement error and smoothing of the data due to the limited recording rate in combination with the low-pass filtering effect of the numerical differentiation schemes. The latter becomes the main limiting factor due to relatively low sampling rates of visual tracking systems. For the balance-mounted measurements, the clamping point has a significant effect since it modifies the structural dynamics of the flexible body. Clamping at a location far from the exertion point of the unsteady forces results in the structural resonance of the body that generates oscillatory forces with comparable amplitudes and in the frequency range of the forces of interest. Due to the particular layout of the DelFly, these structural oscillations interfere with the Z-force component, while the X-force is mostly insensitive to the clamping point. Comparison of the unsteady forces obtained by use of the above-mentioned methods reveals that the X-force component shows a good correspondence whereas the Z-force component displays deviations depending of the flight condition. This concludes that the restriction of the dynamic body modes does not have a significant effect on the X-force component, whereas its effects on the Z-force is not fully resolved due to interference of

the structural oscillations in the balance-mounted wind tunnel measurements. Moreover, this study shows the success of the free-flight force estimation model based on the general aircraft equations of motion (under the assumption of non-flapping/rigid body kinematics) in the determination of forces acting on the DelFly.

Flapping frequency and wing geometry effects on the aerodynamic performance

In the hovering flight configuration of the DelFly, the X-force generation increases with flapping frequency, yet the variation is quasi-linear instead of a quadratic relation (Chapter 3). The increase in the flapping frequency also introduces a phase lag in the temporal evolution of the forces. The force generation increases with increasing Mylar foil thickness at the expense of a higher power consumption. Wing span has a significant effect on the X-force production such that increasing the span length by 4 cm results in an 28 % enhancement in the flap-averaged X-force component compared to the standard DelFly II wings with a span length of 28 cm.

Wing deformation characteristics

Wing deformation measurements (Chapter 3) provide valuable information regarding the force generation characteristics of the different cases as mentioned under the previous item. First, it is shown that the DelFly flapping wings perform a sort of delayed rotation during stroke reversals, which is due to flexibility of the wing such that the trailing edge starts moving in the new stroke direction at a later phase than the leading edge. The delay is further enhanced when increasing the flapping frequency, which also causes a delay in the build-up of the circulatory force generation mechanisms. This explains the phase lag observed between the force histories of the different wing-beat frequency cases. Second, the wings experience a considerable amount of spanwise distortion during the course of the flapping cycle, which results in a formation of time-varying twist angle. The twist angle increases with the flapping frequency, while the angle of attack of a given spanwise location displays a decreasing trend due to higher fluid loads and consequently increasing chordwise deformation. These two variations can account for the less-than-a-quadratic increase of the X-force generation with the flapping frequency. Third, it is shown that during the stroke reversals a cambered wing profile forms, which was shown to be favourable in terms of aerodynamic efficiency in a number of studies in the literature in the context of flapping-wing aerodynamics (see Section 3.4.1). The wing camber is promoted by the clap-and-peel motion, which is in correlation with the generation of higher forces during the outstroke. Apparently, the wing-wing interaction does not only create favourable flow conditions around the wings but also influences the aerodynamic forces indirectly via its effects on the wing geometry. Stiffener orientation has a major impact on the wing camber depending on the intersection point of a stiffener with the chordline at a given spanwise location. In the specific case of the DelFly II, for the spanwise positions with the intersection points located in the upper half of the chordline, a cambered wing profile exists. Otherwise, the bending of the stiffener results in a decrement in the geometric angle of attack. Comparison of the structural deformations of the wings with different wing surface thicknesses reveals a similar evolution of the wing profile properties throughout the flapping cycle. This indicates the dominant role of the stiffeners in providing structural support to the DelFly wings. Small differences in force generation and power consump-

tion of the two cases, on the other hand, are attributed to slight deviations in the wing profiles.

Evolution of flow fields around the flapping wings and in the wake in hovering flight
Flow visualizations around the flapping wings of the DelFly reveal the formation of conical LEVs on both wings during the instroke and outstroke as discussed in Chapter 4. During the peeling phase (i.e., the onset of the outstroke), the newly formed LEVs of the outstroke interact with the LEVs of the previous instroke, which are shed and convected upstream with their induced velocities. This interaction leads to a modification in the entrained stream toward the opening between the wings such that induced velocities of the vortex pair help aligning the flow with the wings and prevent excessive decrease of the effective angle of attack in the outstroke direction. Although the influence of the counter-rotating instroke LEVs on the growth of the LEV circulations at the beginning of the outstroke is not fully resolved, their negative contribution to the force generation is not considerable as assessed on the basis of the vorticity moment theorem since they are rather stationary and diminishing in strength. The inrush velocity toward the cleft between the wings reaching comparable magnitudes with the mean wing-tip velocity results in a formation of a low-pressure region and thus increment in the forces. Flapping at a lower frequency causes generation of less vorticity, which scales with the flapping frequency, yet the overall flow topology is similar. In the case of the longer-span wing (HAR10), a delay in the build-up of the circulation levels occurs in correlation with the force histories.

The wake velocity measurements in the chordwise oriented measurement planes reveal existence of a vortex pair, which sheds at the end of the instroke, and a jet-velocity profile due to the clapping motion of the wings. These flow features results in the formation of a momentum-surfeit wake that is indicative of a positive X-force generation (i.e., thrust). A momentum-based approach in a control volume around the DelFly in hovering configuration is employed to estimate the flap-averaged X-force under a number of simplifying assumptions. This approach, which only uses the streamwise velocity at a downstream location, is still able to calculate the forces within an error range of $5-15$ %.

Three-dimensional wake reconstruction in forward flight
Unsteady three-dimensional wake structures generated by the flapping wings of the DelFly II in forward flight configuration are reconstructed from several spanwise-oriented measurement planes by means of two techniques: (1) spatiotemporal wake reconstruction; (2) spatial wake reconstruction (Chapter 5). For the latter, a modified Kriging regression technique was developed, which also takes into account the measurement uncertainty in the regression process. In the specific case of the DelFly, each velocity vector is accompanied by an uncertainty value that is estimated based on the signal-to-noise ratio (peak-to-peak ratio in the cross-correlation plane) of the stereo-PIV measurements. Despite the fact that peak-to-peak ratio is not necessarily sufficient to provide an accurate model of the local PIV measurement uncertainty, it is efficient in modeling the error resulting from shadow regions, severe reflection and low seeding quality. As a result, Kriging regression with local error estimates outperforms conventional Kriging [see de Baar et al (2014)] as well as cubic spline interpolation in reconstructing the three-dimensional wake structures (Section 5.2.3). Three-dimensional wakes reconstructed by the two strategies display a good agreement in terms of behaviour, phase and orientation of the vortical

structures, which validates the assumptions underlying the spatio-temporal reconstruction (i.e., non-deforming wake and free-stream velocity as the convection velocity) for this specific case. The spatiotemporal reconstruction method allows to characterize the general three-dimensional structure of the wake, but the spatial reconstruction method can reveal more details due to higher streamwise resolution.

Comparison of the wake reconstructions for different values of the reduced frequency allows assessing the impact of the flapping frequency on the formation and interaction characteristics of the vortical structures. For low values of the reduced frequency, it is observed that the vortex structure formation of instroke and outstroke is relatively independent of each other, but that increasing interaction occurs at higher reduced frequencies. There is a phase lag in the appearance of the structures for increasing flapping frequency, which is in correlation with the generation of the forces. Comparison of thrust generated during the instroke and the outstroke phases of the flapping motion in conjunction with the development of the wake structures indicates that wing–wing interaction at the start of outstroke (peel motion) becomes a dominant feature for reduced frequencies greater than 0.62, while being relatively inactive at a lower reduced frequency.

Part II: Fundamental Research in Flapping-Wing Aerodynamics

Similarity analysis of wing deformation characteristics for in-air and in-water conditions

The two-dimensional Euler-Bernoulli beam equation is used to simulate the chordwise deformations of a plunging thin plate and to compare the deformation characteristics between in-air and in-water conditions (Chapter 6). Non-dimensional analysis of the equation yields two similarity parameter, which characterize: (1) the ratio of elastic to aerodynamic forces (bending stiffness parameter); (2) the ratio of inertial to aerodynamic forces. The equation is solved analytically by defining an equivalent-DelFly-wing, which is a simplified version of the actual wings in terms of structural properties. It is revealed that the inertial effects play a significant role in the structural deformation of the wings under in-air conditions. However, it is not straightforward to use this analysis to interpret the structural dynamics in actual conditions due to the approximating assumptions regarding the structural characteristics of the wings and the calculations of the forcing terms. Yet, this simplified analysis can assist in the design of flapping flexible wing experiments in a different medium. In this respect, comparison of in-air and in-water deformation characteristics reveals that it is not possible to achieve identical deformation characteristics because the inertial forces are significantly reduced in-water conditions. Comparison of the flow structures of flexible and rigid wings undergoing clap-and-fling type flapping motion reveals that the vortical structures (i.e., LEV and TEV) are rather detached from the wing surface in the case of the rigid wing and convects upwards and downwards during the clapping phase due to strong up-downwash generated as a result of interaction with the wall, which mimics the counter wing in the experiments. In the case of the flexible wing, they are more attached to the wing surface and shed into the wake of the wings at the end of the instroke. Consequently, the flexible wing interacts with these vortical structures at the onset of the new stroke, whereas this interaction does not take place in the case of the rigid wing.

Comparison of surging and pitching revolving flat plates

Comparison of the force histories shows that the pitching wing generates considerably higher forces during the build-up phase, where the lift reaches 2.5 times the steady-state value and the drag increases quasi-linearly due to increasing wing surface area in the stroke direction. The temporal evolution of the forces and their magnitudes are estimated fairly well by a quasi-steady model, that is primarily based on the thin airfoil theory. The difference in the build-up phases affects the force histories until six chords of travel after the end of build-up phase. In both cases, a vortex system that is comprised of an LEV, a TV and a TEV is formed during the initial period of the motion. The LEV lifts off, forms an arch-shaped structure and bursts into substructures, which occur at slightly different phases of the motions, such that the revolving-surging wing flow evolution precedes that of the revolving-pitching wing. The delay is shown to be in accordance with the behaviour of the spanwise flow which is affected by the interaction between the tip vortex and revolving dynamics. In the case of the pitching wing, during the build-up phase the spanwise flow is dominated by a strong tip vortex, the formation of which is promoted by a relatively higher pressure difference between the suction and pressure sides of the plate. The tip vortex influences the spanwise flow pattern also in the surging case, however its effect does not persist as long as in the pitching case. In order to assess the relation between the vortical structures and the unsteady forces, the vorticity moment theory is utilized. Further analysis shows that the enhanced force generation of the revolving-pitching wing during the pitch-up phase originates from: (1) increased magnitude and growth rate of the LEV circulation; (2) relatively favourable position and trajectory of the LEV and the starting vortex; (3) generation of bound circulation during the pitching motion, whereas that of the revolving-surging wing is negligible in the acceleration phase.

In addition to the above-mentioned conclusions regarding the flow physics, this study also documents the applicability of the quasi-steady model in order to estimate the force histories. The advantage of this method is that it does not require a priori knowledge of the flow fields and uses only motion kinematics to calculate the forces. In contrast, knowledge of vortex behaviour is required to employ the vorticity moment theory to predict the force histories.

Effects of Reynolds number and motion kinematics in revolving flat plates

Comparison of force coefficient histories in the Re range of 5,000 - 25,000 shows that the force generation increases slightly with increasing Re. Mean force coefficients display an increasing trend with the curve flattening toward the higher end of the measurement Re range. Comparison of the LEV circulation for Re of 10,000 and 20,000 points out a higher amount of vorticity being generated at higher Re, although normalized LEV circulations have almost the same magnitude and variation for both cases. Moreover, the LEV trajectories show a good agreement which, in the context of vorticity moment theory, explains the similar force coefficient histories. The differences in force magnitudes are likely to originate from the diffusive effects of viscosity, that presumably result in variations in the vorticity distributions in different Re cases.

Force histories in the angle of attack range of 15°-75° show that mostly normal forces are generated under all conditions. The normal force component increases with the angle of attack due to promoted flow separation and consequently higher circulation is accumulated in the LEV. Due to the orientation of the wing surface with respect to the stroke

direction, drag continuously increases with the angle of attack, whereas lift peaks at 45° and starts to decrease for higher angles. Variation of the angle of attack also influences the phase of the maxima in the force histories such that 45° angle of attack case reaches the maximum the latest of the cases considered. This phase difference is shown to be in correlation with the trajectory of the LEV such that the LEV reaches the trailing edge and occupies the complete suction side of the plate earlier for the cases of $\alpha = 30°$ and 60°. Once this occurs, the forces level at more-or-less steady-state values. A stronger spanwise flow pattern at 60° angle of attack compared to the other cases at the same stage of the revolving motion indicates the significant influence of the spanwise pressure gradient.

For the acceleration values considered in this study, it is shown that different kinematics of the build-up period do not have an influence on the force histories and flow field characteristics in the post-build-up period. Higher forces are generated in the build-up period due to the increase in the added mass reaction force and a more rapid build-up of the LEV circulation in the fast case, yet once the terminal conditions are reached, forces and flow structures of the different cases become mostly identical.

In the case of multiple revolutions, the flat plate interacts with its wake which causes a decrease in the steady-state force values. The relative decrease is higher at lower angles of attack, which can be attributed to a faster decay of the wake structures at high angles of attack.

9.2. Recommendations

Notwithstanding the increased interest in flapping-wing flight, there are still many open questions concerning the unsteady flapping-wing aerodynamics of flying animals and vehicles. The complexity of these systems increase substantially as one progresses from a model of a two-dimensional rigid wing placed in a free-stream flow with a limited effect of viscosity toward a three-dimensional flapping flexible wing. The complexity is further enhanced by the two-way fluid-structure interaction with the presence of wing flexibility: the wings do not only influence the surrounding flow but they are also deformed by the same stream. Clearly, the study of flapping-wing aerodynamics particularly with three-dimensional flexible wings is not straightforward and requires a systematic approach to properly identify effects and contributions of different elements. This strategy has been followed in the studies reported in this thesis to simplify the given complex mechanism and to gain a better understanding of the phenomenon. Regardless of these efforts, there have been significant difficulties particularly regarding the experimental research on the DelFly.

The most crucial improvement will be to improve the manufacturing techniques of the wings for the experimental DelFly model in a way that better repeatability of the experiments can be attained. In the current manufacturing process, the DelFly wings are mostly hand-made. Although always the same person built the wings which were used in the experiments and followed a systematic procedure to minimize human-related inconsistencies in the final product, still some variations were observed between the measurements for the same experimental parameters performed in different experimental campaigns. They are likely to originate from the imperfections in the wing structure as well as the pretensioning of the wing surface associated to how the wings are mounted on the DelFly fuselage and to the driving system. In this respect, an important step will be to comput-

erize the wing manufacturing process. A suitable option can be use of three-dimensional printing technology, which have progressed considerably in the last five years. In this way, the stiffeners and the wing surface can be built as a complete body which will also prevent possible failures which could otherwise occur due to the bounding between the two structures becoming loose in time.

Regarding the force estimations from the free-flight position tracking measurements, it will be useful to implement onboard sensors which can provide time-resolved information of acceleration and angular rates. This will eliminate the need for the use of numerical differentiation algorithms to calculate these quantities from the temporally-coarse position data, which appears to be the bottleneck in the determination of time-resolved forces. On the wind-tunnel force measurements side, a stiffer DelFly body can be used in the experimental model in order to minimize the clamping point effects and acquire more reliable force measurements in the body-normal directions.

The structural deformation measurements constitutes an extensive database which combines instantaneous force, power consumption and three-dimensional wing deformation information. This data can be used in two main applications: (1) design of a (semi-empirical) quasi-steady force estimation model in the context of the blade-element theory; (2) use of the three-dimensional deformation data in numerical simulations with prescribed flexible wing kinematics. The latter has already been under development and has delivered promising results in the preliminary numerical simulations (Deng et al, 2015).

The wake velocity measurements both in hovering and forward flight configurations are shown to be promising in terms of providing insight about the force generation mechanisms. However as mentioned earlier, in these experiments the experimental DelFly II model was mounted on a balance mechanism, which limits the dynamic oscillations of the ornithopter that are otherwise present in free-flight conditions. Therefore, the flow field measurements in free-flight conditions can reveal relevant flow dynamics that were not captured in the previous studies. To achieve this goal, a control system that allows the DelFly II to fly autonomously in the wind tunnel was developed and tested in an open test section wind tunnel up to free-stream velocity of 0.8 m/s (Koopmans, 2012). The control system was able to keep the DelFly within an acceptable displacement range from a prescribed position in space. Moreover, the momentum-based force estimation model can be improved to predict time-resolved forces in a flapping cycle by transforming the unsteady volume integral term (i.e., time rate of change of total momentum in the control volume) to a surface integral term (i.e., moment of velocity on the control surface) for a divergence-free velocity field (Mohebbian and Rival, 2012).

Regarding the water tank experiments, it would be useful to extend the measurement region to capture the entire flow field around the wing including the root side and to acquire more phases of the motion particularly in the period of first three chord lengths of the revolving motion. This can allow to better identify the mechanisms that are responsible for the formation of spanwise flow and bursting of the LEV. Another important further step would be to include and explore wing flexibility as an experimental parameter in the measurements so as to assess the influence of the structural deformations on the flow fields and force generation mechanisms.

Bibliography

Aditya K, Malolan V (2007) Investigation of Strouhal number effect on flapping wing micro air vehicle. In: 45th AIAA Aerospace Sciences Meeting and Exhibit, American Institute of Aeronautics and Astronautics, Reno, Nevada, January, DOI 10.2514/6.2007-486

Adrian R, Westerweel J (2010) Particle Image Velocimetry. Cambridge Aerospace Series, Cambridge University Press

Anderson JD (2001) Fundamentals of Aerodynamics. McGraw-Hill

Anderson JM, Streitlien K, Barrett DS, Triantafyllou MS (1998) Oscillating foils of high propulsive efficiency. Journal of Fluid Mechanics 360:41–72

Bahill AT, Kallman JS, Lieberman JE (1982) Frequency limitations of the two-point central difference differentiation algorithm. Biological Cybernetics 45:1–4

Baker PS, Cooter RJ (1979) The natural flight of the migratory locust, Locusta migratoria L. - I. Wing movements. Journal of Comparative Physiology 131(1):79–87, DOI 10.1007/BF00613086

Baskan O (2009) Experimental and numerical investigation of flow field around flapping airfoils making figure-of-eight in hover. Master's thesis, Middle East Technical University

Beals N, Jones AR (2015) Lift production by a passively flexible rotating wing. AIAA Journal

Betz A (1912) Ein beitrag zur erklaerung des segelfluges. Zeitschrift fur Flugtechnik und Motorluftschiffahrt 3:269–272

BilimDurağı(2015) Hazerfen Ahmet Çelebi kimdir? http://bilimduragi.com/konu-hazerfen-ahmet-celebi-kimdir.html, (Visited on 06/29/2015)

Birch JM, Dickinson MH (2001) Spanwise flow and the attachment of the leading-edge vortex on insect wings. Nature 412(6848):729–33, DOI 10.1038/35089071

Birch JM, Dickinson MH (2003) The influence of wing-wake interactions on the production of aerodynamic forces in flapping flight. The Journal of Experimental Biology 206(13):2257–2272, DOI 10.1242/jeb.00381

Birch JM, Dickson WB, Dickinson MH (2004) Force production and flow structure of the leading edge vortex on flapping wings at high and low Reynolds numbers. The Journal of Experimental Biology 207(7):1063–1072, DOI 10.1242/jeb.00848

Bohorquez F, Samuel P, Sirohi J, Pines D, Rudd L, Perel R (2003) Design, analysis and hover performance of a rotary wing micro air vehicle. Journal of the American Helicopter Society 48(2):80–90

Bohorquez F, Pines D, Samuel PD (2010) Small rotor design optimization using blade element momentum theory and hover tests. Journal of Aircraft 47(1):268–283, DOI 10.2514/1.45301

Bomphrey RJ, Lawson NJ, Taylor GK, Thomas ALR (2006) Application of digital particle image velocimetry to insect aerodynamics: measurement of the leading-edge vortex and near wake of a Hawkmoth. Experiments in Fluids 40(4):546–554, DOI 10.1007/s00348-005-0094-5

Bomphrey RJ, Taylor GK, Thomas ALR (2009) Smoke visualization of free-flying bumblebees indicates independent leading-edge vortices on each wing pair. Experiments in Fluids 46(5):811–821, DOI 10.1007/s00348-009-0631-8

Bomphrey RJ, Henningsson P, Michaelis D, Hollis D (2012) Tomographic particle image velocimetry of desert locust wakes: instantaneous volumes combine to reveal hidden vortex elements and rapid wake deformation. Journal of the Royal Society, Interface / the Royal Society 9(77):3378–86, DOI 10.1098/rsif.2012.0418

Bos FM, Lentink D, Van Oudheusden B, Bijl H (2008) Influence of wing kinematics on aerodynamic performance in hovering insect flight. Journal of Fluid Mechanics 594:341–368

Bouabdallah S, Siegwart R (2007) Design and control of a miniature quadrotor. In: Valavanis KP (ed) Advances in Unmanned Aerial Vehicles, Intelligent Systems, Control and Automation: Science and Engineering, vol 33, Springer Netherlands, pp 171–210, DOI 10.1007/978-1-4020-6114-1_6

Bross M, Rockwell D (2014) Flow structure on a simultaneously pitching and rotating wing. Journal of Fluid Mechanics 756:354–383, DOI 10.1017/jfm.2014.458

Bross M, Rockwell D (2015) Three-dimensional flow structure along simultaneously pitching and rotating wings: effect of pitch rate. Experiments in Fluids 56(4):82, DOI 10.1007/s00348-015-1952-4

Bruggeman B (2010) Improving flight performance of DelFly II in hover by improving wing design and driving mechanism. Master's thesis, Delft University of Technology

Caetano J, Percin M, de Visser C, van Oudheusden B, de Croon G, De Wagter C, Remes B, Mulder M (2014) Tethered vs. free flight force determination of the DelFly II flapping wing micro air vehicle. In: 2014 International Conference on Unmanned Aircraft Systems (ICUAS), pp 942–948, DOI 10.1109/ICUAS.2014.6842344

Caetano J, Percin M, van Oudheusden B, Remes B, de Wagter C, de Croon G, de Visser C (2015) Error analysis and assessment of unsteady forces acting on a flapping wing micro air vehicle: free flight versus wind-tunnel experimental methods. Bioinspiration & Biomimetics 10(5), DOI 10.1088/1748-3190/10/5/056004

Caetano JV, de Visser CC, Remes B, de Wagter C, Mulder M (2013a) Controlled flight maneuvers of a flapping wing micro air vehicle: a step towards the DelFly II identification. In: AIAA Atmospheric Flight Mechanics Conference

Caetano JV, de Visser CC, Remes B, de Wagter C, Mulder M (2013b) Modeling a flapping wing MAV: flight path reconstruction of the DelFly II. In: AIAA Modeling and Simulation Technologies (MST) Conference, AIAA

Caetano JV, de Visser C, de Croon G, Remes B, de Wagter C, Verboom J, Mulder M (2013c) Linear aerodynamic model identification of a flapping wing MAV based on flight test data. International Journal of Micro Air Vehicles 5(4):273–286

Campbell JF (1976) Augmentation of vortex lift by spanwise blowing. Journal of Aircraft 13(9):727–732

Carmichael B (1981) Low Reynolds number airfoil survey. Technical Report NASA-CR-165803-VOL-1, NASA

Carr ZR, Chen C, Ringuette MJ (2013) Finite-span rotating wings: three-dimensional vortex formation and variations with aspect ratio. Experiments in Fluids 54(2):1444, DOI 10.1007/s00348-012-1444-8

Combes SA, Daniel TL (2003a) Flexural stiffness in insect wings I. Scaling and the influence of wing venation. The Journal of Experimental Biology 206(17):2979–2987, DOI 10.1242/jeb.00523

Combes SA, Daniel TL (2003b) Flexural stiffness in insect wings II. Spatial distribution and dynamic wing bending. The Journal of Experimental Biology 206(17):2989–2997, DOI 10.1242/jeb.00524

Daniel TL, Combes SA (2002) Flexible wings and fins: bending by inertial or fluid-dynamic forces? Integrative and Comparative Biology 42(5):1044–1049

David CT (1978) The relationship between body angle and flight speed in free-flying Drosophila. Physiological Entomology 3(3):191–195

de Baar J, Dwight RP, Bijl H (2013) Speeding up kriging through fast estimation of the hyperparameters in the frequency-domain. Computers & Geosciences 54:99–106

de Baar J, Percin M, Dwight R, Oudheusden BW, Bijl H (2014) Kriging regression of PIV data using a local error estimate. Experiments in Fluids 55(1):1650, DOI 10.1007/s00348-013-1650-z

de Clercq K, de Kat R, Remes B, van Oudheusden B, Bijl H (2009) Aerodynamic experiments on DelFly II: unsteady lift enhancement. International Journal of Micro Air Vehicles 1(4):255–262

de Clercq KME (2009) Flow visualization and force measurements on a hovering flapping-wing MAV 'DelFly II'. Master's thesis, Delft University of Technology

de Croon GCHE, de Clercq KME, Ruijsink R, Remes B, de Wagter C (2009) Design, aerodynamics, and vision-based control of the DelFly. International Journal on Micro Air Vehicles 1(2):71 – 97

de Croon GCHE, Groen MA, de Wagter C, Remes BDW, Ruijsink R, van Oudheusden BW (2012) Design, aerodynamics, and autonomy of the DelFly. Bioinspiration and Biomimetics 7(2)

de Wagter C, Tijmons S, Remes BDW, De Croon GCHE (2014) Autonomous flight of a 20-gram flapping wing MAV with a 4-gram onboard stere vision system. In: 2014 IEEE International Conference on Robotics and Automation (ICRA 2014)

Degani D, Seginer A, Levy Y (1990) Graphical visualization of vortical flows by means of helicity. AIAA Journal 28(8):1347–1352

Deng S, Percin M, Van Oudheusden B, Remes B, Bijl H (2014) Experimental investigation on the aerodynamics of a bio-inspired flexible flapping wing micro air vehicle. International Journal of Micro Air Vehicles 6(2):105–115

Deng S, Xiao T, Percin M, van Oudheusden B, Bijl H, Remes B (2015) Numerical simulation of an X-wing flapping wing MAV by means of a deforming overset grid method. In: 22nd AIAA Computational Fluid Dynamics Conference, AIAA Aviation, American Institute of Aeronautics and Astronautics, DOI doi:10.2514/6.2015-2615

Denny MW (1993) Air and Water: The Biology and Physics of Life's Media. Princeton University Press

Dickinson MH (1994) The effects of wing rotation on unsteady aerodynamic performance at low Reynolds numbers. The Journal of Experimental Biology 192(1):179–206

Dickinson MH, Götz KG (1993) Unsteady aerodynamic performance of model wings at low Reynolds numbers. The Journal of Experimental Biology 174:45–64

Dickinson MH, Lehmann FO, Gotz K (1993) The active control of wing rotation by Drosophila. The Journal of Experimental Biology 182(1):173–189

Dickinson MH, Lehmann FO, Sane SP (1999) Wing rotation and the aerodynamic basis of insect flight. Science 284(5422):1954–1960, DOI 10.1126/science.284.5422.1954

Du G, Sun M (2008) Effects of unsteady deformation of flapping wing on its aerodynamic forces. Applied Mathematics and Mechanics (English Edition) 29(20070404):731–743, DOI 10.1007/s10483-008-0605-9

Du G, Sun M (2010) Effects of wing deformation on aerodynamic forces in hovering hoverflies. The Journal of Experimental Biology 213:2273–2283, DOI 10.1242/jeb.040295

Eisma HE (2012) Flow visualization and force measurements on a flapping-wing MAV DelFly II in forward flight configuration. Master's thesis, Delft University of Technology

Ellington CP (1984a) The aerodynamics of hovering insect flight. II. Morphological parameters. Philosophical Transactions of the Royal Society of London Series B, Biological Sciences (1934-1990) 305:17–40

Ellington CP (1984b) The aerodynamics of hovering insect flight. III. Kinematics. Philosophical Transactions of the Royal Society B: Biological Sciences 305(1122):41–78, DOI 10.1098/rstb.1984.0051

Ellington CP (1984c) The aerodynamics of hovering insect flight. IV. Aeorodynamic mechanisms. Philosophical Transactions of the Royal Society of London Series B, Biological Sciences (1934-1990) 305(1122):79–113, DOI 10.1098/rstb.1984.0052

Ellington CP (1999) The novel aerodynamics of insect flight: applications to micro-air vehicles. The Journal of Experimental Biology 202:3439–3448

Ellington CP, van den Berg C, Willmott AP, Thomas ALR (1996) Leading-edge vortices in insect flight. Nature 384:626–630

Elsinga GE, Scarano F, Wieneke B, Van Oudheusden B (2006) Tomographic particle image velocimetry. Experiments in Fluids 41(6):933–947

Ennos AR (1988) The inertial cause of wing rotation in Diptera. The Journal of Experimental Biology 140(1):161–169

Farren WS (1935) The reaction on a wing whose angle of incidence is changing rapidly. Rep. Mem. Aeronaut. Res. Comm. (Great Britain) 1648, Aeronautical Research Committee, Great Britain

Fung Y (1993) An Introduction to the Theory of Aeroelasticity. Dover Publications

Garmann DJ, Visbal MR (2014) Dynamics of revolving wings for various aspect ratios. Journal of Fluid Mechanics 748:932–956, DOI 10.1017/jfm.2014.212

Garmann DJ, Visbal MR, Orkwis PD (2013) Three-dimensional flow structure and aerodynamic loading on a revolving wing. Physics of Fluids 25(3):034,101, DOI 10.1063/1.4794753

Garrick IE (1937) Propulsion of a flapping and oscillating airfoil. NACA: Report 567, National Advisory Committee for Aeronautics, Unites States

Gerdes JW, Gupta SK, Wilkerson Sa (2012) A review of bird-inspired flapping wing miniature air vehicle designs. Journal of Mechanisms and Robotics 4(2):021,003, DOI 10.1115/1.4005525

Ghosh SK, Dora CL, Das D (2012) Unsteady wake characteristics of a flapping wing through 3D TR-PIV. Journal of Aerospace Engineering 25:547–558, DOI 10.1061/(ASCE)AS.1943-5525.0000185.

Gillebaart T (2011) Influence of flexibility on the clap and peel movement of the DelFly II. Master's thesis, Delft University of Technology

Glauert H (1929) The force and moment on an oscillating aerofoil. Rep. Mem. Aeronaut. Res. Comm. (Great Britain) 1561, Aeronautical Research Committee, Great Britain

Gopalakrishnan P, Tafti DK (2010) Effect of wing flexibility on lift and thrust production in flapping flight. AIAA Journal 48(5):865–877, DOI 10.2514/1.39957

Graftieaux L, Michard M, Grosjean N (2001) Combining PIV, POD and vortex identification algorithms for the study of unsteady turbulent swirling flows. Measurement Science and Technology 12(9):1422–1429, DOI 10.1088/0957-0233/12/9/307

Granlund KO, Ol MV, Bernal LP (2013) Unsteady pitching flat plates. Journal of Fluid Mechanics 733:R5, DOI 10.1017/jfm.2013.444

Grant RG (2007) Flight: The Complete History. DK Publishing

Grasmeyer J, Keennon M (2001) Development of the Black Widow micro air vehicle. In: 39th Aerospace Sciences Meeting and Exhibit

Grauer J, Ulrich E, Jr JH, Pines D, Humbert JS (2011) Testing and system identification of an ornithopter in longitudinal flight. Journal of Aircraft 48(2):660–667

Groen M (2010) PIV and force measurements on the flapping-wing MAV DelFly II. Master's thesis, Delft University of Technology

Groen M, Bruggeman B, Remes B, Ruijsink R, Van Oudheusden B, Bijl H (2010) Improving flight performance of the flapping wing mav delfly ii. In: Int. Micro Air Vehicle Conf. and Competition (IMAV 2010)(Braunschweig, Germany)

Gülçat Ü (2010) Fundamentals of Modern Unsteady Aerodynamics. Springer

Gunes H, Rist U (2007) Spatial resolution enhancement/smoothing of stereo–particle-image velocimetry data using proper-orthogonal decomposition–based and Kriging interpolation methods. Physics of Fluids 19

Gunes H, Rist U (2008) On the use of kriging for enhanced data reconstruction in a separated transitional flat-plate boundary layer. Physics of Fluids 20(10)

Gunes H, Sirisup S, Karniadakis GE (2006) Gappy data: To Krig or not to Krig? Journal of Computational Physics 212:358–382

Halfman R (1951) Experimental aerodynamic derivatives of a sinusoidally oscillating airfoil in two-dimensional flow. NACA: Technical Note 2465, National Advisory Committee for Aeronautics, Unites States

Hamdani H, Sun M (2000) Aerodynamic forces and flow structures of an airfoil in some unsteady motions at small Reynolds number. Acta Mechanica 145:173–187

Hartloper C, Rival DE (2013) Vortex development on pitching plates with lunate and truncate planforms. Journal of Fluid Mechanics 732:332–344

Heathcote S, Gursul I (2007) Flexible flapping airfoil propulsion at low Reynolds numbers. AIAA Journal 45(5):1066–1079, DOI 10.2514/1.25431

Heathcote S, Wang Z, Gursul I (2008) Effect of spanwise flexibility on flapping wing propulsion. Journal of Fluids and Structures 24(2):183–199, DOI 10.1016/j.jfluidstructs.2007.08.003

Hedenström A, Rosén M, Spedding GR (2006) Vortex wakes generated by robins Erithacus rubecula during free flight in a wind tunnel. Journal of the Royal Society, Interface / the Royal Society 3(7):263–76, DOI 10.1098/rsif.2005.0091

Hedenström A, Johansson LC, Wolf M, von Busse R, Winter Y, Spedding GR (2007) Bat flight generates complex aerodynamic tracks. Science (New York, NY) 316(5826):894–7, DOI 10.1126/science.1142281

Hein BR, Chopra I (2007) Hover performance of a micro air vehicle: rotors at low Reynolds number. Journal of the American Helicopter Society 52(3):254, DOI 10.4050/JAHS.52.254

Hsu CK, Evans J, Vytla S, Huang PG (2010) Development of flapping wing micro air vehicles -design, CFD, experiment and actual flight. In: 48th AIAA Aerospace Sciences Meeting Including the New Horizons Forum and Aerospace Exposition

Hu H, Kumar AG, Abate G, Albertani R (2010) An experimental investigation on the aerodynamic performances of flexible membrane wings in flapping flight. Aerospace Science and Technology 14(8):575–586, DOI 10.1016/j.ast.2010.05.003

Hurley D (1959) The use of boundary-layer control to establish free stream-line flows. Advances in Aeronautical Science 2:662–708

Ifju PG, Jenkins DA, Ettinger S, Lian Y, Shyy W, Waszak MR (2002) Flexible-wing-based micro air vehicles. In: 40th AIAA Aerospace Sciences Meeting and Exhibit

Jardin T, David L (2014) Spanwise gradients in flow speed help stabilize leading-edge vortices on revolving wings. Physical Review E 90:013,011, DOI 10.1103/PhysRevE.90.013011

Jardin T, David L (2015) Coriolis effects enhance lift on revolving wings. Physical Review E 91(3):031,001

Jardin T, Farcy a, David L (2012) Three-dimensional effects in hovering flapping flight. Journal of Fluid Mechanics 702:102–125, DOI 10.1017/jfm.2012.163

Jensen M (1956) Biology and physics of locust flight. III. The aerodynamics of locust flight. Philosophical Transactions of the Royal Society B: Biological Sciences 239(667):511–552

Jeong J, Hussain F (1995) On the identification of a vortex. Journal of Fluid Mechanics 285:69–94

Jones A, Babinsky H (2011) Reynolds number effects on leading edge vortex development on a waving wing. Experiments in fluids 51(1):197–210

Jones AR, Babinsky H (2010) Unsteady lift generation on rotating wings at low Reynolds numbers. Journal of Aircraft 47(3):1013–1021, DOI 10.2514/1.46649

Jongerius SR, Straathof MH, van der Veen GJ, Roos WVJ, Moelans P, Lagarde RCA, Kacgor ANA, Heynze CJG, Ashok A, de Clercq KME, van Ginneken D A J (2005) Desing of a flapping wing vision-based Micro-UAV. Design synthesis exercise final report, Faculty of Aerospace Engineering, Delft University of Technology

Katz J, Plotkin A (1991) Low Speed Aerodynamics: From Wing Theory to Panel Methods. McGraw-Hill

Keane RD, Adrian RJ (1992) Theory of cross-correlation analysis of PIV images. Applied Scientific Research 49(3):191–215

Keennon M, Klingebiel K, Won H, Andriukov A (2012) Development of the Nano Hummingbird: a tailless flapping wing micro air vehicle. In: 50th AIAA Aerospace Sciences Meeting including the New Horizons Forum and Aerospace Exposition, Nashville, Tennessee

Kellogg J, Bovais C, Dahlburg J, Foch R, Gardner J, Gordon D, Hartley R, Kamgar-Parsi B, McFarlane H, Pipitone F, et al (2001) The NRL Mite air vehicle. Tech. rep., DTIC Document

Kim D, Gharib M (2010) Experimental study of three-dimensional vortex structures in translating and rotating plates. Experiments in Fluids 49(1):329–339, DOI 10.1007/s00348-010-0872-6

Kitanidis PK (1986) Parameter uncertainty in estimation of spatial functions: Bayesian analysis. Water Resources Research 22(4):499–507

Kitanidis PK, Lane RW (1985) Maximum likelihood parameter estimation of hydrologic spatial processes by the Gauss-Newton method. Journal of Hydrology 79(1-2):53 – 71

Knoller R (1909) Die gesetze des luftwiderstandes. Flug- und Motortechnik (Wien) 3(21):1–7

Koehler C, Liang Z, Gaston Z, Wan H, Dong H (2012) 3D reconstruction and analysis of wing deformation in free-flying dragonflies. The Journal of Experimental Biology 215:3018–3027, DOI 10.1242/jeb.069005

Koopmans JA (2012) DelFly Freeflight - Autonomous flight of the DelFly in the wind tunnel using low-cost sensors. Master's thesis, Delft University of Technology

Kramer VM (1932) Die zunahme des maximalauftriebes von tragflugeln bei plotzlicher anstellwinkelvergrosserung (boeneffekt). Z Flugtech Motorluftschiff 23:185–189

Kroo I, Kunz P (2001) Mesoscale flight and miniature rotorcraft development. In: Mueller TJ (ed) Fixed and Flapping Wing Aerodynamics for Micro Air Vehicle Applications, Progress in Astronautics and Aeronautics, AIAA, pp 503–517

Kweon J, Choi H (2010) Sectional lift coefficient of a flapping wing in hovering motion. Physics of Fluids 22(7):071,703, DOI 10.1063/1.3471593

Lai JCS, Platzer MF (1999) Jet characteristics of a plunging airfoil. AIAA Journal 37(12):1529–1537, DOI 10.2514/2.641

Lee JS, Han JH (2012) Experimental study on the flight dynamics of a bioinspired ornithopter: free flight testing and wind tunnel testing. Journal of Smart Materials and Structures 21, DOI 10.1088/0964-1726/21/9/094023

Lehmann FO (2004) The mechanisms of lift enhancement in insect flight. Die Naturwissenschaften 91(3):101–22, DOI 10.1007/s00114-004-0502-3

Lehmann FO, Pick S (2007) The aerodynamic benefit of wing-wing interaction depends on stroke trajectory in flapping insect wings. The Journal of Experimental Biology 210(Pt 8):1362–77, DOI 10.1242/jeb.02746

Lehmann FO, Sane SP, Dickinson MH (2005) The aerodynamic effects of wing-wing interaction in flapping insect wings. The Journal of Experimental Biology 208(Pt 16):3075–92, DOI 10.1242/jeb.01744

Lehmann FO, Gorb S, Nasir N, Schützner P (2011) Elastic deformation and energy loss of flapping fly wings. The Journal of Experimental Biology 214:2949–2961, DOI 10.1242/jeb.045351

Lentink D, Dickinson MH (2009) Rotational accelerations stabilize leading edge vortices on revolving fly wings. The Journal of Experimental Biology 212(Pt 16):2705–19, DOI 10.1242/jeb.022269

Li D (2008) Encyclopedia of Microfluidics and Nanofluidics, vol 1. Springer

Lian Y, Shyy W, Viieru D, Zhang B (2003) Membrane wing aerodynamics for micro air vehicles. Progress in Aerospace Sciences 39(6):425–465

Lim G, Shkarayev S, Goff Z, Beran P (2012) Studies of flight kinematics of ornithopters. In: International Competition and Conference on Micro Air Vehicles, IMAV 2012, IMAV 2012

Lin CS, Hwu C, Young WB (2006) The thrust and lift of an ornithopter's membrane wings with simple flapping motion. Aerospace Science and Technology 10(2):111–119, DOI 10.1016/j.ast.2005.10.003

Lissaman P (1983) Low-Reynolds-number airfoils. Annual Review of Fluid Mechanics 15(1):223–239

Lu Y, Shen GX (2008) Three-dimensional flow structures and evolution of the leading-edge vortices on a flapping wing. The Journal of Experimental Biology 211(Pt 8):1221–30, DOI 10.1242/jeb.010652

Ma KY, Chirarattananon P, Fuller SB, Wood RJ (2013) Controlled flight of a biologically inspired, insect-scale robot. Science 340(6132):603–607

Manar F, Medina A, Jones AR (2014) Tip vortex structure and aerodynamic loading on rotating wings in confined spaces. Experiments in Fluids 55(9):1–18

Marden JH (1987) Maximum lift production during takeoff in flying animals. The Journal of Experimental Biology 130:235–238

Mardia KV (1989) Maximum likelihood estimation for spatial models. In: Proceedings from the Symposium on Spatial Statistics: Past, Present, and Future, pp 203–253

Mardia KV, Marshall RJ (1984) Maximum likelihood estimation of models for residual covariance in spatial regression. Biometrika 71(1):135–146

Mazaheri K, Ebrahimi A (2011) Experimental investigation on aerodynamic performance of a flapping wing vehicle in forward flight. Journal of Fluids and Structures 27(4):586–595, DOI 10.1016/j.jfluidstructs.2011.04.001

Mettler B (2010) Extracting micro air vehicles aerodynamic forces and coefficients in free flight using visual motion tracking techniques. Experiments in Fluids 49(3):557–569, DOI 10.1007/s00348-009-0803-6

Miller LA, Peskin CS (2009) Flexible clap and fling in tiny insect flight. The Journal of Experimental Biology 212(19):3076–90, DOI 10.1242/jeb.028662

Moffatt H, Tsinober A (1992) Helicity in laminar and turbulent flow. Annual Review of Fluid Mechanics 24(1):281–312

Mohebbian A, Rival D (2012) Assessment of the derivative-moment transformation method for unsteady-load estimation. Experiments in Fluids 53(2):319–330, DOI 10.1007/s00348-012-1290-8

Morris S, Holden M (2000) Design of micro air vehicles and flight test validation. In: Proceeding of the Fixed, Flapping and Rotary Wing Vehicles at Very Low Reynolds Numbers, pp 153–176

Mueller D, Gerdes JW, Gupta SK (2009) Incorporation of passive wing folding in flapping wing miniature air vehicles. In: ASME 2009 International Design Engineering Technical Conferences and Computers and Information in Engineering Conference, American Society of Mechanical Engineers, pp 797–805

Mueller D, Bruck Ha, Gupta SK (2010) Measurement of thrust and lift forces associated with drag of compliant flapping wing for micro air vehicles using a new test stand design. Experimental Mechanics 50(6):725–735, DOI 10.1007/s11340-009-9270-5

Mueller TJ, DeLaurier JD (2003) Aerodynamics of small vehicles. Annual Review of Fluid Mechanics 35(1):89–111

Muijres FT, Johansson LC, Barfield R, Wolf M, Spedding GR, Hedenström A (2008) Leading-edge vortex improves lift in slow-flying bats. Science 319(5867):1250–3, DOI 10.1126/science.1153019

Muijres FT, Spedding GR, Winter Y, Hedenström A (2011) Actuator disk model and span efficiency of flapping flight in bats based on time-resolved PIV measurements. Experiments in Fluids 51(2):511–525, DOI 10.1007/s00348-011-1067-5

Muijres FT, Johansson LC, Bowlin MS, Winter Y, Hedenström A (2012a) Comparing aerodynamic efficiency in birds and bats suggests better flight performance in birds. PloS one 7(5), DOI 10.1371/journal.pone.0037335

Muijres FT, Johansson LC, Hedenström A (2012b) Leading edge vortex in a slow-flying passerine. Biology Letters DOI 10.1098/rsbl.2012.0130

Muijres FT, Johansson LC, Winter Y, Hedenström A (2014) Leading edge vortices in lesser long-nosed bats occurring at slow but not fast flight speeds. Bioinspiration & Biomimetics 9(2):025,006

Muijres FT, Elzinga MJ, Iwasaki NA, Dickinson MH (2015) Body saccades of drosophila consist of stereotyped banked turns. The Journal of Experimental Biology 218(6):864–875

Muniappan A, Duriyanandhan V, Baskar V (2004) Lift characteristics of the flapping wing micro air vehicle. In: AIAA 3rd "Unmanned Unlimited" Technical Conference, Workshop and Exhibit, American Institute of Aeronautics and Astronautics, Chicago, Illinois, September

Muniappan A, Baskar V, Duriyanandhan V (2005) Lift and thrust characteristics of flapping wing micro air vehicle (MAV). In: 43rd AIAA Aerospace Sciences Meeting and Exhibit, American Institute of Aeronautics and Astronautics, Reno, Nevada, January

Munk M (1925) Note on the air forces on a wing caused by pitching. Technical Note 191, NACA

Muren P (2005) Proxflyer. http://www.proxflyer.com/, (Visited on 11/12/2014)

Nakata T, Liu H, Tanaka Y, Nishihashi N, Wang X, Sato a (2011) Aerodynamics of a bio-inspired flexible flapping-wing micro air vehicle. Bioinspiration & Biomimetics 6(4):045,002, DOI 10.1088/1748-3182/6/4/045002

Osborne M (1951) Aerodynamics of flapping flight with application to insects. The Journal of Experimental Biology 28(2):221–245

Ozen CA, Rockwell D (2012) Flow structure on a rotating plate. Experiments in Fluids 52(1):207–223, DOI 10.1007/s00348-011-1215-y

Percin M (2009) Flow around a plunging airfoil in a uniform flow. Master's thesis, Istanbul Technical University

Percin M, van Oudheusden BW (2015a) Flow visualization and force measurements on accelerated revolving flat plates at low Reynolds numbers. In: 45th AIAA Fluid Dynamics Conference, AIAA

Percin M, van Oudheusden BW (2015b) Three-dimensional flow structures and unsteady forces on pitching and surging revolving flat plates. Experiments in Fluids 56(2):1–19, DOI 10.1007/s00348-015-1915-9

Percin M, Hu Y, Van Oudheusden B, Remes B, Scarano F (2011) Wing flexibility effects in clap-and-fling. International Journal of Micro Air Vehicles 3(4):217–228

Percin M, van Oudheusden B, Eisma H, Remes B (2014a) Three-dimensional vortex wake structure of a flapping-wing micro aerial vehicle in forward flight configuration. Experiments in Fluids 55(9)

Percin M, Ziegler L, Van Oudheusden B (2014b) Flow around a suddenly accelerated rotating plate at low reynolds number. 17th International Symposium on Applications of Laser Techniques to Fluid Mechanics

Pines DJ, Bohorquez F (2006) Challenges facing future micro-air-vehicle development. Journal of Aircraft 43(2):290–305

Pitt Ford CW, Babinsky H (2013) Lift and the leading-edge vortex. Journal of Fluid Mechanics 720:280–313, DOI 10.1017/jfm.2013.28

Pitt Ford CW, Babinsky H (2014) Impulsively started flat plate circulation. AIAA Journal 52(8):1800–1802, DOI 10.2514/1.J052959

Platzer MF, Jones KD, Young J, Lai JCS (2008) Flapping-wing aerodynamics: progress and challenges. AIAA Journal 46(9):2136–2149, DOI 10.2514/1.29263

Poelma C, Dickson WB, Dickinson MH (2006) Time-resolved reconstruction of the full velocity field around a dynamically-scaled flapping wing. Experiments in Fluids 41(2):213–225, DOI 10.1007/s00348-006-0172-3

Polhamus EC (1971) Predictions of vortex-lift characteristics by a leading-edge suction analogy. Journal of Aircraft 8(4):193–199

Pornsin-sirirak TN, Lee SW, Nassef H, Grasmeyer J, Tai YC, Ho CM, Keennon M (2000) MEMS wing technology for a battery-powered ornithopter. In: Proceedings IEEE Thirteenth Annual International Conference on Micro Electro Mechanical Systems (Cat. No.00CH36308), Miyazaki, Japan, vol 043, pp 709–804

Pornsin-sirirak TN, Tai YC, Ho CM, Keennon M (2001) Microbat: A palm-sized electrically powered ornithopter. Proceedings of NASA/JPL Workshop on Biomorphic Robotics pp 14 – 17

Raffel M, EWillert C, TWereley S, Kompenhans J (2007) Particle Image Velocimetry: A Practicle Guide (2nd edition). Springer

Reid E (1927) Airfoil lift with changing angle of attack. Technical note, NACA

Ren H, Wu Y, Huang PG (2012) Visualization and characterization of near-wake flow fields of a flapping-wing micro air vehicle using PIV. Journal of Visualization 16(1):75–83, DOI 10.1007/s12650-012-0152-z

Sane SP (2003) The aerodynamics of insect flight. The Journal of Experimental Biology 206(23):4191–4208, DOI 10.1242/jeb.00663

Sane SP, Dickinson MH (2001) The control of flight force by a flapping wing: lift and drag production. The Journal of Experimental Biology 204(Pt 15):2607–26

Sane SP, Dickinson MH (2002) The aerodynamic effects of wing rotation and a revised quasi-steady model of flapping flight. The Journal of Experimental Biology 205(Pt 8):1087–96

Scarano F (2013) Tomographic PIV: principles and practice. Measurement Science and Technology 24(1):012,001, DOI 10.1088/0957-0233/24/1/012001

Schaefer L (2008) Microrotorcraft. In: Li D (ed) Encyclopedia of Microfluidics and Nanofluidics, Springer US, pp 1307–1314, DOI 10.1007/978-0-387-48998-8_1007

Sedov L (1965) Two-Dimensional Problems in Hydrodynamics and Aerodynamics. Interscience Publishers

Seshadri P, Benedict M, Chopra I (2013) Understanding micro air vehicle flapping-wing aerodynamics using force and flow field measurements. Journal of Aircraft 50(4):1070–1087, DOI 10.2514/1.C031968

Shyy W, Berg M, Ljungqvist D (1999) Flapping and flexible wings for biological and micro air vehicles. Progress in Aerospace Sciences 35(5):455–505

Shyy W, Lian Y, Tang J, Viieru D, Liu H (2007) Aerodynamics of Low Reynolds Number Flyers. Cambridge Aerospace Series, Cambridge University Press

Shyy W, Aono H, Chimakurthi S, Trizila P, Kang CK, Cesnik C, Liu H (2010) Recent progress in flapping wing aerodynamics and aeroelasticity. Progress in Aerospace Sciences 46(7):284–327, DOI 10.1016/j.paerosci.2010.01.001

Silverstein A, Joyner U (1939) Experimental verification of the theory of oscillating airfoils. NACA: Report 673, National Advisory Committee for Aeronautics, Unites States

Sirohi J (2013) Chapter 5 - bioinspired and biomimetic microflyers. In: Lakhtakia A, Martín-Palma RJ (eds) Engineered Biomimicry, Elsevier, Boston, pp 107 – 138, DOI http://dx.doi.org/10.1016/B978-0-12-415995-2.00005-2

Smith R, Shyy W (1995) Computational model of flexible membrane wings in steady laminar flow. AIAA Journal 33(10):1769–1777

Spedding GR, Rosén M, Hedenström A (2003) A family of vortex wakes generated by a thrush nightingale in free flight in a wind tunnel over its entire natural range of flight speeds. The Journal of Experimental Biology 206(14):2313–2344, DOI 10.1242/jeb.00423

Srygley RB, Thomas ALR (2002) Unconventional lift-generating mechanisms in free-flying butterflies. Nature 420(6916):660–4, DOI 10.1038/nature01223

Sunada S, Kawachi K, Watanabe I, Azuma A (1993) Fundamental analysis of three-dimensional 'near fling'. The Journal of Experimental Biology 183:217–248

Tarascio MJ, Ramasamy M, Chopra I, Leishman JG (2005) Flow visualization of micro air vehicle scaled insect-based flapping wings. Journal of Aircraft 42(2):385–390, DOI 10.2514/1.6055

Tay W, Van Oudheusden B, Bijl H (2014) Numerical simulation of X-wing type biplane flapping wings in 3D using the immersed boundary method. Bioinspiration and Biomimetics 9(3)

Taylor G, Triantafyllou M, Tropea C (2010) Animal Locomotion. SpringerLink: Springer e-Books, Springer

Theodorsen T (1935) General theory of aerodynamic instability and the mechanism of flutter. NACA: Report 496, National Advisory Committee for Aeronautics, Unites States

Thielicke W, Stamhuis EJ (2015) The influence of wing morphology on the three-dimensional flow patterns of a flapping wing at bird scale. Journal of Fluid Mechanics 768:240–260, DOI 10.1017/jfm.2015.71

Tian X, Iriarte-Diaz J, Middleton K, Galvao R, Israeli E, Roemer A, Sullivan A, Song A, Swartz S, Breuer K (2006) Direct measurements of the kinematics and dynamics of bat flight. Bioinspiration & Biomimetics 1:S10–S18, DOI 10.1088/1748-3182/1/4/S02

Tijmons S (2012) Stereo vision for flapping wing MAVs - Design of an obstacle avoidance system. Master's thesis, Delft University of Technology

Truong QT, Nguyen QV, Truong VT, Park HC, Byun DY, Goo NS (2011) A modified blade element theory for estimation of forces generated by a beetle-mimicking flapping wing system. Bioinspiration & Biomimetics 6(3):036,008, DOI 10.1088/1748-3182/6/3/036008

Tuncer IH, Kaya M (2005) Optimization of flapping airfoils for maximum thrust. AIAA Journal 43(11)

Vanella M, Fitzgerald T, Preidikman S, Balaras E, Balachandran B (2009) Influence of flexibility on the aerodynamic performance of a hovering wing. The Journal of Experimental Biology 212(Pt 1):95–105, DOI 10.1242/jeb.016428

Venkata SK, Jones AR (2013) Leading-edge vortex structure over multiple revolutions of a rotating wing. Journal of Aircraft 50(4):1312–1316, DOI 10.2514/1.C032128

Violato D, Scarano F (2011) Three-dimensional evolution of flow structures in transitional circular and chevron jets. Physics of Fluids 23(12):124,104

Walker SM, Thomas ALR, Taylor GK (2009) Photogrammetric reconstruction of high-resolution surface topographies and deformable wing kinematics of tethered locusts and free-flying hoverflies. Journal of the Royal Society, Interface / the Royal Society 6(August 2008):351–366, DOI 10.1098/rsif.2008.0245

Walker SM, Thomas ALR, Taylor GK (2010) Deformable wing kinematics in free-flying hoverflies. Journal of the Royal Society, Interface / the Royal Society 7(May 2009):131–142, DOI 10.1098/rsif.2009.0120

Wang H, Zeng L, Yin C (2002) Measuring the body position, attitude and wing deformation of a free-flight dragonfly by combining a comb fringe pattern with sign points on the wing. Measurement Science and Technology 13(6):903

Wang ZJ (2005) Dissecting insect flight. Annual Review of Fluid Mechanics 37(1):183–210, DOI 10.1146/annurev.fluid.36.050802.121940

Waszak MR, Jenkins LN, Ifju P (2001) Stability and control properties of an aeroelastic fixed wing micro aerial vehicle. In: AIAA Atmospheric Flight Mechanics Conference and Exhibit

Weis-Fogh T (1973) Quick estimates of flight fitness in hovering animals, including novel mechanisms for lift production. The Journal of Experimental Biology 59:169–230

Westerweel J (1994) Efficient detection of spurious vectors in particle image velocimetry data. Experiments in Fluids 16:236–247, DOI 10.1007/BF00206543

Wieneke B (2008) Volume self-calibration for 3D particle image velocimetry. Experiments in Fluids 45(4):549–556, DOI 10.1007/s00348-008-0521-5

Wikle CK, Berliner LM (2007) A Bayesian tutorial for data assimilation. Physica D: Nonlinear Phenomena 230(1):1–16

Willmott AP, Ellington CP (1997) The mechanics of flight in the hawkmoth Manduca sexta. I. Kinematics of hovering and forward flight. The Journal of Experimental Biology 200(21):2705–2722

Wolf T, Konrath R (2015) Avian wing geometry and kinematics of a free-flying barn owl in flapping flight. Experiments in Fluids 56, DOI 10.1007/s00348-015-1898-6

Wood RJ (2008) The first takeoff of a biologically inspired at-scale robotic insect 24(2):341–347

Wootton RJ (1981) Palaeozoic insects. Annual Review of Entomology 26:319–344

Wootton RJ (1993) Leading edge section and asymmetric twisting in the wings of flying butterflies (insecta, papilionoidea). The Journal of Experimental Biology 180(1):105–117

Wortmann M, Zarnack W (1993) Wing movements and lift regulation in the flight of desert locusts. The Journal of Experimental Biology 182:57–69

Wu J (1981) Theory for aerodynamic force and moment in viscous flows. AIAA Journal 19(4):432–441

Wu J, Vakili A, Wu J (1991) Review of the physics of enhancing vortex lift by unsteady excitation. Progress in Aerospace Sciences 28(2):73–131, DOI 10.1016/0376-0421(91)90001-K

Wu P, Ifju P, Stanford B (2010) Flapping wing structural deformation and thrust correlation study with flexible membrane wings. AIAA Journal 48(9):2111–2122, DOI 10.2514/1.J050310

Yilmaz TO, Rockwell D (2011) Flow structure on finite-span wings due to pitch-up motion. Journal of Fluid Mechanics 691:518–545, DOI 10.1017/jfm.2011.490

Young J, Lai JC (2007a) Vortex lock-in phenomenon in the wake of a plunging airfoil. AIAA Journal 45(2):485–490, DOI 10.2514/1.23594

Young J, Lai JCS (2007b) Mechanisms influencing the efficiency of oscillating airfoil propulsion. AIAA Journal 45(7):1695–1702, DOI 10.2514/1.27628

Young J, S Lai JC (2004) Oscillation frequency and amplitude effects on the wake of a plunging airfoil. AIAA Journal 42(10):2042–2052, DOI 10.2514/1.5070

Young J, Walker SM, Bomphrey RJ, Taylor GK, Thomas ALR (2009) Details of insect wing design and deformation enhance aerodynamic function and flight efficiency. Science 325(September):1549–1552, DOI 10.1126/science.1175928

Yu HT, Bernal L (2013) Effect of pivot point on aerodynamic force and vortical structure of pitching flat plate wings. In: 51st AIAA Aerospace Sciences Meeting including the New Horizons Forum and Aerospace Exposition 2013

Zdunich P, Bilyk D, MacMaster M, Loewen D, DeLaurier J, Kornbluh R, Low T, Stanford S, Holeman D (2007) Development and testing of the Mentor flapping-wing micro air vehicle. Journal of Aircraft 44(5):1701–1711, DOI 10.2514/1.28463

Zhao L, Huang Q, Deng X, Sane SP (2009) Aerodynamic effects of flexibility in flapping wings. Journal of the Royal Society, Interface / the Royal Society 7:485–497, DOI 10.1098/rsif.2009.0200

Summary

The growing need for mobile aerial platforms capable of performing reconnaissance tasks and gathering intelligence in hazardous and physically inaccessible areas has given rise to an increasing interest in the development of micro aerial vehicles (MAVs), in view of their potential capabilities of versatile and highly maneuverable flight. Especially flapping-wing configurations, which often tend to be inspired by nature, have captivated researchers in view of their possible advantages over more conventional (fixed and rotary wing) flight modes. Contrary to these more conventional flight configurations, flapping wing systems benefit from the unsteady flow effects that are associated with the large-scale vortical structures separating from the wing leading and trailing edges, which create low pressure regions around the wings that lead to the generation of higher lift and thrust. In this respect, the present thesis pursues an experimental exploration of the aerodynamic mechanisms of flapping-wing phenomena by use of state-of-the-art flow measurement techniques, which are capable of providing time-resolved three-dimensional information. The study is divided into two parts, in which flapping-wing aerodynamics is investigated in the context of a flapping-wing MAV (Part I) and in a generic experimental setup to gain more fundamental understanding (Part II), respectively.

The first part consists of studies performed with the flapping-wing MAV DelFly II. First, the aerodynamic performance of the DelFly II is assessed by means of extensive force, power consumption and wing deformation measurements. Force and power consumption measurements were performed under in-air and in-vacuum conditions in order to properly identify the contributions associated to the aerodynamic effects. Subsequently, the balance-mounted force measurements are compared to the forces estimated from free-flight visual tracking measurements in order to characterize the effects of fixed-model force measurements, which restrict the dynamic body modes that exist in actual free-flight conditions as well as introducing the effect of the vibrations which depends on the model clamping position. The comparison of the unsteady forces obtained by the two methods reveals that the X-force component (i.e., the force component along the DelFly fuselage as defined in the body axis) shows a good correspondence, whereas the Z-force component displays deviations depending of the flight condition. Reasons for the differences and main drawbacks of the two force determination techniques are discussed. Effects of the flapping frequency, wing surface thickness and wing geometry on the aerodynamic performance in hovering conditions are also investigated in terms of force and power consumption measurements. In order to assess the relation between the force generation mechanisms and wing deformation characteristics, dedicated structural deformation measurements were performed on the flapping wings of the DelFly. These measurements provide information regarding the effects of the flapping frequency and wing surface thickness on the force generation mechanisms and the power consumption characteristics in terms of both amplitude and temporal evolution.

Next, flow field measurements were performed around the wing and in the wake of the

DelFly in hovering and forward flight conditions by using planar and stereoscopic particle image velocimetry (stereo-PIV) techniques. The visualizations of the vortical structures around the wings reveal the formation, shedding and interaction mechanisms, particularly visualizing the clap-and-peel motion of the DelFly wings. A momentum-based approach in a control volume around the DelFly in hovering configuration was employed to estimate the flap-averaged X-force under a number of simplifying assumptions. This approach, which only uses the streamwise velocity at a downstream location, is still able to calculate the forces within an error range of $5-15$ %. The flow field measurements in the wake of the flapping wings in the forward flight configuration are used to reconstruct three-dimensional wake structures. Two wake reconstruction strategies have been compared: (1) a spatio-temporal wake reconstruction based on the Taylor's hypothesis; (2) a spatial wake reconstruction by means of a modified Kriging regression technique, that takes into account the measurement uncertainties. It is shown that wing–wing interaction at the start of outstroke (peel motion) becomes a dominant feature for reduced frequencies greater than 0.62, while becoming relatively inactive at lower reduced frequency.

In the second part, experimental studies concerning the fundamental research in flapping-wing flight are reported. First, the effects of wing flexibility on the unsteady flow around a flexible wing undergoing a clap-and-fling type flapping motion have been investigated by means of tomographic PIV measurements that were performed in a water tank. The two-dimensional Euler-Bernoulli beam equation was used to simulate the chordwise deformations of a plunging thin plate and to compare the deformation characteristics between in-air and in-water conditions. The comparison of in-air and in-water deformation characteristics reveals that it is not possible to achieve identical deformation characteristics, because the inertial forces are significantly reduced under in-water conditions. Second, the evolution of three-dimensional flow fields and unsteady forces are reported for surging and pitching flat plates in revolving motion starting from rest. Tomographic PIV measurements were carried out to acquire the three-dimensional flow fields with force measurements being simultaneously performed. The experiments were carried out for a number of parameters to explore the effects of acceleration period, Reynolds number, angle of attack, number of revolutions and pitch rate. Comparison of the force histories shows that the pitching wing generates considerably higher forces compared to the surging wing. Further analysis was performed to determine the reasons for the enhanced force generation of the revolving-pitching wing. It is shown that the increased force production is associated to a formation of additional circulation (bound and LEV), a higher growth rate of the LEV and more favourable vortex trajectories. It is also revealed that the force generation phenomenon is relatively insensitive to the Reynolds number. Moreover, the forces at the steady-state phase do not depend on the motion kinematics and force histories in the start-up phase.

Samenvatting

De groeiende behoefte aan mobiele luchtplatformen die geschikt zijn voor verkenningstaken in gevaarlijke en fysiek ontoegankelijke gebieden heeft geleid tot een toenemende belangstelling voor de ontwikkeling van micro aerial vehicles (MAVs), gezien hun potentiële capaciteiten voor veelzijdige en zeer wendbare vliegbewegingen. In het bijzonder flappende-vleugel configuraties, die vaak hun inspiratie ontlenen aan de natuur, hebben onderzoekers geïnspireerd vanwege hun mogelijke voordelen ten opzichte van meer conventionele (vaste en roterende vleugel) configuraties. In tegenstelling tot deze configuraties, profiteren flappende-vleugel systemen van de instationaire stromingseffecten die zijn geassocieerd met de grootschalige wervelstructuren die worden afgescheiden van de voor- en achterzijde van de vleugel. Dit resulteert in gebieden van lage druk rondom de vleugels die leiden tot een generatie van hogere lift- en stuwkrachten. In dit kader voert dit proefschrift een experimenteel onderzoek uit naar de aerodynamische mechanismen van flappende-vleugel fenomenen door het gebruik van state-of-the-art stromingsmeettechnieken, die in staat zijn tot het leveren van tijdsopgeloste driedimensionale informatie. De studie is verdeeld in twee delen, waarbij flappende-vleugel aerodynamica wordt onderzocht in het kader van een flappende-vleugel MAV (deel I) en in een generieke experimentele opstelling om meer fundamentele kennis en inzicht te vergaren (deel II).

Het eerste deel bestaat uit studies uitgevoerd aan de flappende-vleugel MAV DelFly II. Eerst zijn de aerodynamische prestaties van de DelFly II bepaald, door middel van uitgebreide meting van krachten, vermogensverbruik en vleugeldeformaties. Krachten en vermogensverbruik werden gemeten onder lucht- en vacuümcondities om de bijdrage die is geassocieerd aan de aerodynamische effecten te kunnen identificeren. Vervolgens zijn de krachtbalansmetingen vergeleken met de krachten afgeleid uit de visuele waarneming van de dynamica in vrije vlucht, om zo de effecten van de krachtmetingen op een gefixeerd model te karakteriseren, die enerzijds de dynamische lichaamsbewegingen in werkelijke vrije vluchtcondities beperken, en anderzijds modelvibraties introduceren, die afhankelijk zijn van de inklempositie. Uit de vergelijking van de instationaire krachten verkregen volgens de twee methoden blijkt dat de X-krachtcomponent (d.w.z., de krachtcomponent in de langsrichting van de DelFly) een goede overeenkomst toont, terwijl de Z-krachtcomponent afwijkingen vertoont afhankelijk van de vluchtconditie. Redenen voor de verschillen en de belangrijkste nadelen van de beide krachtbepalingstechnieken worden besproken. Tevens zijn ook de effecten onderzocht van de flap-frequentie, vleugeldikte en vleugelgeometrie op de aerodynamische prestaties in hovercondities (stil hangen in de lucht) in termen van kracht en het stroomverbruik. Om de relatie tussen de krachtproductie mechanismen en vleugeldeformatie karakteristieken te beoordelen zijn specifieke structurele deformatie metingen uitgevoerd aan de flappende vleugels van de DelFly. Deze metingen geven informatie over de effecten van de flap-frequentie en de vleugeldikte op de krachtproductie mechanismen en de vermogensverbruikskenmerken in termen van zowel amplitude en temporele evolutie.

Vervolgens zijn stromingsveldmetingen rondom de vleugel en in het zog van de DelFly in hover en voorwaartse vliegomstandigheden verricht met behulp van vlakke en stereoscopische particle image velocimetry (stereo-PIV) meettechnieken. De visualisaties van de wervelstructuren rond de vleugels onthullen de formatie-, afstotings- en interactiemechanismen, met het visualiseren van de klap-en-pel beweging van de DelFly vleugels in het bijzonder. Een versimpelde impulsbalans toegepast op een controle volume rond de DelFly in de hoverconfiguratie is gebruikt om een schatting te maken van de gemiddelde krachtscomponent in X-richting onder een aantal vereenvoudigende veronderstellingen. Deze benadering, die alleen de snelheid in stromingsrichting op een stroomafwaarts gelegen plaats gebruikt, is in staat om de krachten binnen een foutmarge van $5-15$ % te berekenen. De stromingsveldmetingen in het zog van de flappende-vleugels in de voorwaartse vlucht configuratie zijn gebruikt om driedimensionale zogsstructuren te reconstrueren. Twee zogreconstructiestrategieën zijn vergeleken: (1) een ruimte-tijd reconstructie op basis van de hypothese van de Taylor; (2) een ruimtelijke reconstructie met behulp van een gemodificeerde Kriging regressietechniek, die rekening houdt met de meetonzekerheid. Er is aangetoond dat vleugel-vleugel interactie aan het begin van uitgaande slag (peel beweging) de dominante eigenschap voor gereduceerde frequenties van meer dan 0.62, terwijl deze eigenschap wordt relatief inactief wordt bij lagere gereduceerde frequenties.

In het tweede deel worden experimentele studies met betrekking tot het fundamenteel onderzoek aan de flappende-vleugel vlucht gerapporteerd. Ten eerste zijn de effecten van de vleugelflexibiliteit op de instationaire stroming rond een flexibele vleugel onderhevig aan een klap-en-peel flappende-beweging onderzocht door middel van tomografische PIV metingen die zijn uitgevoerd in een watertank. De tweedimensionale Euler-Bernoulli balkvergelijking is gebruikt om de vervormingen in de richting van de vleugelkoorde van de translerende dunne plaat te simuleren en de vervormingseigenschappen tussen de condities in lucht en in water te vergelijken. Uit de vergelijking blijkt dat het niet mogelijk is om dezelfde vervormingskenmerken te krijgen omdat de traagheidskrachten significant verminderd zijn in wateromstandigheden. Ten tweede is de ontwikkeling van de driedimensionale stromingsvelden en instationaire krachten onderzocht voor versnellende ("surging") en roterende ("pitching") vlakke platen die een draaiende beweging ondergaan vanuit rust. Tomografische PIV metingen zijn uitgevoerd om de drie-dimensionale stroming velden te verwerven, hierbij zijn tevens krachtmetingen gelijktijdig uitgevoerd. De experimenten zijn uitgevoerd met variatie van een aantal parameters om zo de effecten van versnellingsperiode, Reynoldsgetal, invalshoek, aantal omwentelingen en rotatiesnelheid te onderzoeken. De vergelijking van de krachtgeschiedenis toont aan dat de pitching vleugel aanzienlijk hogere krachten genereert in vergelijking tot de versnellende vleugel. Verdere analyse werd uitgevoerd om de redenen voor de verhoogde krachtgeneratie van de draaiende-pitching vleugel te bepalen. Het is aangetoond dat de verhoogde kracht productie kan worden gerelateerd aan een formatie van extra circulatie (gebonden en LEV), een sterkere groei van de LEV en gunstigere werveltrajecten. Het is ook gebleken dat de krachtgeneratie relatief ongevoelig is voor het Reynoldsgetal. Bovendien hangen de krachten in de stationaire fase niet af van de bewegingskinematica en de krachthistorie in de opstartfase.

Acknowledgements

The present dissertation owes its existence to hard work, patience and many sleepless nights in addition to the help, support and inspiration provided by several people. In this last chapter, I would like to express my sincere appreciation to those who have contributed to this thesis in one way or another.

I am grateful to my supervisor, dr. ir. Bas van Oudheusden, for giving me the opportunity to pursue this research and guiding me with competence and dedication. I am thankful to you, Bas, not only for motivating me to achieve my goals and being available whenever I need but also for being a very patient and understanding person.

I would like to extend my thanks to my promoter, prof. dr. Fulvio Scarano, for fruitful discussions and wealth of ideas in addition to his guidance with a great enthusiasm.

I would also like to thank my co-supervisor, dr. Guido de Croon, for his support and constructive criticism both throughout the Ph.D. research and in the preparation of the book.

This work would not have been possible without the helps and efforts of the MAVLab group. Particularly, I thank Bart Remes, Rick Ruijsink, Christophe de Wagter, Erik van der Horst and Sjoerd Tijmons for many enlightening discussions, inspiration and teaching me how to deal with small-scale electronics.

Special thanks to Colette Russo for her patience, understanding and assistance with the administrative issues. I would like to thank the technical staff members of the Aerodynamics group, Peter Duyndam, Frits Donker Duyvis, Stefan Bernardy, Nico van Beek, Eric de Keizer, Henk-Jan Siemer and Leo Molenwijk for their assistance in providing required equipment and the realization of the experimental setups.

I would also like to express my gratitude to those with whom I collaborated throughout the Ph.D. period. I thank Jouke de Baar for providing the Kriging regression tool that has been used widely in this study. Thanks to Joao Caetano for his valuable friendship and productive discussions. Special thanks to Shuanghou Deng for his company during long-lasting days of experiments, friendship and being available to help whenever I need. Thanks to Maarten Vanierschot for the collaboration and the good company during the experiments. I would like to extend my thanks to the master students I have worked with: Jerke Eisma, Andries Koopmans, Andrea Tenaglia, Lisa Ziegler, Vinod Anantharaman, Roeland Vester and Remco van de Meerendonk for their contribution to the project and friendships. Special thanks to Remco for his valuable help with the translation of the summary.

I would like to thank all my colleagues at the Aerodynamic Section of TU Delft for the company during long office days. Special thanks to Ilya, Andrea, Vahid and Wouter for the good company in the office during the last year of my Ph.D. period. Thanks to Stefan, Valeria, Beppe, Theo, Giuseppe, Iliass, Thijs, Rogier, Kyle, Thomas, Jan, Jacobo, Qingqing, Linfeng, Lei, Matteo, Daniele and Marius for the friendly conversations and their helps whenever needed. I would like to extend my thanks to my friends from Eindhoven, Ergün,

Güneş and İlhan for their support and helpfulness. I would also like to thank Burak, Yakup, Aylin, Çiğdem, Çağrı and all my friends in Delft for all the fun we had together.

I would like to thank Sedat for being such a good friend, all those pleasant moments and wonderful memories. I would also like to thank Caner, Murat, Enes and Koray for their supports and friendships.

At last but not least, I want to thank you, Özge, for your love, unconditional support and being always there. I couldn't have done all these without you taking care of me. I am also curious about the next challenge we have to fight against together.

Hayatım boyunca benden karşılıksız desteğini esirgemeyen, beni nice fedakarlıklarla yetiştirip bugünlere gelmemde çok büyük pay sahibi olan, senelerce yokluğuma katlanan ve uzakta da olsalar varlıklarını her zaman yanımda hissettiğim, başta annem Firdevs ve babam Hüseyin olmak üzere tüm ailem; size ne kadar teşekkür etsem azdır. İyi ki varsınız.

Mustafa Perçin
Delft, August 2015

Curriculum Vitæ

Mustafa PERÇİN

10-06-1984 Born in Izmir, Turkey.

Education

2010–2015 **Doctor of Philosophy**
Thesis Title: *Aerodynamic mechanisms of flapping flight*
Aerospace Engineering
Delft University of Technology, Delft, the Netherlands

2009–2010 **Research Master**
Project Title: *Experimental study in injection system of inductively coupled plasma torch for nanoparticle production*
Environmental and Applied Fluid Dynamics
von Karman Institute for Fluid Dynamics, Rhode-Saint-Genése, Belgium

2007–2009 **Master of Science**
Thesis Title: *Flow around a plunging airfoil in a uniform flow*
Aeronautical-Astronautical Engineering
Istanbul Technical University, Istanbul, Turkey

2002–2007 **Bachelor of Science**
Graduation Project: *Experimental investigation of wake of a bluff body with a span-wise modification*
Aerospace, Aeronautical and Astronautical Engineering
Istanbul Technical University, Istanbul, Turkey

Experience

2014–Present	**Post-Doctoral Researcher** Delft University of Technology, Delft, the Netherlands
2010–2014	**Ph.D. Researcher** Delft University of Technology, Delft, the Netherlands
2006	**Internship** von Karman Institute for Fluid Dynamics, Rhode-Saint-Genése, Belgium
2005	**Internship** Turkish Aerospace Industries, Ankara, Turkey

List of Publications

Journal Articles

- **M. Percin**, B. W. van Oudheusden, *Flow visualization and force measurements on revolving surging and pitching flat plates: a parametric study*, Physics of Fluids, *to be submitted.*

- M. Vanierschot, **M. Percin**, B. W. van Oudheusden, *On the structure of double helix vortex breakdown in turbulent jet flow*, Journal of Fluid Mechanics, *to be submitted.*

- S. Deng, **M. Percin**, B. W. van Oudheusden, H. Bijl, B. D. W. Remes, T. Xiao, *Numerical simulation of a flexible X-wing flapping wing micro-air-vehicle*, Bioinspiration & Biomimetics, *submitted.*

- **M. Percin**, B. W. van Oudheusden, G. C. H. E. de Croon, B. D. W. Remes, *Force generation and wing deformation characteristics of a flapping-wing micro air vehicle 'DelFly II' in hovering flight*, Bioinspiration & Biomimetics, *submitted.*

- S. Deng, **M. Percin**, B. W. van Oudheusden, *Experimental investigation of the aerodynamics of a flapping-wing micro air vehicle by force and flow field measurements*, AIAA Journal, *accepted.*

- J. V. Caetano, **M. Percin**, B. W. van Oudheusden, B. Remes, C. de Wagter, G. C. H. E. de Croon, C. C. de Visser, *Error analysis and assessment of unsteady forces acting on a flapping wing micro air vehicle: free-flight versus wind tunnel experimental methods*, Bioinspiration & Biomimetics, **10(5)**, 2015.

- **M. Percin**, B. W. van Oudheusden, *Three-dimensional flow structures and unsteady forces on pitching and surging revolving flat plates*, Experiments in Fluids **56(2)**, 1–19, 2015.

- **M. Percin**, B. W. van Oudheusden, H.E. Eisma, B. D. W. Remes, *Three-dimensional vortex wake structure of a flapping-wing micro aerial vehicle in forward flight configuration*, Experiments in Fluids **55(9)**, 1–16, 2014.

- S. Deng, **M. Percin**, B. van Oudheusden, B. Remes, H. Bijl, *Experimental investigation on the aerodynamics of a bio-inspired flexible flapping wing micro air vehicle*, International Journal of Micro Air Vehicles **6(2)**, 105–116, 2014.

- J. H. S. de Baar, **M. Percin**, R. P. Dwight, B. W. van Oudheusden, H. Bijl, *Kriging regression of PIV data using a local error estimate*, Experiments in Fluids **55(1)**, 1–13, 2014.

- **M. Percin**, Y. Hu, B. van Oudheusden, B. Remes, F. Scarano, *Wing flexibility effects in clap-and-fling*, International Journal of Micro Air Vehicles **3(4)**, 217–228, 2011.

Conference Proceedings

- **M. Percin**, B. W. van Oudheusden, B. Remes, *Force generation and wing deformation characteristics of the 'DelFly II' MAV in hovering flight conditions*, International Micro Air Vehicles Conference and Flight Competition (IMAV2015), Aachen, Germany, September 15–18, 2015, *accepted*.

- **M. Percin**, B. W. van Oudheusden, *Flow visualization and force measurements on accelerated revolving flat plates at low Reynolds numbers*, 45th AIAA Fluid Dynamics Conference, Dallas, Texas, the USA, June 22–26, 2015.

- S. Deng, T. Xiao, **M. Percin**, B. W. van Oudheusden, H. Bijl, B. Remes, *Numerical simulation of an X-wing flapping wing MAV by means of a deforming overset grid method*, 45th AIAA Fluid Dynamics Conference, Dallas, Texas, the USA, June 22–26, 2015.

- **M. Percin**, B. W. van Oudheusden, *Three-dimensional flow fields and forces on revolving flat plates*, 67th Annual Meeting of the APS Division of Fluid Dynamics, San Francisco, California, the USA, November 23–25, 2014.

- **M. Percin**, L. Ziegler, B. W. van Oudheusden, *Flow around a suddenly accelerated rotating plate at low Reynolds number*, 17th International Symposium on Applications of Laser Techniques to Fluid Mechanics, Lisbon, Portugal, July 7–10, 2014.

- S. Deng, **M. Percin**, B. W. van Oudheusden, *Aerodynamic characterization of 'DelFly Micro'in forward flight configuration by force measurements and flow field visualization*, 2014 Asia-Pacific International Symposium on Aerospace Technology (APISAT2014), Shanghai, China, September 24–26, 2014.

- A. Tenaglia, **M. Percin**, B. W. van Oudheusden, S. Deng, B. Remes, *Vortex formation and force generation mechanisms of the DelFly II in hovering flight*, International Micro Air Vehicle Conference and Competition (IMAV2014), Delft, the Netherlands, August 12–15, 2014.

- S. Deng, **M. Percin**, B. W. van Oudheusden, A. Tenaglia, B. Remes, *Force and flow field measurements of a bio-inspired flapping-wing MAV 'DelFly Micro' in hovering flight*, 32nd AIAA Applied Aerodynamics Conference, Atlanta, Georgia, the USA June 16–20, 2014.

- J. V. Caetano, **M. Percin**, C. C. de Visser, B. W. van Oudheusden, G. C. H. E. de Croon, C. de Wagter, B. Remes, M. Mulder, *Tethered vs. free flight force determination of the DelFly II Flapping Wing Micro Air Vehicle*, International Conference on Unmanned Aircraft Systems (ICUAS), Orlando, Florida, the USA, May 27–30, 2014.

- S. Deng, B. W. van Oudheusden, B. Remes, **M. Percin**, H. Bijl, R. Ruijsink, *Experimental investigation of the flapping performance on 'Delfly Micro'*, International Micro Air Vehicle Conference and Flight Competition (IMAV2013), Toulouse, France, 17–20 September, 2013.

- **M. Percin**, J. H. S. de Baar, B. W. van Oudheusden, R. P. Dwight, *Three-dimensional wake reconstruction of a flapping-wing MAV using a Kriging regression technique*, 10th International Symposium on Particle Image Velocimetry, Delft, the Netherlands, July 1-3, 2013.

- W. B. Tay, **M. Percin**, B. W. van Oudheusden, H. Bijl, O. Cetiner, M. Unal, *Numerical and experimental analysis of tandem flapping flight*, 43rd AIAA Fluid Dynamics Conference, San Diego, California, the USA, June 24–27, 2013.

- **M. Percin**, H. E. Eisma, J. H. S. de Baar, B. W. van Oudheusden, B. Remes, R. Ruijsink, C. Wagter, *Wake reconstruction of flapping-wing MAV DelFly II in forward flight*, International Micro Air Vehicle Conference and Flight Competition (IMAV2012), Braunschweig, Germany, July 3–6, 2012.

- **M. Percin**, H. E. Eisma, B. W. van Oudheusden, B. Remes, R. Ruijsink, C. de Wagter, *Flow visualization in the wake of flapping-wing MAV 'DelFly II'in forward flight*, 30th AIAA Applied Aerodynamics Conference, New Orleans, Louisiana, the USA, June 16–20, 2012.

- **M. Percin**, Y. Hu, B. W. van Oudheusden, F. Scarano, *Wing flexibility effects in clap-and-fling*, International Micro Air Vehicle Conference and Flight Competition (IMAV2011), Nunspet, the Netherlands, September 12–15, 2011.

Contributed Reports

- Extensions of Fundamental Flow Physics to Practical MAV Aerodynamics, NATO STO Technical Report (AVT-202), 2012–2014.

- Characterization of Bio-Inspired Micro Air Vehicle Dynamics, NATO STO Technical Report (AVT-184), 2010–2012.

Books

- G. C. H. E. de Croon, **M. Percin**, B. D. W. Remes, R. Ruijsink, C. de Wagter, *The DelFly - Design, Aerodynamics, and Artificial Intelligence of a Flapping Wing Robot*, Springer, to be available in September 2015.